ISSN-Printed: 2536-5010
ISSN-Online: 2536-5134

Volume 12, No 2, 2022

EJT

EUROPEAN JOURNAL OF TECHNIC

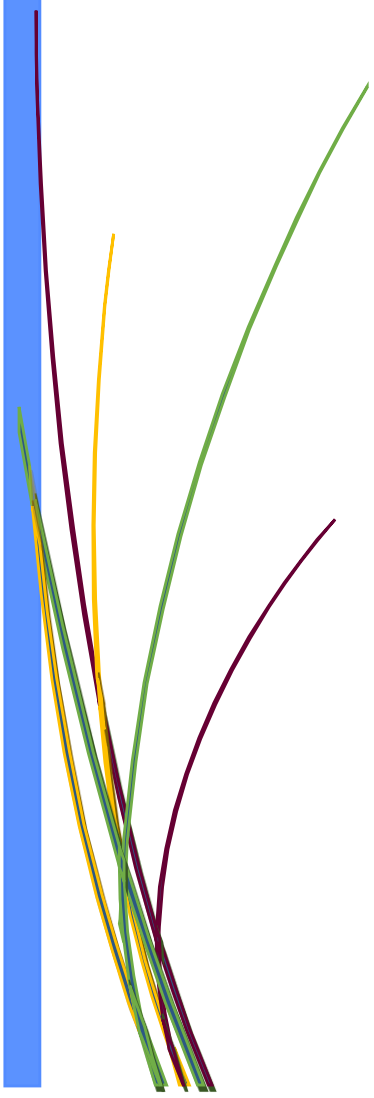

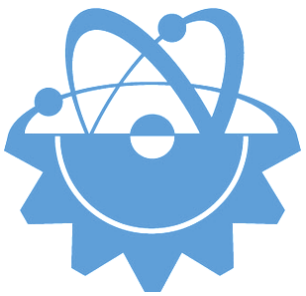

INESEG

Email (for orders and customer services enquiries): info@ineseg.org, ejt@ineseg.org
Visit our home page on www.ineseg.org

EUROPEAN JOURNAL OF TECHNIQUE (EJT)
ISSN-Printed: 2536-5010
ISSN-Online: 2536-5134

Scope: European Journal of Technique (EJT) established in 2010. It is a peer –reviewed international journal to be of interest and use to all those concerned with research in various fields of, or closely related to, Engineering disciplines. European Journal of Technique (EJT) aims to provide a highly readable and valuable addition to the literature which will serve as an indispensable reference tool for years to come. The coverage of the journal includes all new theoretical and experimental findings in the fields of Engineering or any closely related fields. The journal also encourages the submission of critical review articles covering advances in recent research of such fields as well as technical notes.

The scopes include:

- Mechanical Engineering
- Textile Engineering
- Electrical-Electronics Engineering
- Computer and Informatics Engineering
- Civil and Architecture Engineering
- Mining Engineering
- Chemical Engineering
- Metallurgical and Materials Engineering
- Environmental Engineering
- Food Engineering
- Geological Engineering
- Industrial Engineering
- Renewable Energy

EDITORIAL BOARD MEMBERS

Editor-in-Chief

- Musa YILMAZ

Publisher Of Journal

- Heybet KILIÇ

ETHICS and POLICIES

European Journal of Technique (EJT) is committed to following the Code of Conduct and Best Practice Guidelines of COPE (Committee on Publication Ethics). It is a duty of our editors to follow Cope Guidance for Editors and our peer-reviewers must follow COPE Ethical Guidelines for Peer Reviewers We expect all prospective authors to read and understand our Ethics Policy before submitting any manuscripts to our journals.

Please note that submitted manuscripts may be subject to checks using the iThenticate service, in conjunction with CrossCheck, in order to detect instances of overlapping and similar text.

The iThenticate software checks submissions against millions of published research papers, documents on the web, and other relevant sources. If plagiarism or misconduct is found, consequences are detailed in the policy.

The chief goal of our policy is threefold: to provide advice for our authors, to maintain the scholarly integrity of our journals and their content, and to detail the ethical responsibilities of EJT, our editors and authors.

We expect all authors to read and understand our ethics policy before submitting to any of our journals. This is in accordance with our commitment to the prevention of ethical misconduct, which we recognise to be a growing problem in academic and professional publications. It is important to note that most incidents of plagiarism, redundant publication, copyright infringement or similar occur because of a lack of understanding, and not through fraudulent intent. Our policy is one of prevention and not persecution.

If you have any questions, please contact the relevant editorial office, or European Journal of Technique (EJT)' ethics representative: ejtineseg@gmail.com

Download a PDF version of the Ethics and Policies [PDF,392KB].

Authors' Responsibilities

Authors should:

- Ensure that all researched work submitted is original, fully referenced and that all authors are represented accurately. The submission must be exclusive and not under consideration elsewhere.
- Provide accurate contact details for a designated corresponding author, who shall be deemed by the publisher and editor as fully responsible for the authorship of the paper and all communications concerning the ethical status and originality of the paper. This includes any queries or investigations that may arise, pre- or post publication.
- Openly disclose the source of all data and third party material, including previously unpublished work by the authors themselves. Anything that could compromise the originality of the submission should be expressly avoided and/or discussed with the editorial office in the first instance.
- Identify any third party material that they intend to include in their article, and obtain written permission for re-use in each instance from the relevant copyright holders. Such permissions should be submitted once the manuscript is accepted, or requires small changes to be accepted. For further guidance on seeking permission to use 3rd party material please see the Rights and Permissions section.
- Openly disclose any conflict of interest - for example, if publication were to benefit a company or services in which the author(s) has a vested interest.

- Expect to formally agree publication terms which defines the author and the publishers rights for the work. Visit our website for further information.
- Expect the editor to scan submissions using plagiarism detection software at iThenticate to check a paper's originality before sending out for review.
- Fully correspond and comply with the editor and publisher in any requests for source data, proof of authorship or originality in a timely manner, providing reasonable explanation for discrepancies or failures to disclose vital information.
- Fully co-operate with any consequent investigations if the editor and/or publisher are dissatisfied with the evidence available or the explanations provided.
- Expect transparency, efficiency and respect from the publisher and the editor during the submissions process.
- Remain in good communication with both the publisher and the editor.
- When necessary, submit corrigenda in a timely and responsible fashion.
- Co-operate fully with the publication of errata and with the retraction of articles found to be unethical, misleading or damaging.
- Remain in good communication with the editor(s), the publisher and any co-authors.

Editors' Responsibilities

Editors should:

- Read and understand COPE guidelines as well as EJT's ethics policy, and follow them during all editorial processes.
- Protect the reputation of their journal(s) and published work by only publishing content of the highest quality and relevance in a timely and responsible manner.
- Carry out thorough, objective and confidential peer review for original article submissions that pass the initial quality check and editorial assessment, in adherence with COPE guidelines and EJT' ethics policy.
- Detail and justify any article types which will not be peer reviewed (e.g. editorials, opinion pieces etc.).
- Provide a transparent review and publication process as far as is possible, with full respect and care paid to the author(s).
- Provide advice and give reasonable explanation and updates to authors during the submissions process and once a decision has been made.
- Allow authors the right to appeal any editorial decision.
- Only accept papers based on the original merit, quality and relevance of their content.
- Support authors in queries concerning the originality of their submissions and request the support of EJT if necessary.
- Advise the publisher of any third party material which has been included for which they do not believe sufficient permission has been cleared.

- Be ready and prepared to publish corrections, corrigenda, errata when necessary, as well as retract articles that (the editor and EJT) deem unethical, misleading or damaging.
- Remain in good communication with both the publisher and the author(s).

Reviewers' Responsibilities

Reviewers should:

- Adhere to EJT's policy of confidential peer review of their journals. This includes, but is not restricted to, keeping their identity hidden from authors and not externally distributing any work that is passed to them for their eyes only.
- Only accept invitations to review work that is relevant to their own expertise and speciality.
- Review submitted work in a responsible, impartial and timely manner.
- Report any suspected ethical misconduct as part of a thorough and honest review of the work.
- Avoid the use of unnecessarily inflammatory or offensive language in their appraisal of the work.
- Accept the commitment to review future versions of the work and provide 'follow up' advice to the editor(s), if requested.
- Seek advice from the editor if anything is unclear at the time of invitation.
- Remain in good communication with both the publisher and the editor.

EJT's Responsibilities

EJT will:

- Protect the reputation of our journals and published work by only publishing content of the highest quality and relevance in a timely and responsible manner.
- Provide detailed information concerning both our understanding of publication ethics and our implementation of the same. Emphasise a desire for prevention, not eventual detection, of ethical misconduct.
- Uphold our COPE membership (or of such similar organisations) and keep our editorial offices, publishing staff and society partners up-to-date with their guidelines and policies, adapting our own where appropriate (and publicising any update).
- When necessary, request proof of originality/accuracy from the corresponding author of any work submitted to any of our journals.
- Use plagiarism detection software when necessary for any submission to any journal at any stage of the submissions and publication process.
- Provide a transparent submissions and publication process, with full respect and care paid to the author. This includes detailed and dedicated instructions to authors for each journal, outlining referencing style, accepted article types and submission processes.
- Investigate thoroughly any suggestion of ethical misconduct detected during any stage of the submissions process. This can include, but is not restricted to, the following: plagiarism, redundant publication, fabrication or misuse of data and authorial disputes.

- When necessary, retract articles that we deem to be unethical, misleading or damaging.
- When necessary, publish errata, corrigenda and retractions in a timely and responsible fashion, detailing the decision online in an open access format and publishing in print as soon as possible.
- Remain in good communication with editors, authors, reviewers and society partners (where applicable).

Further reading

- Authorship of the paper: Authorship should be limited to those who have made a significant contribution to the conception, design, execution, or interpretation of the reported study.
- Originality and plagiarism: The authors should ensure that they have written entirely original works, and if the authors have used the work and/or words of others that this has been appropriately cited or quoted.
- Data access and retention: Authors may be asked to provide the raw data in connection with a paper for editorial review, and should be prepared to provide public access to such data.
- Multiple, redundant or concurrent publication: An author should not in general publish manuscripts describing essentially the same research in more than one journal or primary publication. EJT do not view the following uses of a work as prior publication: publication in the form of an abstract; publication as an academic thesis; publication as an electronic preprint. Information on prior publication is included within each EJT and its journal Guideline for Authors.
- Acknowledgement of sources: Proper acknowledgment.
- Disclosure and conflicts of interest: All submissions must include disclosure of all relationships that could be viewed as presenting a potential conflict of interest.
- Fundamental errors in published works: When an author discovers a significant error or inaccuracy in his/her own published work, it is the author's obligation to promptly notify the journal editor or publisher and cooperate with the editor to retract or correct the paper.
- Reporting standards: Authors of reports of original research should present an accurate account of the work performed as well as an objective discussion of its significance.
- Hazards and human or animal subjects: Statements of compliance are required if the work involves chemicals, procedures or equipment that have any unusual hazards inherent in their use, or if it involves the use of animal or human subjects.
- Use of patient images or case details: Studies on patients or volunteers require ethics committee approval and informed consent, which should be documented in the paper.

EJT has also accessed and learned from the existing policies of other publishers and leading experts as well as open access articles that detail and define ethical misconduct.

- 'Plagiarism and the law', Joss Saunders, Learned Publishing, 23:279-202: http://www.ingentaconnect.com/content/alpsp/lp/2010/00000023/00000004/art00002
- iThenticate Plagiarism Resources: http://www.ithenticate.com/resources/6-consequences-of-plagiarism

Publisher of Journal

Heybey Kilic Dicle University, Turkey / TU Delft, Netherland

Vol 12, Number 2, 2022
European Journal of Technique (EJT)
ISSN: 2536-5134

CONTENTS

European Journal of Technique

journal homepage: https://dergipark.org.tr/en/pub/ejt

Vol.12, No.2, 2022

Electrode Area Analysis of EEG Signals Received from Schizophrenic Individuals

Omer Akgun[1*]

[1*]Marmara University, Computer Engineering Department, Maltepe, Istanbul, Turkey. (e-mail: oakgun@marmara.edu.tr).

ARTICLE INFO

Received: Jun., 17. 2022
Revised: Jul., 05. 2022
Accepted: Aug, 09. 2022

Keywords:
EEG
Schizophrenia
STFT
PSD Welch method

Corresponding author: *Omer Akgun*

ISSN: *2536-5010* | e-ISSN: *2536-5134*

DOI: https://doi.org/10.36222/ejt.1132451

ABSTRACT

It is very difficult to distinguish between healthy and schizophrenic individuals based on raw data. However, with the analyzes made, the separation of healthy and sick individuals from each other has become quite evident. In the study, EEG signals were obtained by means of electrodes from the anterior region, middle and posterior regions of the brain, and analyzed according to their positions. Apart from the time-amplitude graph, PSD and STFT analyzes have also performed the analyzes and the results were compared. As a result of this study, the results of PSD analysis are quite successful in distinguishing between healthy and schizophrenic individuals. In this sense, this method includes features that can be used by physicians for diagnostic purposes. In addition, the analysis results are compatible with each other and the results are meaningful. In particular, the results of PSD analyses give very distinctive results that can be used for diagnosis. In addition, the results of the analyzes made with the STFT method are also compatible with the PSD analyses, where healthy individuals have a trend of around 10 Hz, and individuals diagnosed with schizophrenia have a trend of up to 20 Hz.

1. INTRODUCTION

Schizophrenia (SZ) is a brain disease that is characterized by the destruction of social bonds, the formation of cognitive deficits, and the impoverishment of the emotional-volitional area of the personality, belonging to the psychosis family, which occurs as a result of a yet unknown pathology in the human population, leading to progressive, chronic mental disorders [1].

If SZ disease is not treated, it generally shows a progressive course and negatively affects the quality of life of the individual. As a result of deterioration in cognitive functionality, which is one of the main features of the disease, the patient also causes personal, social, social and economic negativities. This is largely due to the deterioration of the psychosocial functionality of patients with SZ. Patients have difficulties in developing social relationships, getting or maintaining a job, and even meeting their simple daily needs without environmental support [2, 3].

The prevalence of SZ is approaching 1 percent internationally. Its incidence is 0.8-1% of the total population, and its annual incidence reaches 2 million individuals[4, 5]. Although the conditions leading to SZ are still unclear, many studies suggest that genetic disorders due to strong family relationships play a vital role in the incidence of the disease [6, 7]. Like many common medical diseases in society, SZ is an inherited disorder that arises from the interaction of both genetic and environmental sources. However, unlike disorders such as Huntington's disease, which is the result of a dominant mutation in a single gene, SZ is a common genetic variant such as type 2 diabetes, and ischemic heart disease, but also caused by common variants of many genes, each with a specific effect, but also such as culture, habits, and diet. It is a common medical disease caused by a complex gene/environment interaction that is also affected by other factors [8].

Along with the factors mentioned above, deprivations in individual psychology play an active role in the emergence of the disease. As a matter of fact, as reported in scientific research, it usually manifests itself with a high incidence in early adult people (between 15 and 25 years old) with low socio-cultural structure and income level, single and living alone, and progresses in episodes if not treated. The onset of the disease before the age of 10 and after the age of 60 is rare [4, 9, 10].

The drug treatment of SZ is complex. Treatment is usually a long-term process that lasts until the appropriate dose and drug are determined by trial and error method according to the patient. Antipsychotic drugs targeting positive symptoms are expensive and partially effective, and extrapyramidal side effects such as akathisia and tardive dyskinesia occur with the use of antipsychotics, and important side effects such as agranulocytosis and metabolic syndrome are are occur with the use of atypical antipsychotics [11]. Even if the existing drugs used in the treatment of SZ provide a significant improvement

in the positive symptoms of the disease in the long term, they do not show sufficient effect on the negative and cognitive symptoms. In addition, this area has become an important target in terms of new drug development due to the inability to provide adequate treatment with available medical facilities in typical SZ.

Traditional clinical diagnoses can sometimes be inaccurate because people with schizophrenia sometimes deliberately hide their symptoms, and experts sometimes have trouble distinguishing schizophrenia from other mental illnesses because of similar symptoms.

To meet this challenge, researchers have made incredible progress in recent years, particularly in specialized centers for diagnosing people suffering from mental disorders and improving care in the broader sense and therefore quality of life.

The various tools that have been developed greatly assist psychiatrists and clinical psychologists in diagnosing schizophrenia [12]. Today, apart from the blood test, brain elaritama, positron emission tomography (PET), computerized tomography (CT), which combines cross-sectional images (slices) of the brain from different angles in a computer environment with the help of a series of X-rays, magnetic field to create detailed images of brain tissues, today help in clinical diagnosis. With the help of the Magnetic Resonance Imaging (MRI) technique, which uses computer-generated radio waves and computer-generated radio waves, there is an effort to develop an objective, quantitative biomarkers that can increase the overall accuracy of diagnosis with the help of neuroimaging technologies [13].

Despite all these technological possibilities, definitive objective criteria for the diagnosis of schizophrenia have still not been found and the morphological changes in the brains of the patients that will help the diagnosis have not been fully demonstrated. On the other hand, as a result of functional and structural imaging studies, it was understood that the source of schizophrenic symptoms was distributed in more than one anatomical region. Among the various neuroimaging methods, electroencephalography (EEG) is considered one of the most useful methods due to its ability to directly measure neural activity in the brain, its high temporal resolution, its ability to manage cognitive activities in the absence of behavioural responses, and its low cost [12]. An EEG is a voltage-time graph where the vertical axis (y) is voltage and the horizontal (x) axis is frequency. It is the voltage difference between two electrode areas (at least one of which is on the scalp) placed at a given moment. With EEG analysis, it can be explained how the brain works, which regions of the brain are active and how the active regions communicate with each other.

In this study, spectral features were extracted by comparing EEG data from patients with and without schizophrenia. With this time-frequency analysis, the EEG data of patients and non-patients were compared and its usability for diagnosis was investigated.

2. DATA COLLECTION AND MATHEMATICAL BACKGRAOUND

In the archive where the data were taken [14], there are two groups of EEG data taken from two subject groups. 39 of them were healthy and 45 of them were from the group showing schizophrenic symptoms. The sampling frequency of the data is 128kHz. The topographic locations of the electrodes from which the EEG data were collected are shown in Figure 1. In the study, the analysis of the EEG signals taken from the Cz, F4, P4, Pz, T3 and O1 electrode regions was performed. MATLAB© package program was used in the analysis. In addition, analyzes were made using Welch and STFT mathematical approaches.

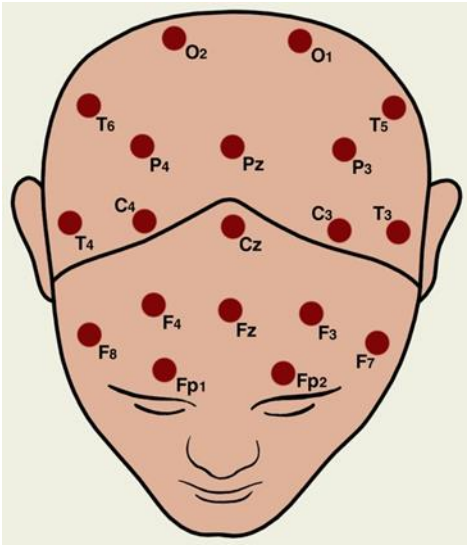

Figure 1. Representative map showing the locations of the electrodes [1]

2.1. Welch Method

The periodogram method used for GSY estimation of the frequency components of a signal is based on the Fourier transform. In order to obtain the GSY of a sign by the periodogram method, the sign is divided into the second power and frames such as 64, 128 and 256. In this method, the data is divided into overlapping segments and the GDP estimation is calculated by averaging the Fourier transform of each segment.

The disadvantage of non-parametric spectral estimation techniques such as the periodogram is that there are leaks in the lobes that occur in finite data sets. To overcome this problem, the Welch method was developed. The Welch method consists of 4 steps. First, the sign is divided into overlapping segments. Each segment of data is windowed to smooth the edges of the marks. Then, the periodogram of each windowed segment is taken and its estimated average is calculated. The Welch method estimates the power spectral density by averaging the improved periodograms. The i th improved periodogram is given in equation 1.

$$S_i(f) = \frac{Y}{K.M}\left|\sum_{n=1}^{M-1} x(n)w(n)e^{-j2\pi}\right|^2 \quad (1)$$

It is given as in the equation. Here f = fsnormalized frequency variable Ys scaling factor, $w(n)$ windowing function and K normalized constant, and the following expression is given.

$$K = \frac{1}{M}\sum_{n=0}^{M-1} w^2(n) \quad (2)$$

The power spectral density estimation of the Welch method is given in Equation 3. Here L is the length of the sign [15].

$$P(f) = \frac{1}{L}\sum_{i=0}^{L-1} S_i\,(f) \quad (3)$$

2.2. Short Time Fourier Transformation (STFT)

The short-time Fourier transform (STFT) is obtained by taking the classical Fourier transform of the signal divided by a time-shifting window. Spectrum estimation can be made by assuming that the part of the examined signal received with the window remains stationary.

FT is applied after the cue is passed through a defined window in the time domain. By shifting the window function in the time axis to cover the entire signal, frequency responses (frequency spectra) of the signal in time intervals in the width of the window function are obtained. In this way, it is as if the variation of the frequency response of the signal with time is obtained. Equation 4, which provides the STFT transformation, is given.

$$STFT(\tau, f) = \int_{-\infty}^{\infty} [x(t).w^*(t-\tau)].e^{-j2\pi ft}dt \quad (4)$$

Here; $x(t)$ is a principal sign, $w(t)$ is the window function, and * is the complex conjugate notation, translation in time. STFT consists of the FT of the sign multiplied by a window function. A new set of STFT coefficients is calculated for each t and f. As such, FT is a function of frequency only, while SFFD is a function of both frequency and time, and as such, it is three-dimensional (third-dimensional amplitude). STFT gains importance if the signal is not stationary. In this case, the signal is divided into segments that are considered stationary and the FT of each segment is different. If the sign is stationary, the FT each segment will be the same (or similar) and thus the CFFD and FT will be the same (or similar) [16-21].

3. DATA ANALYSIS of EEG SIGNALS of SCHIZOFRENIC AND NORMAL INDIVIDUALS

EEG signs of schizophrenic and normal individuals are given in Figure 2 and Figure 3 below. Figure 2 shows the time-amplitude graphs of healthy individuals according to the electrode positions. In terms of the comprehensiveness of the signs, the signs from each part of the brain were examined separately, and in terms of their significance, the electrodes in the anterior-middle and posterior parts were shown in the analysis. When Figure 2 and Figure 3 are examined, amplitude differences can be seen in the EEG data of healthy and schizophrenic patients.

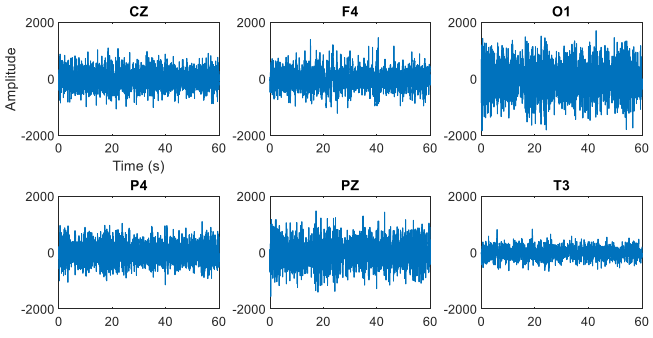

Figure 2 Time variation of EEG signals according to the positions of healthy individuals

In Figure 2, the amplitudes in the EEG data of healthy individuals have an amplitude of around 1000 dB, while in Figure 3 it can be seen that they reach higher amplitude values.

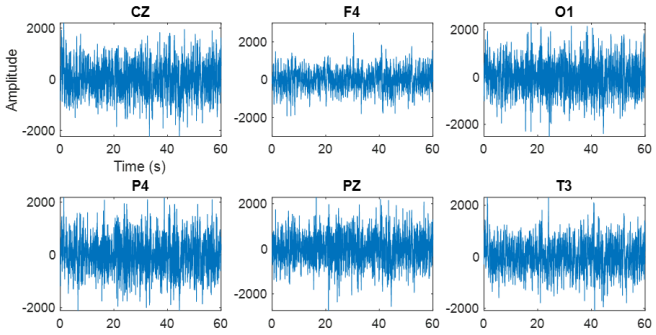

Figure 3. Change of EEG signals over time according to the positions of sick individuals

When an evaluation is made between the healthy and sick signs, it is seen that the amplitudes of the signals from the CZ, P4 and T3 electrodes are significantly higher than those of the sick ones. Especially in T3, this increase is at the maximum level.

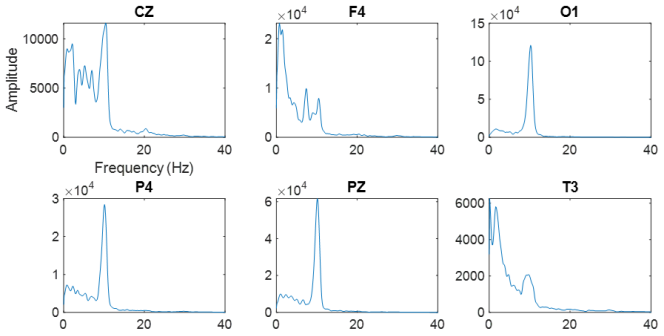

Figure 4. Change of power spectrum of EEG signals according to the positions of healthy individuals

Power spectrum analyzes of EEG signals were performed in Figure 4 and Figure 5. Power spectrum analysis of healthy individuals is given in Figure 4, and PSD analysis of EEG signs of individuals diagnosed with schizophrenia in Figure 5. Here, when the signals taken from the same electrodes are compared, it is seen that schizophrenic and healthy individuals can be detected very clearly in the analyzes with PSD. This application can be evaluated as an important criterion that can be used for diagnosis.

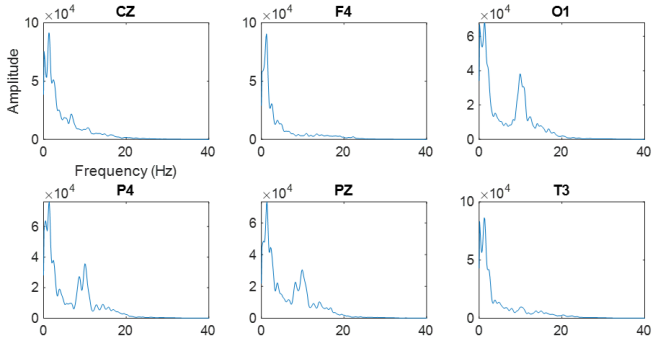

Figure 5. Change of power spectrum of EEG signals according to the positions of sick individuals

When the power spectrums are examined, an increase in the low frequency amplitudes of the diseased signals (delta and theta waves) compared to normal was observed in all electrode signals in general. This increase is more noticeable in the CZ, P4 and T3 electrodes. In high frequency waves (alpha, beta waves) a decrease and fading were observed in general. In particular, the amplitude decrease in O1 and PZ was observed as damping in the other electrodes.

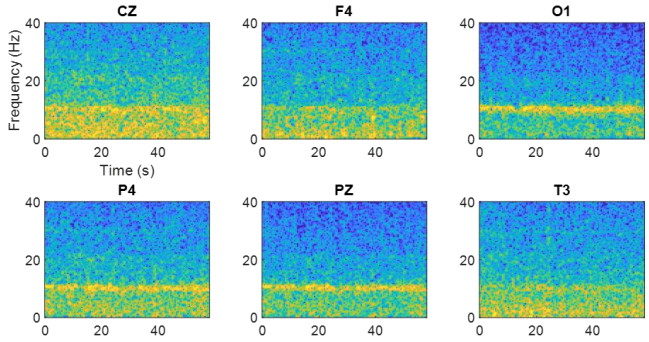

Figure 6. Spectrograms of EEG signals according to the positions of healthy individuals

STFT spectrograms of EEG data of healthy individuals and individuals diagnosed with Schizophrenia are given in Figure 6 and Figure 7. From the analyzes made here, it is possible to make a comparison in terms of frequency between healthy and schizophrenic individuals. In the analyzes made, it was determined that the EEG spectra were around 10 Hz in healthy individuals, while this value doubled, that is, around 20 Hz, although it varies according to the region where the electrodes are attached in patients diagnosed with schizophrenia.

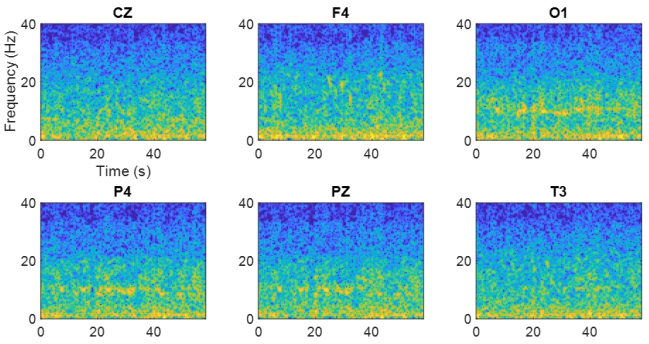

Figure 7. Spectrograms of EEG signals according to the positions of sick individuals

When the normal spectrograms are examined; It has been observed that alpha theta and delta waves are active in CZ, and alpha waves are very noticeable in the signals of O1, P4 and PZ electrodes. It is noteworthy that in general, alpha waves are considerably reduced in patient spectrograms. Again, in general, theta and delta waves are either protected or strengthened. Especially in O1 and P4 electrodes, theta and delta waves became stronger.

4. CONCLUSION

In this study, EEG data obtained from 39 healthy and 45 schizophrenic individuals were analyzed by time-frequency, PSD and Welch methods. It is very difficult to distinguish between healthy and schizophrenic individuals based on raw data. However, with the analyzes made, the separation of healthy and sick individuals from each other has become quite evident. In the study, EEG signals were obtained by means of electrodes from the anterior region, middle and posterior regions of the brain, and analyzed according to their positions. Apart from the time-amplitude graph, PSD and STFT analyzes have also performed the analyzes and the results were compared. As a result of this study, the results of PSD analysis are quite successful in distinguishing between healthy and schizophrenic individuals. In this sense, this method includes features that can be used by physicians for diagnostic purposes. In addition, the analysis results are compatible with each other and the results are meaningful.

REFERENCES

[1] Murashko, A. A., & Shmukler, A. (2019). EEG correlates of face recognition in patients with schizophrenia spectrum disorders: A systematic review. *Clinical Neurophysiology*, *130*(6), 986-996.

[2] Fond, G., Korchia, T., de Verville, P. S., Godin, O., Schürhoff, F., Berna, F., ... & Boyer, L. (2020). Major depression, sleep, hostility and body mass index are associated with impaired quality of life in schizophrenia. Results from the FACE-SZ cohort. *Journal of Affective Disorders*, *274*, 617-623.

[3] Rajji, T. K., Miranda, D., & Mulsant, B. H. (2014). Cognition, function, and disability in patients with schizophrenia: a review of longitudinal studies. *The Canadian Journal of Psychiatry*, *59*(1), 13-17.

[4] Mayorov, O. Y., & Fenchenko, V. N. (1996). Method of detection of schizophrenic row disorders at early stages in patients from groups with «functional psychoses» basing on EEG scaling indicators. *КЛІНІЧНА ІНФОРМАТИКА І ТЕЛЕМЕДИЦИНА*, *52*(3), 45.

[5] Rasool, S., ZeeshanZafar, M., Ali, Z., & Erum, A. (2018). Schizophrenia: An overview. *Clin Pract (Ther)*, *15*, 847-51.

[6] Rivollier, F., Lotersztajn, L., Chaumette, B., Krebs, M. O., & Kebir, O. (2014). Hypothèse épigénétique de la schizophrénie: revue de la littérature. *L'encephale*, *40*(5), 380-386.

[7] Stip, E., Chouinard, S., & Boulay, L. J. (2005). On the trail of a cognitive enhancer for the treatment of schizophrenia. *Progress in Neuro-Psychopharmacology and Biological Psychiatry*, *29*(2), 219-232.

[8] Pearlson, G. D., & Folley, B. S. (2008). Endophenotypes, dimensions, risks: is psychosis analogous to common inherited medical illnesses?. *Clinical EEG and neuroscience*, *39*(2), 73-77.

[9] Aydın, E. (2016). Vaka yönetiminin şizofreni hastalarının klinik belirtileri, sosyal işlevselliği ve yaşam kalitesi üzerine etkisi (Uzmanlık tezi). *İstanbul, İstanbul Üniversitesi*.

[10] Çetin, M., & Ceylan, M. E. (2005). AraĢtırma ve Klinik Uygulamada Biyolojik Psikiyatri. *Üçüncü baskı, Ġstanbul: Yerküre Tanıtım ve Yayıncılık Hizmetleri*, 83-124.

[11] Greenwood, T. A., Shutes-David, A., & Tsuang, D. W. (2019). Endophenotypes in schizophrenia: digging deeper to identify genetic mechanisms. *Journal of psychiatry and brain science*, *4*(2).

[12] Shim, M., Hwang, H. J., Kim, D. W., Lee, S. H., & Im, C. H. (2016). Machine-learning-based diagnosis of schizophrenia using combined sensor-level and source-level EEG features. Schizophrenia research, 176(2-3), 314-319.

[13] Soni, S., Muthukrishnan, S. P., Sood, M., Kaur, S., & Sharma, R. (2020). Altered parahippocampal gyrus activation and its connectivity with resting-state network areas in schizophrenia: An EEG study. *Schizophrenia Research*, *222*, 411-422.

[14] http://brain.bio.msu.ru/eeg_schizophrenia.htm

[15] Ömer, T. Ü. R. K., Özerdem, M. S., & Akpolat, N. (2015). Gözler açık/kapalı durumunda EEG bantlarındaki frekans değişiminin Güç Spektral Yoğunluğu ile belirlenmesi. Dicle Üniversitesi Mühendislik Fakültesi Mühendislik Dergisi, 6(2), 131-138.

[16] Seker, S., Akinci, T. C., & Taskin, S. (2012). Spectral and statistical analysis for ferroresonance phenomenon in electric power systems. Electrical Engineering, 94(2), 117-124.

[17] Kalin, F., Akinci, T. C., Türkpence, D., Seker, S., & Korkmaz, U. (2020). Detection of Epileptic Seizure Using STFT and Statistical Analysis. In *Advances in Neural Signal Processing*. IntechOpen.

[18] Akinci, T. C. (2011). The defect detection in ceramic materials based on time-frequency analysis by using the method of impulse noise. Archives of Acoustics, 36, 77-85.

[19] Kulakli, G., & Akinci, T. C. Psd and Wavelet Analysis of Signals from a Healthy and Epileptic Patient. The Journal of Cognitive Systems, 3(1), 12-14.

[20] Yilmaz, M. (2021). Wavelet Based and Statistical EEG Analysis in Patients with Schizophrenia. Traitement du Signal, 38(5).

[21] Akgün, Ö. (2011). Mitral Kapak Hastalıklarında Kalp Ses işaretlerinin Analizi (Doctoral dissertation, Marmara Universitesi (Turkey)).

BIOGRAPHIES

Omer Akgun is an assistant professor at the, Department of Computer Engineering, Technology Faculty, Marmara University. He received his first Ph.D. in the Communication Engineering in 2009 from Yildiz Technical University and the second Ph.D. in the Electronic and Communication Education Department in 2011 from Marmara University. His current research interests are signal processing, biomedical signal processing, signal modelling and communication systems

European Journal of Technique

journal homepage: https://dergipark.org.tr/en/pub/ejt

Vol.12, No.2, 2022

Comparison of Robust Machine Learning and Deep Learning Models for Midterm Electrical Load Forecasting

Fatma Yaprakdal[1*], **Fatih Bal**[2]

[1*] Kirklareli University, Electrical and Electronics Engineering Department, Kirklareli, Turkey. (e-mail: fatmayaprakdal@klu.edu.tr).
[2] Kirklareli University, Software Engineering Department, Kirklareli, Turkey. (e-mail: fatihbal@klu.edu.tr).

ARTICLE INFO

Received: Nov., 09. 2022
Revised: Nov., 16. 2022
Accepted: Nov, 23. 2022

Keywords:
Medium-term load forecasting
Machine learning
Deep learning
Aggregated-level forecasting
Feature selection

Corresponding author:
Fatma Yaprakdal

ISSN: *2536-5010* | e-ISSN: *2536-5134*

DOI: https://doi.org/10.36222/ejt.1201977

ABSTRACT

Electrical load forecasting (ELF) is gaining importance especially due to the severe impact of climate change on electrical energy usage and dynamically evolving smart grid technologies in the last decades. In this regard, medium-term load forecasting, a crucial need for power system planning (generation optimization and outages plan) and operation control, has become prominent in particular. Machine learning and deep learning-based techniques are currently trending approaches in electrical load estimation due to their capability to model complex non-linearity, feature abstraction and high accuracy, especially in the smart power systems environment. In this study, several load forecasting models based on machine learning methods which comprise linear regression (LR), decision tree (DT), random forest (RF), gradient boosting, adaBoost, and deep learning techniques such as recurrent neural network (RNN) and long short-term memory (LSTM) are studied for medium-term electrical load demand forecasting at an aggregated level. Performance metric results of these analyzes are presented in detail. State-of-the-art feature selection models are examined on the dataset and their effects on these forecasting methods are evaluated. Numerical results show that forecasting performance can be significantly improved. These results are validated by the results of other studies on the subject and found to be superior.

1. INTRODUCTION

The increase in the integration of renewable energy sources in power grids and the intermittent nature of these sources has increased the need for better resolution and accuracy of electrical load forecasting, while creating new problems. In addition, inadequacies in regional energy storage have made ELF extremely essential. Establishing the balance between energy production and consumption is a great necessity in today's modern power system operation, management and planning. Thus ELF plays an important role at this point [1].

In terms of time horizons, ELF methods can generally be split into three forecasting classes as short-term load forecasting (STLF), medium-term load forecasting (MTLF), and long-term load forecasting (LTLF). Although different forecasting horizons are defined in the literature for these categories; STLF, MTLF, and LTLF can last for a few minutes or hours to a week, a week to one year, and a few years up to decades, respectively. Each of these categories takes advantage of several forecasting methods to satisfy the certain objectives of application areas in power systems. In particular, the application areas of MTLF are of great importance as they are vital in power system operation, control and planning at any level such as generation, transmission, and distribution. A proper MTLF is required for getting a better generation and maintenance scheduling, planning programs in unit commitment, demand-side management, hydro thermal coordination, control of the system with many distributed energy resources, economic supply of different fuels, and more power system applications [2, 3].

According to the input data set, the load forecasting is divided into two levels as aggregated level (AL) and individual level (IL). While the dataset used for the forecast at AL contains aggregated datasets belonging to a certain group of end-users like system-level and feeder-level, a dataset of a specific building such as a residential building or commercial building is used for forecasting at IL.

On the other hand, there are various explicit factors such as weather-related factors, electric energy prices, days of the week, public holidays, economic indicators, and the population of a country or a region that affect the aggregated electrical energy consumption [4]. The effects of weather variables on the electricity consumption forecast are equally

addressed in STLF, while in MTLF these variables affect this forecast to a certain extent. In terms of explicit factors affecting the electrical load consumption in [5], it is recommended that MTLF be divided into two classes as the conditional modeling approach and the autonomous approach. Factors affecting the electrical energy consumption addressed in the conditional modeling approach are historical electrical energy consumption and weather data, socio-economic indexes and sustained energy policies. In addition to the electrical energy consumption forecast, weather and socio-economic situation forecasts are also taken into account in this approach. The parameters considered in the autonomous approach are only historical electrical energy consumption and weather data that involves values such as temperature, humidity, and wind speed. This approach is much more suitable for regions with strong economies and especially for forecasting periods of one year or less [5].

ELF methods are examined in two groups as parametric and non-parametric methods. Parametric methods are created on the basis of analytical models and non-parametric methods are created on the basis of artificial intelligence techniques. Among the non-parametric methods, especially machine learning (ML) and deep learning (DL) techniques are preferred more for ELF with the increase in their development rates in the past few years, as they can model the complicated and non-linear relationships between load and external factors [6].

In ELF algorithms, feature selection is extremely important because the sizes of input data are getting bigger with digitalization while the prediction models are complex as well. Feature selection can significantly improve the forecasting model performance by reducing the uncertainty of overfitting, improving the algorithm to a certain extent, and preventing irrelevant features used in training from increasing the system cost and runtime.

In recent decades, most existing works on ELF have focused on ML- and DL-based models due to their remarkable performance in the area. However, most of these studies are on STLF methods. There are a limited number of research studies in the literature regarding MTLF methods \cite{Han19}. Because of the reason that short-term forecasting can be done by fitting a model to a dataset computationally or statistically and then extending a graph, curve, or range of values by making inferences about unknown values from trends in the known data while medium-term forecasting is a completely different and complicated problem than short-term forecasting [7,8].

This paper presents a comparative analysis implementing state-of-the-art machine learning and deep learning methods on MTLF at AL. A great number of robust and most-practiced ELF models as of the date are performed: LR [9–12], DT [13], RF [14–16], gradient boosting [17, 18], AdaBoost [19–22] as the representatives of ML methods; RNN [23] and LSTM [24–29] as the representatives of DL models. The ELF results by all these methods have been achieved as daily forecasting steps for monthly forecasting intervals. In addition, feature selection as a technique that improves the overall performance of the system significantly has been realized based on the autonomous approach to the worked forecasting algorithms by using Pearson, random forest, chi-square, and light gradient boosting machine (Light-GBM) models; different from other existing forecasting methods.

This study is prepared as follows. Section 2 and Section 3 give detailed information on the materials and forecasting methods used, respectively. Section 4 shares experimental results by specifying them with different measurement techniques. These results are validated by related literature studies in Section 5. Finally, Section 6 presents a conclusion related to the overall study covering a few challenging points in MTLF and future aspects.

2. MATERIALS

2.1. Dataset

The electrical load consumption data is obtained as open-source from Czech Transmission System Operator (CEPS) for this study [30].

Electrical load data for the Prague region between January 1, 2015 and February 20, 2021 are used. The considered feature name for electrical load is LOAD-MW and distribution of the aggregated electrical load in TW (terawatt) can be seen in Figure 1. The weather information data belonging to the electrical load is taken from Nasa Power Data Access Viewer [31].Temperature (T2M), dew/frost Point (T2MDEW), wet bulb temperature (T2MWET), and relative humidity is taken for 2 meters. Wind speed (WS10M) and wind direction (WD10M) are taken for 10 meters. Wind speed (WS50M) and wind direction (WD50M) are taken for 50 meters. In addition, all-sky insolation incident on horizontal surface (CLRSKY-SFC-SW-DWN) precipitation (PRECTOT) and surface pressure (PS) are taken for prediction. The unit values and their short names for all features are shown in Table I.

TABLE I
THE UNIT VALUES AND SHORT NAMES FOR FEATURE NAME

#	Feature Name	Short Name	Unit
1	Electrical load	LOAD_MW	TW
2	All sky insolation incident on horizontal surface	CLRSKY_SFC _SW_DWN	kW/hr
3	Temperature at 2 meters	T2M	°C
4	Dew/Frost point at 2 meters	T2MDEW	°C
5	Wet bulb temperature at 2 meters	T2MWET	°C
6	Relative humidity	R2HM	%
7	Precipitation	PRECTOT	mm
8	Surface pressure	PS	kPa
9	Wind speed at 10 meters	WS10M	m/s
10	Wind direction at 10 meters	WD10M	Degrees
11	Wind speed at 50 meters	WS50M	m/s
12	Wind direction at 50 meters	WD50M	Degrees

2.2. Dataset Input Selection and Preparation

Feature selection evaluates the features piece by piece to determine how the features in the dataset are effective on the results. Feature selection methods are employed to reduce the number of relevant features.

Pearson feature selection is a correlation number which stays in the range -1 and 1. It indicates the degree that two variables are linearly related. As it gets closer to zero, a weaker correlation is meant to be found.

Chi-square feature selection aims to test the independence of two events. When the features are independent, the observed count becomes more similar to the expected count. As the chi-square value gets higher, the feature can be inferred to be more dependent on the response thus it can be selected.

In RF feature selection, each tree calculates the importance of a feature by increasing the pureness of the leaves. The

higher the increment in leaves purity the higher the importance of the feature.

Light-GBM feature selection utilizes tree-based learning. Light-GBM grows tree vertically while in parallel growing horizontally; ending up growing the tree leaf-wise and level-wise concurrently. The features selected after performing feature selection methods in this study are shown in Table II.

TABLE II
SELECTED FEATURES OF FEATURE SELECTION METHODS.
(TRUE: SELECTED, FALSE: NOT SELECTED)

Feature	Pearson	Chi-Square	Light GBM	Random Forest
LOAD_MW	Predict	Predict	Predict	Predict
CLRSKY_SFC_SW_DWN	True	True	True	True
T2M	True	True	True	True
T2MDEW	True	True	True	True
T2MWET	True	True	True	True
R2HM	True	False	True	True
PRECTOT	True	False	True	True
PS	True	True	True	True
WS10M	True	True	True	True
WD10M	False	False	False	False
WS50M	True	True	True	True
WD50M	False	False	False	False

3. METHODS

3.1. Linear regression

LR aims to find the best fit straight line or hyperplane for training samples. In this regard, a relationship between the dependent variable and one or more independent variables is provided using the best fit straight line, in other words the regression line.

3.2. Decision tree

DT aims to divide a dataset with many samples into smaller sets by finding a set of decision rules. Simple decision-making steps are learnt from the data for this purpose.

3.3. Random Forest

RF combines the predictions of many decision trees, aiming to end up a single result. It can simply handle classification and regression problems. RF is not heavily dependent on hyper-parameter estimation.

3.4. Adaptive boosting algorithms (AdaBoost)

In this model, learning is initialized by training a weak learner. In the next training, more priority is given to the incorrectly learned training data in the first step. Prioritized data are retrained by increasing their weight. It is continued by training the weak learner output to be the input to the other learner. At the end, the results are fused to form the final decision.

3.4.1 Gradient boosting algorithms

Gradient boosting is available both for regression and classification problems. A combination of weak predictive models typically creates a model of decision trees. The purpose of gradient boosting is to define and minimize a loss function.

3.4. Recurrent Neural Networks

RNN helps extracting information from sequences of time-series data. RNN allows previous outputs to be used as inputs while having hidden states. RNN architecture utilized in this work is described in the [32].

3.4. Long Short-Term Memory

LSTM is an improvement of RNN, originated from the problem of short-term memory. LSTM has feedback connections in addition to feed-forward connections. LSTM networks are well suited for making predictions based on time series data. A common LSTM unit composes of a cell, an input, output, and forget gates. The cell remembers values in variable-length time intervals and these three gates aims to regulate the information flow into and out of the cell. LSTM unit facilitated in this work is described in the [32].

4. EXPERIMENTAL RESULTS

4.1. Metrics

In this part of the study, the regression metrics used are mentioned. Mean squared error (MSE), mean absolute error (MAE) and mean absolute percentage error (MAPE) metrics are frequently practiced regression metrics in the related field in the literature. To more clearly compare the performance of our test results with the concerned studies, performance evaluations of test results are carried out with these metrics. MSE depicts the mean of the squared differences between predicted and expected values in a dataset.

$$MSE = \frac{1}{n}\sum_{j=1}^{n}\left|(A_j - F_j)^2\right|. \quad (1)$$

where Aj is the actual value, Fj is the forecast value and n is the total number of test samples. MAE and MAPE are defined similarly in what follows

$$MAE = \frac{1}{n}\sum_{j=1}^{n}\left|A_j - F_j\right|. \quad (2)$$

4.2. Results

The results related to the prediction of electrical load are shown in Table III, IV, V. According to all these tables it seen that in the application without feature selection, the model that gives the best results is the LSTM model with the MAPE value which is evaluated as 8.66%. Among the models made by applying Pearson, RF and Light-GBM feature selection techniques, the model that gives the best result according to the MAPE value is the LSTM model with 2.02%. Based on chi-square feature selection results, LSTM gives the best result in the MAPE metric evaluation, with the value of 2.12%. Graphical comparisons of the actual and predicted electrical load values for the best performing models are illustrated in Figure 1.

TABLE III
THE RESULTS OF THE REGRESSION MODEL PERFORMED ON DATA WITHOUT USING FEATURE SELECTION.

Model	MAE (%)	MSE (%)	MAPE (%)
Random Forest	1,38	3,30	10,93
Decision Tree	3,17	4,30	11,09
Linear Regression	6,32	8,01	14,78
Ada Boosting	6,42	0,67	13,45
Gradient Boosting	6,11	0,60	13,36
RNN	1,23	2,61	12,18
***LSTM**	2,04	0,22	8,67

TABLE IV
THE RESULTS OF REGRESSION MODELS PERFORMED ON DATA USING PEARSON, RF AND LIGHT-GBM FEATURE SELECTION.

Model	MAE (%)	MSE (%)	MAPE (%)
Random Forest	3,05	5,50	9,37
Decision Tree	4,23	5,89	10,90
Linear Regression	5,88	7,93	13,61
Ada Boosting	6,88	0,77	13,98
Gradient Boosting	5,97	0,58	13,07
***LSTM**	4,93	0,37	2,02
RNN	1,96	0,07	2,52

TABLE V
THE RESULTS OF REGRESSION MODELS PERFORMED ON DATA USING CHI-SQUARE FEATURE SELECTION.

Model	MAE (%)	MSE (%)	MAPE (%)
Random Forest	3,05	5,45	10,37
Decision Tree	4,23	5,90	10,90
Linear Regression	6,24	7,93	13,61
Ada Boosting	6,26	0,63	13,30
Gradient Boosting	6,04	0,59	13,23
***LSTM**	1,61	0,04	2,12
RNN	2,57	0,11	9,58

5. BENCHMARKING STUDY

At a glance to the comparison Table IV, the result of our research is superior in terms of the accuracy of forecasting, and on par with [17]. However, [17] has longer period of data compared to our data and just 12 points have been forecasted while we forecast 100 points considering point forecasting. It is clearly seen from the table that other studies have estimated much less points compared to ours, with a maximum of 24-point forecasting. Our study nevertheless seems to be more successful in MTLF, as the accuracy of the prediction decreases while the prediction interval is getting larger. From here it can be easily inferred that; Pearson, RF and Light GBM feature selection methods are of great importance in increasing the accuracy of the estimations made with ML and especially deep neural network (DNN) models. Proposed study uses Czech Republic (2015-2021) as the dataset. Historical power load and meteorological data are used as input features. Pearson, RF and Light-GBM are used for feature selection. LSTM is considered as the best forecasting model. [1] studies a small region in Ontario, Canada over 10 years. Input features are historical power load and meteorological data. Non-linear auto-regressive exogenous (NARX) and RNN-LSTM are utilized as forecasting models.

[17] studies United States (1987-2009) as the data. As for the features; historical power load, natural gas load, natural gas price, average retail price of electricity, electric power sector natural gas consumption and CO2 emissions are facilitated. Quantile regression and kernel density estimation are utilized as models. [33] studies Seoul, South Korea over 14 months. Input features are historical power load and air temperature. A hybrid model based on dynamic and fuzzy time series is facilitated. [34] covers 35 European countries until 2014. Features in use are historical power load and meteorological data. Exponential smoothing is used for feature selection. Residual dilated LSTM is utilized as the forecasting model. [35] studies 25 districts in Seoul between 2005 and 2018. Considered features are calendar, population and meteorological data. Feature selection is applied with Pearson correlation coefficient. DNN is utilized via transfer learning.

TABLE VI
COMPARISON WITH THE RELATIVE LITERATURE STUDIES.

Works	Forecasting steps	Forecasting intervals	MAPE (%)
Proposed	Daily	~3,5 months	2,12
[1]	Hourly	12 months	4-10
[17]	Monthly	12 months	2,12
[33]	Monthly	4 months	~3
[34]	Monthly	12 months	4,46
[35]	Monthly	24 months	6,46

6. CONCLUSION

Machine learning models including deep learning have been successful and performing better than traditional time series and regression techniques. However, non-linear energy consumption patterns are in need to be better modelled while obtaining high accuracy and prediction performances for the medium-term monthly forecasting [25]. In this study, the electricity load estimation of the Prague region of the Czech Republic for the years 2015-2021 has been carried out. In order to better observe the results of the methods used, initially, all the features of the data are used without applying any feature selection process. Then, feature selection techniques are applied and the results are evaluated. Among all the ML and DL-based ELF methods studied, the LSTM approach gives the best results both with feature selection and without feature selection study. While the MAPE value difference between the results obtained with this approach and the results obtained with other approaches is at least 3% without applying feature selection, it is around 9% when feature selection is applied. Such an improvement is of great importance for ELF. Moreover, when the results of the applications performed with three different methods are examined, it is seen that the results of the deep learning methods are close to each other when the Pearson, RF, Light-GBM feature selection is applied. In this context, it has been concluded that these feature selection methods are more effective in terms of comparison of the methods discussed and the accuracy of the results obtained.

 ISSN 2536-5010 | **e-ISSN** 2536-5134 https://dergipark.org.tr/en/pub/ejt

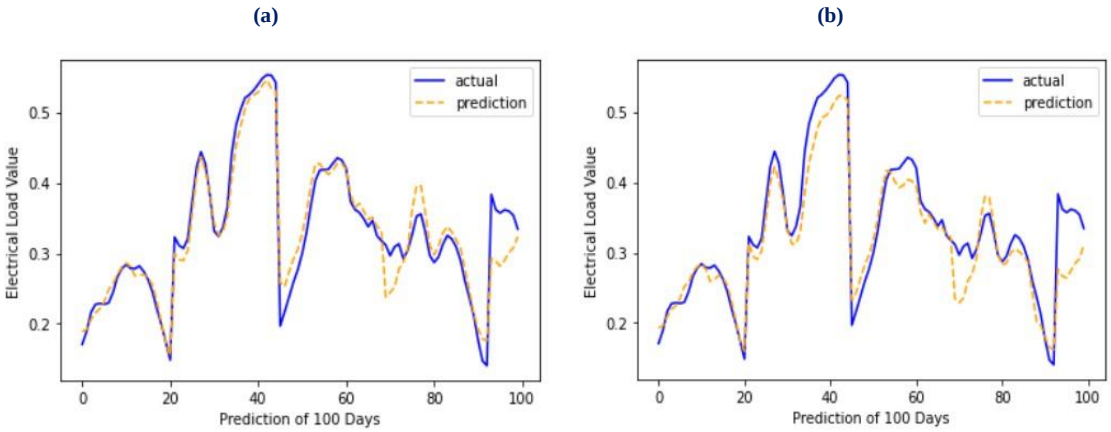

Figure 1. (a) LSTM with Pearson, RF and Light-GBM feature selection, **(b)** LSTM with chi-square feature selection.

For future studies, the facilitated forecasting methods will also be analyzed for the LTLF which is of great importance especially in the expansion planning of real-world power systems [36]. Since LTLF shows similar structures to MTLF in terms of algorithms and features, the applications of the same feature selection methods will be carried out for LTLF, and improvement studies will be made on it. In addition to these estimation methods and feature selection techniques that have been studied on aggregated load data, all the proposed techniques will be studied for individual loads, and the impacts of these methods and development techniques on all load types will be evaluated.

REFERENCES

[1] N. Shirzadi, A. Nizami, M. Khazen, M.Nik-Bakht, "Medium-term regional electricity load forecasting through machine learning and deep learning," Designs 5, 2, 2021.

[2] I. Samuel, C. Felly-Njoku, A. Adewale, A. Awelewa, "Medium-term load forecasting of covenant university using the regression analysis methods," Journal of Energy Technologies and Policy 4, 2014.

[3] A. Zare-Noghabi, M. Shabanzadeh, H. Sangrody, "Medium-term load forecasting using support vector regression, feature selection, and symbiotic organism search optimization," IEEE Power & Energy Society General Meeting (PESGM), 2019, pp. 1–5.

[4] L. Han, Y Peng, Y. Li, B. Yong, Q. Zhou et al, "Enhanced deep networks for short-term and medium-term load forecasting," IEEE Access, 2019, pp. 4045–4055.

[5] M. Ghiassi, D.K. Zimbra, H. Saidane, "Medium term system load forecasting with a dynamic artificial neural network model," Electric Power Systems Research 76, 5, 2006, pp. 302–316.

[6] P. Matrenin, M. Safaraliev, S. Dmitriev, S. Kokin, A. Ghulomzoda et al, "Medium-term load forecasting in isolated power systems based on ensemble machine learning models," Energy Reports 8, 2022, pp. 612–618.

[7] S.R. Khuntia, J. Rueda, M. Meijden, "Forecasting the load of electrical power systems in mid- and long-term horizons - a review," IET Generation Transmission & Distribution, 2016.

[8] G. Box, G.M. Jenkins, G.C. Reinsel, G.M. Ljung, "Time Series Analysis: Forecasting and Control," 5th ed. John Wiley and Sons Inc., 2015.

[9] M. Braun, H. Altan, S. Beck, "Using regression analysis to predict the future energy consumption of a supermarket in the uk," Applied Energy 130, 2014, pp. 305–313.

[10] M. Yilmaz. "Real measure of a transmission line data with load fore-cast model for the future." Balkan Journal of Electrical and Computer Engineering 6.2 (2018): 141-145.

[11] R. Torkzadeh, A. Mirzaei, M.M. Mirjalili, A.S. Anaraki, M.R. Sehhati et al, "Medium term load forecasting in distribution systems based on multi linear regression & principal component analysis: A novel approach," 19th Conference on Electrical Power Distribution Networks (EPDC), 2014, pp. 66–70.

[12] A. Papalexopoulos, T. Hesterberg, "A regression-based approach to short-term system load forecasting," IEEE Transactions on Power Systems 5, 4, 1990, pp. 1535–1547.

[13] M.D.C. Ruiz-Abell´on, A. Gabald´on, A. Guillam´on, "Load forecasting for a campus university using ensemble methods based on regression trees," Energies 11, 8, 2018.

[14] Z. Wang, Y. Wang, R. Zeng, R.S. Srinivasan, S. Ahrentzen, "Random forest based hourly building energy prediction," Energy and Buildings 171, 2018, pp. 11–25.

[15] A. Lahouar, J. Ben Hadj Slama, "Day-ahead load forecast using random forest and expert input selection" Energy Conversion and Management 103, 2015, 1040–1051.

[16] M.W. Ahmad, M. Mourshed, Y. Rezgui, "Trees vs neurons: Comparison between random forest and ANN for high30 resolution prediction of building energy consumption" Energy and Buildings 147, 2017, pp. 77–89.

[17] S. Wang, S. Wang, D. Wang, "Combined probability density model for medium term load forecasting based on quantile regression and kernel density estimation," Energy Procedia 158, Innovative Solutions for Energy Transitions, 2019, pp. 6446–6451.

[18] K. Zhu, J. Geng, K. Wang, "A hybrid prediction model based on pattern sequence-based matching method and extreme gradient boosting for holiday load forecasting" Electric Power Systems Research 190, 2021, 106841.

[19] P.W. Khan, Y.C. Byun, S.J. Lee, D.H. Kang, J.Y. Kang et al, "Machine learning-based approach to predict energy consumption of renewable and nonrenewable power sources," Energies 13, 2020, no. 18: 4870.

[20] P.W. Khan, Y.C. Byun, "Genetic algorithm based optimized feature engineering and hybrid machine learning for effective energy consumption prediction" IEEE Access 8, 2020, pp. 196274–196286.

[21] K.P. Waqas, Y.C. Byun, S.J. Lee, N. Park, "Machine learning based hybrid system for imputation and efficient energy demand forecasting," Energies 13, 11, 2020.

[22] K. Zeng, J. Liu, H. Wang, Z. Zhao, C. Wen, "Research on adaptive selection algorithm for multi-model load forecasting based on adaboost," In IOP Conference Series: Earth and Environmental Science vol. 610, IOP Publishing, 2020, pp. 012005.

[23] A. Rahman, V. Srikumar, A.D. Smith, "Predicting electricity consumption for commercial and residential buildings using deep recurrent neural networks," Applied Energy 212, 2018, pp. 372–385.

[24] S. Bouktif, A. Fiaz, A. Ouni, M.A. Serhani, "Single and multi-sequence deep learning models for short and medium term electric load forecasting," Energies 12, 1, 2019.

[25] S. Bouktif, A. Fiaz, A. Ouni, M.A. Serhani, "Optimal deep learning LSTM model for electric load forecasting using feature selection and genetic algorithm: Comparison with machine learning approaches," Energies 11, 7, 2018.

[26] T. Bashir, C. Haoyong, M.F. Tahir, Z. Liqiang, "Short term electricity load forecasting using hybrid prophet-LSTM model optimized by BPNN," Energy Reports 8, 2022, pp. 1678–1686.

[27] H.S. Nogay, T. C. Akinci, and M. Yilmaz. "Detection of invisible cracks in ceramic materials using by pre-trained deep convolutional neural network." Neural Computing and Applications 34.2 (2022): 1423-1432.

[28] Y. Wang, N. Zhang, X. Chen, "A short-term residential load forecasting model based on LSTM recurrent neural network considering weather features," Energies 14, 10, 2021.

[29] C. Fan, Y. Li, L. Yi, L. Xiao, X. Qu et al, "Multi-objective LSTM ensemble model for household short-term load forecasting," Memetic Computing 14, 2022, pp. 1–18.

[30] Czech transmission system operator (Ceps) [online], Website https://www.cleanenergywire.org/experts/7, [accessed 22 08 22]

[31] Nasa power data access viewer [online]. Website https://power.larc.nasa.gov/data-access-viewer [accessed 22 08 22]

[32] Stanford University CS-230 Recurrent Neural Networks cheatsheet [online], Website https://stanford.edu/shervine/teaching/cs-230/cheatsheet-recurrent-neural-networks [accessed 22 08 22].

[33] W.J. Lee, J. Hong, "A hybrid dynamic and fuzzy time series model for mid-term power load forecasting," International Journal of Electrical Power & Energy Systems 64, 2015, pp. 1057–1062.

[34] G. Dudek, P. Pe lka, S. Smyl, "A hybrid residual dilated LSTM and exponential smoothing model for midterm electric load forecasting," IEEE Transactions on Neural Networks and Learning Systems 33, 7, 2022, pp. 2879–2891.

[35] S.M. Jung, S. Park , S.W. Jung, E. Hwang, "Monthly electric load forecasting using transfer learning for smart cities," Sustainability 12, 16, 2020.

[36] A. Samuel, M. Krishnamoorthy, B. Ananthan, K. Subramanian, K.P.Murugesan, "Application of metaheuristic algorithms for solving real-world electricity demand forecasting and generation expansion planning problems," Iranian Journal of Science and Technology, Transactions of Electrical Engineering 46, 2, 2022, pp. 413–439.

BIOGRAPHIES

Fatma Yaprakdal obtained her BSc degree in electrical engineering from Yildiz Technical University (YTU) in 2004. She received the MSc. diploma in Energy Science and Technology Department from the Istanbul Technical University in 2012, and PhD degrees in Electrical Engineering from the Yildiz Technical University in 2021. Her research interests are electrical power systems, microgrids, energy forecasting and machine learning. In 2010, she has started her academic career as a research assistant in Yalova University. In 2021 she joined the Faculty of Engineering, Kirklareli University as a assistant professor, where she is presently working at the same position.

Fatih Bal obtained his BSc degree in software engineering from Istanbul Maltepe University in 2014. He received the MSc. diploma in Computer Engineering from Beykent University in 2017. He is still doing his PhD education in Duzce University. His research interests are Deep Learning, Machine Learning, Computer Vision, Data Science. In 2016 he has started his academic career as a research assistant in Maltepe University. After 2 years experience there, in 2018 he joined Kirklareli University as a lecturer, where he is presently a lecturer.

European Journal of Technique

journal homepage: https://dergipark.org.tr/en/pub/ejt

Vol.12, No.2, 2022

Thermal Analysis of Insulation Materials Used for Exterior Walls of Buildings Considering the Wind Effect

Aynur UÇAR[1*]

[1*]Department of Mechanical Engineering, Firat University, 23279 Elazığ, Turkey. (e-mail: aucar@firat.edu.tr).

ARTICLE INFO

Received: Dec., 30. 2021
Revised: Aug., 18. 2022
Accepted: Nov, 30. 2022

Keywords:
Optimum insulation thickness
Wind speed
Insulation material
Thermal analysis

Corresponding author: *Aynur Uçar*

ISSN: | e-ISSN: *2536-5134*

DOI: https://doi.org/10.36222/ejt.1051230

ABSTRACT

The optimum thickness of insulation material dependent on wind speed and wall orientation were determined for selected insulation materials and external wall types in different compositions and orientations by using the Life Cycle Cost method. The methodology is applied as a case study by comparing the different combinations of thermally insulated walls with four different insulation materials for four different degree-day regions of Turkey considering the effect of wind speed and direction. In the economic analysis, the costs of the life cycle of each different combination of insulated walls were calculated. It was obtained from these results that heating requirement of the north orientation wall was the maximum and heating requirement of the south orientation wall was the minimum. The optimum thickness of insulation changes from 4.77 to 13.35 cm dependent on the insulation materials and orientations.

1. INTRODUCTION

Residential buildings have a considerable share in the consumption of renewable energy resources [1]. Today, energy consumption in buildings constitutes approximately 40% of total energy consumption, and the capacity of the residential sector will reach 67% by 2050 [2].

The recent works towards energy-saving design is not only in conditions of providing lower U-values, but also in the improving and use of natural and local insulation materials. In last years, the areas of thermal conservation in buildings are more concentrating on environmental properties. Preventions to prevent environmental pollution are not only limited to energy savings [3]. The optimum insulation thickness is determined by some researchers [4-10]. Özel et al. [11] are determined the optimum insulation thickness using the environmental and life cycle cost analyses. They calculated the fuel consumption, the CO_2 emission and the environmental impacts of the system related to entransy loss. Jie et al. [12] determined the optimum thickness of insulation for walls and roofs of buildings and they have developed an optimization model for this purpose. Their results showed that the optimum insulation thickness of walls and roofs could be calculated from this optimization model.

In this study, the optimum thermal insulation thickness is determined depending on the available costs of insulation materials and fuel for building external walls with different structure and orientation in the selected cities from four different climate regions of Turkey.

2. ANALYSIS

2.1. The investigated wall structures

The four walls in different structures are researched in this working. The place of insulation can be replaced by putting to different places in the wall. Fig.1 shows the examined wall structures.

Wall 1 consists of 2 cm interior and exterior plaster, 13 cm thick brick and insulation material. Wall 2 is a sandwich wall which has a compound structure consisting of 2 cm interior and exterior plaster, 10 cm each of two brick layers. Wall 3 consists of interior and exterior plaster, hollow concrete block, and insulation. In this wall configuration, the concrete thickness is 20 cm and interior and exterior plaster is 2 cm.

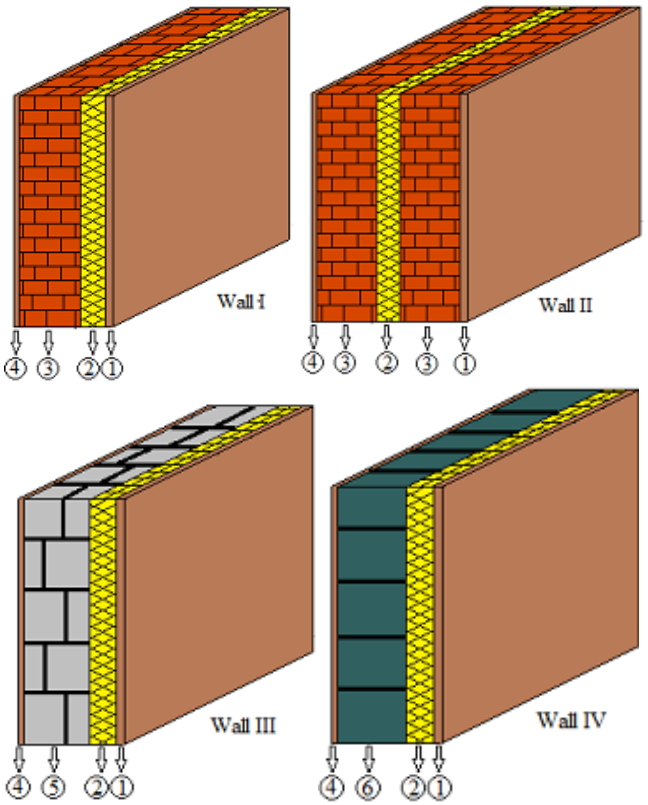

Figure 1. Cross-sectional views of the investigated external wall structures.

Wall 4 consist of 2 cm interior plaster, 30 cm CSEB (Compressed Stabilised Earth Block), insulation material and 2 cm exterior plaster. In this working, polyurethane (PU), extruded polystyrene (XPS), glass wool (GW) and expanded polystyrene (EPS) are preferred as insulation materials. The physical properties of each material used in the wall structures and economical parameters are shown in Table 1.

2.2. Climatic zones

Turkey has four different degrees-day regions according to TS 825 'Thermal Insulation Requirements for Buildings' standard. [13]. Each region has different heating and cooling degree-days values. The temperature of the different heating degree-day regions is about 7 times increases at the base temperature of 18 ° C [14]. The International Energy Agency (IEA) (2008) is defined six basic climatic regions for 18 °C base temperature and these regions is shown in Table 2.

TABLE 1.
PHYSICAL PROPERTIES OF WALL STRUCTURE AND ECONOMIC PARAMETERS

Wall type	Thickness (m)	Thermal conductivity (W/mK)	Resistance (m^2 K/W)	Insulation cost ($/$m^3$)
Wall 1			0.335	
Interior plaster	0.02	0.87		
Brick	0.13	0.45		
External plaster	0.02	0.87		
Wall 2			0.490	
Interior plaster	0.02	0.87		
Brick	0.10	0.45		
Brick	0.10	0.45		
External plaster	0.02	0.87		
Wall 3			0.379	
Interior plaster	0.02	0.87		
Hollow concrete block	0.20	0.60		
External plaster	0.02	0.87		
Wall 4			0.387	
Interior plaster	0.02	0.87		
CSEB	0.30	0.88		
External plaster	0.02	0.87		
Insulation Materials				
Polyurethane	*	0.024		260
Extruded polystyrene	*	0.031		180
Expanded polystyrene	*	0.039		120
Glass wool	*	0.040		75
Interest rate, i Inflation rate, d Lifetime, N	9% 8.81% 10			

* The optimum thickness of insulation material calculated using the life cycle cost analysis

TABLE 2.
CLASSIFIED CLIMATIC ZONES, AND HEATING AND COOLING DEGREE-DAY RANGES [13]

Climatic regions	**Heating degree-days**	**Cooling degree-days**
Cold climate	4000 ≤ HDD	CDD < 500
Medium cold climate	3000 ≤ HDD	500 ≤ CDD < 1000
Rather cold climate	2000 ≤ HDD	CDD < 1000
Moderate climate	HDD < 2000	CDD < 1000
Cooling-based climate	1000 ≤ HDD < 2000	1000 ≤ CDD
Hot climate	HDD < 1000	1000 < CDD

In this working, Hatay, Batman, Elazığ and Bayburt from the four different degree-day regions of Turkey are chosen and optimum values of insulation thickness for these cities found. The annual heating degree-days of Hatay in the southern region of Turkey is 1119, while degree-days of Bayburt in the north-east of Turkey is 4149. Batman is a Turkish province southeast of Anatolia and the annual heating degree-day of its is 1823. The yearly heating degree-days of Elazığ is 2653. Table 3 is given the climate characteristics of the selected cities.

 ISSN 2536-5010 | **e-ISSN** 2536-5134 https://dergipark.org.tr/en/pub/ejt

TABLE 3.
CLIMATE CHARACTERISTIC OF SELECTED CITIES

City	Elavation (m)	Longitude (deg)	Latitude (deg)	Cooling degree-days (ºC-days)	Heating degree-days (ºC-days)
Hatay	85	36 º12'	36º 52'	614	1119
Batman	525	41º 07'	37º 52'	763	1823
Elazığ	1067	39º 14'	38º 41'	337	2653
Bayburt	1556	40º 15'	40º 16'	8	4149

2.3. Heat transfer from walls

The heat transfer in building walls is realized by three mechanisms of heat transfer. Firstly, the solar radiation coming to the outside surface of the building wall is absorbed by wall surface and then, the heat transfer into the wall by conduction is occurred. The heat transfer between ambient air with the outside surface of wall and also between the internal surface of the wall with indoor air are occurred by convective. Heat transfer rate from a unit area of building wall can be found as

$$q = U\left(T_i - T_o\right) \tag{1}$$

The total heat transfer coefficient for an insulated wall can be written by

$$U = \frac{1}{1/h_i + R_w + x_{ins}/k_{ins} + 1/h_o} \tag{2}$$

In this study, the convective heat transfer coefficient between internal surface of the wall with air is evaluated as follows

$$h_i = 1.31\left(T_{s,i} - T_i\right)^{1/3} \tag{3}$$

The convective heat transfer coefficient on the outer surface of wall depending on direction and speed of the wind can be calculated by using Eqs. (4) and (5) for the windward (ww) and leeward side (lw) as

$$h_{o,ww} = 1.53v + 1.43 \tag{4}$$

$$h_{o,lw} = 0.90v + 3.28 \tag{5}$$

It is accepted that Eq. (4) is for the north, west, and east wall surface, when Eq. (5) is for the south facing wall surface.

The Weibull distribution is the most widely used to represent the frequencies of the wind speed. The Weibull distribution function can be given as [15]

$$f(v) = \frac{k}{c}\left(\frac{v}{c}\right)^{k-1} \exp\left[-\left(\frac{v}{c}\right)^{k}\right] \tag{6}$$

In this study, k and c parameters are calculated from mean wind speed–standard deviation method.
The yearly energy need can be calculated by

$$E_A = \frac{86400\ HDD\ U}{\eta_s} \tag{7}$$

2.4. Economic analysis

In this working, the P_1-P_2 method is used the energy savings of each type of wall. The annual cost of heating for per unit area is found as [16]

$$C_A = \frac{86400\ HDD\ C_f}{\left(R_{wt} + \frac{x_{ins}}{k_{ins}}\right) H_u\ \eta_s} \tag{8}$$

Costs, lower heating values and efficiencies of various fuel types used in this analysis are given in Table 4. P_1 is the rate of energy savings obtained from fuel during the life cycle to the energy savings provided during the first year. P_2 is the rate of expenses during life cycle to first investment. This method facilitates economic analysis by collecting all the parameters in the economic analysis into P_1 and P_2. The P_1 and P_2 are determined

$$P_1 = \left[(1+d)/(d-i)\right]\left[1-\left((1+i)/(1+d)\right)^N\right] \tag{9}$$

$$P_2 = 1 + P_1\ M_S - R_v\left(1+d_f\right)^{-N} \tag{10}$$

The total insulation cost (C_{ins}) can be defined by

$$C_{ins} = C_i\, x_{ins} \tag{11}$$

The heating energy savings during the life time per unit area

$$S = C_A\ P_1 - P_2 C_{ins} \tag{12}$$

or

$$S = \frac{86400\ HDD\ C_f}{\left(R_{wt} + \frac{x_{ins}}{k_{ins}}\right) H_u\ \eta_s} P_1 - P_2\ C_i\ x_{ins} \tag{13}$$

The maximum value of the energy gain is the optimum value. In MATLAB optimization Toolbox, Eq. (13) was received as an objective function and the optimum thickness of insulation was found.

The payback period N_p is determined as

$$N_p = \frac{\ln\left[1 - \frac{P_2 C_i\ H_u\ \eta_s \left(R_{wt} + R^2{}_{wt} k_{ins}\right)(d-i)}{86400\ HDD\ C_f\ (1+d)}\right]}{\ln\left[(1+i)/(1+d)\right]} \tag{14}$$

TABLE 4.
PRICES, LOWER HEATING VALUES AND EFFICIENCIES OF FUELS [17]

Fuel	Price	H_u	η_s
Coal	0.240 $/kg	29.295x10^{6}J/kg	0.65
Natural gas	0.332 $/m^3	34.526 x10^{6}J/m^3	0.90
Fuel-oil	0.343 $/kg	40.594 x10^{6}J/kg	0.80
LPG	1.265 $/kg	46.453 x10^{6}J/kg	0.88

3.RESULTS AND DISCUSSION

In the use of wind energy, it is very important to determine the wind speed according to the wind direction. The long-term wind data containing hourly wind speed and direction recorded during the last decade period were taken from Turkish State Meteorological Service and were used in this study. The relative frequencies of wind directions for four

stations are shown in the wind rose diagram in Fig. 2. A wind rose is a graphic that shows distribution of the wind speed and direction at a specific area. The northwest and west-north-west wind directions at Elazığ and Bayburt are most windward directions. the most windward direction at Hatay and Batman are south–southwest and northeast, respectively. Fig. 3 shows the possibility density function of the yearly wind speed distribution. The peak point of frequencies values for selected the stations are shifted towards the high values of mean wind speed.

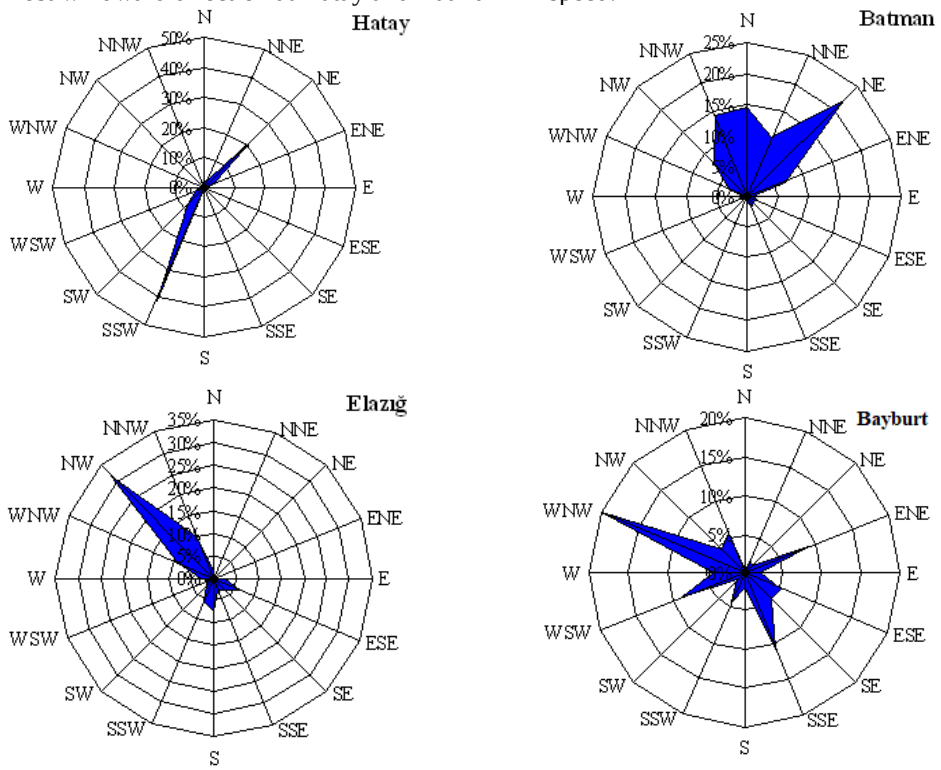

Figure 2. Frequencies (%) of wind directions for four cities.

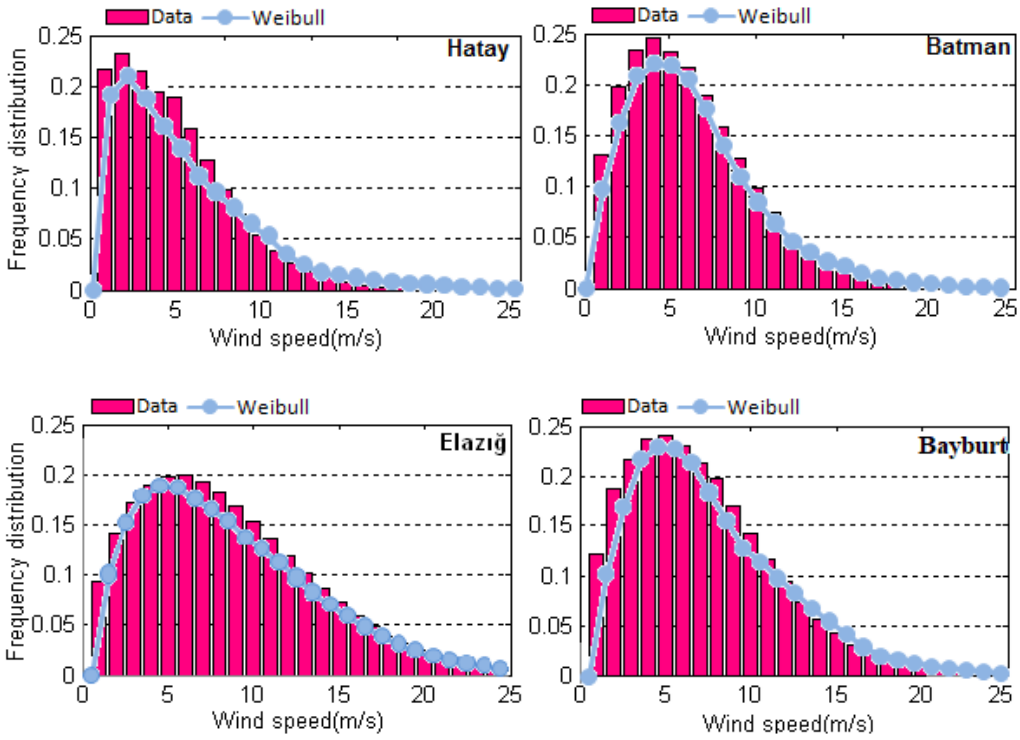

Figure 3. Annual frequency distributions of wind speed for four cities.

Fig.4 shows variation of the heating load with insulation thickness according to different directions and selected cities for sandwich wall with insulation. The heating load of the wall area reduces with the insulation thickness increasing. The heating load is found as highest for north facing wall. The heating load of south facing wall is lowest according to other orientations, because this surface has the high solar heat gain.

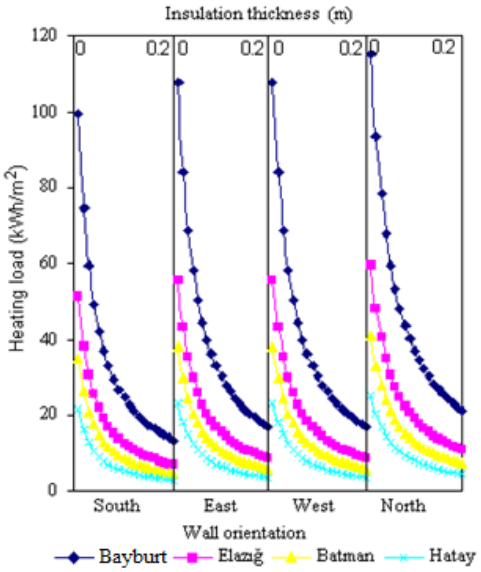

Figure 4. Variation of the heating load with insulation thickness according to different directions and selected cities for sandwich wall with insulation (Wall 2).

Fig. 5 shows the influence on energy savings of insulation thickness and wall orientations for four wall types. The energy savings increases with the insulation thickness increases and it achieves a maximum value in the optimum thickness of insulation. The insulated wall with polyurethane is reached greatest energy savings according to selected insulation materials for different orientations. The cost of polyurethane is higher than other selected insulation materials, while the thermal conductivity of polyurethane is lower.

The influence on energy savings of insulation thickness and wall orientations for four fuel types and insulated sandwich wall is shown in Fig.6 for Elazığ. The energy savings varies attached to the fuel cost. The energy savings of high cost fuels like LPG, coal and fuel-oil are higher than energy savings of other cheap fuels. It is found that LPG is the most suitable energy source in terms of energy savings, besides natural gas has the worst performance. Figs.7 presents the variations of energy savings and payback period with different wall structures and orientations for four fuel types and extruded polystyrene in Elazığ. The insulated sandwich wall (Wall 2) with thermal resistance of 0.49 m^2K/W has the lowest energy savings and highest payback period, while insulated external wall (Wall 1) with thermal resistance of 0.34 m^2K/W has the highest energy savings and lowest payback period.

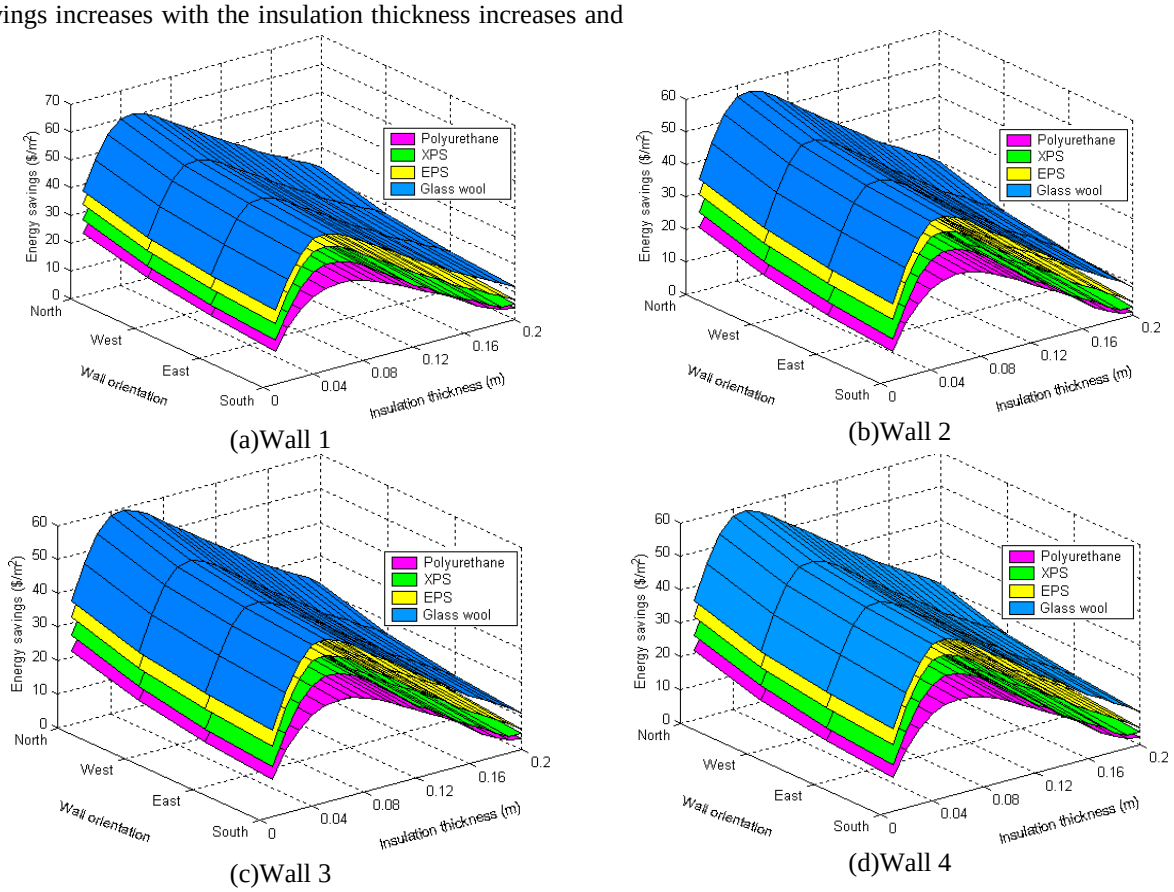

(a)Wall 1 (b)Wall 2

(c)Wall 3 (d)Wall 4

Figure 5. Influence on energy savings of insulation thickness and wall orientations for four wall types.

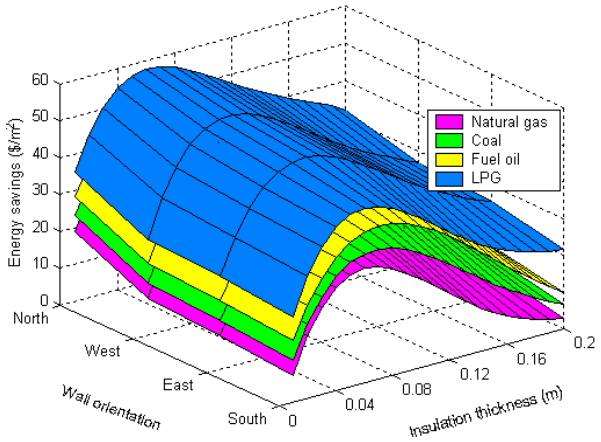

Figure 6. Influence on energy savings of insulation thickness and wall orientations for four fuel types and insulated sandwich wall (Wall 2).

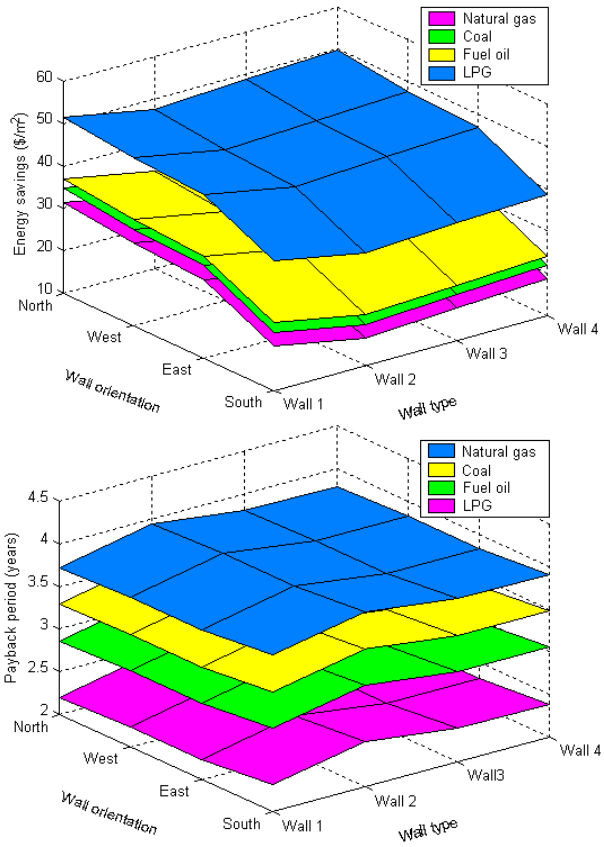

Figure 7. Variation of energy savings and payback period with different wall structures and orientations for different fuel types and extruded polystyrene insulation material in Elazığ

Fig.8 shows variation of optimum insulation thickness with wall orientations for selected insulation materials and selected cities. The optimum insulation thickness varies depending on the climatic conditions of the region. The larger insulation thickness require for the cities in cold climate region which have higher heating degree days. The optimum insulation thickness in Bayburt is higher compared to regions of Hatay and Batman, located in the low-latitude region. The highest optimum insulation thickness is achieved in Bayburt for glass wool insulation material, when its lowest value is obtained in Hatay for polyurethane.

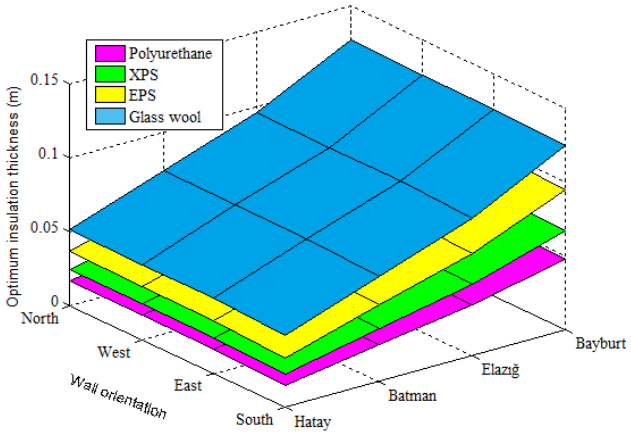

Figure 8. Variation of optimum insulation thickness with different wall orientations for selected four insulation materials and cities (for using fuel-oil as fuel type).

Fig.9 shows the effect on payback period of insulation thickness and different orientations for sandwich wall insulated with extruded polystyrene and selected cities. It is observed this figure that the payback periods vary depending on the heating degree days. For all orientations, the payback period reduces with heating degree days increasing. The cost of insulation increases because of the applying higher insulation thickness in cold climatic regions. But, the payback period is conversely shorter. For this reason, it is more advantageous to apply insulation in cold climatic regions. It is seen that the lowest payback period is reached for Bayburt having higher degree days and the north wall, while the highest payback period is obtained for Hatay having lower degree days and south wall.

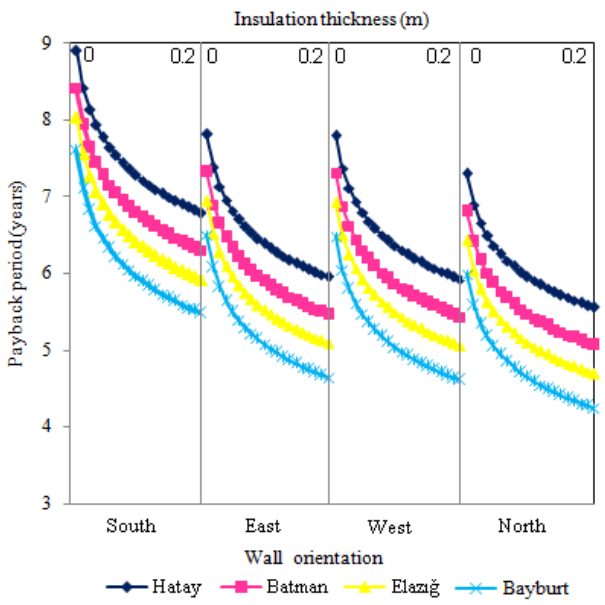

Figure 9. Effect on payback period of insulation thickness and different orientations for sandwich wall insulated with extruded polystyrene and selected cities.

Table 5 shows the results of optimization and economic analysis calculated for selected four wall types, all wall orientations and selected insulation materials in Bayburt city. The optimum thickness of insulation changes from 4.77 to 13.35 cm dependent on the insulation materials and orientations.

TABLE 5.
RESULTS OF OPTIMIZATION AND ECONOMIC ANALYSIS CALCULATED FOR SELECTED FOUR WALL TYPES, INSULATION MATERIALS AND ALL ORIENTATIONS IN BAYBURT CITY.

Orientation	Type of wall	Insulation material	Optimum insulation thickness, cm	Energy savings,$/m^2	Payback period years
South	Wall 1	Polyurethane	5.15	26.81	3.24
		Extruded polystyrene	7.15	29.46	3.18
		Expanded polystyrene	10.06	33.30	3.10
		Glass wool	13.04	36.03	2.91
	Wall 2	Polyurethane	4.77	26.13	3.45
		Extruded polystyrene	6.67	28.59	3.39
		Expanded polystyrene	9.45	32.21	3.31
		Glass wool	12.42	34.91	3.12
	Wall 3	Polyurethane	5.04	26.61	3.30
		Extruded polystyrene	7.01	29.21	3.25
		Expanded polystyrene	9.89	32.99	3.16
		Glass wool	12.86	35.71	2.97
	Wall 4	Polyurethane	5.02	26.58	3.31
		Extruded polystyrene	6.99	29.17	3.26
		Expanded polystyrene	9.86	32.93	3.17
		Glass wool	12.83	35.65	2.98
East	Wall 1	Polyurethane	5.29	27.06	3.15
		Extruded polystyrene	7.33	29.78	3.09
		Expanded polystyrene	10.29	33.71	3.00
		Glass wool	13.27	36.45	2.81
	Wall 2	Polyurethane	4.91	26.39	3.38
		Extruded polystyrene	6.85	28.92	3.32
		Expanded polystyrene	9.68	32.62	3.23
		Glass wool	12.65	35.33	3.04
	Wall 3	Polyurethane	5.18	26.87	3.22
		Extruded polystyrene	7.19	29.54	3.16
		Expanded polystyrene	10.12	33.40	3.07
		Glass wool	13.09	36.13	2.88
	Wall 4	Polyurethane	5.16	26.83	3.23
		Extruded polystyrene	7.17	29.49	3.17
		Expanded polystyrene	10.09	33.35	3.09
		Glass wool	13.06	36.07	2.90
West	Wall 1	Polyurethane	5.29	27.06	3.15
		Extruded polystyrene	7.33	29.78	3.09
		Expanded polystyrene	10.29	33.71	3.00
		Glass wool	13.27	36.45	2.81
	Wall 2	Polyurethane	4.91	26.39	3.38
		Extruded polystyrene	6.85	28.92	3.32
		Expanded polystyrene	9.68	32.62	3.23
		Glass wool	12.65	35.33	3.04
	Wall 3	Polyurethane	5.18	26.87	3.22
		Extruded polystyrene	7.19	29.54	3.16
		Expanded polystyrene	10.12	33.40	3.07
		Glass wool	13.09	36.13	2.88
	Wall 4	Polyurethane	5.16	26.83	3.23
		Extruded polystyrene	7.17	29.49	3.17
		Expanded polystyrene	10.09	33.35	3.09
		Glass wool	13.06	36.07	2.90
North	Wall 1	Polyurethane	5.33	27.14	3.12
		Extruded polystyrene	7.39	29.89	3.06
		Expanded polystyrene	10.36	33.84	2.97
		Glass wool	13.35	36.58	2.78
	Wall 2	Polyurethane	4.96	26.47	3.35
		Extruded polystyrene	6.91	29.02	3.29
		Expanded polystyrene	9.76	32.75	3.21
		Glass wool	12.72	35.46	3.02
	Wall 3	Polyurethane	5.23	26.95	3.19
		Extruded polystyrene	7.25	29.64	3.13
		Expanded polystyrene	10.19	33.53	3.05
		Glass wool	13.17	36.26	2.86
	Wall 4	Polyurethane	5.21	26.91	3.20
		Extruded polystyrene	7.23	29.60	3.15
		Expanded polystyrene	10.16	33.48	3.06
		Glass wool	13.14	36.21	2.87

ISSN 2536-5010 | **e-ISSN** 2536-5134
https://dergipark.org.tr/en/pub/ejt

TABLE 6.
RESULTS OF OPTIMIZATION AND ECONOMIC ANALYSIS FOR SELECTED CITIES, ALL FUEL TYPES AND ALL ORIENTATIONS.

Orientation	City	Fuel type	Optimum insulation thickness, cm	Energy savings, $/m^2	Payback period years
South	Hatay	Coal	2.23	12.64	4.05
		Natural gas	1.85	11.27	4.13
		Fuel-oil	1.83	11.19	4.14
		LPG	4.95	22.41	3.60
	Batman	Coal	3.56	17.40	3.80
		Natural gas	3.07	15.66	3.89
		Fuel-oil	3.04	15.55	3.90
		LPG	7.02	29.87	3.36
	Elazığ	Coal	4.82	21.94	3.62
		Natural gas	4.23	19.84	3.70
		Fuel-oil	4.20	19.71	3.71
		LPG	8.99	36.98	3.17
	Bayburt	Coal	6.66	28.59	3.39
		Natural gas	5.93	25.96	3.48
		Fuel-oil	5.89	25.79	3.49
		LPG	11.89	47.40	2.94
East	Hatay	Coal	2.41	12.97	3.98
		Natural gas	2.03	11.60	4.06
		Fuel-oil	2.01	11.51	4.07
		LPG	5.13	22.73	3.53
	Batman	Coal	3.74	17.73	3.74
		Natural gas	3.25	15.98	3.81
		Fuel-oil	3.22	15.88	3.82
		LPG	7.20	30.20	3.29
	Elazığ	Coal	5.00	22.27	3.55
		Natural gas	4.41	20.16	3.63
		Fuel-oil	4.38	20.03	3.64
		LPG	9.18	37.31	3.09
	Bayburt	Coal	6.84	28.92	3.32
		Natural gas	6.11	26.28	3.40
		Fuel-oil	6.07	26.12	3.41
		LPG	12.07	47.73	2.87
West	Hatay	Coal	2.41	12.97	3.98
		Natural gas	2.03	11.60	4.06
		Fuel-oil	2.01	11.51	4.07
		LPG	5.13	22.73	3.53
	Batman	Coal	3.74	17.73	3.74
		Natural gas	3.25	15.98	3.81
		Fuel-oil	3.22	15.88	3.82
		LPG	7.20	30.20	3.29
	Elazığ	Coal	5.00	22.27	3.55
		Natural gas	4.41	20.16	3.63
		Fuel-oil	4.38	20.03	3.64
		LPG	9.18	37.31	3.09
	Bayburt	Coal	6.84	28.92	3.32
		Natural gas	6.11	26.28	3.40
		Fuel-oil	6.07	26.12	3.41
		LPG	12.07	47.73	2.87
North	Hatay	Coal	2.47	13.07	3.95
		Natural gas	2.09	11.70	4.03
		Fuel-oil	2.07	11.62	4.04
		LPG	5.19	22.84	3.50
	Batman	Coal	3.79	17.83	3.71
		Natural gas	3.31	16.09	3.79
		Fuel-oil	3.28	15.98	3.80
		LPG	7.26	30.30	3.26
	Elazığ	Coal	5.06	22.37	3.52
		Natural gas	4.47	20.27	3.60
		Fuel-oil	4.44	20.14	3.61
		LPG	9.23	37.41	3.07
	Bayburt	Coal	6.90	29.02	3.29
		Natural gas	6.17	26.39	3.38
		Fuel-oil	6.13	26.23	3.39
		LPG	12.13	47.83	2.85

ISSN 2536-5010 | **e-ISSN** 2536-5134
https://dergipark.org.tr/en/pub/ejt

It is observed this table that the north-facing insulated wall (Wall 1) has highest optimum thickness for glass wool insulation material. The insulated sandwich wall (Wall 2) for selected insulation materials and wall orientations has lowest optimum thickness and the highest payback period. Besides, the minimum value of optimum insulation thickness and the largest value of payback period are found for the south-facing wall compared to the other orientations. Therefore, this wall is not economically advantageous. The energy savings of the south-facing sandwich wall (Wall 2) insulated with polyurethane insulation material is lowest compared to other wall types.

Table 6 shows the results of optimization and economic analysis for selected cities, all fuel types and all orientations. The energy savings change from 11.19 to 47.83 $/m^2 dependent on thermal properties of fuel. The highest energy savings and smallest payback period is found for LPG as fuel type and north-facing wall in Bayburt, when the smallest energy savings and highest payback period is found for fuel-oil as fuel type and south-facing wall in Hatay.

3. CONCLUSION

The optimum insulation thickness as a function of wall orientation and wind speed were calculated for selected insulation materials and four wall types in this working. Besides, the energy savings and payback periods were examined for four different cities of Turkey representing four different degrees-day regions.

It was obtained from these results that heating requirement of the north wall was the highest and heating requirement of the south wall was the lowest. The optimum insulation thickness was dependent on the climatic conditions. For glass wool insulation material and external wall (Wall 1) in Bayburt, the optimum thickness of insulation was the highest and payback period was the lowest, whereas the optimum thickness of insulation was the lowest and payback period was the highest for polyurethane insulation material and sandwich wall (Wall 2) in Hatay.

This study was applied here four different climate regions and four different wall types, but the same methodology can be replicated to other types of external wall and to different climatic conditions. The results obtained in this study will be helpful guide the choice of insulation material for building walls in different climates.

NOMENCLATURE

c	Weibull scale parameter
C_A	yearly energy cost ($/m^2 year)
C_i	unit cost of insulation material ($/m^3)
C_f	cost of fuel ($/kg)
d	inflation rate
HDD	heating degree days (ºC-days)
H_u	lower calorific value of fuel (J/kg)
i	interest rate
k	dimensionless shape parameter
k_{ins}	heat conduction coefficient of insulation material (W/m K)
M_s	rate of first year maintenance costs to first investment cost
N	lifetime (years)
N_p	payback period (years)
R_w	total thermal resistance of the wall (m^2 K/W)
S	savings ($/m^2)
T_i	inside air temperature (ºC)
T_o	average daily temperature (ºC)
U	total heat transfer coefficient (W/m^2 K)
v	wind speed (m/s)
q	yearly heat loss from wall (W/m^2)
x_{ins}	insulation material thickness (m)
η_s	efficiency of fuel

REFERENCES

[1] UNEP-SBCI Buildings and Climate Change: Status, Challenge and Opportunities, UNEP Publication, Paris, France, 2007.

[2] K. Yiğit and B. Acarkan, "Assessment of energy performance certificate systems: a case study for residential buildings in Turkey", Turkish Journal of Electrical Engineering & Computer Sciences, vol.24, pp. 4839 – 4848, 2016.

[3] A. Stephan, R.H. Crawford and K. Myttenaere, "Towards a comprehensive life cycle energy analysis framework for residential buildings," Energy Building, vol.55, pp. 592–600, 2012.

[4] M.K. Nematchoua, P. Ricciardi, S. Reiter and A. Yvon, "A comparative study on optimum insulation thickness of walls and energy savings in equatorial and tropical climate," International Journal of Sustainable Built Environment, vol.6, pp.170-182, 2017.

[5] M. Kayfeci, A. Keçebas and E. Gedik, "Determination of optimum insulation thickness of external walls with two different methods in cooling applications," Applied Thermal Engineering, vol.50 pp. 217-224, 2013.

[6] N. A. Kurekci, "Determination of optimum insulation thickness for building walls by using heating and cooling degree-day values of all Turkey's provincial centers," Energy and Buildings, vol. 118, pp.197–213, 2016.

[7] K. Çomaklı and B. Yüksel, "Optimum insulation thickness of external walls for energy saving," Applied Thermal Engineering, vol. 23, no.4, pp. 473–479, 2003.

[8] K. Saafi and N. Daouas, "A life-cycle cost analysis for an optimum combination of cool coating and thermal insulation of residential building roofs in Tunisia," Energy, vol.152, pp. 925-938, 2018.

[9] A. Bolattürk, "Determination of optimum insulation thickness for building walls with respect to various fuels and climate zones in Turkey," Applied Thermal Engineering, vol.26, no.11, pp. 1301–1309, 2006.

[10] I. Axaopoulos, P. Axaopoulos, G. Panayiotou, S. Kalogirou and J. Gelegenis, "Optimal economic thickness of various insulation materials for different orientations of external walls considering the wind characteristics," Energy, vol. 90, pp. 939-952, 2015.

[11] G. Özel, E. Açıkkalp, B. Görgün, H.Yamık and N. Caner, "Optimum insulation thickness determination using the environmental and life cycle cost analyses based entransy approach," Sustainable Energy Technologies and Assessments, vol.11, pp. 87-91, 2015.

[12] P. Jie, F. Zhang, Z. Fang, H. Wang and Y. Zhao, "Optimizing the insulation thickness of walls and roofs of existing buildings based on primary energy consumption, global cost and pollutant emissions," Energy, vol. 159, pp. 1132–1147, 2018.

[13] TS 825, Thermal Insulation Rules in Buildings, Turkish Standard Institution, Ankara, Turkey, 1998.

[14] O. Buyukalaca, H. Bulut and T. Yılmaz, "Analysis of variable-base heating and cooling degree days for Turkey," Applied Energy, vol.69, pp. 269–283, 2001.

[15] C. Ozay and M.S. Celiktas, "Statistical analysis of wind speed using two-parameter Weibull distribution in Alaçatı region," Energy Conversion and Management, vol.121, pp. 49–54, 2016.

[16] A. Ucar and F. Balo, "Effect of fuel type on the optimum thickness of selected insulation materials for the four different climatic regions of Turkey," Applied Energy, vol. 86, pp.730–736, 2009.

[17] Energy and Environmental Systems Magazine (Enerji dünyası dergisi), Teknik yayıncılık tanıtım AŞ, 2008.

BIOGRAPHIES

Aynur UÇAR was born and lives in Elazığ (Turkey) in 1973. She holds a Master's Degree in 1999 and a doctoral degree in 2005 from Institute of Science of the Fırat University. She is an associate professor in Mechanical Engineering at the University of Fırat since 2012. Her research has ranged over heat transfer, renewable energy, energy storage, thermal insulation, finite element analysis, energy and heat pump.

European Journal of Technique

journal homepage: https://dergipark.org.tr/en/pub/ejt

Vol.12, No.2, 2022

Investigation of Mechanical Properties of Layered Composites Formed from Glass, Carbon and Aramid Fibers and Aluminum Plates

İbrahim Biliz[1*], Yahya Hışman Çelik[2]

[1] Batman University, Faculty of Engineering and Architecture, Department of Mechanical Engineering, Batman, ibrahim.biliz@batman.edu.tr
[2] Batman University, Faculty of Engineering and Architecture, Department of Mechanical Engineering, Batman, yahyahisman.celik@batman.edu.tr

ARTICLE INFO

Received: May., 27. 2022
Revised: Aug., 10. 2022
Accepted: Sep, 20. 2022

Keywords:
Laminated Composite
Tensile Strength,
Bending Strength

Corresponding author: *Ibrahim Biliz*

ISSN: *2536-5010* | e-ISSN: *2536-5134*

DOI: https://doi.org/10.36222/ejt.112260

ABSTRACT

Technological developments and differences in application areas increase the importance of laminated composites. Laminated composites with complex properties exhibit features such as high strength, high corrosion and thermal resistance, low specific gravity, resistance to environmental conditions. These properties generally reflect components that make up laminated composite. In this study, effects of reinforcements on mechanical properties of laminated composites were investigated. In production of laminated composites, aluminum 5754 is used for metal layers, and aramid, glass and carbon fibers are used for fiber reinforcements. Epoxy was also preferred as resin. First of all, the resin was applied on the cleaned aluminum plate and the aramid fiber was added on it. By continuing the processes in this way, Arall laminated composite consisting of five layers was obtained. Similar processes were applied to carbon fiber and glass fiber materials, and Carall and Glare laminated composites were produced, respectively. In addition, by subjecting the fiber layers to a combination among themselves, Ar-Carall, Ar-Glare and Car-Glare laminated composites were produced. The produced laminated composites were subjected to tensile and bending tests and their strengths were compared. As a result of the experiments, the highest tensile and bending strength was obtained from the Carall laminated composite. The strength of the Ar-Carall and the Car-Glare laminated hybrid composites containing carbon fiber were better than the Arall and the Glare laminated composites.

1. INTRODUCTION

Layered composites consist of thin plates and panels with high strength in a certain direction. Very high strength values are obtained by combination of layers with different fiber orientations. FML (fiber metal laminated) composites are a good example. It is based on stacking thin metal plates with different properties and prepreg materials on top of each other [1]. Metal plate and prepreg forming FML layered composites are shown in Figure 1.

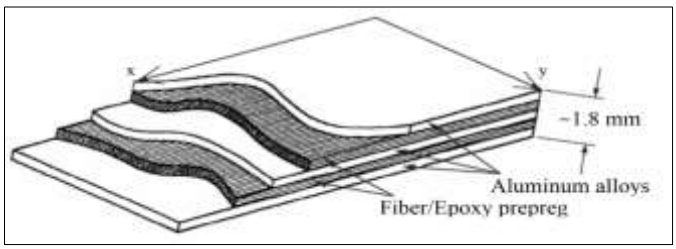

Figure 1. Fiber metal laminate (FML) laminated composite [1]

Arall (Aramid Reinforced Aluminum Laminates) was originally developed for applications in the airframe [2]. In later stages, two other variants of FML, Glare (Glass laminate aluminum reinforced epoxy) [3] and Carall (Carbon Reinforced Aluminum Laminates) [4], laminated composites began to be produced. These layered composites have been used in aircraft construction since 1980. In these composites, ductile aluminum alloy and linear elastic rigid fibers are in same material, and properties of layered composites bear characteristics of phases forming composite [5]. Arall, Glare and Carall laminated composites offer many advantages in industrial field, thanks to their low density, high strength to weight ratio and excellent corrosion resistance. Therefore, it has attracted attention of researchers. Wu and Yang (2005) stated that Glare layered composites offer a unique combination of properties such as outstanding fatigue resistance, high specific static properties, excellent impact resistance, good residue and blind notch strength, good corrosion properties and ease of fabrication/repair [6]. They also stated that Glare layered composites can be adapted to a wide variety of applications by changing the fiber/resin system, alloy type and thickness, stacking order, fiber orientation, surface pretreatment technique, etc. Armatlı Kayrak (2006) stated that specific elastic modulus, specific shear modulus and poison ratio in fiber direction and perpendicular to fiber direction of Arall

plates have higher values than Glare and aluminum alloy materials [5]. It was emphasized that Glare, which has unidirectional layers, shows high properties comparable to aluminum alloys, and also has advantage of low density. Qaiser et al. (2015) stated that the curing process has an important effect on increasing strength of resin, but its effect on interface of layers is limited [2]. However, they emphasized that interfacial interaction of Arall composites could be improved after anodizing. Scanning electron microscope images and subsequent electron scattering spectrum data showed that adhesion on aluminum was much better in anodized and cured layers. Khalid et al. (2022) treated their manufactured composites with surface de-greasing, mechanical abrasion, and anodizing. In order to perform mechanical characterization, uniaxial tensile tests were conducted at various strain rates. The results revealed that, in the case of Carall, 1.7% increase in tensile strength and its tensile strength was increased from 741 MPa to 754 MPa. Whereas, Arall and Glare laminates exhibited high degree of strain rate-sensitivity. When the strain rate is the values are increased in the following patterns: 389 MPa, 411 MPa, and 475 MPa for Glare laminates (22% increase), and 253 MPa, 298 MPa 352 MPa for Arall laminates (39% increase) [7]. Asghar et al. (2017) stated that ultimate tensile strength of sheets is related to nature of their components [8]. They observed that Carall's tensile strength (215 MPa) and fracture toughness (87.554 MPa) were 50% higher than Arall's maximum tensile strength and 47% higher than fracture toughness, 22% higher than Glare's maximum tensile strength and 23% higher than fracture toughness. They also stated that Carall exhibited superior fatigue performance compared to Arall and Glare due to its fiber bridging effect. They emphasized that behavior of the experimental Paris curves also confirms the similar behavior. The most important disadvantage of composites is formation of cracks at matrix and fiber interface and propagation of this crack. It is stated that the most important reason for preference of laminated composites used in aircraft construction is low crack formation and low crack propagation characteristics. It is stated that the fibers were not damaged by arranging them in the load direction and the crack remains on the aluminum matrix plates and reduces stress intensity [2] (Figure 2).

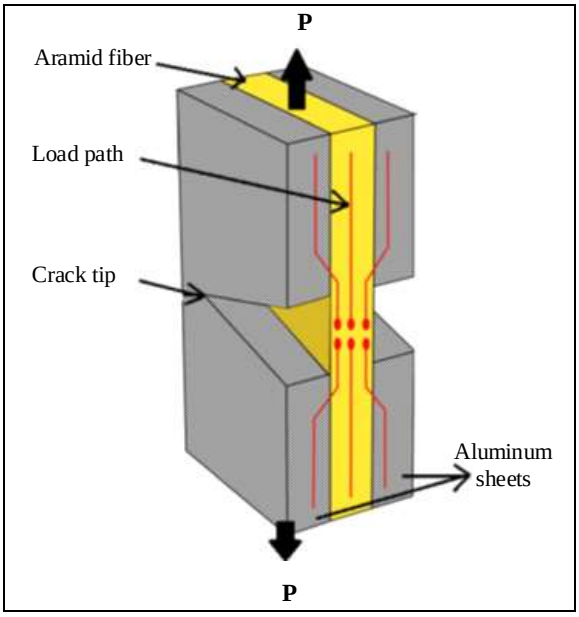

Figure 2. Crack-stopping mechanism of Arall [2]

It was seen that detailed analyzes were made on Arall, Glare and Carall layered composites in literature. In this study, in addition to Arall, Glare and Carall layered composites, Ar-Carall, Ar-Glare and Car-Glare layered hybrid composites were produced by combining the fibers in the layered composites. Tensile and bending strengths of the produced laminated composites were determined and compared with the each other.

2. MATERIALS AND METHOD

2.1. Production of Samples

In this study, metal sheet, different synthetic fibers, epoxy and hardener were used to produce laminated composite. Aluminum 5754 H111 alloy, purchased from Avas Metal, which has high corrosion and fatigue resistance, light weight, good weldability, resistant to industrial atmosphere and sea water, and suitable for coating, was preferred as metal sheet. The chemical composition of aluminum 5754 alloy, which has a thickness of 0.5 mm, is given in Table I, and some mechanical properties and hardness values are given in Table II.

TABLE I.
Chemical composition of aluminum 5754 H111 alloy (wt. %)

Fe	Si	Cu	Mn	Mg	Zn	Cr	Ti	Other	Al
0.4	0.4	0.1	0.5	3.1	0.2	0.3	0.15	0.15	Balance

TABLE II.
Mechanical properties of aluminum 5754 H111 alloy

Yield strength (MPa)		Tensile strength (MPa)		Elongation (%)	Hardness (Brinell (kg/mm^2))	
Min	Max	Min	Max	Max	Min	Max
80	100	190	215	24	50	55

Synthetic aramid, glass and carbon fibers, which are widely used in different fields and have become today's indispensable materials, have been used as fiber materials. Aramid, glass and carbon fibers which purchased from Dost Kimya, have the same weave and their weight is 200 gr/m^2. Arc 152 multi-purpose epoxy resin and W152 hardener, which purchased from Arc Marin, are specially designed for lamination and have protection and impermeability, are used as resin and hardener. Aluminum sheet cut by a saw and the fibers by a special scissors into dimensions of 120 mm x 20 mm. Epoxy and hardener were weighed on a precision balance at a ratio of 4/1 as written in the product introduction and mixed in a Heidolph brand MR Hei-Standard model magnetic stirrer for 15 minutes, at 50 °C table temperature and 750 rpm rotational speed. Epoxy resin was applied by hand lay-up method on the cleaned aluminum 5754 alloy sheet and aramid fiber was laid on it. An aluminum 5754 alloy plate was placed on aramid fiber again, on which the epoxy was impregnated, and the epoxy resin was applied on aluminum sheet. By adding aramid fiber on the resinized sheet, the resin was impregnated and the last layer of aluminum 5754 alloy sheet was placed on it and left to cure. Similar processes have also been applied to aluminum laminated composites using carbon and glass fibers. Thus,

composites with aramid aluminum layer (Arall), carbon aluminum layer (Carall) and glass aluminum layer (Glare) were produced. In addition to these, Ar-Carall (one aramid fiber layer and one carbon fiber layer between three aluminum layers), Ar-Glare (one aramid fiber layer and one glass fiber layer between three aluminum layers) and Car-Glare (carbon aramid fiber layer and one glass fiber layer between three aluminum layers) layered composites were produced by combining fiber layers within themselves. All samples have 2 mm thickness and the other information including the layer types and numbers of produced laminated composites are given in Table III.

TABLE III.
Layer types and numbers of samples

Sample Number	Composite Name	Aluminum	Aramid Fiber	Carbon Fiber	Glass Fiber	Thickness (mm)
1 and 7	Arall	3	2	-	-	2
2 and 8	Ar-Carall	3	1	1	-	2
3 and 9	Ar-Glare	3	1	-	1	2
4 and 10	Glare	3	-	-	2	2
5 and 11	Carall	3	-	2	-	2
6 and 12	Car-Glare	3	-	1	1	2

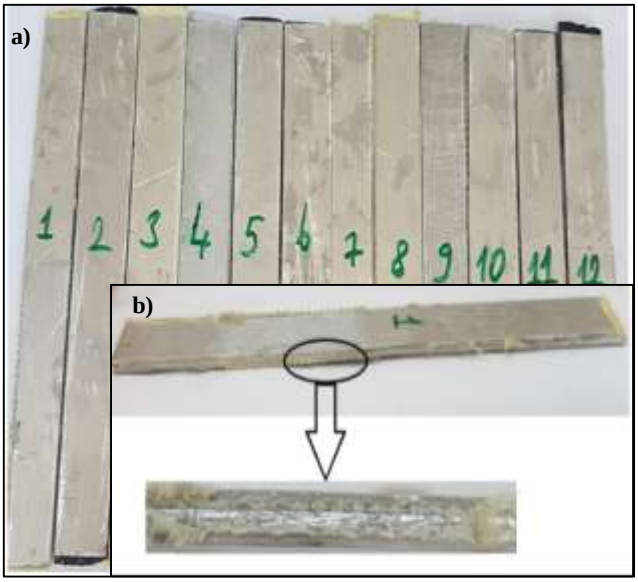

Figure 3. a) Image of produced laminated composite samples, b) Close-up view of the layers

Manufactured fiber metal laminated and hybrid fiber metal laminated samples image is given in Figure 3a. Close-up view of the layers of Arall is given in Figure 3b.

Manufactured samples were subjected to tensile test and bending tests with 250 kN capacity load cells in a Shimadzu brand universal test device to determine mechanical properties of the layered composite specimens. The test setup of the samples subjected to tensile and bending tests is given in Figure 4. The specimens were clamped to the jaws. Each jaw was given a clamping margin of 20 mm and the distance between the jaws was adjusted to 80 mm for the tensile test. The other hand the distance between the supports was kept at 80 mm and the center of the supports was adjusted to the force direction the bending test.

2.2. Mechanical Calculations and Experiments

Two samples were tested for each test. The force and elongation graphs were drawn by taking the average of two samples. Tensile and bending strengths of the laminated composites were calculated by considering the maximum forces in the force and elongation graph and the dimensions of the test specimens. The formula used for the calculation of the tensile strength is given in equation 1, and the formulas used for the calculation of the bending strength are given in equation 2-6.

$$\sigma_T = F/A \quad (1)$$

$$M = F * (L/4) \quad (2)$$

$$y = h/2 \quad (3)$$

$$I = (b * h^3)/12 \quad (4)$$

$$W = I/y = (b * h^2)/6 \quad (5)$$

$$\sigma_B = M/W \quad (6)$$

Here; σ_T: tensile strength, F: maximum applied load, A: sample cross-sectional area, M: moment, L: bending distance, h: sample thickness, b: sample width, I: moment of inertia, W: moment of strength and σ_B: bending strength.

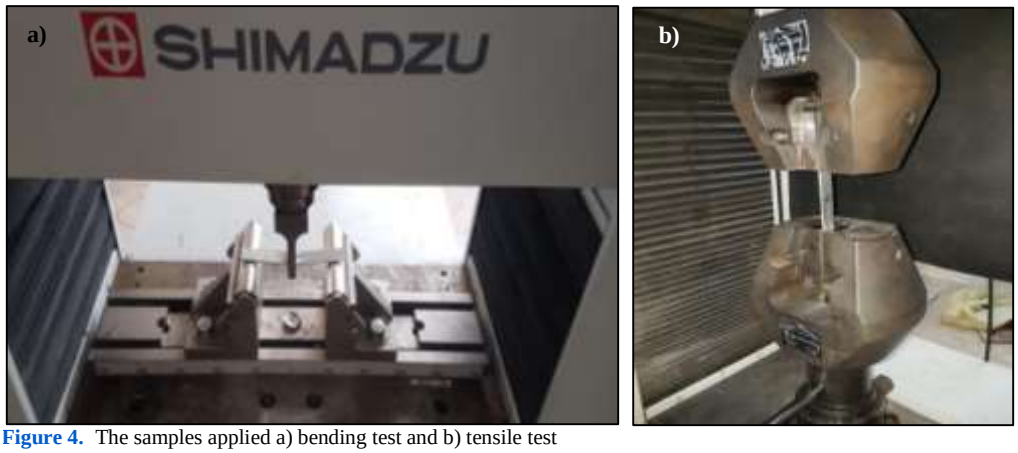

Figure 4. The samples applied a) bending test and b) tensile test

3. EXPERIMENTAL RESULTS AND DISCUSSION

In this study, tensile and three-point bending tests of Arall, Glare and Caral composites, and Ar-Carall, Ar-Glare and Car-Glare layered hybrid composites obtained by replacing the fibers were carried out with Schimadzu Universal test device. The Force (N) – Elongation (mm) graph as a result of the tensile test of Arall, Carall and Glare layered composites is given in Figure 5, and for Ar-Carall, Ar-Glare and Car-Glare layered hybrid composites in Figure 6.

For Arall composite, the maximum force was 12445 N and the maximum elongation was 6.2%. The tensile strength of Arall sample was calculated as 325.1 MPa by dividing the maximum tensile force obtained by the cross-sectional area of the sample. Although the calculated result is compatible with the literature data (390 MPa), the small differences are due to the strength-enhancing heat treatment of the aluminum alloy used in other studies [9].

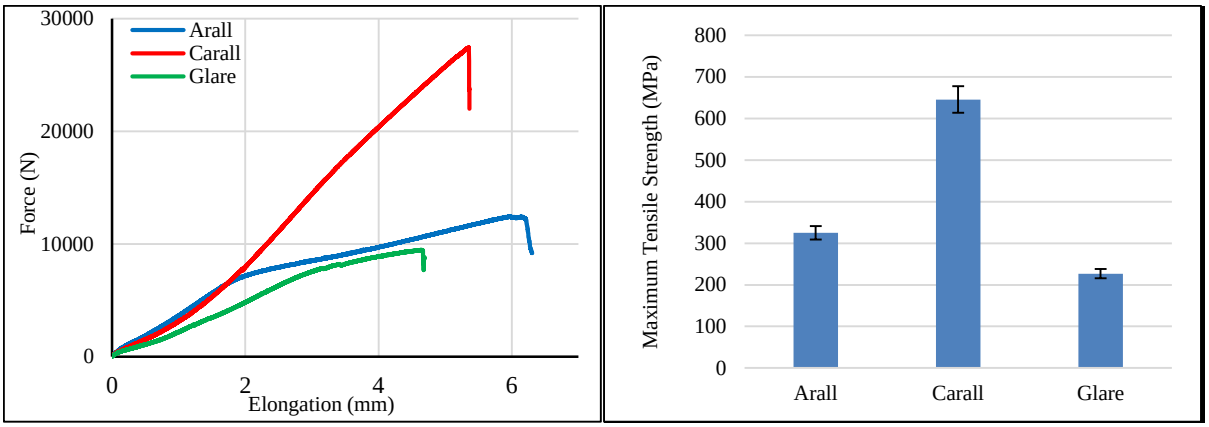

Figure 5. Tensile test graph of laminated Arall, Carall and Glare composites and their maximum tensile strengths

The tensile stress of Carall was calculated as 645.4 MPa by dividing the maximum force (27460 N at 5.3% elongation) by the cross-sectional area of the sample. In the literature, it was stated that the tensile strength of Carall at room temperature was 568±17 MPa as a result of the tensile test [10]. In the Glare layered composite, the maximum force was 9480 N and the maximum elongation was 4.6%. The tensile stress of the Glare sample was calculated as 226.9 MPa, and this value was found to be consistent with the data in the literature (~215 MPa) [11].

The maximum tensile strengths of Ar-Carall and Car-Glare laminated composites were very close to each other, measuring 16600 N and 16470 N, respectively, and their tensile strengths were calculated as 394.1 MPa and 397.2 MPa, respectively. If Figure 5 and Figure 6 are taken together, it is seen that the use of carbon fiber with other fibers leads to an increase in tensile strengths. In Arall composite, when a layer of carbon fiber is placed instead of a layer of aramid fiber (Ar-Carall), it has been determined that the tensile strength increases by 33%, and when the same process is applied in Glare composite (Car-Glare), it increases the tensile strength by 73%. The tensile strength of Ar-Glare composite was 22% lower than Arall and 11% higher than Glare.

The images of the fracture regions formed as a result of the tensile test of the laminated composites are given in Figure 7. As a result of the tensile test, it was observed that the fibers were separated from each other in a characteristic way by a mechanism in which the weave type and fiber orientation (0^0) were effective, showing similarity to the results found in the literature [12]. As shown in Figure 7a, it was determined that only the fibers in the tensile direction were separated from each other and damaged due to the anisotropic nature of the aramid fiber in the fracture regions of the aramid fiber reinforced laminated composites [13]. In the fracture regions of the carbon fiber reinforced laminated composites, in Figure 7b, the fibers are broken, similar to the studies in the literature, with the damage occurring in several regions, largely indented and protruding [14]. In the rupture regions of the glass fiber reinforced laminated composites, the glass fiber is separated from each other along a straight line perpendicular to the drawing direction (Figure 7c) [12].

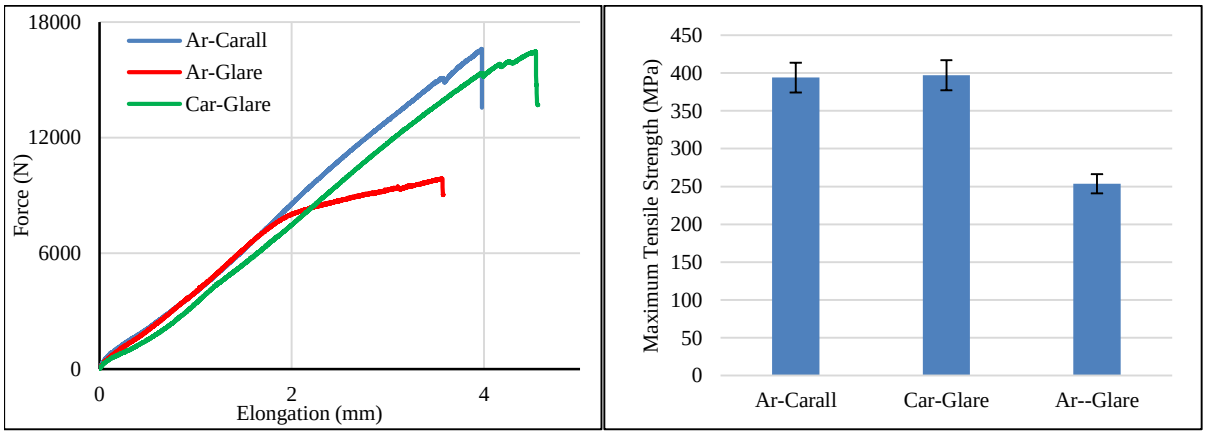

Figure 6. Tensile test graph of Ar-Carall, Ar-Glare and Car-Glare composites and their maximum tensile strengths

Figure 7. Fracture regions of Al layer composites a) Aramid Fiber Reinforced b) Carbon Fiber Reinforced c) Glass Fiber Reinforced

Force (N) – Deflection (mm) graph as a result of three-point bending test of Arall, Carall and Glare layered composites is given in Figure 8, and for Ar-Carall, Ar-Glare and Car-Glare layered composites in Figure 9.

As a result of the three-point bending test of Arall layered composite, the maximum bending force was measured as 190.6 N and the bending stress was calculated as 440.5 MPa. In research carried out in the literature, since the unit of measurement was given as force (N) in the bending test of the Arall layered composite, a comparison in MPa could not be made. In the same study, since the tensile test is given in MPa and it is compatible with the tensile test we have done, it is thought that the bending stress is also compatible [8]. As a result of the three-point bending test of Carall layered composite, the maximum bending force was measured as 456.2 N and the bending strength was calculated as 690.7 MPa. In the studies, the bending strengths for Carall were similar to the test results we performed and it was stated to be between 675-610 MPa [15]. As a result of the three-point bending test of Glare layered composite, the maximum bending force was measured as 232.8 N and the bending strength was calculated as 449.1 MPa. In the studies, the bending strengths for Glare are close to the test results we have done, and it has been stated to be between 520-690 MPa [16].

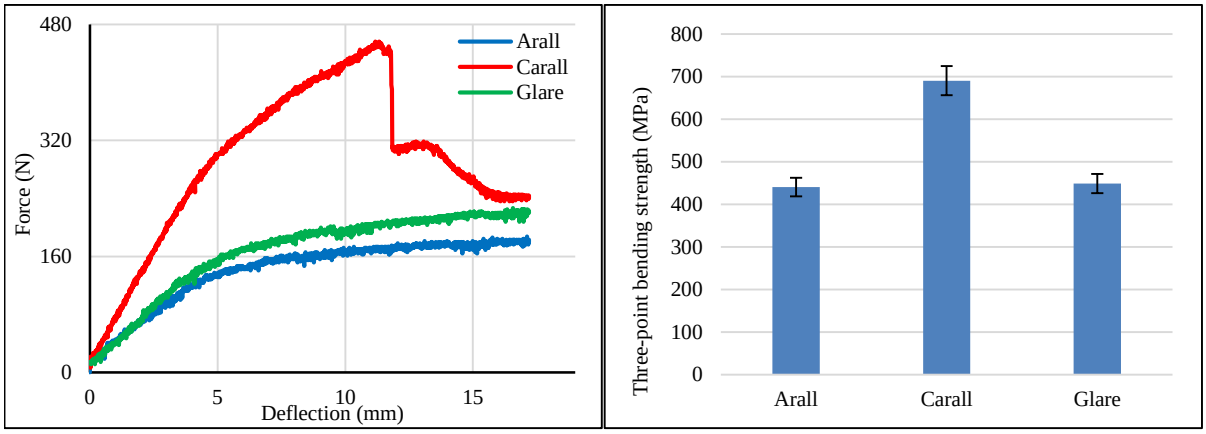

Figure 8. Three-point bending test graph of layered composites and their bending strengths

Ar-Carall and Car-Glare laminated composites have the highest and lowest bending strengths of the layered composites produced by adding binary combinations of aramid, carbon and glass fibers between aluminum plates. Ar-Carall layered composite was damaged at 382.2 N and Car-Glare layered composite was damaged at 341.1 N bending force. Ar-Glare layered composite, on the other hand, carried a maximum bending force of 277.2 N. The bending strengths of Ar-Carall, Ar-Glare and Car-Glare laminated composites were calculated as 518.9 MPa, 415.7 MPa and 501.7 MPa, respectively.

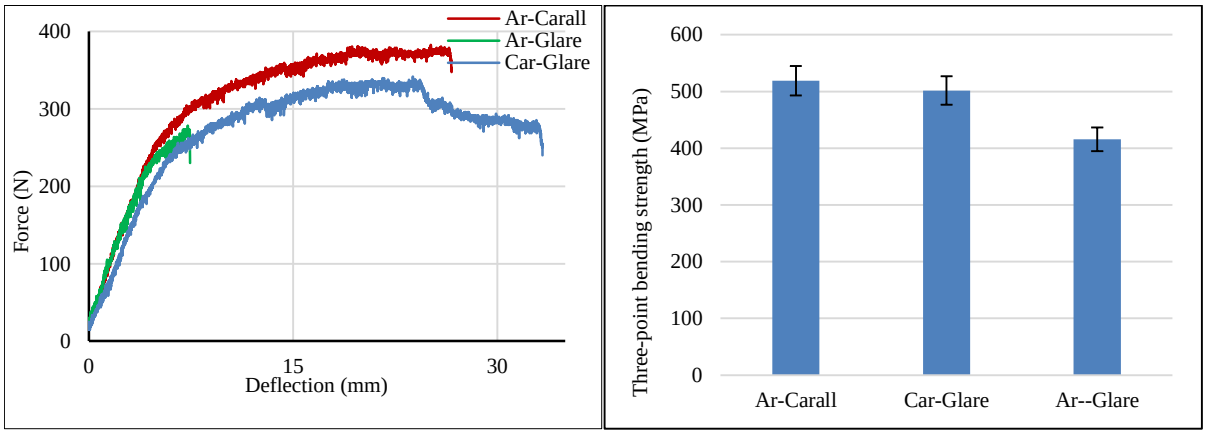

Figure 9. Three-point bending test graph of Ar-Carall, Ar-Glare ve Car-Glare laminated composites and their bending strengths

4. CONCLUSION

In this study, Arall, Carall, Glare, Ar-Carall, Ar-Glare and Car-Glare layered composites were produced using aramid, carbon and glass fibers and aluminum laminates, and tensile and bending tests of these layered composites were performed. Obtained results are given below.

1. The highest tensile strength value was measured in Carall laminated composite (645.4 Mpa). It was determined that the result obtained was quite higher than Arall (325.1) and Glare (226.9 MPa) layered composites.

2. It has been observed that the tensile strength values of the layered composites with carbon fiber are higher than the layered composites without carbon fiber.

3. While the flexural strength was highest in Carall layered composite (690.7 MPa), it was close to each other in Arall (440.5 MPa) and Glare (429.1 MPa) layered composites.

4. In bending strength as well as tensile strength, layered composites with carbon fiber were obtained better than layered composites without carbon fiber.

REFERENCES

[1] Botelho, E. C, Silva, R. A., Pardini, L. C. and Rezende, M. C., A review on the development and properties of continuous fiber/epoxy/aluminum hybrid composites for aircraft structures, Materials Research, 9 (3), 247-256, 2006.

[2] Qaiser, H., Umar, S., Nasir, A., Shah, M. and Nauman, S., Optimization of interlaminar shear strength behavior of anodized and unanodized ARALL composites fabricated through VARTM process, International Journal of Material Forming, 8, 481–493, 2015.

[3] Khalid, M. Y., Al Rashid, A. and Sheikh, M. F., Effect of anodizing process on inter laminar shear strength of GLARE composite through t-peel test: experimental and numerical approach, Experimental Techniques, 45, 227–235, 2021.

[4] Khan, F., Quayyum, F., Asghar, W., Azeem, M., Anjum, Z., Nasir, A. and Shah, M., Effect of various surface preparation techniques on the delamination properties of vacuum infused carbon fiber reinforced aluminum laminates (CARALL): experimentation and numerical simulation, Journal of Mechanical Science and Technology, 31 (11), 5265–5272, 2017.

[5] Armatlı Kayrak, M., Düzlemsel gerilmeler etkisindeki Arall ve Glare kompozit plakaların rijitlik analizleri, Mühendis ve Makine, 47 (560), 26–32, 2006.

[6] Wu, G. and Yang, J.-M., The mechanical behavior of GLARE laminates for aircraft structures, The Journal of the Minerals, Metals & Materials Society, 57, 72–79, 2005.

[7] Khalid MY, Arif ZU, Ahmed W, Arshad H., Evaluation of tensile properties of fiber metal laminates under different strain rates, Proceedings of the Institution of Mechanical Engineers, Part E: Journal of Process Mechanical Engineering, 236(2), 556-564, 2022 .

[8] Asghar, W., Nasir, M. A., Quayyum, F., Shah, M., Azeem, M, Nauman, S and Khushnood, S., Investigation of fatigue crack growth rate in CARALL, ARALL and GLARE, Fatigue Fracture of Engineering Materials and Structure, 40 (7), 1086–1100, 2017.

[9] Monsalve, A., Parra, L., Baeza, D., Solis, R., Palza, H., Mechanical properties and morphological characteristics of ARALL reinforced with TRGO doped epoxy resin, RevistaMateria, v. 23, n. 4, 2018.

[10] Botelho, E. C, Almeida, R. S., Pardini, L. C. and Rezende, M. C., Influence of Hygrothermal Conditioning on the Elastic Properties of Carall Laminates, 2017

[11] Megahed, M., Abd El-baky, M.A., Alsaeedy, A.M., Alshorbagy, A.E., An experimental investigation on the effect of incorporation of different nanofillers on the mechanical characterization of fiber metal laminate, Composites Part B, 176, 2019.

[12] Deniz, M. E., Aydin F., Determination of fatigue life of the unidirectional GFRP/Al hybrid composite laminates, Composites Part B: Engineering, Volume 166, 580-587, 2019

[13] Bandaru, A. K., Shivdayal, P., Yogesh, S., Suhail, A., R. Alagirusamy, Naresh B., Mechanical behavior of Kevlar/basalt reinforced polypropylene composites, Composites: Part A 90 642–652, 2016

[14] Korkmaz, N, Çakmak, E., Dayık, M., Mechanical and thermal characterization of woven carbon fiber reinforced carbon nanotube-epoxy composites, Journal of Natural and Applied Sciences, 20 (2), 338-353, 2016.

[15] Bellini, C., Di Cocco, V, Iacoviello, F., Sorrentino, L., Experimental analysis of aluminium carbon/epoxy hybrid laminates under flexural load, Frattura ed Integrità Strutturale, 49, 739-747, 2019.

[16] Dahshan, B., El-Habbak, A.-H. M., Adly, M. A., Shazly, M., Experimental and numerical study on the tensile, threepoint-bending, and interlaminar fracture toughness of GLARE. Journal of Mechanical Science and Technology, 34, 8, 3273~3281, 2020.

BIOGRAPHIES

İbrahim BILIZ obtained his BSc degree in metalurgical and materials engineering from Yildiz Technical University (YTU) in 2013. He also received the MSc. diploma in Metalurgical and Materials Engineering from the Yildiz Technical University in 2019. His PhD education in continuing in Batman University, Department of Mechanical Engineering. His research interests are powder metalurgy, composite materials and welding. In 2010 he joined the Faculty of Engineering Architecture, Metalurgical and Materials Engineering, Batman University as a research assistant.

Yahya Hışman ÇELIK obtained his BSc degree in mechanics education from Firat University in 2002 and in mechanical engineering from Batman University in 2016. He received the MSc., and PhD. diploma in machinery training from Firat University in 2005 and 2010 respectively. His research interests are manufacturing technologies, material desing and behaviors, machine desingn and machine equipment. In 2010 he joined the Faculty of Engineering-Architecture, Department of Mechanical Engineering, Batman University as an assistant professor, where he is presently a professor.

European Journal of Technique

journal homepage:https://dergipark.org.tr/en/pub/ejt

Vol.12, No.2, 2022

IoT Based Home Automation System using a REST API Architecture

Zaw Lin Oo[1*], Theint Win Lai[2], Aung Moe[3]

[1*]Department of Atomic Energy, Ministry of Science and Technology, Yangon, Myanmar. (e-mail: kozawlinoo@gmail.com).
[2]Info Myanmar University, Faculty of Computer System and Technology, Yangon, Myanmar. (e-mail: t-winlei@imu.edu.mm).
[3]Department of Atomic Energy, Ministry of Science and Technology, Nay Pyi Taw, Myanmar.(e-mail: aung2011m@gmail.com).

ARTICLE INFO

Received: Nov., 02.2021
Revised: Jun., 26.2022
Accepted: Aug., 18.2022

Keywords:
Arduino MKR Wifi 1010
Home automation system
Internet of things (IOT)
REST API

Corresponding author: *Zaw Lin OO*

ISSN:*2536-5010* | e-ISSN: *2536-5134*

DOI: https://doi.org/10.36222/ejt.1018131

ABSTRACT

Internet of things (IOT) imagines a world where every device at any place can be connected. Home Automation system is growing rapidly and now becoming the requirement of the modern world. IoT based Home Automation System is getting more important as it increases security, comfort and improves the quality of life. In this paper, we have proposed the details of how we can automate the home appliances using ARDUINO and REST API architecture. The result also shows how the use of ARDUINO and REST API architecture is beneficial as client/server communication in the field of the Internet of Things. In this paper, the REST API architecture is implemented practically, tested, and gave the accepted results for controlling home appliances. Home appliances such as TV, lighting, Water pump, Fans and etc were controlled from the web page that was created in the XAMPP platform as a client-side. The aim of this study is to develop a home automation system for controlling electronic appliances from a far range by using the Internet of things (IOT).

1. INTRODUCTION

Nowadays, peoples created home automation systems with different designs based on their different needs. For example, some people need to control their home appliances wirelessly within their house but some want to control remotely from anywhere that they can get internet access. This research is commonly used to operate a device from an internet webpage and provide safety and convenience to the user. The user can control different home appliances like room lighting, air conditioners, fan, televisions, etc. from a webpage remotely by just clicking on and off buttons what they want it to do.

Many types of commercially home automation systems that are intended to control all lights and electrical appliances in a home or office can easily be available. But, they have challenges which are high cost, need to replace all legacy home appliances with new compatible ones, not user-friendly, limited range of control system and not easy to operate. Some requirements have proceeded for home automation system to satisfy their needs and comfort while for people who stay outside of the home and they want to control their devices for great assistance with easy user-friendly operation. This paper tried to develop a cost-effective, simple, and user-friendly system capable of automating home appliances. This is further improved because the client/server communication based REST API architecture is used in the field of the Internet of Things.

2. RELATED WORK

There have been several types of research and projects related to home automation systems. The home automation system with voice recognition and touch screen technology [1] uses a wireless home automation system to control lights and other electrical appliances at home or office using voice commands and touch screen responses. The Microsoft Speech API is running on the PC to recognize the voice commands. The RF transceiver is used to send these commands to the controller to control the various electrical devices. The use of the Voice Recognition Module makes this system more expensive and difficult to handle.

Arduino Based Home Automation System that Implementation on REST Architecture [2] proposed a system that uses Arduino UNO board with Ethernet Shield to provide local network connectivity and controlled by an android application. The Arduino gets the voice command and works according to the speak control of the users. This research project used REST Architecture for communication but voice control is not accurate for controlling home appliances.

Design and Implementation of Modular Home Automation Based on Wireless Network, REST API, and WebSocket [3] use Raspberry Pi 2 as a localhost server, XBee module as a wireless communication module between the Raspberry Pi with Arduino Uno, Arduino Uno which receives commands from Raspberry Pi and Android application for HTTP

requests. This paper [3] used two hardware devices, Raspberry Pi and the Arduino Uno, that make them more costly and difficult to maintain.

Design and Implementation of an Internet of Things based Prototype for a Smart Home Automation System [4] is designed and implemented for IoT based prototype of a smart home automation system. The main controller ATmega16 and Android App is used for intra-home network and the interoperable layer. This prototype has been implemented for the status monitoring purpose and also used for demonstration of controlling the action.

The appliances employed in this project are Arduino MKR WIFI 1010 microcontroller and 5V Four-Channel Optical Isolated Relay Module as hardware devices. REST API and XAMPP are used for software development. REST API standardised the communication between Arduino and the external world via WiFi or Ethernet and XAMPP, a web server software package used for website development.

In this project, Arduino MKR WIFI 1010 performs as the server side and the web browser is used as the client side for client/server communication. The Arduino MKR WIFI 1010 microcontroller is a new generation of Arduino product and also cheap for use. Home appliances are controlled easily through the internet by opening a web browser and contain easy features for user-friendly design. No need to install special apps for Home Automation control and wide range control using internet connections are main developments of this project.

3. SYSTEM DESIGN

This paper will contribute to designing and developing IoT based Home Automation System with a REST API Architecture on client/server communication. The webpage created with HTML and CSS on the XAMPP package is used to control the devices and contains the interface. XAMPP is the software that has a complete PHP, Apache, and MySQL web development environment. In this project, A JavaScript file is also used to handle the commands coming from the interface of the HTML page. A PHP file is worked for communication function with the Arduino board by making REST calls. In this study, Arduino MKR WiFi 1010 Board microcontroller is used to connect with the webpage interface via WiFi connectivity for the IoT applications module. The overall design and architecture of the system is illustrated in Fig. 1, where the communication of web browser to the microcontroller via WiFi connection calling REST API and microcontroller also control home appliances using a relay as a switch are shown.

3.1. Arduino MKR WiFi 1010

MKR WIFI 1010 is the evolution of the MKR1000 and is equipped with an ESP32 module made by U-BLOX. The MKR Wifi 1010 aims to speed up and simplify the prototyping of WI-FI based IoT applications thanks to the flexibility of the ESP32 module and its low power consumption. The design includes a Li-Po charging circuit that allows the Arduino MKR WIFI 1010 to run on battery power or external 5V, charging the Li-Po battery while running on external power. Switching from one source to the other is done automatically.

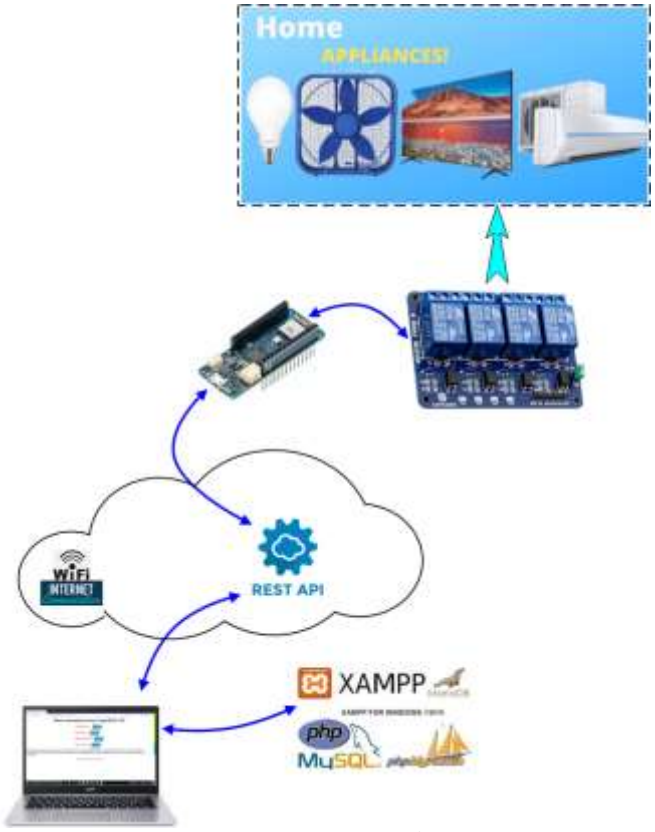

Figure 1. Overall Design and Architecture of the Proposed System

A good 32 bit computational power, the usual rich set of I/O interfaces, low power Wi-Fi with a Cryptochip for secure communication, and the ease of use of the Arduino Software (IDE) for code development and programming. All these features make this board the preferred choice for the emerging IoT battery-powered projects in a compact form factor. The USB port can be used to supply power (5V) to the board. The Arduino MKR WIFI 1010 is able to run with or without the Li-Po battery connected and has limited power consumption [5].

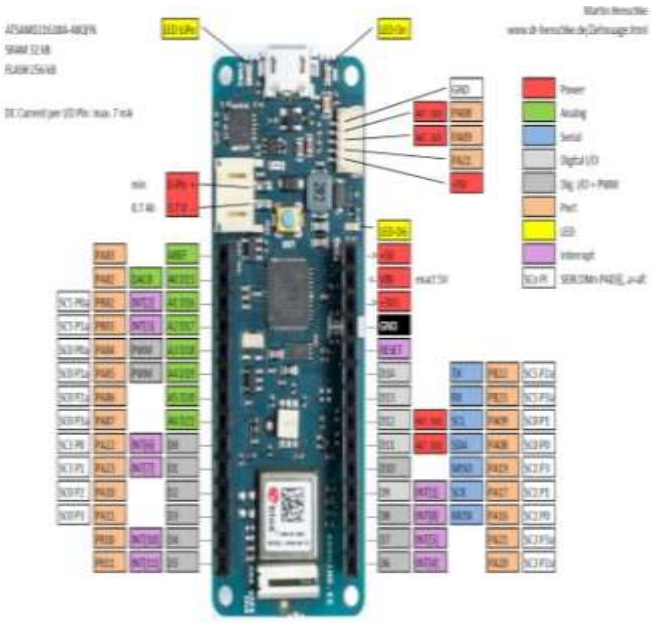

Figure 2. Arduino MKR Wifi 1010 Board
https://www.henschke-geraetebau.de/dr/MKR_WiFi_1010_Pinout.pdf

3.2. REST API

REST stands for REpresentational State Transfer, and is a communication architecture that was created back in 2000. The concept of REST that is widely used by many web applications like SaaS (Software as a Service) [6]. It uses HTTP protocol for data communication and all the components that are involved in the communication are accessed by the standard HTTP version. REST is web based architecture and it treats every component as a resource which is easily accessible by the HTTP Standards [7].

This allowed to standardise communication between web applications, and made them more scalable, faster, and simplified the development of more complex applications. And for our research projects, it allows to standardise the communication between Arduino and the external world via WiFi or Ethernet, and develop complex applications without having to modify Arduino sketch every time. With this REST API, it's easy to load a sketch once for all on the Arduino, and then only work on the interface on computer browser that makes REST calls on the Arduino board. And for now, this kind of interface was only available on the official Arduino boards, like the WiFi & Ethernet shields, and the Yun. The library that will handle the REST calls, which is called aREST. The sketch that will create a web server on the Arduino MKR WIFI 1010 board, and then accept REST commands from an external client, like from an interface running on the computer web browser [6].

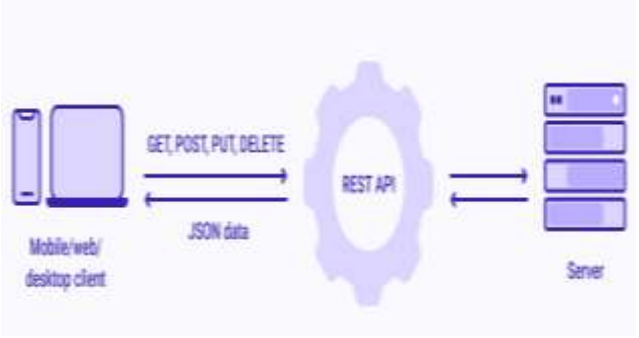

Figure 3. REST API communication architecture

3.3. XAMPP

In this research work, XAMPP is installed and tested on a local PC using the Apache HTTP server component of the XAMPP package. XAMPP, a free, open-source software package produced by the non-profit organization Apache Friends, is the most popular web server software package used for website development. XAMPP is (X) cross-platform, and, at minimum, contains the (A) Apache HTTP server, and supports the (M) MySQL database, (P) PHP scripts, and (P) Perl scripts. XAMPP distribution packages are available for Windows, Linux, and OS X system operating environments. Officially, XAMPP's designers intended it for use only as a development tool, to allow website designers and programmers to test their work on their own computers without any access to the Internet. To make this as easy as possible, many important security features are disabled by default. XAMPP has the ability to serve web pages on the World Wide Web. A special tool is provided to password-protect the most important parts of the package. XAMPP also provides support for creating and manipulating databases in MariaDB and SQLite among others. Once XAMPP is installed, it is possible to treat a localhost like a remote host by connecting using an FTP client. Using a program like FileZilla has many advantages when installing a content management system (CMS) like Joomla or WordPress. It is also possible to connect to localhost via FTP with an HTML editor [8].

XAMPP is used that to build a simple web application that will run in the browser, with buttons to control the home appliances that are connected to the Arduino board.

For this part, a working web server (like Apache) is needed for running on the computer with appropriate web page, and also required to put all the files at the root of the web server's main folder.

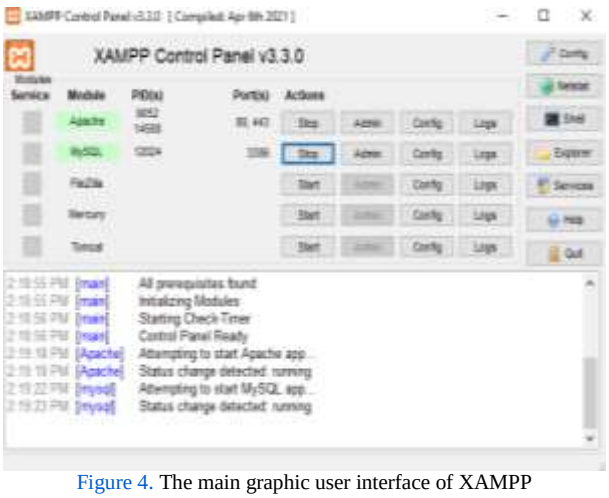

Figure 4. The main graphic user interface of XAMPP

3.4. 5V Four-Channel Optical Isolated Relay Module

This is a LOW Level 5V four-channel relay interface board, and each channel needs a 15-20mA driver current. It can be used to control various appliances and equipment with large current. It is equipped with high-current relays that work under AC250V 10A or DC30V 10A. It has a standard interface that can be controlled directly by microcontroller. This module is optically isolated from high voltage side for safety requirement and also prevent ground loop when interface to microcontroller [9].

Relay Maximum output: DC 30V/10A, AC 250V/10A [9]. Four Channel Relay Module with Opto-coupler. LOW Level Trigger expansion board, which is compatible with Arduino control board [9].

Standard interface that can be controlled directly by microcontroller (8051, AVR, *PIC, DSP, ARM, ARM, MSP430, TTL logic) [9].

Relay of high quality low noise relays SPDT. A common terminal, a normally open, one normally closed terminal [9].

Opto-Coupler isolation, for high voltage safety and prevent ground loop with microcontroller [9].

The switching transistors act as a buffer between the relay coils that require high currents, and the inputs which don't draw much current. They amplify the input signal so that they can drive the coils to activate the relays. The freewheeling diodes prevent voltage spikes across the transistors when the relay is turned off since the coils are an inductive load. The indicator LEDs glow when the coil of the respective relay is energized, indicating that the relay is active. The optocouplers form an additional layer of isolation between the load being switched and the inputs. The isolation is optional and can be selected using the VCC selector jumper. The input jumper contains the main V-CC, GND, and input pins for easy connection using female jumper wires [10].

Figure 5. 5V Four-Channel relay module https://components101.com/sites/default/files/components/Four-Channel-Relay-Module.jpg

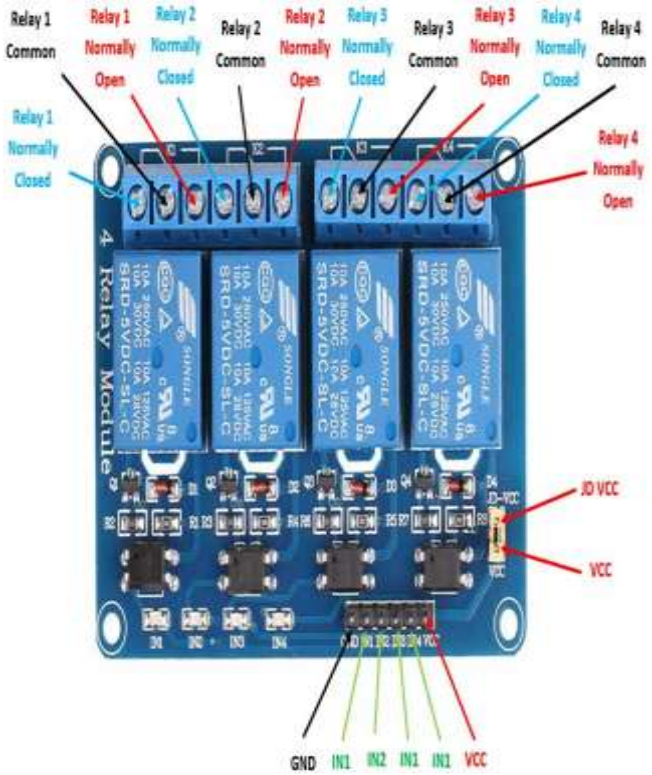

Figure 6. 5V Four-Channel relay module pinout https://components101.com/sites/default/files/component_pin/Four-Channel-Relay-Module-Pinout.jpg

3.5. WiFiNINA Library

This library enables network connection (local and Internet) with the Arduino MKR WiFi 1010, Arduino MKR VIDOR 4000, Arduino UNO WiFi Rev.2, and Nano 33 IoT. This library can instantiate Servers, Clients and send/receive UDP packets through WiFi. The board can connect either to open or encrypted networks (WEP, WPA). The IP address can be assigned statically or through a DHCP. The library can also manage DNS. The WiFiNINA library is very similar to the Ethernet and the library WiFi, and many of the function calls are the same [11].

Arduino MKR WiFi 1010 is used an ESP32 module made by U-BLOX for connecting of Wifi network. WiFiNINA Library is helping to enable the network connection of Arduino board with the local network to control home appliances via the internet.

Figure 7. WiFiNINA library for Arduino IDE

4. IMPLEMENTATION OF SYSTEM

The proposed system allows users to control their home appliances remotely at any desired time, using smart phones, tablets, and PCs via a web browser application. Using REST API and IoT platform, the user can control their home appliances easily through the internet by remote access.

For web interfacing, HTML with CSS is used in developing the web page on the XAMPP cross-platform software. The main section of web pages has a very simple interface and is easy to control the desired home appliances. Firstly, The HTML part that interfaces for control consist of eight buttons which are defined by the id code. These id codes need to assign for each button for "on" and "off" states of home appliances control. So, each click of the button is passed with "this.id" argument that contains HTML codes.

Secondly, the JavaScript file handles the commands coming from the web interface to control the devices correctly. So, a JavaScript file manipulates the command that to guide the Arduino board by using the REST API. For this particular button, pin number and state are handled by the JavaScript file. So, this is the important part of REST API Architecture for connection with Arduino and hardware devices. Finally, The PHP file named "curl.php" is created to use when each button is pressed. This PHP file contains a set of functions to make the REST call to the Arduino board. This PHP file starts by getting the pin and state assigned with the JavaScript file to be sent to the Arduino board. And then the cURL object is initialized and executed to make the REST call. So, A web-based app and the Arduino IoT board can make a standard way of communicating using the REST API library over the wireless communication platform.

On the other side, Arduino MKR WiFi 1010 microcontroller is connected with a 5V four-channel optical isolated relay module's input pins. VCC and GND pins of the relay module are connected with 5V and GND pins of Arduino respectively to get the power of the relay breakout board. The next step is the individual trigger terminals of the relay module that are needed to connect with Arduino output pins for switching on and off actions for home appliances.

Arduino Digital Pin 6 will be connected to the pin "IN1" on the relay breakout board, Arduino pin 7 to "IN2", Arduino pin 8 to "IN3", and Arduino pin 9 to "IN4" connect with different wire color disciplines. The relay module output pins COM and NO are joined with the home appliance to get a normally open connection. This situation sets no contact between COM and NO pins when the corresponding IN pins of the relay module has a LOW state. Circuit diagram for IoT-based home automation system with hardware components shown in Figure 8.

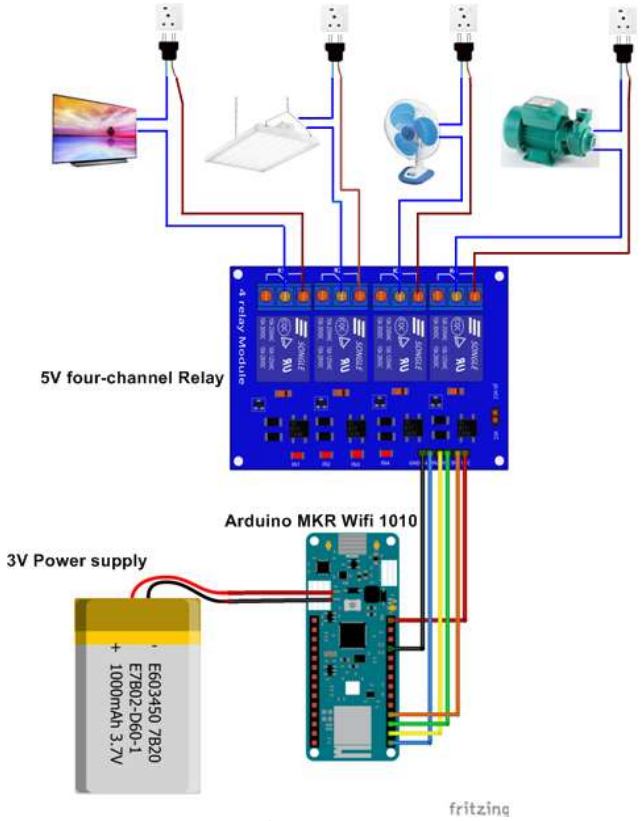

Figure 8. Circuit diagram for IoT-based home automation system

5. RESULTS AND DISCUSSION

The project implementation includes aREST library installation, testing the project with basic functions of the REST API from the browser address bar, and testing from a simple web application that will run in the XAMPP platform. The aREST library is directly installed from the Arduino library manager. Figure 9 shows the aREST installation for Arduino IDE to make a client/server communication.

Figure 9. aREST library installation

For testing the project with basic functions of the REST API from the browser address bar, the sketch is compiled and uploaded to the Arduino board. And then, one of the Arduino pins is set as an output by typing http://192.168.100.19/mode/7/o from the address bar of the favourite browser. Figure 11 shows confirmation printed for the output setup of the Arduino D7 pin. In this step, the IP address of the Arduino board can get from the connection details of the serial monitor shown in Figure 10.

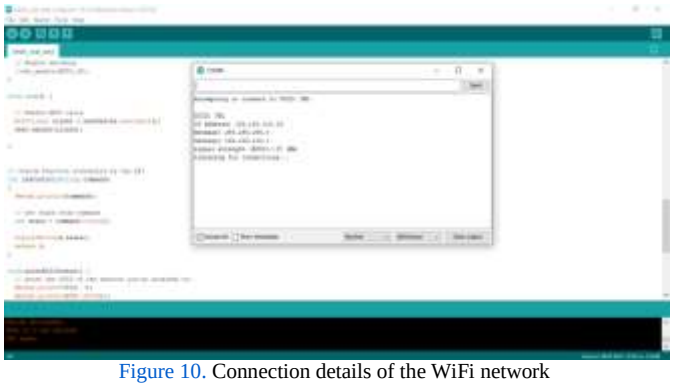

Figure 10. Connection details of the WiFi network

Figure 11. Output setup confirmation printed of the Arduino D7 pin

For testing from a web application included building a simple web application on an Apache web server that runs on the XAMPP platform and testing completed interface with the web server and Home appliances. In this step, An HTML page that contains the CSS interface, a JavaScript file for handling the commands, and a PHP file for communicating with the microcontroller board by making REST calls are used for Home Automation System.

Figure 12. Simple web application on an Apache web server for home automation system

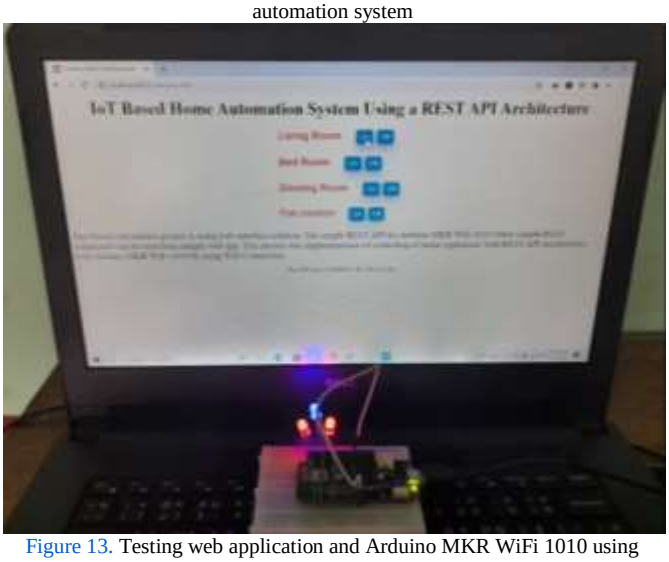

Figure 13. Testing web application and Arduino MKR WiFi 1010 using REST API architecture

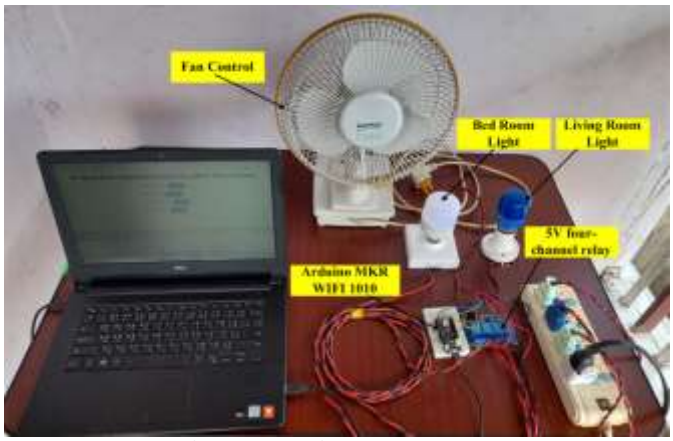

Figure 14. Set up for prototype of IoT based home automation system

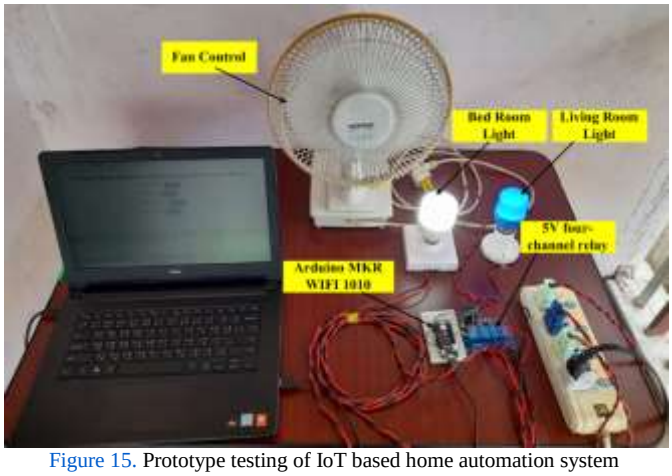

Figure 15. Prototype testing of IoT based home automation system

6. CONCLUSION

Presently, the Home Automation project could be used to control three rooms' lighting and fan for prototype testing. In the initial stage, the prototype was tested with LED for safer testing of REST API architecture. The system was successfully tested with a chrome web browser on a local PC using the Apache HTTP server. This system implements the WI-FI based IoT applications and low power consumption using Arduino MKR WIFI 1010.

The network security protection system is still needed for this project. So, the system needs to develop a good network security part for a Secure Home Automation System. We need a secure login page for specific users or visitors that will be assigned the needed login credentials before they can log in to the dashboard area of the Home Automation Web page.

REFERENCES

[1] T. Kirankumar and B. Bhavani, "A Sustainable Automated System for Elderly People Using Voice Recognition and Touch Screen Technology". International Journal of Science and Research (IJSR), Volume 2, Issue 8, August 2013, pp. 265-267.

[2] Shankey Garg and Mohd. Shajid Ansari, "Implementation of REST Architecture in ARDUINO Based Home Automation System" International Conference on Innovations in Control, Communication and Information Systems (ICICCI) 2017, 12-13 Aug. 2017. DOI: 10.1109/ICICCIS.2017.8660936.

[3] Atas Hasibuan, Muhammad Mustadi, Dr. Ir. Eniman Y Syamsuddin, Ir. M. Anis Rosidi, "Design and Implementation of Modular Home Automation Based on Wireless Network, REST API, and WebSocket", 2015 International Symposium on Intelligent Signal Processing and Communication Systems (ISPACS) November 9-12, 2015. DOI: 10.1109/ISPACS.2015.7432797.

[4] Kshirod Kumar Rout, Samuchita Mallick, Sivkumar Mishra , "Design and Implementation of an Internet of Innovations in Electrical, Electronics & Communication Engineering (ICRIEECE), 27-28 July 2018. DOI:10.1109/ICRIEECE44171.2018.9008410.

[5] Zaw Lin Oo, Theint Win Lai, Aung Moe, "Iot Based Low-cost Physical Protection and Alarm System for Gamma Irradiation Facility". Conference on Science and Technology Development (CSTD-2019), Oct 31- Nov 1, 2019.

[6] Marc-Olivier Schwartz, "A REST API for Arduino & the CC3000 WiFi Chip". Adafruit Learning System, [online]. Available: https://learn.adafruit.com/a-rest-api-for-arduino-and-the-cc3000-wifi-chip.

[7] Zhang Xinshuang, Wen Zhigang, Wu Yuexin, Zou Junwei, "The Implementation and Application of the Internet of Things Platform based on the REST Architecture". International Conference on Business Management and Electronic Information 2011, 13-15 May 2011. DOI:10.1109/icbmei.2011.5917838.

[8] Zaw Lin Oo, Theint Win Lai, Maung Maung Than, "Web Server Base RFID Attendance Record System". International Conference on Recent Innovations in Nanoscience and Technology 2018 (ICRINT2018), December 26–28, 2018.

[9] User Guide for 4 Channel 5V Optical Isolated Relay Module, [online]. Available: https://www.handsontec.com/dataspecs/4Ch-relay.pdf

[10] Datasheet for 5V Four-Channel Relay Module, [online]. Available: https://components101.com/switches/5v-four-channel-relay-module-pinout-features-applications-working-datasheet

[11] WiFiNINA arduino libraries, [online]. Available: https://github.com/arduino-libraries/WiFiNINA

BIOGRAPHIES

Zaw Lin Oo obtained his B.E (Bachelor of Engineering) and M.E (Master of Engineering) degrees in Nuclear Engineering from Yangon Technological University, Yangon, (Myanmar) Burma, in 1999 and 2003, respectively and a Ph.D. degree in Nuclear Engineering in the year 2007 from Yangon Technological University, Yangon, (Myanmar) Burma. His research interests include computer science and engineering- embedded systems, cloud computing, artificial intelligence, Electrical and electronic engineering- electronic, control system.

Theint Win Lai is presently associate professor at the Faculty of Computer System and Technology, Info Myanmar University, Yangon, (Myanmar) Burma. She received the B.S. degrees in Physics from the Pathein University, in 1999 and the M.S. degree in computer Hardware Technology from Yangon Technological University, Yangon, (Myanmar) Burma, in 2002. She received the Ph.D. degree in computer Hardware Technology from University of Computer Studies, Yangon (UCSY), in 2006. Her research interests are computer science and engineering- embedded systems, cloud computing, artificial intelligence, Electrical, electronic engineering- electronic, control system and IoT based control system.

Aung Moe is presently Director in the Myanma Scientific and Technological Research Department at the Ministry of Science and Technology. Nay Pyi Taw, Myanmar (Burma). He obtained B.Sc and M.Sc degrees in Physics from University of Yangon, Yangon, (Myanmar) Burma, in 1992 and 1997, respectively. He received the Ph.D. degree in Nuclear Engineering from National Research Nuclear University MEPhI (Moscow Engineering Physics Institute), in 2006. His research interests are computer science and engineering- embedded systems, Advanced diagnostic systems, and Advanced Information System Modeling Technologies.

European Journal of Technique

journal homepage: https://dergipark.org.tr/en/pub/ejt

Vol.12, No.2, 2022

Development of a Mathematical Model that Calculates Combustion, Emission and Engine Performance Values of Internal Combustion Engines

Ozan Yazar[1*], Bünyamin Demir[2]

[1*]Yozgat Bozok University, Department of Transportation Services, 66700, Yozgat, Turkey. (ozan.yazar@yobu.edu.tr).
[2] Mersin University, Department of Mechanical Engineering, 33340, Mersin, Turkey. (bd@mersin.edu.tr).

ARTICLE INFO

Received: Jul., 22. 2022
Revised: Sep.., 22. 2022
Accepted: Oct., 10. 2022

Keywords:
Internal combustion engines
Engine performance
Exhaust emission
Graphical user interface (GUI)

Corresponding author: *Ozan Yazar*

ISSN: *2536-5010* | e-ISSN: *2536-5134*

DOI: https://doi.org/10.36222/ejt.1147020

ABSTRACT

In this study, a simulation program was developed that can calculate combustion, emission and engine performance values depended on variable parameters for internal combustion engines by mathematical modelling. This simulation program was created with the Java programming language. Graphical user interface (GUI) was used in this simulation program. With the simulation program created, it can calculate many values such as in-cylinder pressure, temperature, gas amounts generated as a result of combustion, power, torque, specific fuel consumption, both in spark ignition engines and compression ignition engines. This simulation program presents the results both numerically and graphically. The calculations are obtained at every crankshaft angle at 0.25 ˚ intervals. With this simulation program, analyses were made in different excess air coefficients (1-1.1-1.2) and the effects of in-cylinder pressure, temperature, mass ratios of gas components and engine performance values were compared. According to the simulation results, as the excess air coefficient increases, the temperature and pressure values decrease. CO_2 and NO mass ratios decrease as the excess air coefficient increases in case the excess air coefficient is greater than 1. H_2O mass ratio increased as the excess air coefficient increased.

1. INTRODUCTION

Nowadays, many problems arise with the increase of automobile use. The most important of these problems are the increase in environmental pollution caused by exhaust emissions and the decrease in fuel reserves. Due to these problems, many improvement studies are carried out to reduce fuel consumption and exhaust emission in internal combustion engines and alternative fuel is sought [1].

At the design process of internal combustion engines, it is not possible to experimentally predict the parameters that affect the engine's exhaust emission, fuel consumption, engine efficiency and performance. Calculating these factors affecting internal combustion engine design is very difficult and time consuming due to complex equations [2].

With the development of software engineering and computer technology, simulation programs started to be used. Thanks to the simulation programs, the analysis results replace the experimental analysis by giving results much closer to the reality [3].

The most important goal in simulation programs is to obtain the closest values to the truth. For this reason, there are many studies in the literature on simulation programs created using different mathematical and thermodynamic modeling for internal combustion enginesFor example, a software program was created with the thermodynamic model of a four-stroke direct injection diesel engine developed by Balcı. The created program is written in the GW Basic language. Engine performance values were examined by making calculations with different compression and air-fuel ratios [4]. A software program was created with a thermodynamic model for four-stroke, single-cylinder diesel engines developed by Polat. The software program was created using Matlab programming language. Calculations were made in the intervals of one-degree crank angle. Calculations were made depending on different engine parameters, n-dodecane (C12H26) was used as fuel and the results were interpreted with graphics [5]. In the model developed by Esin, a software program was created with a graphical user interface (GUI) by using the combustion model for emission estimation. In the combustion model of the program created, the thermodynamic properties of the combustion products, their changes depending on pressure and temperature were calculated with the equilibrium coefficient method [6]. Kutlar et al. created a single-zone thermodynamic computational model to analyze the 13B multi-port rotary engine on the basis of the Mazda RX-8. With this model, many parameters such as combustion chamber pressure, mass and engine torque were investigated at

different speeds and full load conditions [7]. Experimental study was carried out by Cihan et al. using Wankel engine at 2 bar and 3 bar and different engine speeds. In addition, the results obtained by analyzing in the AVL Boost program under the same conditions were compared with the test results in terms of specific fuel consumption and exhaust emissions. [8].

In this study, a simulation program was developed that can calculate combustion, performance and emission values depending on variable parameters for both spark ignition engines and compression ignition engines. The simulation program was created using the Java programming language. Graphical user interface (GUI) is used in this simulation program. While creating this simulation program, firstly thermodynamic model of internal combustion engines was created. This thermodynamic modeling was created according to the real cycle. Calculations are made at each crankshaft angle at 0.25 degree intervals. Friction losses and heat transferred to the cooling water were included in the calculations. In the calculations, the exhaust gases remaining from the previous cycle in the cylinder due to the engine geometry was taken into account. Specific heat values were calculated for each crank angle (CA) depending on the temperature. In addition, in this simulation program, analysis can be made for the desired fuel by entering the atomic numbers of the fuel. Then, with this simulation program, analyzes were made in different excess air coefficients (1-1.1-1.2) and the effect of excess air coefficient on in-cylinder pressure, temperature, mass ratios of gas components and engine performance values were examined.

2. METHOD

2.1. Thermodynamic and mathematical modeling

The working principle of internal combustion engines is based on thermodynamic laws and principles. Cycle analyzes are performed in internal combustion engines based on thermodynamic principles with certain assumptions and known data [9].

2.1.1. Engine geometry and calculations

For calculations to be made in the simulation program, it is necessary to know the geometric properties of the engine. With the geometric properties of the engine, cylinder volume, combustion chamber volume, cylinder surface area, piston speed values are calculated. These values change depending on the CA.

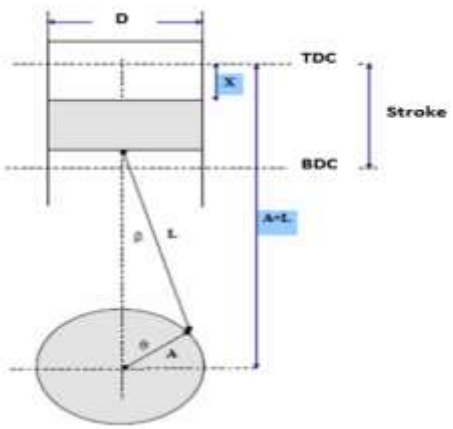

Figure 1. Engine geometry

In calculating the cylinder's volume and area, it is necessary to know the distance between the top of the piston and the top dead center of the piston. Eq. (1) is used to calculate the position of the piston depending on the CA.

$$x(\theta) = A + L - \sqrt{L^2 - A^2.sin^2(\theta)} - A.\cos(\theta). \quad (1)$$

Where $x(\theta)$ is the position of the piston relative to the (CA), θ is the crankshaft angle, A is the crank radius, L is the connecting rod length.

The combustion chamber volume is calculated by using the Eq. (2).

$$V_c = \frac{\frac{\pi.D^2}{4}}{(r-1)}.S \quad (2)$$

Where V_c is combustion chamber volume, D is cylinder diameter, S is stroke length, r is compression ratio.

The instantaneous cylinder volume depending on the CA is calculated using Eq. (3).

$$V(\theta) = Vc + \frac{\pi.D^2}{4}.x(\theta). \quad (3)$$

The instantaneous cylinder surface area depending on the CA is calculated by using Eq. (4).

$$A(\theta) = \frac{\pi.D^2}{2} + \pi.D.x(\theta). \quad (4)$$

The instantaneous piston speed depending on the CA is calculated using Eq. (5).

$$V(\theta) = \frac{\pi}{2}.\sin(\theta) + \left(1 + \frac{\cos(\theta)}{\sqrt{(R^2 - \sin(\theta)^2)}}\right).\frac{2.N.S}{60}. \quad (5)$$

Where $V(\theta)$ is instantaneous piston speed, N is engine speed, S is stroke length.

2.1.2. Combustion and 1st law of thermodynamic

Combustion is the reaction of fuel and oxygen under suitable conditions. Combustion is a chemical process and is also called oxidation. Heat energy is released as a result of burning reaction. This energy is generated as a result of breaking the bond between the molecules in the fuel during the reaction. The fuel must be at the ignition temperature for the combustion reaction to occur. Each fuel has its own ignition temperature due to its chemical properties. In addition, there must be sufficient oxygen in the environment for the burning reaction [10]. Hydrocarbons (CaHb) are generally used as fuel in internal combustion engines [11]. The combustion of hydrocarbons occurs when the carbon and hydrogen atoms react with oxygen. General combustion equations of carbon and hydrogen with oxygen are given in Eq. (6) and Eq. (7).

$$C + O_2 \rightarrow CO_2 \quad (6)$$

$$H_2 + \frac{1}{2}O_2 \rightarrow H_2O \quad (7)$$

The first law of thermodynamics is the energy conservation law. According to this law, it does not disappear when there is energy, it does not exist when it is absent. But energy can be transformed into another form. In internal combustion engines, the chemical energy of the fuel is converted into mechanical energy. For this reason, the first law of thermodynamics is valid in internal combustion engines [10].

According to the first law of thermodynamics;

$$\Delta E = \Delta U = U_2 - U_1 \tag{8}$$

$$\Delta U = \Delta Q + \Delta W \tag{9}$$

$$\Delta Q = Q_{in} - Q_{out} \tag{10}$$

$$\Delta W = \int_2^1 p\, dV \tag{11}$$

Where ΔU is the internal energy change of the system, ΔQ is the net heat in the system, ΔW is the work in the system.

2.1.3. Stoichiometric air-fuel ratio

The stoichiometric air-fuel ratio is the ratio of the amount of air required for the complete combustion of the fuel to the fuel amount. If the fuel reacts with air less than the stoichiometric ratio, not all of the fuel is burned. The stoichiometric air fuel ratio is calculated by the equilibrium coefficients of the exact combustion equation of the fuel. The exact combustion equation of hydrocarbon fuels is established as in Eq. (12) [12].

$$C_aH_bO_cN_d + a_s(O_2 + 3{,}76N_2) \rightarrow n_1CO_2 + n_2H_2O + n_3N_2 \tag{12}$$

In the equation, the coefficient of oxygen and nitrogen (a_s) are calculated using Eq. (13)

$$a_s = a + \frac{b}{4} - \frac{c}{2} \tag{13}$$

Where n_1, n_2, n_3 values calculated using Eq. (14), Eq. (15) and Eq. (16).

$$n_1 = a \tag{14}$$

$$n_2 = \frac{b}{2} \tag{15}$$

$$n_3 = \frac{d}{2} + 3{,}76\, a_s \tag{16}$$

The stoichiometric air-fuel ratio (A_s) is calculated using Eq. (17).

$$A_s = \frac{28{,}84(4.76\, a_s)}{(12{,}01\, a + 1{,}008\, b + 16{,}00\, c + 14{,}01\, d)} \tag{17}$$

2.1.4. Determination of air fuel amount air-fuel ratio

When determining the amount of air fuel, the air excess coefficient must be known. Air excess coefficient was calculated using Eq. (18).

$$\lambda = \frac{(\frac{m_{air}}{m_{fuel}})_{real}}{(\frac{m_{air}}{m_{fuel}})_{stoic}} \tag{18}$$

Where λ is the air excess coefficient, m_{fuel}, fuel mass of the mixture, m_{air} is the air mass of the mixture.

Air-fuel mixture is called a poor and rich mixture in terms of fuel amount. A poor mixture is a condition in which the fuel enters into combustion reactions with more air than the amount of air required to burn. A rich mixture is a condition in which the fuel enters combustion reactions with less air than the amount of air required to burn. Whether the mixture is a poor or rich mixture is determined by the equivalence ratio. Equivalence ratio is indicated by the symbol (ϕ). Equivalence ratio and air excess coefficient are inversely proportional [10].

$$\Phi = \frac{1}{\lambda} \tag{19}$$

- Stoichiometric mixture: $\phi = 1$ or $\lambda = 1$
- Poor mixture: $\phi < 1$ or $\lambda > 1$
- Rich mixture: $\phi > 1$ or $\lambda < 1$

During the suction process, it is assumed that air is taken into the cylinder as much as the stroke volume, depending on the volumetric efficiency. The fresh air taken into the cylinder was assumed to be 21% O2 and 79% N2. The amount of air taken into the cylinder;

$$m_{N_2} = \frac{P_{air}.V(\theta)}{R_{N_2}.T_{air}}.\%N_2 \tag{20}$$

$$m_{O_2} = \frac{P_{air}.V(\theta)}{R_{O_2}.T_{air}}.\%O_2 \tag{21}$$

$$m_{air} = m_{N_2} + m_{O_2} \tag{22}$$

The amount of fuel taken into the cylinder;

$$m_{yakıt} = \frac{m_{air}}{\lambda.A_s} \tag{23}$$

Where m_{N_2} is mass of N_2 in air, m_{O_2} is mass of O_2 in air, P_{air} is air pressure, T_{air} is air temperature, $V(\theta)$ is volume, R_{N_2}, R_{O_2} is gas constant, $\%N_2, \%O_2$ is percentage of components in air, λ is air excess coefficient, A_s is stoichiometric ratio.

2.1.5. Exhaust gases remaining in the cylinder

Due to the engine geometry, exhaust gases remain in the cylinder as much as the combustion chamber volume from the previous cycle. These exhaust gases remaining in the cylinder are mixed with fresh air or air fuel absorbed during the intake stroke. Since the temperature of the exhaust gases is high, it increases the temperature of the mixture. In order to start the cycle in the created mathematical model, it is necessary to know the molar amount, pressure and temperature of the filler before compression. The temperature of the exhaust gases in the cylinder is calculated using Eq. (24) and Eq. (25).

Temperature at the moment the exhaust valve is opened;

$$T_{ex} = T_{exo}.\left(\frac{P_{atm}}{P_{exo}}\right)^{\left(\frac{n-1}{n}\right)} \quad (24)$$

The temperature when the exhaust valve is closed is;

$$T_{exm} = T_{ex}.\left(\frac{P_{atm}}{P_{ex}}\right)^{\left(\frac{n-1}{n}\right)} \quad (25)$$

Where T_{ex} is the temperature at the time of opening of the exhaust valve, T_{exo} is the opening temperature of the exhaust valve, T_{exm} is the temperature at the moment of closing of the exhaust valve, P_{atm} is atmospheric pressure, P_{exo} is exhaust back pressure, n, polytropic index.

The total amount of exhaust gas remaining in the combustion chamber is calculated with Eq. (26).

$$m_{eg} = \frac{P_{ex}\,.\,V(\theta)}{R\,.\,T_{ex}} \quad (26)$$

Where P_{ex} is the exhaust counter pressure, $V(\theta)$ is volume, R is gas constant, T_{ex} is the exhaust gas temperature.

2.1.6. Lower heating value of fuel

Heating value is the amount of energy released as a result of combustion fuel. It is divided into two as higher heating value and lower heating value. The higher heating value is the highest heat value obtained by combustion a fuel. The lower heating value is the lowest heat value obtained by combustion the fuel under the worst conditions [13,14]. In the calculations, the lower heating value is used.

The lower heating value of hydrocarbons is calculated using the Mendeleyev equation in Eq. (27).

$$H_u = [3{,}4013C + 125{,}6H - 10{,}89(O - S) - 2{,}512(9H + W)].1000 \quad (27)$$

Where, C, H, O, S, W values indicate the weight ratios of the components in the fuel. Since there is no sulfur and water in the fuels used in internal combustion engines, S, W values are accepted as zero.

2.1.7. Specific heats

Specific heat is the amount of heat required to increase the unit mass of the substance by one degree. Specific heat is divided into two as specific heat at constant volume (c_v) and specific heat at constant pressure (c_p) [15].

While calculating the specific heat, Janaf tables were used. Janaf tables are tables in which the thermodynamic properties of substances and components are found [16].

For the specific heat of gases at constant pressure, the following equations are used.

$$c_{p_{N_2}} = (39{,}060 - 512{,}790.\theta^{-1{,}5} + 1072{,}78.\theta^{-2} - 820{,}40.\theta^{-3}) \quad (28)$$

$$c_{p_{O_2}} = (37{,}432 + 0{,}02010.\theta^{1{,}5} - 178{,}57.\theta^{-1{,}5} + 236{,}88.\theta^{-3}) \quad (29)$$

$$c_{p_{H_2}} = (56{,}505 - 702{,}74.\theta^{-0{,}75} + 1165{,}0.\theta^{-1} - 560{,}70.\theta^{-1.5}) \quad (30)$$

$$c_{p_{CO}} = (69{,}145 - 0{,}70463.\theta^{0{,}75} - 200{,}770.\theta^{-0{,}5} + 176{,}76.\theta^{-0.75}) \quad (31)$$

$$c_{p_{NO}} = (59{,}283 - 1{,}7096.\theta^{0{,}5} - 70{,}613.\theta^{-0{,}5} + 74{,}889.\theta^{-1.5}) \quad (32)$$

$$c_{p_{H_2O}} = (43{,}05 - 183{,}540.\theta^{0{,}25} + 82{,}751.\theta^{0{,}5} - 3{,}6989.\theta) \quad (33)$$

$$c_{p_{CO_2}} = (-3{,}7357 + 30{,}529.\theta^{0{,}5} - 4{,}1034.\theta + 0{,}024198.\theta^{2}) \quad (34)$$

Here;

$$\theta = \frac{T}{100} \quad (35)$$

For constant volume specific heat (c_v) values, Eq. (36) was used.

$$R = c_p - c_v \quad (36)$$

2.1.8. Percentage of fuel burned

To calculate the percentage of fuel burned based on crankshaft angle, the Wiebe function was used. The Wiebe function is an equation created by considering ignition delay, sudden and controlled combustion processes. Wiebe function is given in Eq. (37).

$$X_y = 1 - exp^{\left[-a\left(\frac{\theta_x - \theta_0}{\Delta\theta}\right)^{m+1}\right]} \quad (37)$$

Where X_y is the percentage of instantaneous burning fuel, θ_x, instantaneous CA, θ_0 is the CA at which combustion begins.

According to Heywood, a = 6.908, m = 2 [10].

2.1.9. Heat transfer

Approximately 10-35% of the heat generated as a result of combustion in internal combustion engines passes to the cooling system. Since heat transfer is temperature dependent, it is calculated for each CA. While calculating the amount of heat transferred to the cooling system, Eq (38) created by Woschni was used [17].

$$Q_w = \frac{A(\theta).(T_I - T_w)}{\left[\left(\frac{1}{h_g}\right) + \left(\frac{X}{k_s}\right) + \left(\frac{1}{h_c}\right)\right]} \quad (38)$$

Where Q_w is heat transfer, $A(\theta)$ is instantaneous cylinder surface area depending on CA, T_I is cylinder temperature, T_w is cylinder surface temperature, h_g is heat transfer coefficient of gases, X is thickness of cylinder wall, k_s is heat transfer coefficient of cylinder wall and it is taken as 50 W/m^2.K, h_c is the heat transfer coefficient of the cooling water and it is taken as 30 W/m^2.K.

Heat transfer coefficient (h_g) was calculated using Eq. (39) [18].

$$h_g = 0{,}820.D^{-0{,}2}.P^{0{,}8}.W^{0{,}8}.T^{-0{,}53} \quad (39)$$

Where D is cylinder diameter, P is cylinder pressure, T is cylinder temperature, W is the average velocity of gases.

$$W = \left[C_1.C_m + C_2.\frac{V_d.T_1}{P_1+V_1}.(P-P_0)\right] \quad (40)$$

Where C_m is piston speed.

C_1, C_2 values;

For exhaust time C_1=6.18 C_2=0

For compress time C_1=2.28 C_2=0

For the burning time C_1=2.28 C_2=3.24. 10^{-3} [18].

2.1.10. Modeling of combustion

In order to calculate the parameters inside the cylinder, the amount of instantaneous gases must be known. The air fuel mixture entering the cylinder turns into different combustion products as a result of the combustion reaction, the type and quantity of combustion products vary depending on the combustion temperature. The calculations are modeled according to the instantaneous temperature and mass quantities of the components depending on the CA. The combustion products formed as a result of the combustion of high temperature hydrocarbons with air are CO_2, H_2O, N_2, O_2, CO, H_2, O, OH, NO, H.

The combustion model was created by the equilibrium coefficient method. The equilibrium coefficient (K) describes the behavior of the reaction and can be formed bidirectional. Equilibrium coefficient (K) is obtained from the ideal gas equation and its partial pressures [19].

The equation of the high temperature combustion reaction and the coefficients of the components are shown in Eq. (41). The equation is constructed for one mole of fuel [20].

$$C_aH_bO_cN_d + \frac{a_s}{\emptyset}(O_2 + 3.76\,N_2) \rightarrow v_1CO_2 + v_2H_2O + v_3N_2 + v_4O_2 + v_5CO + v_6H_2 + Hv_8O + v_9OH + v_{10}NO \quad (41)$$

Here;

$$x_i = \frac{v_i}{N} \quad (42)$$

$$a = (x_1 + x_5).N \quad (43)$$

$$b = (2x_2 + 2x_6 + x_7 + x_9).N \quad (44)$$

$$c + \frac{2a_s}{\emptyset} = (2x_1 + x_2 + 2x_4 + x_5 + x_8 + x_9 + x_{10}).N \quad (45)$$

$$d + \frac{2a_s(3{,}773)}{\emptyset} = (2x_3 + x_{10}).N \quad (46)$$

Equilibrium coefficients of combustion products of partial pressure type;

$$\frac{1}{2}H_2 \leftrightarrow H \qquad K_1 = \frac{x_7P^{1/2}}{x_8^{1/2}} \quad (47)$$

$$\frac{1}{2}O_2 \leftrightarrow O \qquad K_2 = \frac{x_8P^{1/2}}{x_4^{1/2}} \quad (48)$$

$$\frac{1}{2}H_2 + \frac{1}{2}O_2 \leftrightarrow OH \qquad K_3 = \frac{x_9}{x_4^{1/2}\,x_6^{1/2}} \quad (49)$$

$$\frac{1}{2}O_2 + \frac{1}{2}N_2 \leftrightarrow NO \qquad K_4 = \frac{x_{10}}{x_3^{1/2}\,x_4^{1/2}} \quad (50)$$

$$H_2 + \frac{1}{2}O_2 \leftrightarrow H_2O \qquad K_5 = \frac{x_2}{x_4^{1/2}\,x_6^{1/2}} \quad (51)$$

$$CO + \frac{1}{2}O_2 \leftrightarrow CO_2 \qquad K_6 = \frac{x_1}{x_4^{1/2}\,x_5^{1/2}} \quad (52)$$

Where K_1, K_2, K_2, K_3, K_4, K_5 and K_6 values are calculated using Eq. (53). This equation was obtained from Janaf tables in the range of 600K-4000K by curve fitting method [19].

$$\log K_i = A_i \ln\left(\frac{T}{1000}\right) + \frac{B_i}{T} + C_i + D_iT + E_iT^2 \quad (53)$$

A_i, B_i, C_i, D_i, and E_i values in the equation are given in Table I.

TABLE I

CURVE COEFFICIENTS FOR EQUILIBRIUM CONSTANTS [17].

i	A_i	B_i	C_i	D_i	E_i
1	0.432168	$-0.112464.10^5$	0.267269×10^1	-0.745744×10^{-4}	0.242484×10^{-8}
2	0.310805	-0.129540×10^5	0.321779×10^1	-0.738336×10^{-4}	0.344645×10^{-8}
3	−0.141784	-0.213308×10^4	0.85346^1	0.355015×10^{-4}	-0.310227×10^{-8}
4	0.150879×10^{-1}	-0.470959×10^4	0.646096	0.272805×10^{-5}	-0.154444×10^{-8}
5	−0.752364	0.124210×10^5	-0.260286×10^1	0.259556×10^{-3}	-0.162687×10^{-7}
6	-0.415302×10^{-2}	0.148627×10^5	-0.475746×10^1	0.124699×10^{-3}	-0.900227×10^{-8}

2.2. Engine performance calculations

Engine performance values are examined in two ways, indicative and effective. Indicated parameters are engine parameters calculated with the values obtained in the cylinder. The effective parameters are the values measured from the flywheel or crankshaft [21].

Power is the work done per unit time. Indicated power is derived from the in-cylinder pressure value. Indicated power is the thrust that occurs on the piston with the effect of the pressure created as a result of patching inside the cylinder. The effective power is the power obtained by subtracting the losses such as friction in the engine from the indicated power. Effective power is the real power of the engine. Indicated power is obtained using Eq. (54) [22].

$$N_i = \frac{P_i.V.n.i}{60.T} \quad (54)$$

Where; N_i is indicated power, P_{me} is indicated pressure (mean pressure), V is stroke volume, n is crankshaft revolution, i is number of cylinders, T is the number of strokes in a cycle (it is 2 for 4-stroke engines).

Effective power is obtained using Eq. (55) [21].

$$N_e = \frac{P_e.V.n.i}{60.T} \quad (55)$$

$$P_e = P_i.\eta_m \quad (56)$$

Where N_e is effective power, P_e is effective pressure, η_m is mechanical efficiency.

Moment is the force of rotation. The pressure force generated as a result of combustion in the cylinder moves the piston. The connecting rod transfers this linear motion to the crankshaft and creates a moment effect on the crankshaft. The moment value is obtained by using Eq. (57) [22].

$$M_e = 9549.\frac{N_e}{n} \quad (57)$$

WhereM_e is moment, N_e is effective power, n is engine speed.

Specific fuel consumption is the amount of fuel spent in unit time for unit power. Specific fuel consumption is obtained using Eq. (58) [21].

$$B_e = \frac{m_f}{N_e} \quad (58)$$

Where; B_e is specific fuel consumption, m_f is amount of fuel consumed per unit time, N_e is effective power.

2.2. Conversion of mathematical model to software language

Mathematical modeling that created with thermodynamic formulas was turned into a software program with Java programming language.

Java was generated in 1995 by the Sun Microystems company. Java is an object-oriented programming language. Java is a programming language that can work on all operating systems without rearrangement [23].

NetBeans platform was used while creating the simulation program. NetBeans is the Java development platform developed by Oracle. NetBeans is a code development environment that offers opportunities such as writing, compiling, and debugging [23].

For this simulation program can be easily used by the user, graphical user interface (GUI) was created. While creating the GUI, Java's Swing library was used. The Swing library is a library that is used to develop components such as panels, buttons, tables and menus required for the GUI [23].

3. RESULTS AND DISSCUSSION

The generated software contains approximately 3520 lines of code. Codes were created to calculate values at each crankshaft angle at 0.25˚ intervals. The calculations are obtained by creating arrays in a repeating loop. The calculations of the in-cylinder parameters are set to be made with the CA values between the closing of the intake valve and the opening of the exhaust valve. Engine performance parameters have been obtained in the range of 900-5500 (rpm).

The created GUI is the screen where the parameters required for the calculations of internal combustion engines are entered. This screen consists of 3 sections. These sections are the section where the menus are grouped with the engine parameters, the section where the engine parameters are entered and the message section. The main screen encountered by the user when the program is opened is shown in Fig. 2.

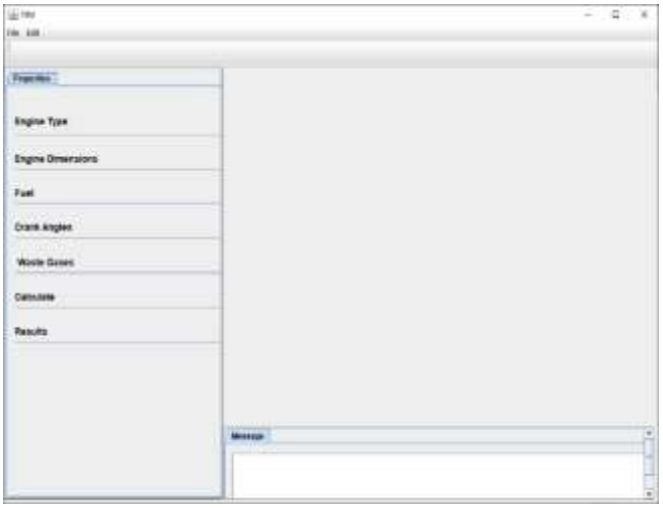

Figure 2. Main screen of created interface.

Properties menu of the interface created; It consists of 7 menu buttons in order to enter engine parameters, to make calculations and to see the results.

The engine type button is the section where the spark ignition engine or compression ignition engine type is entered. The screen where the engine type is entered is shown in Fig. 3.

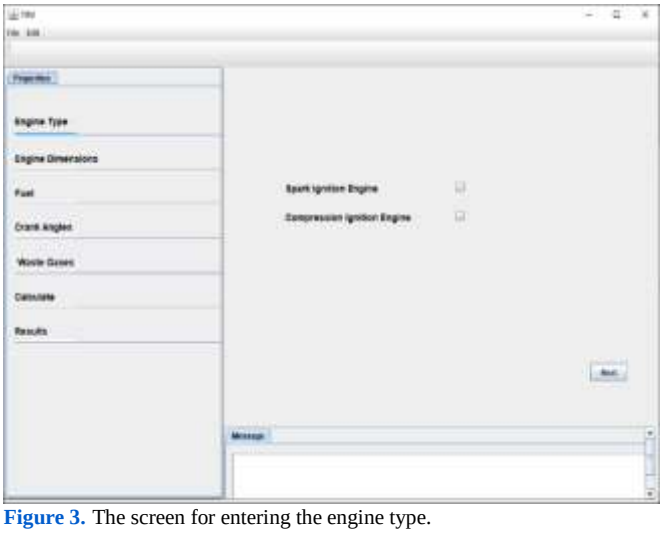

Figure 3. The screen for entering the engine type.

It is the section where the engine dimensions button, cylinder number, cylinder diameter, stroke length, connecting rod length, compression ratio and engine speed are entered. The screen where motor dimensions are entered is shown in Fig. 4.

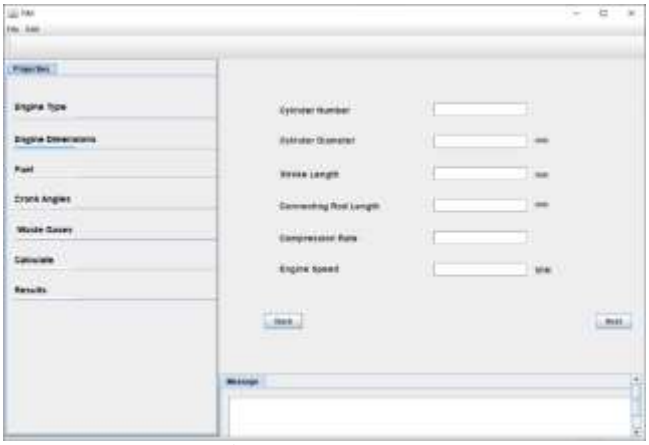

Figure 4. The screen for entering motor dimensions.

The fuel button is the section where the atomic numbers of the fuel, the excess air coefficient, the pressure of the sucked air, the temperature of the sucked air and the temperature of the cooling water are entered. This screen is shown in Fig. 5.

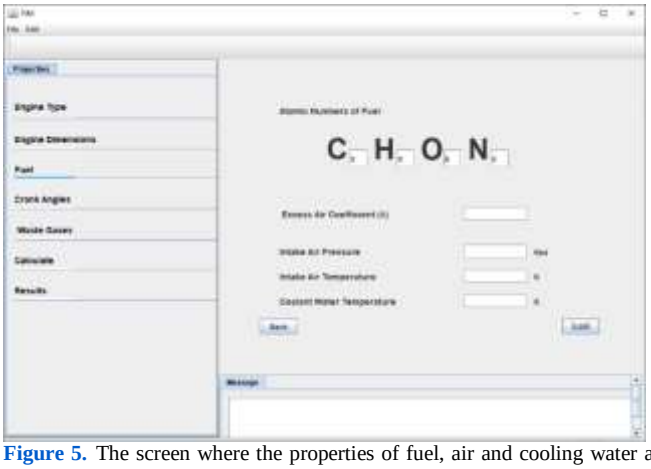

Figure 5. The screen where the properties of fuel, air and cooling water are entered.

The crank angles button is the section in which the closing of the intake valve, the opening of the exhaust valve, the ignition starts and end for spark ignition engines, the start and end of the spraying for compression ignition engines are entered as the CA value. This screen is shown in Fig. 6.

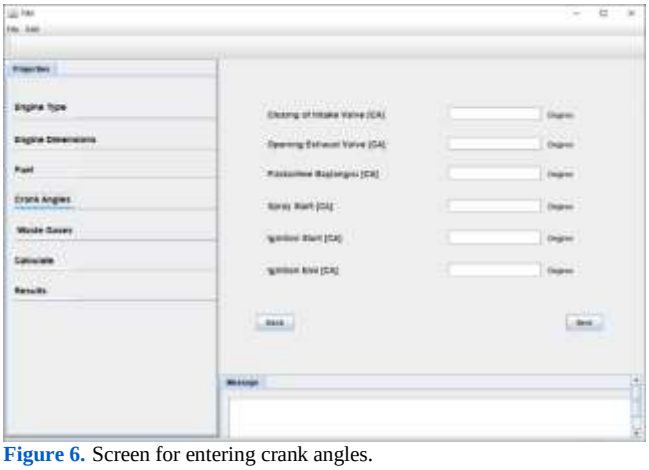

Figure 6. Screen for entering crank angles.

The waste gases button is the section where the temperature of the exhaust gases from the previous cycle due to the engine geometry and the mass ratios of the components are entered. In the calculations, CO2, H2O, O2, N2 components in the exhaust gases remaining in the cylinder were taken into account. Since the mass ratios of other components in the exhaust gases are low, they are not taken into account in the calculations. The screen where the properties of exhaust gases are entered is shown in Fig. 7.

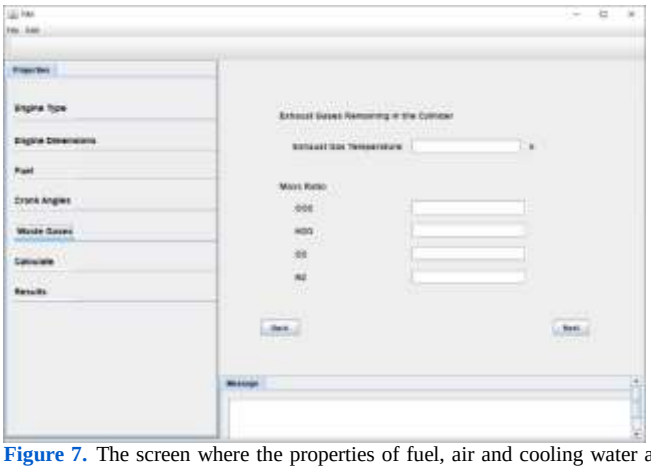

Figure 7. The screen where the properties of fuel, air and cooling water are entered.

There is a button in the calculation menu. When this button is clicked, it provides the calculation by transferring all the entered data to the software. After the calculations are completed, the simulation program creates an Excel file containing the results to analyze the results numerically. After the calculations are completed, the screen with the graphics created is shown in Fig. 8.

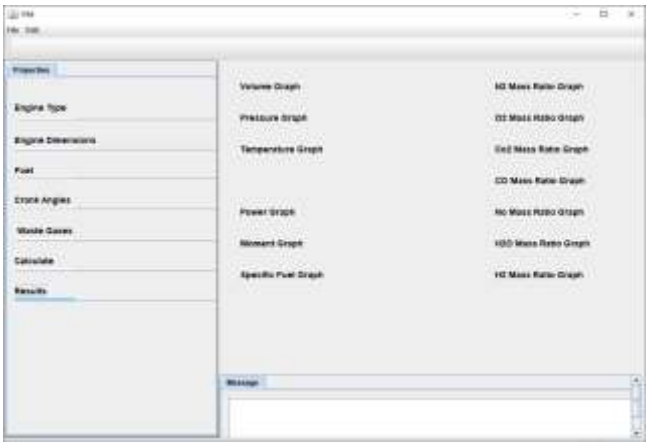

Figure 8. Graphics screen.

With this simulation program, analyzes were made with different excess air coefficients for gasoline engines, and in-cylinder pressure, temperature, mass ratios of gases and engine performance values were compared. Different excess air coefficients (1-1.1-1.2) values were used for the analyzes. The characteristics of the internal combustion engine used in the analysis and the values entered are given in Table 2.

TABLE II
MOTOR CHARACTERISTICS AND ENTERED VALUES

Parameters	Feature
Engine type	Spark ignited
Number of cylinders	4
Cylinder diameter	73 mm

Stroke length	80 mm
Connecting rod length	149mm
Compression ratio	10.8
Engine Speed	3000 (rpm)
Fuel	Gasoline (C_8H_{18})
Excess air coefficient (EAC)	1-1.1-1.2
Pressure of intake air	100 kPa
Temperature of the intake air	300 K
Ignition time	351-368
Coolant water temperature	340 K
Exhaust gas temperature	850K
The ratio of N_2 in waste gas	0.7
The ratio of O_2 in waste gas	0
The ratio of CO_2 in waste gas	0.17
The ratio of H_2O in waste gas	0.13

The graph of the change in the cylinder temperature depending on the CA created from the values obtained as a result of the calculations in the simulation program is shown in Figure 9, and the change in the cylinder pressure depending on the CA is shown in Figure 10.

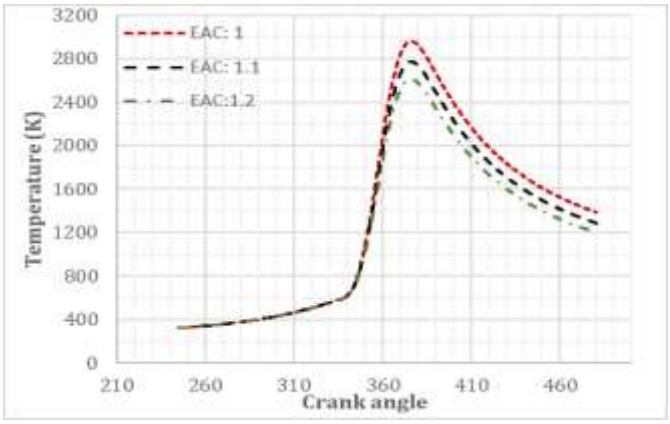

Figure 9. The change of cylinder inside temperature depending on crank angle in different EAC.

When the temperature graph inside the cylinder depending on the CA is examined, the maximum temperature values for 1-1.1-1.2 EAC values respectively; 2960 K at 375 CA, 2772 K at 375 CA, 2612 K at 375 CA. According to these values, as EAC increases, temperature values decrease. The reason for this is that as the EAC increases, the air fuel mixture gets poorer, thus the amount of fuel decreases. Therefore, depending on the amount of fuel, the amount of heat generated as a result of combustion decreases

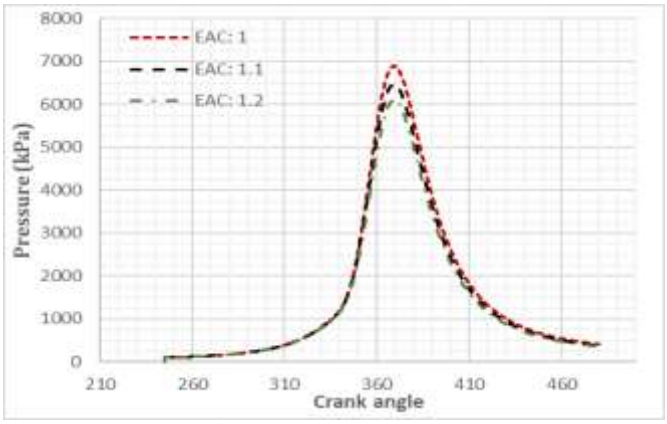

Figure 10. The change of in-cylinder pressure depending on the crank angle in different EAC.

When the in-cylinder pressure graph depending on the CA is examined, the maximum pressure values for 1-1.1-1.2 EAC values respectively; 6892 kPa at 369 CA, 6892 kPa at 369 CA, 6099 kPa at 369 CA. When these values are examined, as the EAC increases, the pressure values decrease as well as the temperature values.

The graphs of the mass ratios of gas components in the cylinder depending on the CA are shown in Figure 11 for CO_2, Figure 12 for H_2O, Figure 13 for NO.

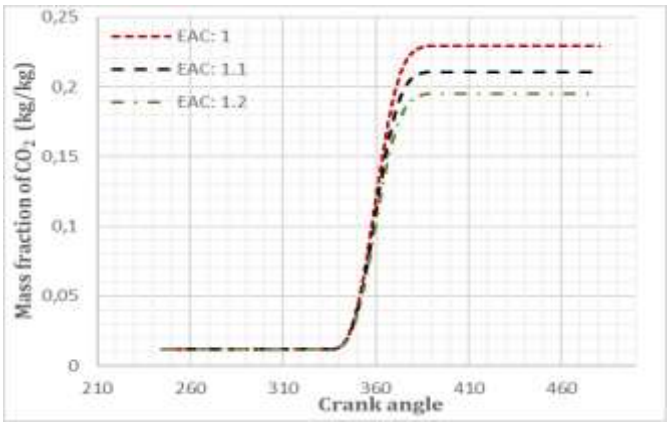

Figure 11. The change of CO_2; mass fraction in different EAC depending on the crank angle.

For CO_2; When the mass ratios in the cylinder are examined depending on the CA, as the EAC increases, the in-cylinder CO_2 mass ratio as a result of combustion decreases.

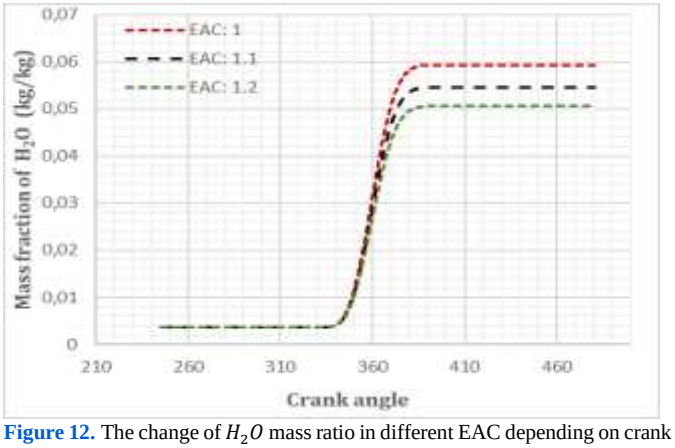

Figure 12. The change of H_2O mass ratio in different EAC depending on crank angle

For H_2O, When the mass ratios in the cylinder depending on the CA are examined, the H_2O mass ratio decreased as the EAC value increased.

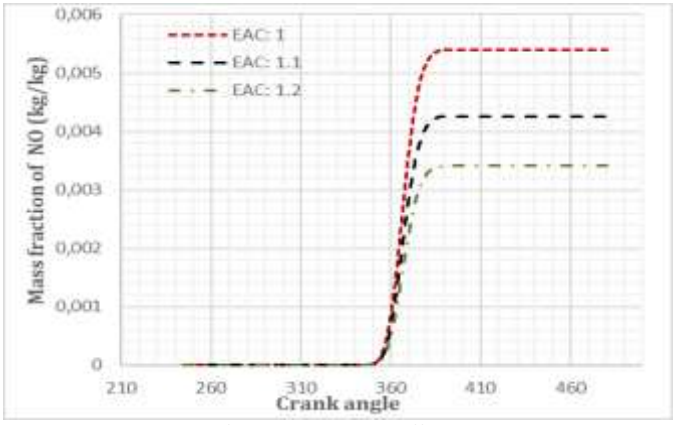

Figure 13. The change of NO mass ratio in different EAC depending on the crank angle.

For NO, when the mass ratios in the cylinder depending on CA are examined, as the EAC value increases, the mass ratio of NO also decreases.

The change of effective power (kW) in different EAC depending on engine speed is shown in Figure 14.

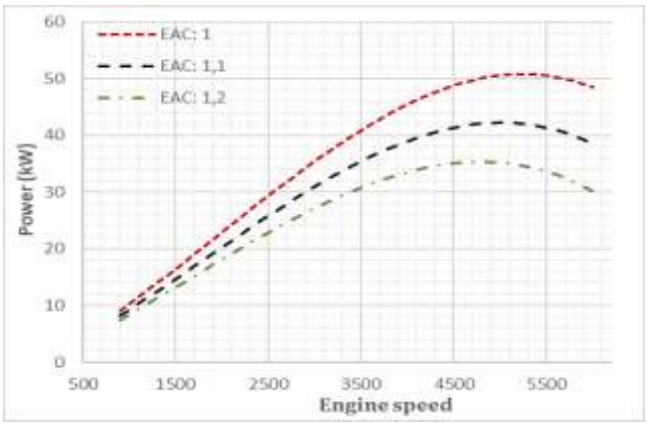

Figure 14. Change of effective power (kW) in different EAC depending on engine speed.

The change of moment in different EAC depending on engine speed is shown in Figure 15.

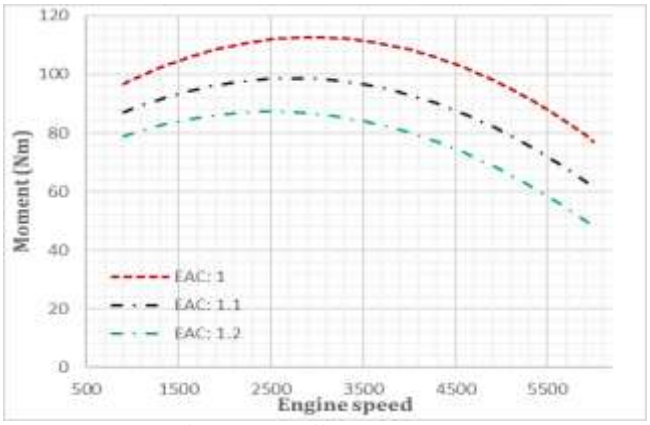

Figure 15. Change of moment in different EAC depending on engine speed.

The change of specific fuel consumption in different EAC depending on engine speed is shown in Figure 16.

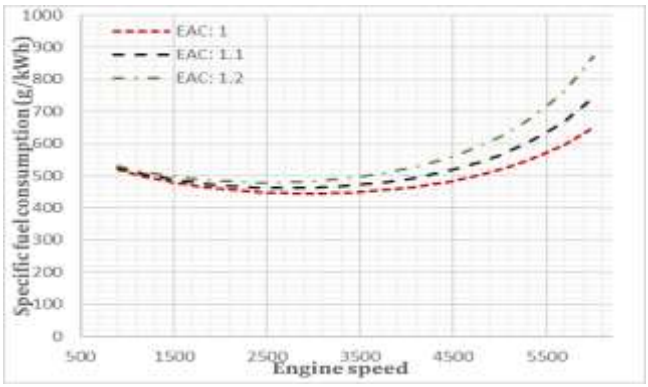

Figure 16. Change of specific fuel consumption in different EAC depending on engine speed.

When effective power and moment graphs are examined, power; 50.82 kW at 5200 rpm at 1 EAC, maximum moment; It was obtained as 112.65 Nm at 2900 rpm at 1 EAC. The most important factor when calculating engine performance values is the in-cylinder pressure value. As the EAC value increases, the in-cylinder pressure value decreases. Therefore, as the EAC value increases, the power and moment values decrease.

When the specific fuel consumption graph is examined, it is seen that the specific fuel consumption increases as the EAC value increases.

The results obtained by using Honda L13A4 i-DSI spark ignition engines in the simulation program created are compared with the data obtained from the experimental study in Table III [24].

The comparison was made with the values of the engine at full load and the mass ratios of the gases obtained from the simulation program were converted into volume ratios for comparison.

TABLE III
COMPARISON OF THE OBTAINED DATA.

Parameters	Experimental	Simulation Results
Power (kW)	70	63.7
Torque (Nm)	127,3	133.2
Specific fuel consumption (kg/kWh) 3000 (rpm)	310	366
CO_2 (volume%) 3000(rpm)	10,65	12,3
CO (volume %) 3000(rpm)	5,5	5,72
NO (ppm) 3000(rpm)	2220	2153

The most important goal in simulation programs is to obtain values closest to reality. When the results obtained for the Honda L13A4 i-DSI spark ignition engine in the developed software program are compared with the data obtained from the experimental study of the engine, it is seen that they are compatible. The resulting differences can be caused by entered or selected motor parameters, omissions and calculation deviations.

4. CONCLUSION

In this study, a simulation program was developed that can calculate combustion, emission and engine performance values depended on variable parameters for internal combustion engines by mathematical modeling. This simulation program was created with the Java programming language.

Since liquid hydrocarbons are generally used as fuel in internal combustion engines, the simulation program has been created to make calculations based on the atomic numbers of the desired fuel. Thermodynamic calculations were created to be performed for each angle within the 0.25 degree range of the crankshaft. At each crank angle, the masses of the fuel and gases in the cylinder and the specific heat of these gases depending on the temperature, the heat released and the amount of heat transferred to the cooling water were calculated instantly.

With this simulation program, analyzes were carried out in different excess air coefficients, and in-cylinder pressure, in-cylinder temperature, mass ratios of gas components in the cylinder, power, moment and specific fuel consumption values were compared.

When the analysis results for the excess air coefficient (EAC) are examined, as the EAC increases, the pressure and temperature values in the cylinder decreased. Due to the decrease in pressure, the power and moment values decreased as the EAC increased.

When the CO_2, H_2O, NO values in the cylinder after combustion were examined, it was seen that the mass ratios of CO_2, H_2O, NO decreased as EAC increased.. H_2O mass ratio decreased as the EAC value increased. On the other hand, specific fuel consumption increased as EAC increased.

REFERENCES

[1] M. Ö. Ültanır, "21. yüzyıla Girerken Türkiye'nin Enerji stratejisinin değerlendirilmesi". İstanbul: TÜSİAD, 1998.

[2] D. Stepanenko and Z. Kneba, "Thermodynamic modeling of combustion process of the internal combustion engines – an overview," Combustion Engines, vol. 178, no. 3, pp. 27–37, 2019.

[3] S. Aïta, A. Tabbal, G. Munck, K. Fujiwara, H. Hongoh, E. Tamura, and S. Obana, "Numerical simulation of port-valve-cylinder flow in reciprocating engines," SAE Technical Paper Series, 1990.

[4] M. Balcı, "Computer simulation of a Four-Stroke turbo charged direct injection diesel engine," PhD Thesis,, Gazi University Institute of Science and Technology, Ankara, 1986.

[5] S. Polat, "Computer aided simulation and performance analysis of a four stroke, single cylinder, variable compression ratio diesel engine," M.S. thesis, Gazi University Institute of Science and Technology, Ankara, 2010.

[6] E. Esin, "Combusting modeling and emissions predictions by using a graphical user Interface," M.S. thesis, Atatürk University Graduate School of Applied Sciences, Erzurum, 2014.

[7] O. A. Kutlar and Ö. Cihan, "Investigation of parameters affecting rotary engine by means of a one zone thermodynamic model," Journal of Energy Resources Technology, vol. 144, no. 4, 2021.

[8] Ö. Cihan, M. Aydın, O. A. Kutlar, "Experımental and 1-D model analysıs of Wankel engıne at part load" International Journal of Advances on Automotive and Technology, 2(3), 197-204, doi.org/10.15659/ijaat.18.09.912

[9] G. P. Blair, "Design and simulation of four-stroke engines. Warrendale" PA: Society of automotive engineers, 1999.

[10] J. B. Heywood, "Internal Combustion Engine Fundamentals," Singapore: Mc Graw Hill International Editions, 1988.

[11] S. Behçet, M. Ergeneman, Arslan H. Ertuğrul, and Soruşbay Cem, "İçten Yanmalı Motorlar." İstanbul: Birsen Yayınevi, 2013.

[12] U. Kiencke and L. Nielsen, "Automotive control systems: For engine, driveline, and vehicle." Berlin: Springer Berlin, 2010.

[13] M. J. Moran, "Introduction to thermal systems engineering: Thermodynamics, Fluid Mechanics, and heat transfer". New York: John Wiley & Sons, 2003.

[14] A. I. Kolchin, V. P. Demidov, and P. Zabolotnyi, "Design of automotive engines." Moscow: Mir, 1984.

[15] Çengel Yunus Ali, M. A. Boles, and Pınarbaşı Ali, "Mühendislik Yaklaşımıyla termodinamik," Konak, İzmir: İzmir Güven Kitabevi, 2012.

[16] C. Borgnakke and R. E. Sonntag, "Borgnakke's fundamentals of Thermodynamics." Singapore: Wiley, 2017.

[17] G. Borman and K. Nishiwaki, "Internal-combustion engine heat transfer," Progress in Energy and Combustion Science, vol. 13, no. 1, pp. 1–46, 1987.

[18] K. Sihling and G. Woschni, "Experimental investigation of the instantaneous heat transfer in the cylinder of a high speed diesel engine," SAE Technical Paper Series, 1979.

[19] C. Olikara and G. L. Borman, "A computer program for calculating properties of equilibrium combustion products with some applications to I.C. engines," SAE Technical Paper Series, 1975.

[20] C. R. Ferguson and A. T. Kirkpatrick, "Internal Combustion Engines: Applied thermosciences". Chichester: Wiley, 2015.

[21] M. D. Artamonov, Morin Mikhail Mikhaĭlovich, and V. A. Ilarionov, "Motor vehicles: Fundamentals and design." Moscow: Mir, 1976.

[22] P., Ülger, "Termik Motorlar". İstanbul: Hiperlink, 2011.

[23] J. Jaworski, "Java 1.1 Developer's Guide." Sams Publishing, 1997.

[24] A. A., Yontar, "Numerical and experimental investigation of the effects of pure and mixed alternative fuels on engine performance and emissions in spark ignition engine", PhD Thesis, Kırıkkale University, Institute of Science and Technology, Kırıkkale, 2016.

BIOGRAPHIES

Ozan Yazar completed his undergraduate education at Afyon Kocatepe University, Automotive Engineering Department, and his master's degree at Mersin University, Institute of Science, Mechanical Engineering Department. He is currently continuing his doctoral studies at Tarsus University, Graduate Education Institute, Mechanical Engineering Department. He works as a lecturer at Yozgat Bozok University. His fields of study are; Internal combustion engines, Electric vehicles, Energy management in hybrid electric vehicles, cooperative adaptive cruise control, Car following models, Connected vehicle control, Autonomous vehicles.

Bünyamin Demir obtained his BSc MSc and Ph. D. degree from Atatürk University. He is currently working as an Associate Professor in the Mechanical Engineering Department at Mersin University. His research interests include agricultural machinery design parameters, artificial neural networks, image processing, data mining and spray characteristics of nozzles.

European Journal of Technique

journal homepage: https://dergipark.org.tr/en/pub/ejt

Vol.12, No.2, 2022

EEG based Schizophrenia Detection using SPWVD-ViT Model

Mesut Şeker[1*], Mehmet Siraç Özerdem[2]

[1*]Dicle University, Electrical-Electronics Engineering Department, Diyarbakir, Turkey. (e-mail: mesut.seker@dicle.edu.tr).
[2] Dicle University, Electrical-Electronics Engineering Department, Diyarbakir, Turkey. (e-mail: sozerdem@dicle.edu.tr).

ARTICLE INFO

Received: Oct., 20. 2022
Revised: Nov., 30. 2022
Accepted: Nov., 30. 2022

Keywords:
EEG
Schizophrenia
Neurological Disease
Vision Transformer
Diagnosis
Detection
Time-frequency image

Corresponding author: *Mesut Şeker*

ISSN: *2536-5010* | e-ISSN: *2536-5134*

DOI: https://doi.org/10.36222/ejt.1192140

ABSTRACT

Schizophrenia is a typical neurological disease that affects mental state, and daily behaviours of patients. Combining image generation techniques with effective machine learning algorithms may accelerate treatment process. Moreover, possible early alert systems prevent diseases from reaching out crucial phase. The purpose of current study is to develop an automated EEG based schizophrenia detection with the Vision Transformer (ViT) model using Smoothed Pseudo Wigner Ville Distribution (SPWVD) time-frequency (TF) input images. EEG recordings from 35 schizophrenia (sch) patients and 35 healthy controls (hc) are analysed. We have used 5-fold cross validation for evaluation and testing of the method. Classification task is carried out via. subject-independent and subject-dependent method. We achieved overall accuracy of 87% for subject-independent and 100% for subject-dependent approach for binary classification. While ViT has been extensively used in Natural Language Processing (NLP) field, dividing input images within a sequence of embedded image patches via. transformer encoder is a practical way for medical image learning and developing diagnostic tools. SPWVD-ViT model is recommended as a disease detection tool not only for schizophrenia but other neurological symptoms.

1. INTRODUCTION

Neurological disorders may affect human's thinking ability and result general behavioral disorders. Schizophrenia is such neurological disease in same manner [1]. According to Word Health Organization (WHO), 24 million patients sufferer from schizophrenia has been reported in [2]. Within the early diagnosis of schizophrenia and the relevant treatment methods, the disease will be prevented from reaching out crucial phase, and the treatment process will be accelerated with the supply of required medications [3].

Most of mental disorders has been investigated by image and signal processing techniques. Electroencephalography (EEG) has been considered as a popular screening tool in Brain Computer Interfaces (BCI), neuroscience, engineering, and rehabilitation applications [4]. EEG provides muti-channel setup and higher time resolution , and has cheap, easy and practical aspect as a neuro-screening tool [5]. This method provides significant information process belongs to brain dynamics and has remained its prevalence for detection of neurological diseases in recent years.

Classification-based studies used in the diagnosis of schizophrenia show advanced feature engineering, but it is still observed that the desired level of qualified features haven't been investigated yet. Some of the recent studies based on disease detection techniques and diagnosis methods of schizophrenia can be summarized as follows: Kim et al. (2015) calculated spectral values of EEG sub-bands using Fast Fourier Transform (FFT) from 90 schizophrenia (SCH) patients with equal size of Healthy Controls (HC) and obtained 62.2% accuracy within Receiver Operating Characteristic (ROC) by delta sub-band frequency [5]. In another study including 25 healthy and 25 patients, time-frequency conversion was performed with EEG recordings and the best 5 electrodes for classification were determined [6]. In the related study, the highest performance with 93.9% accuracy was obtained from the F2 channel. Johannesen et al. (2016) extracted a total of 60 features from 40 schizophrenic and 12 healthy participants in their study and performed classification task with Multilayer Perceptron (MLP) and Support Vector Machine (SVM) [7]. Using theta and alpha frequencies in the frontal region, 87% accuracy was obtained for distinguishing patients from controls. In a complexity and entropy features based study [8], a total of 14 non-linear features has been proposed and highest accuracy of 92.91% is achieved using Radial Function based Support Vectors Machine (RFB-SVM).

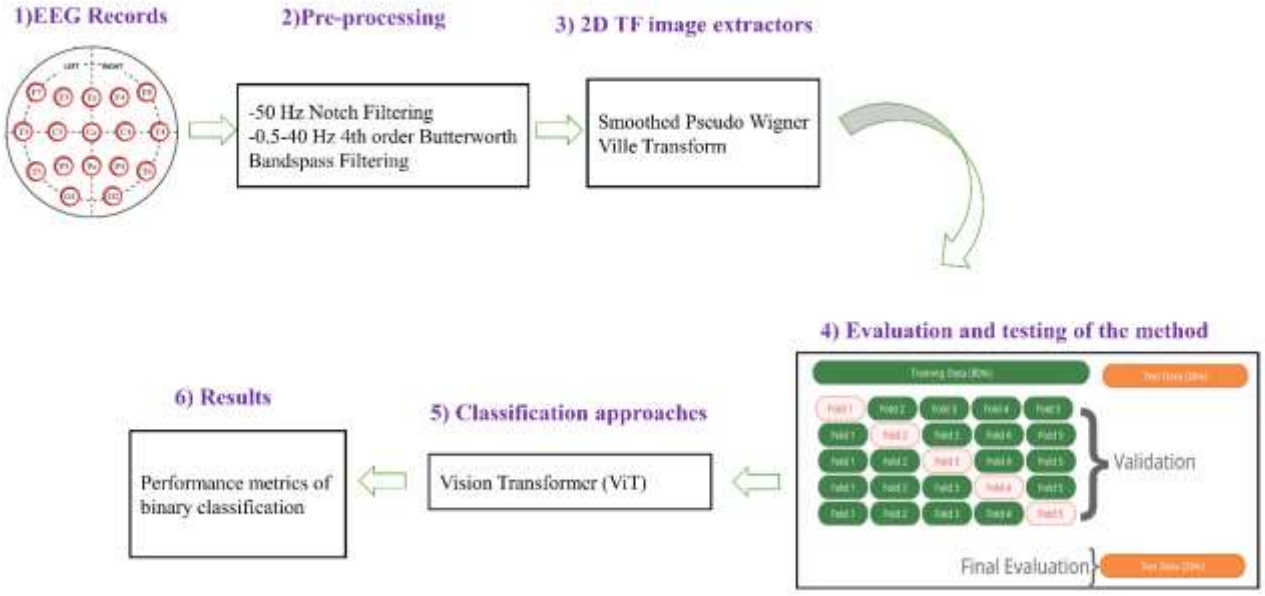

Figure 1. The followed methods in proposed study

Resting state EEG based deep learning algorithms for detection of schizophrenia have been yielded growing attention using in studies. Oh et al. [9] utilized from 14 sch patients and 14 controls with 19 channel EEG using time-domain representation. They proposed 11 layered Convolutional Neural Network (CNN) with SoftMax classifier. 10-fold cross validation is used for train(72%), validation(18%), and test (%10) split, and 81.26% accuracy is obtained by subject-independent classifications task. Phang et al. [10] acquired EEG from 39 HC and 45 SCH, proposed fusion of time, frequency, and brain topological connectivity as input data. RNN, CNN architectures are used with SoftMax classifier. 5-fold cross validation is used for train (60%), validation (20%), and test (20%) sets, and 92.87% accuracy is obtained. Calhas et al. [11] used time-frequency EEG representation using Siamese Neural Network with SVM, Random Forest (RF), Extreme Gradients Boosting (XGBoost), Naïve Bayes (NB), and k-Nearest Neighbors (k-NN) classifiers and leave-one-out validation. Highest accuracy of 83% is obtained from the experiment. Naira et. al. [12] proposed a CNN architecture with softmax classifier using matrices of correlation between EEG channels from 39 HC and 45 SCH participants. They obtained 90% of accuracy based on subject-dependent classification within 70%-30% train-test split evaluation method. A separate summary of previous studies for EEG based schizophrenia detection is given in Table I.

In current study, a time-frequency representation called Smoothed Pseudo Wigner Ville Distribution (SPWVD) is applied to EEG records of schizophrenic and healthy participants. Both subject dependent and independent evaluation are applied during train, validation, and test split. We propose a Vision Transformer (ViT) model to discriminate schizophrenic EEG from controls. Performance metrics of binary classification task will be given. The overall steps followed in current study is given in Fig. 1.

The rest of this paper is organized as follows: Section 2 explains experimental dataset, pre-processing steps, describes generated SPWVD time-frequency images, and architectural mechanism of ViT. Section 3 explains performance metrics of ViT using SPWVD images of SCH and HC. Finally, proposed method for detection of schizophrenic EEG records via. HC is concluded in Section 4.

2. DATASET, PRE-PROCESSING STAGE, TIME-FREQUENCY INPUTS, AND CLASSIFICATION TASK

2.1. EEG Data Acquisition

EEG datasets are acquired from 35 schizophrenia patients and 35 healthy controls aged between 11-13 years. All participants are male. Resting state EEGs are recorded using 16 channel 10-20 system of electrode placement during eyes closed. EEG channels are F7, F3, F4, F8, T3, C3, Cz, C4, T4, T5, P3, Pz, P4, T6, O1 and O2. Electrode replacement is shown in Fig2. Frequency range of records is 0.5-45 Hz, and electrode impedance is below 10 kΩ. Sampling frequency f_s is 128 Hz and length of each participant's record is 1 minute. Dataset is publicly available at http://brain.bio.msu.ru/eeg_schizophrenia.htm.

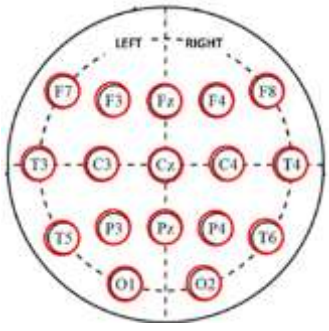

Figure 2. 10-20 electrode replacement of 16 EEG channels

2.2. Pre-processing Step

In order to process with specific band-range and obtain clean EEG, we applied 4th order Butterworh band-pass filtering due to its linear response [13]. Moreover, a 50 Hz band-rejected Notch filter is applied to remove power line inference [14]. 60s length of signal is divided into 1s epoch, and TF image inputs are generated from each epoch.

2.3. Time-Frequency (TF) Inputs

We converted 1D time series EEG signals to 2D time-frequency domain. There are many algorithms such as continuous wavelet transform (CWT) based scalogram [15], Short Time Fourier Transform based spectrogram [16], Hilbert Spectrum [17], Fourier and Wavelet based Synchro-squeezing transform [18]. According to our knowledge, there is only single study that achieves best results (acc. 93.36%) with Smoothed Pseudo Wigner Ville Distribution (SPWVD) with CNN for automated detection of schizophrenia using EEG [19].

The EEG records obtained from 16 channels of each participant is divided into 1s epochs. We obtain one-dimensional vector with combining epochs belongs to each channel. Dimension of vector within combined channels is 128x16. We obtained 60 SPWVD images from each participant. Dimension of each generated TF images is 434x343x3. We totally have 2100 images from SCH and 2100 images from HC. We resized the images as 224x224x3 with inter_area interpolation provided by OpenCV. Sample images are given in Fig. 3. All images are generated in MATLAB R2021a environment.

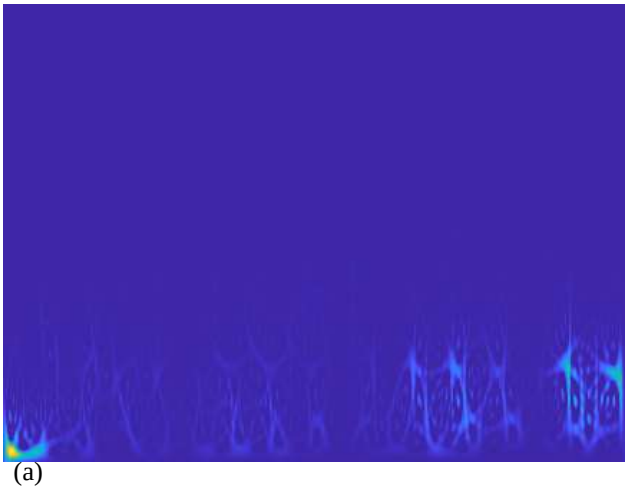

(a)

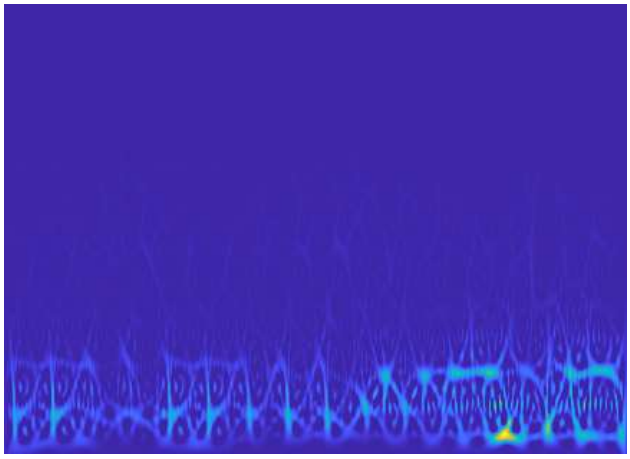

(b)

Figure 3. Some sample images using SPWVD for (a) HC and (b) SCH with original size of 434x343x3

SPWVD is an effective conversion technique that includes content of time-frequency localization of signal energy. This TF representation methods evaluates higher harmonics and time-domain localization. It reduces cross-term inference using TF windows. Formula for calculation of SPWVD can be written as follows:

$$\mathrm{SPWVD}(t,f)=\int_{-\infty}^{\infty}\int_{-\infty}^{\infty} v\left(\frac{\tau}{2}\right)v^{*}\left(-\frac{\tau}{2}\right)u(t-t')\ldots \times z\left(t'+\frac{\tau}{2}\right)z^{*}\left(t'-\frac{\tau}{2}\right)\exp^{-j2\pi f\tau}\mathrm{d}t'\mathrm{d}\tau$$

,where $v(t)$ is cross-term reducing in time and $u(t)$ is cross-term reducing in frequency domains. In order to adjust the frequency and temporal resolution, length of the time and frequency windows are set individually. The superiority of SPWVD can be explained as follows: STFT assumes a signal to be stationary ovel all windows, and CWT generates cross-term inference in frequency domain. There is a tradeoff between spectrogram and scalogram due to TF localization and TF cross term. SPWVD overcomes this tradeoff and serves practical solutions for TF representation [19].

2.4. Vision Transformer (ViT) Model

Vaswani et al. added another dimension to previous attention models mainly rely on recurrence and convolutions. They have used proposed model to a specific approach of natural language processing [20]. From the inspiration of this success, Dosovitskiy et al. attempted to apply the standard Transformer model to images for image classification application [21].

To convert an input image as a structure in a sense of having a sequence of words, we divide input image into smaller N number of 2-dimensional patches via. $N = HW/P^2$, where H: height of image, W: width of image and P: resolution pixel. Each image patch is flattened into a vector length of P^2xC, where C is number of channels. A sample input of before/after dividing patches is given in Fig. 4.

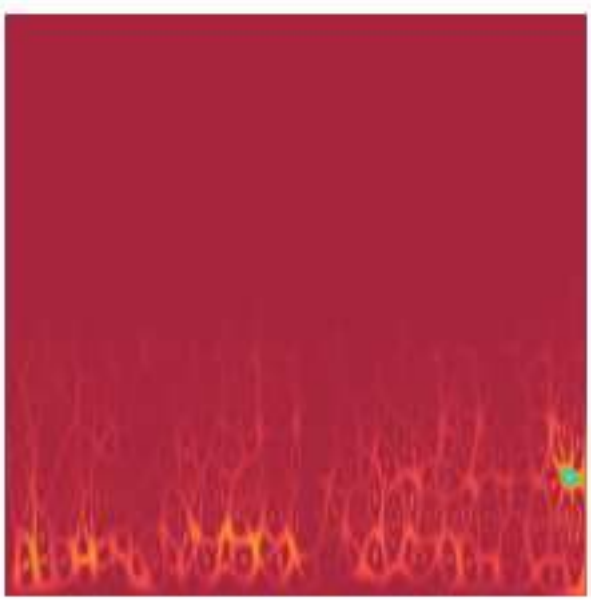

(a)

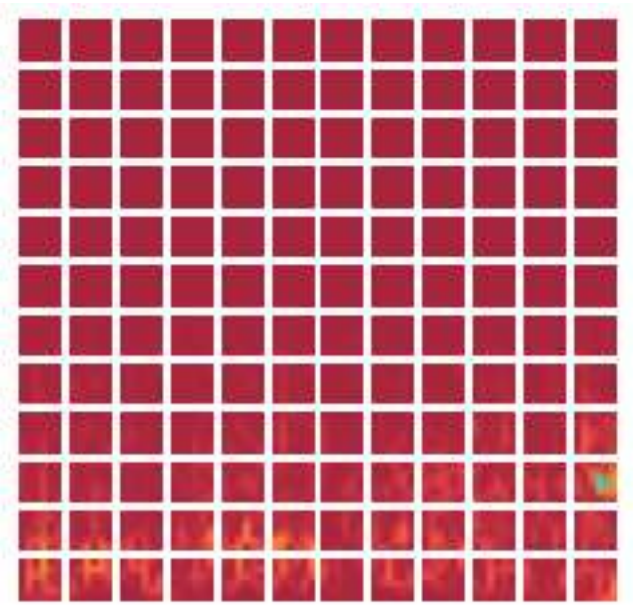

(b)

Figure 4. (a) A sample input image before dividing patches (b) divided patches in input images

We resized (224,224,3) input images to (72x72x3). Size of the patches to be extracted from input images is 6. Number of patches per images is calculates as 144 (12*12). Other hyperparameters belongs to ViT are as follows: learning rate= 0.001, weight decay= 0.0001, batch size=32, number of epochs= 500, projection dimension= 64, number of heads= 4, projection dimension in transformer unit=2, size of transformer layer=8, size of the head layer of the final classifier Multi-Layer Perceptron (MLP)= [2048,1024], and dropout rate=0.5. We have normalized all image data in range of [0-1] to avoid high range of pixels and improve convergence speed.

We have also used data augmentation to increase number of images with following operation: random flip with "horizontal", random rotation with factor=0.2, and random zoom with height and width factor= 0.2. The proposed architecture of ViT can be seen in Fig. 5. ViT employs the encoder feature of the original Transformer design. The encoder receives the sequence of embedded image patches as input. Values of the learnable class embeddings are received by the classification head that is attached to the output to produce a classification output. This implementation is carried out by a MLP with one hidden layer and Gaussian Error Linear Unit (GELU) non-linearity. We developed the code given publicly available at https://keras.io/examples/vision/image_classification_with_vision_transformer/ and classification task is carried out as subject dependent and subject independent approaches in a workstation with AMD Ryzen 7 3700X 8-Core Processor 3.60 GHz, 32 GB RAM, and NVIDIA GeForce 3060 with 12 GB VRAM using TensorFlow library on Spyder (Python 3.9) environment.

3. PRACTICAL RESULTS

We first divided TF images of SCH and HC class as 80% train and 20% test set. Stratified 5-fold cross validation is applied to the train set to achieve validation set. Classification task is divided 2 sub-sections: subject dependent and subject independent classification. In subject-dependent classification task, we randomly shuffled TF images to the train, validation, and test set. In subject independent classification task, TF images of each participant are only in train, validation, or test set. Accuracy and loss values in each epoch is drawn to prove there is no overfitting. Accuracy needs to be increased and loss may be decreased along 500 epochs. Confusion matrices are given to indicate true and predicted label for each class. Finally, performance metrics of accuracy, precision, recall and f1-score are given. The procedure to calculate related metrics are given in Table I. In an ideal classifier, FP and FN should be zero. Moreover, precision and recall values needs to be one. F1-score is a metric that takes precision and recall into account and show trustworthy results. Calculation of f1-score is given as follows:

$$F1 - core = 2 * \frac{Precision * Recall}{Precision + Recall} \quad (1)$$

3.1. Subject-Dependent Classification

Performance metrics after subject-dependent classification task is given in Fig 4. (a). 373 TF images out of 420 are classified as sch, and 354 TF images out of 420 are recognized as hc. Discrimination of sch patients TF patterns is greater than discrimination of hc. Overall accuracy is achieved as 87%.

3.2. Subject-Independent Classification

Performance metrics after subject-dependent classification task is given in Fig 4. (b). All sch patients are correctly classified, and only one TF images of hc is misclassified as schizophrenia. Overall accuracy is obtained approximately as 100%.

Considering the studies in literature, researchers have preferred spectral features, non-linear measurements, functional connectivity, correlation between EEG channels, and TF EEG conversion techniques. ROC analysis, conventional classifiers (i.e. k-NN, SVM), CNN with softmax, and hybrid architectures (i.e. feature extraction with deep neural networks, and classification with conventional classifiers) are considered as machine learning methods. There are many methodological differences, namely datasets (lengths of records, number of participants, demographics of participants, etc), pre-processing approaches, length of EEG epochs, different evaluation methods, extracted features and classification architectures between current work and other studies. Therefore, it is not easy to make a direct comparison and evaluation. On the other hand, none of previous studies have included ViT for classification stage, and current study has both subject-dependent, and independent classification task. We believe that it is more convenient to validate a network with a previously unseen test set. Even if all extracted TF images from successive epochs for a participant are not same due to non-linear behavior of EEG , epochs from same participant may include some common patterns, and this will result with overfitting in performance. If the test set has totally separate patterns considering train set, or train set doesn't include enough diversity to enable classifiers to capture common pattern with test set, lower accuracy in test set will be obtained. This trade-off can be taken into consideration during evaluation and testing of method. In a nutshell, 87% of accuracy for subject-independent method still provides sufficient diagnostic rate for clinical purposes.

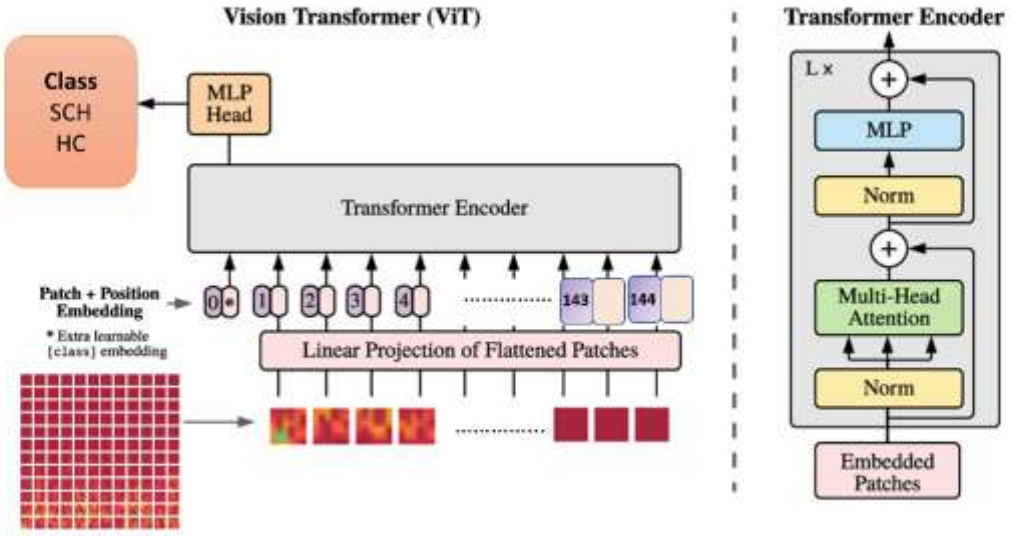

Figure 3. The proposed architecture of Vision Transformer (ViT) Model

TABLE I
CALCULATION OF PERFORMANCE METRICS FROM CONFUSION MATRICES

		Predicted Label		
		Positive	**Negative**	
True Label	**Positive**	TP	FN	Sensitivity $\frac{TP}{TP+FN}$
	Negative	FP	TN	Specificity $\frac{TN}{TN+FP}$
		Precision $\frac{TP}{TP+FP}$	Recall $\frac{TP}{TP+FN}$	Accuracy $\frac{TP+TN}{TP+FP+FN+TN}$

TABLE II

SUMMARY OF STUDIES FOR EEG BASED AUTOMATED DETECTION OF SCHIZOPHRENIA

Authors	**Input Data**	**Architecture/ Classifier**	**Accuracy (%)**
Kim et al. [5] +	FFT based spectral values of 5 EEG sub-bands	ROC Analysis	62.20
Dvey- Aharon et al. [6] +	Time-frequency conversion	k-NN	93.9
Johannesen et al. [7] +	Theta1, theta 2, alpha, beta, And gamma frequency features	SVM	87.0
V. Jahmunah et al. [8] +	Non-linear features, t-test for feature selection	RBF-SVM	92.91
Oh et al. [9]*	Time-domain representation	CNN with softmax	81.26
Phang et al. [10] +	TF and topological connectivity	RNN, CNN with softmax	92.87
Calhas et al. [11] +	TF EEG representation	Siamese Neural Network With SVM, RF, XGBoost, NB, k-NN	83
Nairan et al. [12]**	Matrices of correlation between channels	CNN with softmax	90
Proposed work	Smoothed Pseudo Wigner Ville Transform (SPWVD)	Vision Transformer (ViT)	87 * 100**

*:subject-independent evaluation, **:subject-dependent evaluation, +:not attended

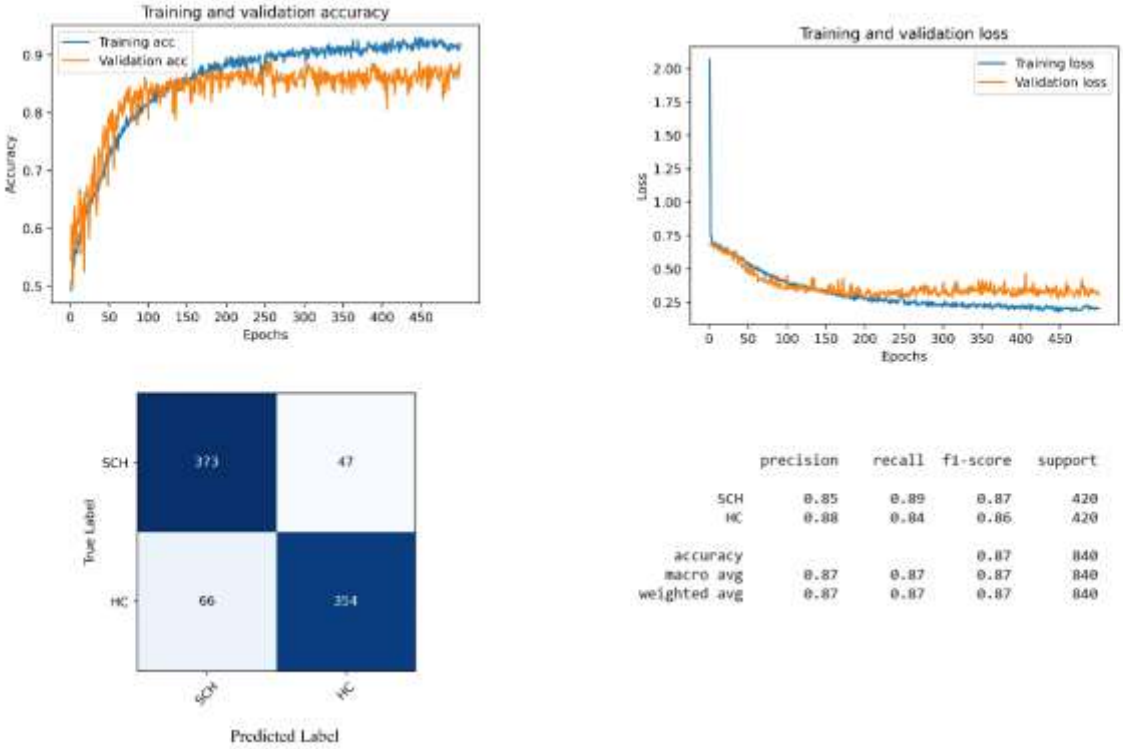

(a)

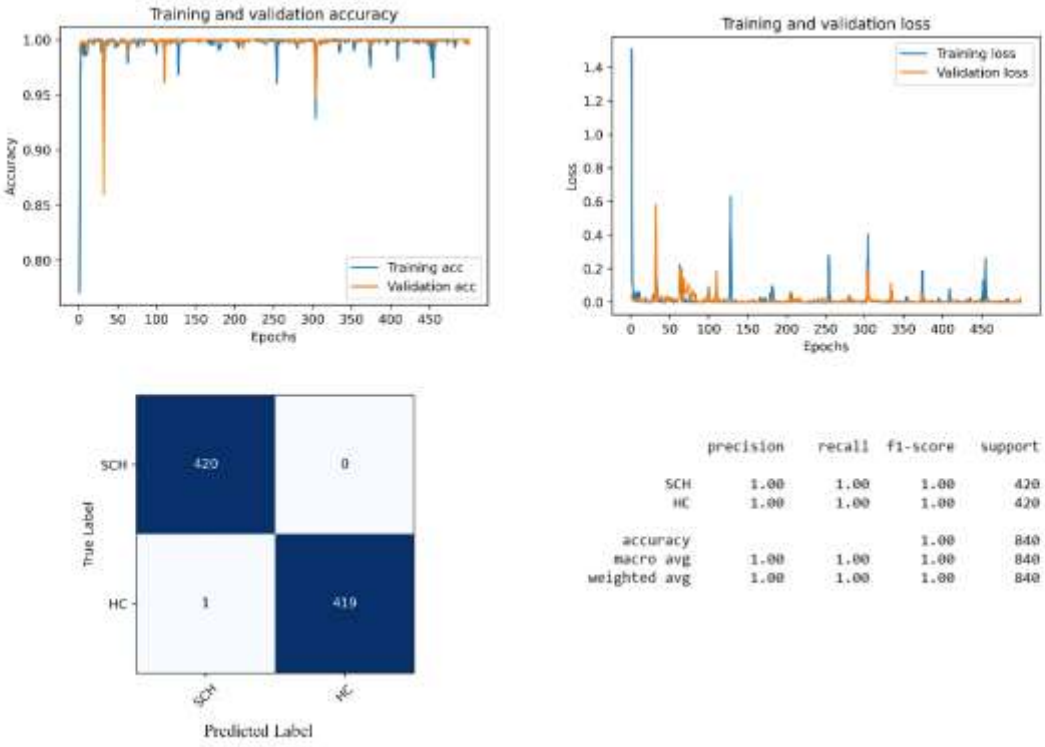

	precision	recall	f1-score	support
SCH	1.00	1.00	1.00	420
HC	1.00	1.00	1.00	420
accuracy			1.00	840
macro avg	1.00	1.00	1.00	840
weighted avg	1.00	1.00	1.00	840

(b)

Figure 4. Training and validation accuracy/loss, confusion matrices and performance metrics for **(a)** Subject-Independent and **(b)** Subject-Dependent Classification Approach

2. SUMMARY AND FUTURE WORK

In current study, ViT architecture is proposed for EEG based schizophrenia detection for image classification application. Analyzing and recognizing images within a sequence of embedded image patches via. transformer encoder gives rise to medical image classification for disease detection. We extracted 2D SPWVD TF images from 1D schizophrenic and healthy EEG time series. SPWVD is an efficient alternative TF image extractor over widely used spectrogram and scalogram images by providing solutions for cross-term inference and TF localization. Unlike previous studies for schizophrenia detection with resting state EEG, we combined subject dependent, and independent classification methods in SPWVD-ViT model. We obtained 87% overall accuracy for subject-independent, and 100% overall accuracy for subject-dependent approach for automated schizophrenia detection.

It would be also interesting to add more participants and increase number of EEG records to validate current results. Including sub-types or different stages of schizophrenia in dataset and performing a multi-class method will also be another potential work for future. We can even apply same disease detection method to other patients with epilepsy, dementia, or Parkinson to put forward robustness of developed tool. ViT architectures need more powerful hardware basement to reach out better performance. We aim to increase the rate of subject-independent schizophrenia detection by using high performance resources. As an alternative work, image sets generated from an advanced method are fed into a CNN, and then feature maps of CNN are passed onto the Transformer encoder in future investigations. Finally, performance of ViT model with pre-trained or trained from scratch deep learning pipelines is also targeted future study.

ACKNOWLEDGEMENT

This research did not receive any specific grant from funding agencies in the public, commercial, or not-for-profit sectors. A sincere appropriation to Julius Bamwenda for his diligent proofreading of the manuscript.

REFERENCES

[1] V. Rajinikanth, S. C. Satapathy, S. L. Fernandes, and S. Nachiappan, “Entropy based segmentation of tumor from brain MR images – a study with teaching learning based optimization,” Pattern Recognit. Lett., vol. 94, pp. 87–95, 2017.

[2] “Schizophrenia.” [Online]. Available: https://www.who.int/news-room/fact-sheets/detail/schizophrenia. [Accessed: 10-Jan-2022].

[3] Z. Wang and T. Oates, “Imaging time-series to improve classification and imputation,” IJCAI Int. Jt. Conf. Artif. Intell., vol. 2015-Janua, no. Ijcai, pp. 3939–3945, 2015.

[4] M. Seker and M. S. Ozerdem, “EEG Coherence as a Neuro-marker for Diagnosis of Schizophrenia,” in 2020 28th Signal Processing and Communications Applications Conference, SIU 2020 - Proceedings, 2020.

[5] J. W. Kim, Y. S. Lee, D. H. Han, K. J. Min, J. Lee, and K. Lee, “Diagnostic utility of quantitative EEG in un-medicated schizophrenia,” Neurosci. Lett., vol. 589, pp. 126–131, 2015.

[6] Z. Dvey-Aharon, N. Fogelson, A. Peled, and N. Intrator, “Schizophrenia detection and classification by advanced analysis of EEG recordings using a single electrode approach,” PLoS One, vol. 10, no. 4, pp. 1–12, 2015.

[7] J. K. Johannesen, J. Bi, R. Jiang, J. G. Kenney, and C.-M. A. Chen, “Machine learning identification of EEG features predicting working memory performance in schizophrenia and healthy adults,” Neuropsychiatr. Electrophysiol., vol. 2, no. 1, pp. 1–21, 2016.

[8] V. Jahmunah et al., “Automated detection of schizophrenia using nonlinear signal processing methods,” Artif. Intell. Med., vol. 100, no. June, p. 101698, 2019.

[9] S. L. Oh, J. Vicnesh, E. J. Ciaccio, R. Yuvaraj, and U. R. Acharya, “Deep convolutional neural network model for automated diagnosis of Schizophrenia using EEG signals,” Appl. Sci., vol. 9, no. 14, 2019.

[10] C. R. Phang, F. Noman, H. Hussain, C. M. Ting, and H. Ombao, "A Multi-Domain Connectome Convolutional Neural Network for Identifying Schizophrenia from EEG Connectivity Patterns," IEEE J. Biomed. Heal. Informatics, vol. 24, no. 5, pp. 1333–1343, 2020.

[11] J. Tudela, M. Martínez, R. Valdivia, J. Romo, M. Portillo, and R. Rangel, "On the use of pairwise distance learning for brain Signal classification with limited observations," Nature, vol. 388. pp. 539–547, 2010.

[12] C. A. T. Naira and C. J. L. Del Alamo, "Classification of people who suffer schizophrenia and healthy people by EEG signals using deep learning," Int. J. Adv. Comput. Sci. Appl., vol. 10, no. 10, pp. 511–516, 2019.

[13] S. S. Daud and R. Sudirman, "Butterworth Bandpass and Stationary Wavelet Transform Filter Comparison for Electroencephalography Signal," Proc. - Int. Conf. Intell. Syst. Model. Simulation, ISMS, vol. 2015-Octob, pp. 123–126, 2015.

[14] X. Jiang, G. Bin Bian, and Z. Tian, "Removal of artifacts from EEG signals: A review," Sensors (Switzerland), vol. 19, no. 5, pp. 1–18, 2019.

[15] Z. Aslan and M. Akin, "A deep learning approach in automated detection of schizophrenia using scalogram images of EEG signals," Physical and Engineering Sciences in Medicine, vol. 45, no. 1. pp. 83–96, 2022.

[16] Z. Aslan and M. Akin, "Automatic detection of schizophrenia by applying deep learning over spectrogram images of EEG signals," Trait. du Signal, vol. 37, no. 2, pp. 235–244, 2020.

[17] A. Zülfikar and A. Mehmet, "Empirical mode decomposition and convolutional neural network-based approach for diagnosing psychotic disorders from eeg signals," Appl. Intell., vol. 52, no. 11, pp. 12103–12115, 2022.

[18] K. Jindal, R. Upadhyay, P. K. Padhy, and L. Longo, "6 - Bi-LSTM-deep CNN for schizophrenia detection using MSST-spectral images of EEG signals," in Artificial Intelligence-Based Brain-Computer Interface, V. Bajaj and G. R. Sinha, Eds. Academic Press, 2022, pp. 145–162.

[19] S. K. Khare, G. S. Member, V. Bajaj, S. Member, U. R. Acharya, and S. Member, "SPWVD-CNN for Automated Detection of Schizophrenia Patients Using EEG Signals," vol. 70, 2021.

[20] A. Vaswani, N. Shazeer, and N. Parmar, "Attention is All You Need," in 31st Conference on Neural Information Processing Systems (NIPS), 2015.

[21] A. Dosovitskiy, L. Beyer, A. Kolesnikov, and D. Weissenborn, "An Image is Worth 16x16 Words: Transformers for Image Recognition at Scale," in ICLR 2021, 2021.

BIOGRAPHIES

Mesut Şeker received the B.Sc. degree in 2014 from Zirve University, Gaziantep, Turkey. He received his M.Sc degree in Electrical-Electronics Engineering in 2017 from Dicle University and he is currently studying for Ph.D in Electrical-Electronics Engineering at Dicle University. He is also Research Assistant in the same department. His research interest include neural time series analysis, EEG signal processing, neuroscience, pattern recognition and machine learning.

Mehmet Siraç Özerdem received the B.Sc. degree in Electrical-Electronics Engineering in 1994 from Eastern Mediterranean University in Northern Cyprus. He received his M.Sc degree in Electrical Engineering in 1998 from Yıldız Technical University. He received the Ph.D. degree in Computer Engineering in 2003 from Istanbul Technical University. Currently, he works as Professor and researcher at Dicle University, Diyarbakır, Turkey. His research focuses on machine learning, biomedical signal processing, bioinformatics and embedded system design.

European Journal of Technique

journal homepage: https://dergipark.org.tr/en/pub/ejt

Vol.12, No.2, 2022

Composition, Morphology, Optical, Thermal and Mechanical Properties of Yogurt Containers

Gizem Cihanoğlu[1], Merve Karabıyık[2], Iklima Odabası[3], Devrim Balkose[4]

[1] İzmir Institute of Technology, Department of chemical engineering, Gülbahçe, Urla, İzmir (payergizem@gmail.com)
[2] İzmir Institute of Technology, Department of chemical engineering, Gülbahçe, Urla (merveozpirin@gmail.com)
[3] USCA winery Urla İzmir Turkey (iklimaodabaşı@gmail.com)
[4] İzmir Institute of Technology, Department of chemical engineering, Gülbahçe, Urla, İzmir (devrimbalkose@gmail.com)

ARTICLE INFO

Received: Jan., 10. 2022
Revised: June, 27. 2022
Accepted: Nov., 07. 2022

Keywords:
Polypropylene
Polystyrene
Calcite
Titanium dioxide
Composites

Corresponding author: *Devrim Balköse*

ISSN: *2536-5010* | e-ISSN: *2536-5134*

DOI: https://doi.org/10.36222/ejt.1054357

ABSTRACT

The morphology, composition, optical, thermal and mechanical properties of two randomly selected commercial yogurt containers, container 1 and container 2 were determined using advanced analytical techniques in the present study. The container 1 which was based on polypropylene labelled as "5 "had 18.1 % $CaCO_3$ and 1.2% TiO_2. On the other hand container 2 which was based on polystyrene labelled as "6" had 1.2 % TiO_2, $CaCO_3$ and olivine. The melting point of container 1 was 166.4 ^oC and the glass transition point of container 2 was 99.9^oC. The surface of the container 1 was smoother than the container 2 with the average surface roughness values of inside surfaces 10.3 and 19.4 nm respectively. Both containers were white in color and had very low values of light transmission. The samples had close values of tensile strength and tensile modulus. The presence of fillers made the containers had lower tensile strength and higher stiffness than their base polymers. the future recycling methods for yogurt packing materials. The containers labelled as "5 "and "6" should be collected separately from the source since they will have different processes for reuse.

1. INTRODUCTION

The goal of food packaging is to contain food in a cost-effective way that satisfies industry requirements and consumer desires, maintains food safety, and minimizes environmental impact [1]. People consume yogurt, which is one of the most important food product that is made of fermented milk [2]. This fermented feed product was stored in containers derived from animal skins and earthenware pots approximately fifteen thousand years ago. By the time of progress, yogurt diversity increased so packaging technology needed to develop. Muniandy et al. [3] investigated the antioxidant activity of probiotic yogurt set in disposable plastic containers during refrigerated storage. Preferable materials, which are used recently in yogurt containers, are polystyrene (PS) and polypropylene (PP). While polystyrene is clear, hard and brittle, polypropylene is resistant to chemicals, heat and over fatigue and has lowest density among plastics suitable for packaging. Aroma compound sorption of yogurt with polystyrene and polypropylene packing was investigated by Saint-Eve et al. [2]. It was found that polystyrene packaging seemed to be preferable for limiting aroma compound losses and subsequent fruity note intensities, and for avoiding the development of odor and aroma defects. Less significant packaging effect was observed for 4% fat yogurts [2]. At the storage temperature, 4^oC in refrigerator, polystyrene is totally amorphous in a vitreous state, while polypropylene is a semi-liquid crystalline polymer in a rubbery state. Thus, these differences in the structure could explain why the kinetics of aroma compound sorption was slower in polystyrene packaging than in polypropylene packaging [4].

The main disadvantage of polystyrene as a rigid or semi-rigid container is the fact that it is brittle. This can be overcome by blending with styrene butadiene copolymer, SB or SBC, an elastomeric polymer. The blend is known as high-impact polystyrene or HIPS. Blending produces a tougher material. It is translucent and is often used in a white pigmented form. The sheet can be thermoformed for short shelf life. The high impact polystyrene (HIPS) is the most popular material used in yogurt containers. It is normal to add pigments such as TiO_2 to the HIPS in order to improve the appearance of the package and to provide some barrier to light. This also helps in heating and softening the HIPS sheet for thermoforming when radiant heating is used. White is most often used, but other colors are also common [5].

In the present study, the characterization of randomly selected two yogurt containers was aimed. Advanced instrumental techniques such as Fourier Transform Infrared Spectroscopy(FTIR), X-ray diffraction, scanning electron

microscopy (SEM), Energy dispersive analysis(EDX), atomic force microscopy(AFM), Differential scanning calorimetry (DSC), Thermal Gravimetric analysis (TG), visible spectroscopy and tensile testing were used the determine the chemical composition, morphology, thermal and mechanical properties.

2.EXPERIMENTS

2.1.Samples

Samples selected from the market shown in Figure 1 were container 1, which is polypropylene based, and container 2, which is polystyrene, based. They were stamped at the bottom as recyclable polymers as 5 (polypropylene) and 6 (polystyrene) respectively. The bottom parts of the containers were examined by FTIR, X-ray, SEM, EDX, AFM, DSC and TG analysis. The samples cut from sides of the containers were used for mechanical tests.

Shimadzu-8400S infrared spectrophotometer was used as an instrument for the transmission technique of infrared spectroscopy. The microstructure of samples was investigated with Scanning Electron Microscopy (SEM), FEI Quanta250, with a field emission gun. The scissor cut surfaces from the bottom of the samples examined. The fracture surface of sample d after tensile test was also investigated with SEM. Before viewing the sample, sputter coater was used to coat surface of sample with this layer of gold at 15 mA under vacuum condition at $7x10^{-2}$ mbar during 75 s to increase its surface conductivity.

The inner and outer surfaces of the 1 cm x 1 cm pieces from the bottom part of the yogurt cups were examined by atomic force microscopy. Contact mode of AFM was used to determine the surface topography. AFM (Nanoscope IV) and silicon tip was used to obtain surface morphology and roughness of the film. 1 Ohm Silicon tip has coating: front side: none, back side: 50 ± 10nm Al. Cantilever properties are T:3.6-5.6 µm, L:140-180 µm, k:12-103 N/m, fo:330-359 kHz, W:48-52µm. USRS 99-010, AS 01158-060 serial no OD57C-3930 standard was used in reflection mode.

DSC analysis of samples was made by using Perkin Elmer Jade DSC. The samples were heated at 10ºC /min rate from room temperature up to 200ºC under 50 cm^3/min nitrogen gas flow. Thermal gravimetric analysis of the samples was made using Mettler Star SW 8.10 thermal gravimetric analyzer. 70 µdm^3 open cap-alumina crucibles were used for experiments. Samples were heated at 10ºC/min rate from 25ºC to 650ºC under 50 cm^3 min^{-1} N_2 gas flow, at 20ºCmin^{-1} rate from 650ºC to 1000ºC in 50 cm^3 min^{-1} air flow and kept at 1000ºC for 5 minutes in 50 cm^3 min^{-1} air flow.

Perkin Elmer 25 UV-Vis spectrophotometer was used in obtaining visible spectrum of the samples in transmission and reflection modes. The inside and outside surfaces of the films were examined in reflection mode. The effect of the exposed surface first to light was investigated in transmission mode.

Stress-strain measurements of the samples cut from the side surface of the containers were performed on a tensile test machine (Shimadzu AGS-J) equipped with a 5 kN load cell. The cross-head speed used was of 5 mm min^{-1}. The width of the test sample was 5.0 mm and gauge length was 50 mm.

3. RESULTS AND DISCUSSION

The two samples container 1 and container 2 examined in the present study carried the symbols 5 and 6 indicating they were basically polypropylene and polystyrene respectively.

3.1 Functional Groups by FTIR Analysis

The FTIR spectrum of Container 1 in Figure 2 displays the bands assigned to different stretching vibrations of the methyl and methylene groups. In the 3800–2700 cm^{-1} four prominent bands at 2959, 2920, 2873, and 2839 cm^{-1} assigned to asymmetric and symmetric stretching vibrations of methyl and methylene groups respectively are observed. The bands at 1458 and 1377 cm^{-1} are assigned to CH_3 asymmetric and symmetric bending vibrations. The peak at 1362 cm^{-1} belonged to CH bending and CH_2 wagging vibrations. Other important bands are located at 1166 and 1044 $cm^{-1}$are assigned to C-C chain stretching vibration, 998 cm^{-1} is assigned to CH_3 rocking, CH_2 wagging and CH bending vibrations, 973 and 941 cm^{-1} are assigned to CH_3 rocking and C-C chain symmetric stretching vibration, 899 cm^{-1} is assigned to C-C chain symmetric stretching vibration , 841 cm^{-1} is assigned to CH_2 rocking and C-CH_3 stretching vibrations and 809 cm^{-1} is assigned to C-C chain symmetric stretching vibration and CH_2 rocking vibration [6-7]. Thus, FTIR spectrum of Container 1 confirmed that it was mainly made of polypropylene.

Additionally, the peaks at 1460 and 712 cm^{-1} indicated the existence of calcium carbonate ($CaCO_3$) in container 1, because these peaks are the characteristic peaks of the $CaCO_3$ [8].

The FTIR spectrum of Container 2, which is seen in Figure 2, had characteristic peaks of polystyrene [9] as expected. The peaks at 3025 and 2850 cm^{-1} are due to aromatic and aliphatic C-H stretching vibrations respectively. The peaks at 1492 and 1452 cm^{-1} are assigned to the aromatic ring stretching vibrations. Besides, the unique peaks at 1601 and 1580 cm^{-1} are caused by the aromatic C=C stretching vibration. The C-H deformation vibration band of benzene ring hydrogen's (5 adjacent hydrogen's) appeared at 758 cm^{-1}. Ring deformation vibration was observed at 698cm^{-1} [10].

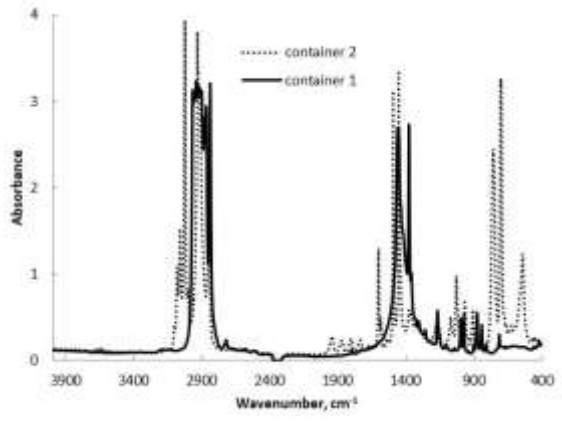

Figure 2. FTIR transmission spectra of container 1 and container 2

The presence of polybutadiene in polystyrene could not be detected by FTIR spectroscopy since both polystyrene and polybutadiene have similar functional groups. The FTIR and Raman peaks of the cis and trans polybutadiene was investigated by Nallasamy et al. [11] and they coincided with the FTIR peaks present in polystyrene. Further studies with composites prepared from polystyrene and polybutadiene is necessary to make a quantitative analysis.

3.2. X-Ray Diffraction Analysis of Samples

The x-ray diffraction diagram of container 1 is shown in Figure 3 . The first six XRD peaks observed at 2θ values of 14.2°, 17.1°, 18.7°, 21.2°, 22°, and 25.6° are the well-known "fingerprint" of α-phase isotactic propylene (JCPDS 50-2397), which are also consistent with the XRD results in the literature carried out by Wang et al.[12], Obadal et al.[13] and Ulku et al.[14]. When these results are compared to the reference data of alpha phase polypropylene, it can be said that container 1 mainly consist of α-phase isotactic propylene. The peaks observed at 27.6°, 36.2°, 39.4° in x-ray diffraction diagram of container 1 in Figure 3 indicated the presence of rutile titanium dioxide (JCPDS file number of 04-0551). The peaks 29.4°, 31.6°, 36°, and 39.4° indicated the presence of calcium carbonate in calcite form with JCPDS 83-0578 [15].

The x-ray diffraction diagram of Container 2 is shown in Figure 3 also. The broad peak in the range of 14° and 24° (maximum at around 19°) indicate the existence of polystyrene. These obtained peaks are consistent with the data stated for polystyrene in Alsharaeh et al [16], Wu et al.[17] and also Hu et al.[18]. The peak at 27.4° for container 2 shows the presence of rutile titanium dioxide (JCPDS file number of 04-0551), and the peaks at 29.4°, 31.6o and 39.4° strongly fit to that of calcite (JCPDS 83-0578). The sharp peaks at 2θ values of 20° and 28.5°, fit well to the olivine group-$Mg_2(SiO_4)$ JCPDS 87-2039[19].

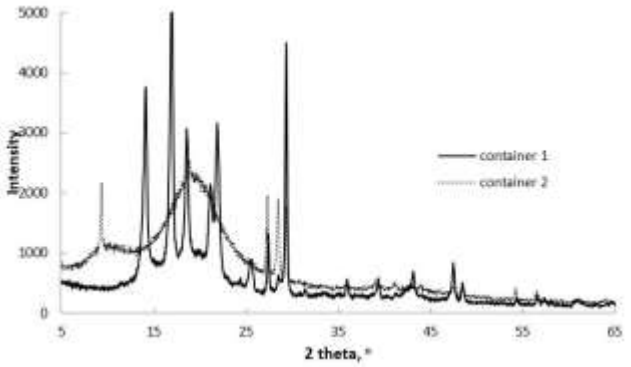

Figure 3. X ray diffraction diagrams of container 1 and container 2

3.3. Morphology of scissor cut surfaces

The SEM micrographs of cross sections of container 1 and 2 are shown in Figure 4. As shown in Figure 4a and 4b, their thicknesses are 275.1 µm and 256.5 µm, respectively. When the scissor cut surfaces were examined closely in 100 000 x magnification the presence of solid particles are clearly seen. Container 1 in Figure 4c had more particles than container 2 in Figure 2d. These particles could be TiO_2 and calcite as their presence were indicated by X-ray diffraction. Additionally olivine particles could be seen in container 2.

3.4. EDX Analysis of the Particle Surfaces in Cross Sections and Cross sections

The surface of the particles was analyzed by EDX for elemental composition. The hydrogen free composition of the surface of the particles is reported in Table 1. The particles contained mainly C, Ca and Ti in both container 1 and container 2 confirming the presence of calcite and titania. The Container 2 had a minor quantities of magnesium and silicon confirming the presence of olivine (Mg_2SiO_4).

Distribution of elements in an area in the cross sections of containers 1 and 2 are shown in Figure 5a and 5b respectively. Ca element which is shown by green color for container 1 is present in the particles only. Ca element shown by fucia color for Container 2 is also present only in particles which are few in number. Distribution of C element which is shown by red color for both samples were different for container 1 and container 2. While the surface of the particles were partially covered by C element in container 1, C was present as a continuous matrix in container 2. Ti element represented by blue color in container 1 and green color in container 2. Ti element was scarcer in container 1 and more abundant in container 2.

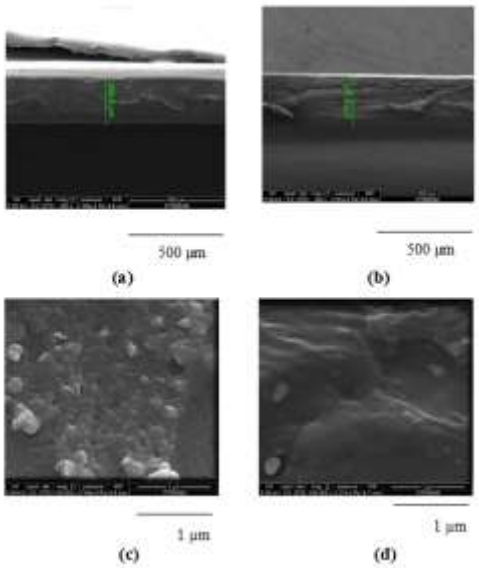

Figure 4. SEM micrographs of the crossections of Container 1 at a. 250x c. 100 000x , Container 2 b. at 250x d. 100 000x magnification

TABLE 1.

ELEMENTEL COMPOSITIONS IN MASS % OF POINTS ON THE PARTICLES ON THE SCISSOR CUT SURFACES

Elem	Container 1			Container 2				
ent	P 1	P 2	P 3	P 1	P 2	P 3	P 4	P 5
C	71.7	11.3	11.7	92.4	94.8	65.4	64.0	54.4
O	-	-	-	6.82	4.65	19.1	20.8	32.2
Si		-	-	0.05	-	-	-	0.33
Mg	0.20	-	-	-	-	0.13	0.13	0.21
Ca	26.9	88.7	88.3	0.47	0.19	15.4	14.9	12.5
Ti	1.15	-	-	0.22	0.36	-	0.11	0.29

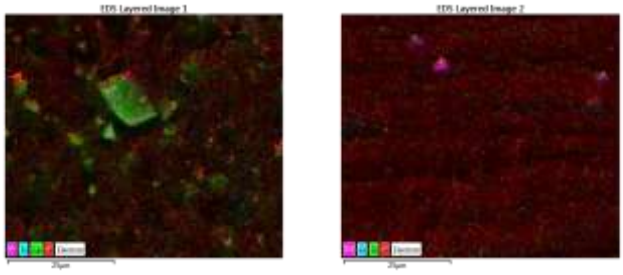

(a) **(b)**

Figure 5. Element distribution in an area in crossections of a. container 1, b. container 2

3.5. Atomic Force Microscopy

Atomic Force Microscopy was used to examine the surface topography of yogurt containers by using contact mode.

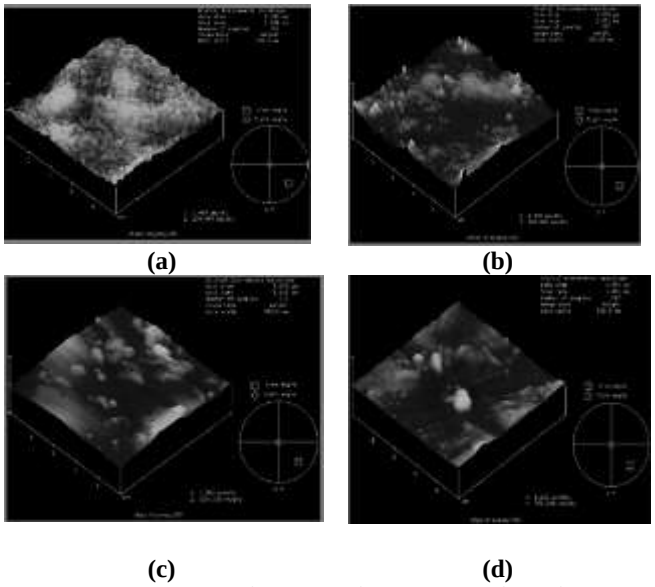

(a) **(b)** **(c)** **(d)**

Figure 6. AFM 3D images of a. outer surface, b. inner surface of container 1, c. outer and d. inner surface of container 2 at scanning range of 5 µm

The AFM three dimensional (3D) images of the outer and inner surfaces of containers 1 and 2 are seen in Figure 6. The darker and lighter parts in the images are the lower and higher parts of the surfaces respectively. The outer surface of container 1 in Figure 6a consisted of many spherical particles. However, the inner surface seemed to be smoother with less number of particles. These particles could be either the filler particles coated with the polymer phase or the spherulites formed during crystallization of polypropylene phase. The outer surface of container 2 had smaller number of particles compared to that of container 1. Container 2 is mainly polystyrene. However, it could have a second dispersed phase of a second polymer such as polybutadiene to improve its impact resistance. Thus, these particles could be polymer coated filler particles or dispersed phase of the second polymer. Arithmetic-mean surface roughness, Ra, root-mean-square surface roughness, R_q; and maximum peaks height, R_{max} values of the surfaces are reported in Table 2. The outer and inner surfaces had close R_q values (9.8 nm and 10.3 nm respectively) for container 1. Container 2 surfaces had higher R_q values than that of container 1, 20.4 and 19.4 nm for outer and inner surfaces respectively. Funke et al. [20] studied the polystyrene/polypropylene mixture droplets surfaces by atomic force microscopy. They showed that the surface of the droplets were covered with α isotactic polypropylene with characteristic crosshatched lamellar structure both for mixtures of 50/50 and 95/05 Polystyrene/Polypropylene blends. However, in the container 1 these crosshatched structures were not observed.

TABLE 2

AFM SURFACE CHARACTERISTICS OF OUTER AND INNER SURFACES OF CONTAINER 1 AND CONTAINER 2 IN 5 MM SCALE.

Sample	Surface	R_a, nm	R_q, nm	R_{max}, nm
Container 1	Outer	7.2	9.8	188.3
Container 1	Inner	8.1	10.3	77.1
Container 2	Outer	15.5	20.4	175.8
Container 2	Inner	13.8	19.4	20.3

3.6. Thermal Analysis

The DSC and TG curves of the containers are shown in Figure 7 and the thermal properties determined from the curves are reported in Table 3a and Table 3b. The DSC curves in Figure 7a indicated that container 1 had melting temperature (T_m) of 166.6ºC and The container 2 did not have a melting peak and had only glass transition temperature (T_g) of 99.9 ºC. DSC analysis also confirmed that container 1 had the melting temperature of

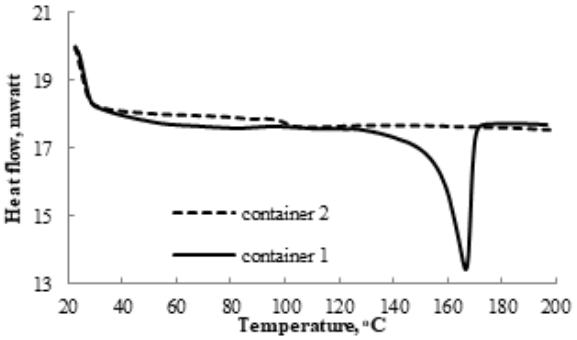

(a)

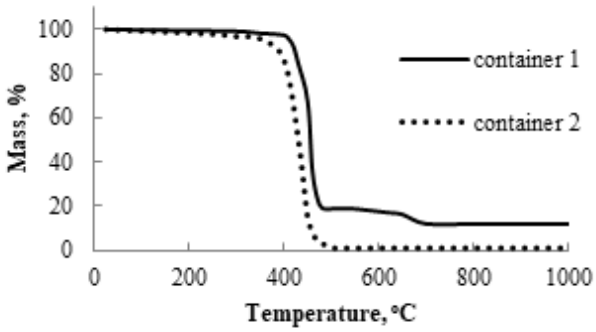

(b)

Figure 7. a.DSC, b. TG curves of container 1 and container 2

polypropylene [8] and container 2 had the glass transition temperature of polystyrene[21]. The heat of melting of container 1 was determined as 74.7 J g^{-1} from the area of the melting curve of container 1 in Figure 7a. The TG curves of the samples in Figure 7b indicated that the onset temperature (T_{onset}) of thermal degradation was 400ºC and 250ºC for container 1 and container 2 respectively.

The degradation of container 1 had two steps. Container 1 lost 80.7 % mass up to 505ºC in the first step corresponding to degradation of the polypropylene phase. The remaining mass at 505ºC is due to presence of inorganic fillers in the sample. The second step in TG curve of container 1 started at 505ºC and end at 719oC with 7.97 % mass loss, which is due to decomposition of the $CaCO_3$ filler to CO_2 and CaO according to Equation 1 [8].

$$CaCO_3(s) \rightarrow CaO(s) + CO_2(g) \quad (1)$$

Container 1 should have 18.1 % in mass of $CaCO_3$ as calculated from the mass % of CO2 evolved. The total ash at 1000ºC, 11.3% is due to CaO from $CaCO_3$ decomposition and TiO_2 present in the sample. Thus, there is 1.2 % TiO_2 in the Container 1. In Table 4, the

composition of Container 1 is reported.

TG curve of Container 2 in Figure 7b had only one step. The mass loss up to 505ºC, 98.1% should be due to decomposition of polystyrene. The mass loss from 505ºC up to 1000ºC did not have a step change. Thus, the remaining mass at 1000ºC, 1.9 % should be due to presence of inorganic additives such as calcite, olivine and TiO_2 as x-ray diffraction and EDX analysis indicated. The presence of $CaCO_3$ in Container 2 was very low and could not be detected by TG analysis even if its presence was indicated by x-ray diffraction and EDX analysis. Table 4 also reports the composition of the container 2.

Table 3.a

TG PROPERTIES OF CONTAINER 1 AND CONTAINER 2

Sample	T_{onset}, ºC	T_{max}, ºC	Mass % at		
			505ºC	719ºC	1000ºC
Container 1	400	458	20.3	12.33	11.3
Container 2	250	539	1.9	1.9	1.9

Table 3.b

DSC PROPERTIES OF CONTAINER 1 AND CONTAINER 2

Sample	T_m,ºC	T_g,ºC	ΔH_m,J g^{-1}
Container 1	166.6	Lower than room temperature	74.7
Container 2	Does not melt	99.3	-

DSC evaluation can be used to measure amount of crystallinity in a crystalline polymer sample. Crystallinity is indication of amount of crystalline

Table 4.

THE COMPOSITION (% IN WEIGHT) OF CONTAINER 1 AND CONTAINER 2 BY TG ANALYSIS

	Container 1	Container 2
Polypropylene	80.7	0
Polystyrene	0	98.1
$CaCO_3$	18.1	-
TiO_2	1.2	-
$CaCO_3$+TiO_2+olivine		1.9

region in polymer with respect to amorphous content. High crystallinity leads to increase in hardness, strength, wear resistance. Low crystallinity causes good processability, better transparency in polymers. The degrees of crystallinity (%) of the sample from DSC melting peak was determined as follows. The percentage of crystallinity (X_c) was calculated from the melting enthalpy (ΔH_m) using Equation 2.

$$Xc(\%) = {}^{\Delta Hm}/_{w\Delta Hf}\ x100 \qquad (2)$$

where ΔH_m is the melting enthalpy of the samples (J g^{-1}) and ΔH_f is the heat of the fusion of polypropylene at 100% crystallinity, corresponding to 207 J $g^{-1}$and w is the weight fraction of polypropylene in the sample [8]. The crystallinity of polypropylene in Container 1 was found as 44 % from Equation 2.

3.7. Optical Properties

The polypropylene and polystyrene are polymers, which are transparent to light. However, the fillers and pigments in the yogurt containers make them nontransparent. In both samples, calcite and titania were present and additionally olivine was present in container 2. It was shown that nano calcite assists better dispersion of TiO_2 particles in polypropylene [22]. The light transmission at 680 nm from both containers is very low as seen in Figure 8a, while container 2 transmits only 0.19%, container 1 transmits 0.16 % of light. The yogurt inside both containers was protected from the harmful effects of light. The container 2 and container 1 reflected 72 % and 78% of light at 680 nm respectively. In 400-420 nm region, the reflection increased from 45 % to 81% and 84 % for container 2 and container 1 respectively. The containers do not transmit light but reflect all the visible light making them to appear as white colored. However, the PS-grafted-TiO_2–PS hybrid films at 0.20 and 0.52 wt % showed high transmittance in the visible light region accompanied by ultraviolet absorption characteristic of TiO_2 due to the fine dispersion of nanoparticles in the PS matrix [23]. The Container 2 was not transparent in the visible region. This indicated that the TiO_2 particles were not nano sized.

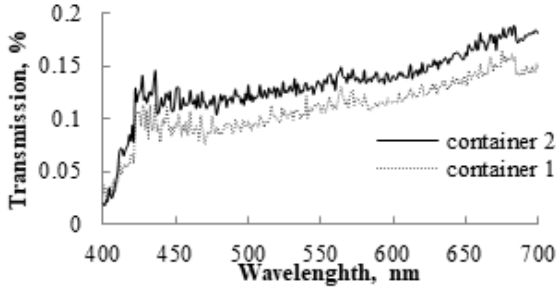

(a)

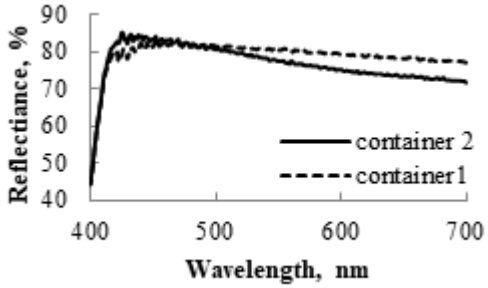

(b)

Figure 8.Visible spectra of container 1 and container 2 in a. transmission, b. reflection mode

3.8. Mechanical Properties

Representative stress-strain diagrams of container 1 and container 2 are seen in Figure 9 and the tensile properties are reported in Table 5. Average tensile strengths for container 1 and container 2 are 21.2 and 21.9 MPa, respectively. Also, their average elastic modulus values are 2870 and 2829 MPa, respectively. The examination of the samples with other methods such as FTIR, XRD, SEM and EDX indicated that $CaCO_3$ and TiO_2 were used as fillers or

pigments and as a main polymer matrix polypropylene for Container 1, and high impact polystyrene for Container 2 was used. The yield strength for pure polypropylene is between 31 and 37 MPa whereas it is around 28 MPa and higher HIPS [24]. A sharp yield point was not observed for container 1. The point at which the stress strain diagram started to deviate from the linearity was taken as the yield point. The yield strength was 14.9 MPa and 14.2 MPa for container 1 and container 2 respectively. Both of these results are lower than the values of their pure polymers. Therefore, it can be sad that these results are consistent with the findings of Zuiderduin et al.[25] and Parparita et al. [6] since the solid inorganic particles were used as fillers, the tensile strength for both samples are lower than that of the pure polymers. This can be because of the debonding of the filler particles from the polymer matrix, which do not contribute to the yield stress. Most probably, fillers lead to the weak interfacial interactions between the filler and the polymer matrix, which decreased the strength.

Elastic Modulus for pure polypropylene is between 1.14 and 1.55 GPa, and for pure HIPS it is between 2 and 3.30 GPa. The modulus of elasticity of the the container 1 and container 2 (2.87 GPa and 2.82 GPa respectively) are higher than the modulus of elasticity of pure polymers. The fillers in container 1 and 2

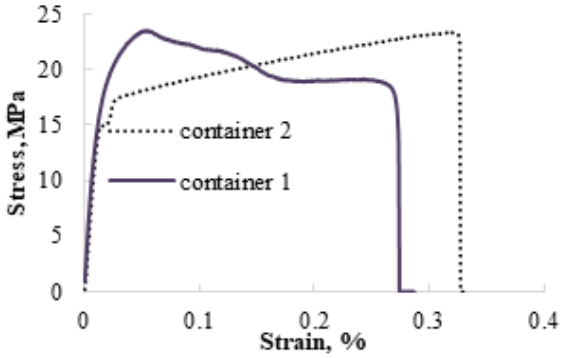

Figure 9. Representative stress-strain diagrams of container 1 and container 2

Table 5.

MECHANICAL PROPERTIES OF CONTAINER 1 AND CONTAINER 2

Property	container 1	container 2
Yield Stress, MPa	14.9±2.9	14.2±0.43
Yield strain	0.016±0.003	0.012±0.001
Elastic Modulus, MPa	2870±619	2829±122
Tensile stress, MPa	21.2±2.6	21.9±1.4
Tensile strain, %	0.19±0.08	

caused stiffening of the materials increasing the modulus of elasticity similar to the studies of Zuiderduin et al. [25], Parparita et al.[6] and Zhang et al [15].

The fracture surfaces SEM micrographs of container 1 and container 2 are shown in Figure 10. While Container 1 shows a fibrillary structure due to orientation of crystallites in polypropylene phase during the drawing of the Container 1, The Fracture of Container 2seemed to be brittle as expected from the amorphous nature of polystyrene. Indeed the Container 2 has longer elongation at break value (0.30%) than that of Container 1 (0.18%).

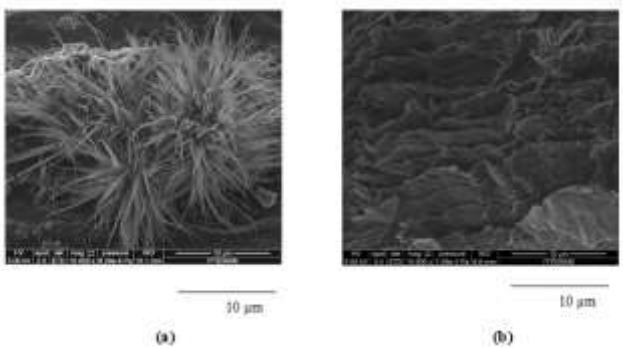

Figure 10. SEM micrograph of the fracture surfaces after tensile tests a. container 1, b. container 2 at 10 000x magnification

4. CONCLUSION

The two yogurt containers selected with plastic codes 5 (polypropylene) and 6(polystyrene) were characterized in the present study. FTIR spectra of the samples indicated the presence of polypropylene and calcium carbonate in container 1 and polystyrene in container 2. X ray diffraction diagram of container 1 indicated that it mainly consisted of alpha phase isotactic polypropylene with the evidence of characteristic well-known fingerprints at 2θ values of 14.2°, 17.1°, 18.7°, 21.2°, 22°, and 25.6°. In addition to this, it was demonstrated that calcite and rutile titanium oxide were used as fillers represented with the peaks at 29.4° and 27.6° respectively. Unlike container 1, container 2 was mainly formed by high impact polystyrene with a peak in a wide range of 14° and 24°, and calcite at 2θ 29.4°, olivine group (Mg_2SiO_4) at at 2θ 28.5°, and also again rutile titanium dioxide at at 2θ 27.4° were also present. The presence of particles in SEM micrographs of fracture surfaces confirmed the existance of additives, which could be titanium dioxide and calcium carbonate in the samples. The EDX analysis of the particles in crossections indicated the presence of C, Ca, Ti, O in both samples and addionally presence of Mg element in container 2. The addition of TiO_2 was used in packaging materials as pigments in order to improve the appearance of the package and to provide some barrier to light. The containers did not transmit light but reflected all the visible light making them to appear as white colored. The surface roughness values of the front and back sides of container 1 were found as 8.12 nm and 7.17 nm respectively for 5µm scanning range. On the other hand, the surface roughness values of the front and back sides of Container 2 were found as 13.84 nm and 15.47 nm respectively for 5µm scanning range. From these values, it could be said that container 2's surface was rougher than that of container 1's . The melting point of container 1 was 166.4ºC and the glass transition point of container 2 was 99.9ºC confirming they were based on polypropylene and polystyrene. . The container 1 which had 18.1 % CaCO3 , 1.2% TiO_2 and container 2 which was based had 1.2 % TiO_2, $CaCO_3$ and olivine as indicated by TG analysis. The samples had close values of tensile strength and tensile modulus. The container 2 has longer elongation at break value (0.30%) than that of container 1 (0.18%).The presence of fillers made the containers had lower tensile strength and higher stiffness than their base polymers..

The two yogurt containers were characterized in terms of the type of the polymers, the fillers, thermal properties such as the melting point or the glass transition point, the onset temperature of thermal degradation, surface roughness and

mechanical properties. This information could be used determining the future recycling methods for yogurt packing materials. The containers labeled 5 and 6 should be collected separately from the source since they will have different processes for reuse.

ACKNOWLEDGEMENTS

The authors thanks to Izmir Institute of Technology forsupporting this project The authors acknowledge the contributions made to experimental work of this study by Ece Namli Gözükara, Sema Kirkose Beyaznar, Canbike Bar Tamcı, Emre Demirkaya and Okay Germen.

REFERENCES

[1] K. Mars ,B. Bugusu, "Food Packaging-Roles, Materials and Environmental Issues" J. Food Sci., vol. 72, no. 3, pp 39-55, Apr.2007.

[2] A. Saint Eve, C. Levy, M. L. Moigne, V. Ducruet and I Souchon" Quality Changes in Yogurt during storage in different packing matrials," Food Chem., vol. 110, No.2, pp 285-293, sep 208.

[3] P. Muniandy, A. B. Shori, A. S. Baba, " Influence of green, white and black tea addition on the antioxidant activity of probiotic yogurt during refrigerated storage." Food Packaging and Shelf Life, vol. 8, no 1, pp 1-8, Jun. 2016.

[4] M.G. Sajilata, K. Savitha, R.S. Singhal, V.R. Kanetkar, "Scalping of flavors in packaged foods." Comprehensive Reviews in Food Science and Food Safety, vol.6, no 1, pp 17–35 ,jan. 2007.

[5] R. Coles, D. McDowell, M.J. Kirwan, Food Packaging Technolog, Oxford, UK: Blackwell Publishing Ltd., 2003.

[6] E. Părpăriţă, R. N. Darie, C. Popescu, M.. A. Uddin, C. Vasile."Structure-morphology-mechanicalproperties relationship of some polypropylene/lignocellulosic composites", Mater. Des.,vol.56, pp763-772, Apr. 2014.

[7] J. L., Dwyer, M. Zhou, "Polymer Characterization by Combined Chromatography-Infrared Spectroscopy." Int. J. Spectro., vol 2011, Article ID 694645, Dec. 2011. http://doi.org/10.1155/2011/694645

[8] Arkis, E.et.al. Characterization Of A Pearlescent Biaxially Oriented Multilayer Polypropylene Film. Chem. Chemical Techn., vol.91,no 1, pp. 77-84, Mar. 2015.

[9] Smith, C.B., Fundementals of Fourier Transform Infrared Spectroscopy, Florida, USA: Taylor & Francis Group, 2011.

[10] K Kaniappan, S.Latha, "Certain Investigations on the Formulation and Characterization of Polystyrene / Poly(methyl methacrylate) Blends." I. J.Chem Tech Res., vol 3, no2, pp7.Apr.2011.

[11] P. M Anbarasan,., S. Mohan "Vibrational spectra and assignments of cis- and trans-1,4-polybutadiene." Turk. J. Chem., vol 26, no 1, pp 105-111, 2002.

[12] M. Wang, et. al.,"Compression-rate dependence of solidified structure from melt in isotactic polypropylene." J. Phys. D: Appl. Phys., vol.46 ,no 14, pp 145307 , 2013.

[13] M.Obadal,R. Cermak, and S.Karel,"Tailoring of three-phase crystalline systems in isotactic poly(propylene)," Macromol Rapid Commun., vol. 26, no. 15, pp1253-1257, Aug. 2005

[14] S. Ulku, D. Balköse, E.Arkış and M. Sipahioğlu. "A study of chemical and physical changes during biaxially oriented polypropylene film production," J. Polym. Eng.Vol.23, no 6, pp 437-456, nov. 2003.

[15] Q. Zhang, Z. Yu, X. Xie and Y. Mai, "Crystallization and impact energy of polypropropylene/CaCO3 nanocomposites with nonionic modifier," Polym.,Vol. 45, No 17, pp5985-5994. Aug. 2004.

[16] E. Alsharaeh, A.A. Othman and M. Al-Dosar "Microwave Irradiation Effect on the Dispersion and Thermal Stability of RGO Nanosheets within a Polystyrene Matrix," Mater., Vol 7, No.7, pp 5212-5224, Jul. 2014.

[17] N. Wu, et al. "Synthesis of network reduced graphene oxide in polystyrene matrix by a two-step reduction method for superior conductivity of the composite," J. Mater. Chem.,vol. 22, no 33, pp 17254-17261, jun 2012.

[18] K. Hu, Z. Cui, Y. Yuan, Q. Zhuang, T. Wang, X. Liu and Z. Han "Synthesis, Structure, and Properties of High-Impact Polystyrene/Octavinyl Polyhedral Oligomeric Silsesquioxane Nanocomposites," Polym. Compos., Vol. 37, No. 4, pp1049-1055, 2016.

[19] J. Li and M. Hitch," Characterization of the microstructure of mechanically-activated olivine using X-ray diffraction pattern analysis." Miner. Eng.,Vol.86, pp24-33, 2016.

[20] Z. Funke, C.Schwinger, R. Adhikari and J. Kressler, "Surface tension in polymer blends of isotactic Poly(propylene) and atactic Polystyrene," Macromol. Mater. Eng., vol. 286, no 12, pp744-751. Dec. 2001.

[21] Gedde, U. W., Polymer Physics. London, UK: Chapman and Hall,1995.

[22] Z. Guo, et. al. "Assistant effect of nano-CaCO3 particles on the dispersion of TiO2 pigment in polypropylene composites, " J. Mater. Sci.,vol. 39, no. 8, pp2891 – 2893, Apr. 2004.

[23] Matsuno, R. et. al. Polystyrene-grafted titanium oxide nanoparticles prepared through surface initiated nitroxide-mediated radical polymerization and their application to polymer hybrid thin films, Soft Mater., Vol 2, No 5, pp415-421, Mar.2006 .

[24] Callister, W.D., Rethwisch, D.G. Materials Science and Engineering (8th ed,). New York, USA: John Wiley & Sons, Inc., 2011.

[25] W.C.J Zuiderduin, C. Westzaan, . Huétink,and R.J. Gaymans, "Toughening of polypropylene with calcium carbonate particles,"Polym., vol. 44, no. 1, pp 261-275, Jan 2003.

BIOGRAPHIES

Gizem Cihanoğlu received her BSc degrees in Chemical Engineering in 2010 from Yildiz Technical University. She got her MS and PhD degrees from Izmir Institute of Technology in 2014 and 2021, respectively. She worked as a research assistant in Chemical Engineering at Izmir Institute of Technology between 2013 and 2021. Now, she is doing a postdoc in Ebil's group in Chemical Engineering at Izmir Institute of Technology. Her research interests are the synthesis of nanomaterials for zinc electrodes, the development of polymers for gas diffusion layers in gas diffusion electrodes for metal-air batteries, and the evaluation of electrochemical performance gas diffusion electrodes.

Merve Özpirin had her BS and MS degree in chemical engineering from İzmir Institute of Technology in 2014 and 2016 respectively. She is continuing her studies for PhD degree in chemical engineering in the same university. She worked as TÜBİTAK 1001 project assistant in 2014-2016 in the same department . Her research interests are production of thin film coatings by cold vapor deposition, development of protective coatings for electro-optical systems, production of polymeric coatings and sensory technologies.

İklima Odabasi graduated from Bilecik Şeyh Edabali University as chemical and process engineering in 2013. She completed MS studies in 2017 in chemical engineering department of Izmir Institute of Technology. She worked as TÜBİTAK 1001 project assistant in 2014-2017 in the same department. She worked as process engineer in USCA winery in 2017-2019 and as process director since 2019. Her research areas are winemaking, viticulture, production style of winemaking, blending wine, filtration and stabilization for wine, tasting technique, the human factors in the winery that influence style, quality and price.

Devrim Balköse graduated from Middle East Technical University Chemical Engineering Department in 1969. She got her MS and PhD degrees from Ege University in 1974 and 1977 respectively. She worked as research assistant, assistant professor, associate professor and professor between 1970-2000 at Ege University. She was the head of Chemical Engineering Department at İzmir Institute of Technology between 2000 and 2009. She is a retired faculty member at the same department since 2013. Her research interests are in polymer reaction engineering, polymer foams and films, polymer additives and adsorbent development and adsorption

European Journal of Technique

journal homepage: https://dergipark.org.tr/en/pub/ejt

Vol.12, No.2, 2022

Experimental Investigation of the Variation of Power and Iron-Copper Losses in the Loaded Operation of the Transformer

Mehmet Ali Özçelik[1*], Ahmet Aycan[2]

[1*]Gaziantep University, Technical Science, Electrical and Energy Department, Gaziantep, Turkey. (e-mail: ozcelik@gantep.edu.tr).
[2]Gaziantep University, Technical Science, Electrical and Energy Department, Gaziantep, Turkey. (e-mail: aycan@gantep.edu.tr).

ARTICLE INFO

Received: October, 31.2022
Revised: December, 22.2022
Accepted: December, 26.2022

Keywords:
Transformers
Iron losses
Copper losses
Hysteresis losses

Corresponding author: *M.Ali Özçelik*

ISSN: *2536-5010* | e-ISSN: *2536-5134*

DOI: https://doi.org/10.36222/ejt.1196829

ABSTRACT

Transformers are one of the vital equipment widely used in the transmission, distribution, and power systems of electrical energy. An equivalent circuit can be created, and losses can be calculated according to various operating experiments of the transformer. In the study, the variation of iron losses according to the voltage values applied to the primary circuit of the transformer was examined, and a non-linear change in iron losses was observed depending on the applied voltage. When a load is connected to the transformer's secondary, it has been observed that as the load increases, the iron losses do not change and remain constant depending on the load. The copper losses at various loads were calculated by increasing the load connected to the secondary transformer. It has been shown with experimental studies and calculations that copper losses show a non-linear variation depending on the load.

1. INTRODUCTION

Although the demand for electrical energy is increasing day by day, the alternating current (AC) voltage level must be increased to transmit electrical energy effectively [1-2]. Power transformers have been used to raise and lower the electrical energy at constant power and constant frequency [3]. In the operation of transformers, electrical energy has been transferred between two or more circuits by electromagnetic induction [4-5]. Although there are no moving parts in transformers, losses occur in transformers like in all electrical machines [6]. Energy losses due to hysteresis and eddy currents in the transformer core are called iron losses, and energy losses due to resistance in the winding are called copper losses [7].

As long as the transformer is connected to the energy system, apart from the power that draws power from the system and the load draws, the current-carrying part (conductor) and the magnetic flux-forming part (iron core) are the power losses [8-9]. Although mathematical expressions have been developed to include hysteresis and eddy current losses in the calculations, the experimentally measured core losses are greater than the value obtained by the calculations [10]. It is accepted that while iron losses are directly proportional to the square of the voltage value, copper losses are proportional to the square of the winding current [11].

In this study, the load operation of the transformer was made experimentally, and the power change and the change of iron and copper losses in the ohmic and inductive loads were examined and commented on.

2. MATERIAL AND METHOD

2.1. Loaded circuit of transformer and experimental setup

In the AC operation of transformers, the primary and secondary windings have effective resistance (R) and inductive reactance (X_L). Using the conversion ratio (a) between the primary and secondary windings, the primary circuit can be drawn by converting it to secondary terms. In Figure 1, the connection circuit of the transformer is loaded operation is given. Variable AC is applied to the Tr transformer with a regulated autotransformer (variac), the mains frequency is 50 Hz. The idle power of the transformer meets the iron losses. Resistive and inductive loads are used at the transformer's secondary output.

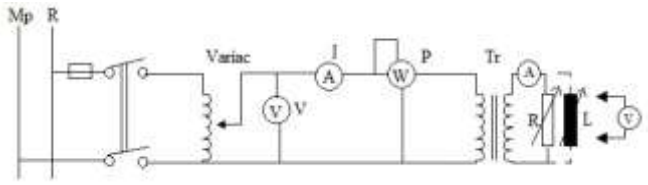

Figure 1. Loaded Operating Circuit of the Transformer

The experimental setup is shown in Figure 2. The power coefficient of the transformer was measured with a cosφ-meter. Incandescent lamps were used as ohmic load. The voltage applied to the transformer has been reduced by the autotransformer starting from high. The current drawn by the circuit at each voltage value, the power, and the power coefficient were measured and recorded in the tables.

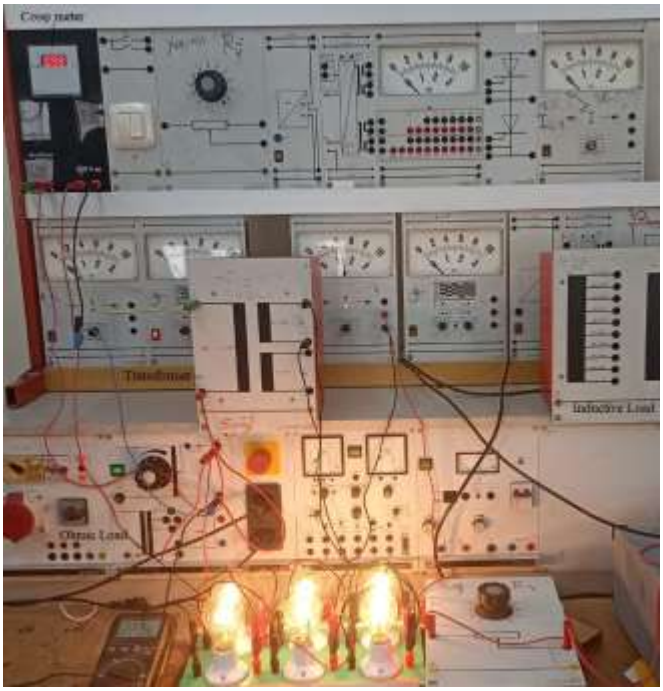

Figure 2. Experimental Setup

Core losses due to fuco-hysteresis losses are constant at all working loads. These losses are found by the no-load test of the transformer. Fuko losses are minimized by making the core from thin hair. Hysteresis losses are also reduced by adding silicon to the iron.

2.2. Values taken in the loaded operation of the transformer

The values in Table 1 were taken by loading a single-phase transformer with an ohmic load. The transformer is loaded up to 1.2 times the rated secondary current.

TABLE I
CURRENT VARIATION AT OHMIC LOAD

U_1 (V)	U_2 (V)	I_2 (A)
220	115	0 (idle)
220	114	0,215
220	113	0,430
220	112	0,650
220	111	1,22
220	110	1,45
220	109	1,65

The difference between the voltage values when the secondary voltage of the transformer is empty and loaded is called voltage regulation. Transformer voltage regulation, the rate of change of output terminal voltage of a transformer as a result of changes in connected load current is given below. Here, U20 is the no-load secondary voltage and U2 is the loaded secondary voltage.

$$\%Reg = \frac{U_{20}-U_2}{U_2}100 = \frac{115-110}{110}100 = \%4{,}5 \qquad (1)$$

Current and power changes in inductive load are given in Table 2.

TABLE II
CURRENT AND POWER VARIATION IN INDUCTIVE LOAD

U_1 (V)	P_{fe} (W)	Q_1 (VAR)	V_2(V)	I_2(A)	Load (Henry)
220	15	32	115,7	0	0
220	15	60	115,5	0,264	1,2
220	15	65	115,4	0,32	1
220	15	75	115,2	0,4	0,8
220	15	90	115,1	0,54	0,6
220	15	120	114,6	0,81	0,4
220	15	205	113	1,64	0,2

In inductive load, as the current value increased, the reactive power drawn from the grid increased significantly. This shows us that in the case of inductive load, the reactive component of the current drawn from the grid increases significantly. The inductance-reactive power change is seen in Figure 3.

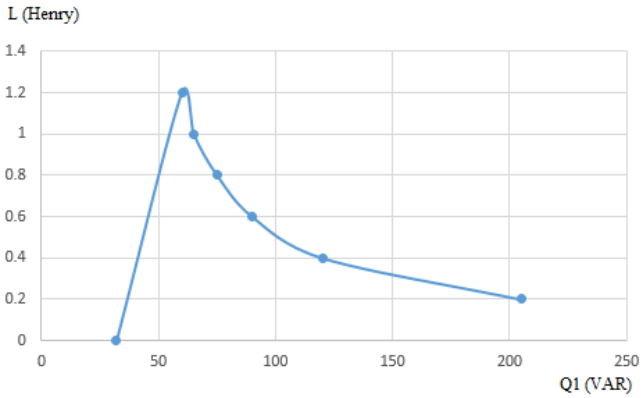

Figure 3. Inductance-Reactive Power Change

The regulation value in the inductive load shows a decreasing value according to the ohmic load.

$$\%Reg = \frac{U_{20}-U_2}{U_{20}}100 = \frac{115{,}7-113}{115{,}7} = \%2{,}33 \qquad (2)$$

The transformer is loaded 1.2 times the rated current. The transformer was loaded with an ohmic load of 1.2 times the rated current and the values in the table below were taken.

TABLE III
CURRENT AND REACTIVE POWER VALUES ACCORDING TO OHMIC LOAD

U_1 (V)	U_2 (V)	I_2 (A)	Q_1 (VAR)
220	115	0	25
220	114	0,215	25
220	113	0,43	25
220	112	0,65	24
220	110	1,45	21
220	109	1,65	20

 ISSN 2536-5010 | **e-ISSN** 2536-5134 https://dergipark.org.tr/en/pub/ejt

At the ohmic load, the reactive power drawn by the transformer from the grid did not change much. The variation of reactive power according to the ohmic load is given in Figure 4.

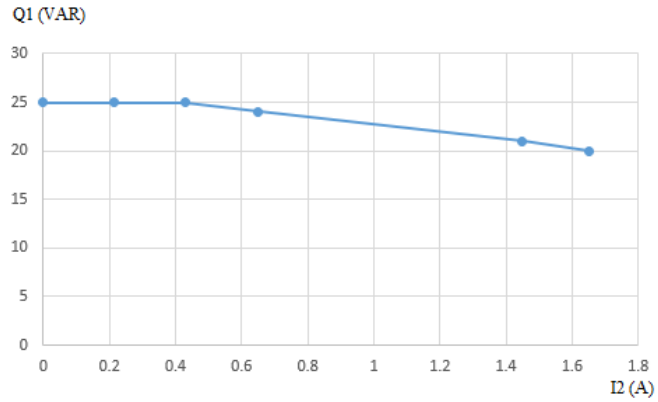

Figure 4. Variation of reactive power according to ohmic load

Copper losses are the losses caused by the currents passed in the Primary-Secondary windings. It occurs due to the winding resistances. They increase with the increase of the current passing through the windings. Copper losses P'cu occurring at various load values, including P_{TCU} total copper losses, have been given below.

$$P'_{cu} = P_{TCU}(\frac{I'_2}{I_2})^2=6,2(\frac{0,215}{1,65})^2=0,104\ W \qquad (3)$$

The finding of copper losses at any load and the change values of copper losses according to the load is given in Table 4.

TABLE IV
VARIATION VALUES OF COPPER LOSSES ACCORDING TO LOAD

P_{TCU} (W)	I_2 (A)	I_2' (A)	P'cu (W)
6,2	1,65	0,215	0,104
6,2	1,65	0,43	0,419
6,2	1,65	0,65	0,957
6,2	1,65	1,45	4,77
6,2	1,65	1,65	6,2

The variation of copper losses according to the load is shown in Figure 5.

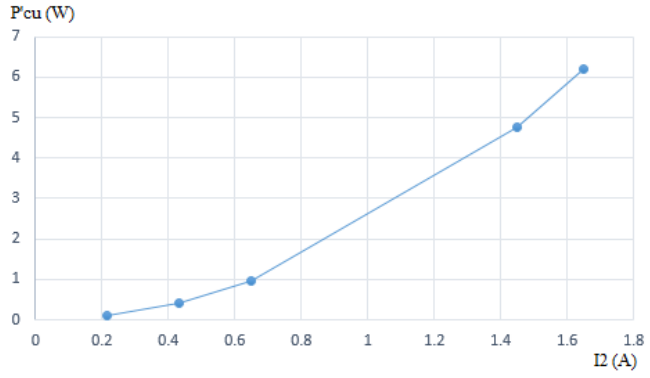

Figure 5. Variation of copper losses with load

As seen in Figure 5, it is seen transformer copper losses increase as the load increases.The variation of iron losses depending on the voltage at idle and the iron loss at any voltage are given in the expression in (4).

$$P'_b = (\frac{U'_1}{U_1})^2P_b= (\frac{30}{220})^2 16=0,295\ W \qquad (4)$$

TABLE V
VARIATION VALUES OF STRESS-DEPENDENT IRON LOSSES

U_1(V)	U_1'(V)	P_b (W)	P_b' (W)
220	30	16	0,295
220	70	16	1,617
220	150	16	7,42
220	190	16	11,87
220	220	16	16

The variation of the voltage-related iron losses can be seen in Figure 6.

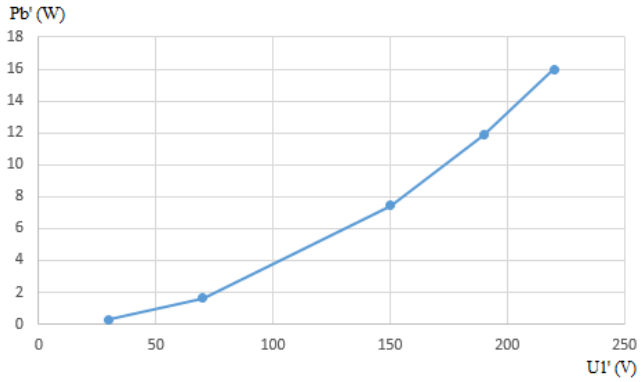

Figure 6. Variation of voltage-related iron losses

In Figure 6, it is seen that as the voltage applied to the transformer increases, the iron losses increase, that is, the iron loss increases depending on the voltage and the change is not linear. The variation of the power factor according to the current drawn by the ohmic load is shown in Table 6 and Fig.7

TABLE VI
VARIATION OF THE POWER FACTOR ACCORDING TO THE CURRENT DRAWN BY THE OHMIC LOAD

Cosφ meter	I_2 (mA)
0.22	0
0.78	285
0.91	540
0.97	790
0.98	1010

The power factor increases when the transformer is loaded. Since the energy component of the current drawn in its no-load operation is small, the reactive component is large, the power coefficient cosα will be low in the no-load condition.

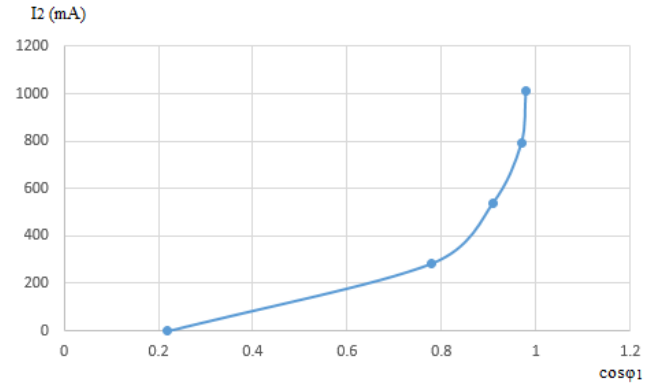

Figure 7. Variation of the power factor according to the current drawn by the ohmic load

The variation of the power factor according to the current drawn by the ohmic load is shown in Table 6 and Figure 7.

Variation values of the power factor according to inductive load have been given in Table 7.

In the inductive case, it is observed that the power coefficient Cosφ1 remains constant as the load current I_2 increases.

Variation of power factor according to inductive load

TABLE VII
VARIATION VALUES OF STRESS-DEPENDENT IRON LOSSES

Cosφ1	I_2 (mA)	L (Henry)
0.16	125	2.4
0.16	255	1
0.16	380	0.8
0.16	520	0.6
0.16	790	0.4

The variation of the power factor according to the inductive load is seen in Figure 8.

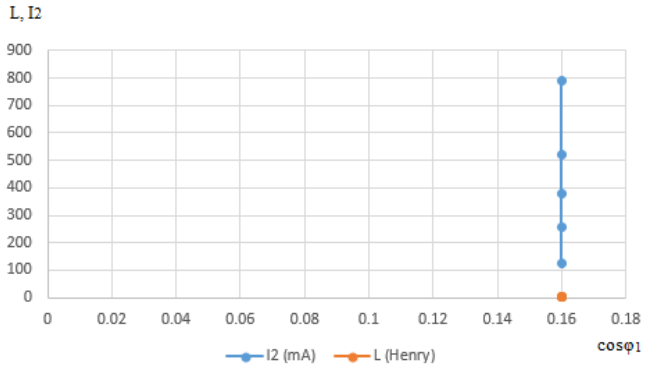

Figure 8. Change of power factor according to inductive load

In Figure 8, it is seen that the inductance load current does not change the power factor.

3. CONCLUSION

In this study, the iron losses from the unloaded test of the transformer and the copper losses in the loaded operation were found experimentally according to various load values. Copper losses and iron losses were also calculated, and it was determined that the occurring iron losses showed a non-linear increase according to the applied voltage. It has been observed that the reactive power drawn from the grid remains almost constant as the load current increases, while the power coefficient increases as the load increase at the ohmic load. In inductive load, as the load current increased, the reactive power drawn from the grid increased significantly. In inductive load, it has been observed that the power coefficient remains constant as the load current increases. It was observed that the reactive power drawn from the grid remained almost endless as the load current increased at no-load and ohmic load, while the power coefficient increased as the load increased at the ohmic load. In inductive load, as the load current increased, the reactive power drawn from the grid increased significantly. In inductive load, it has been observed that the power coefficient remains constant as the load current increases.

REFERENCES

[1] M. Yılmaz , "Real Measure of a Transmission Line Data with Load Fore-cast Model for The Future", Balkan Journal of Electrical and Computer Engineering, c. 6, sayı. 2, ss. 141-145, Nis. 2018, doi:10.17694/bajece.419646

[2] T. Demirdelen , "Kuru Tip Transformatör Optimizasyonuna Yeni Bir Yaklaşım: Ateş Böceği Algoritması", Çukurova Üniversitesi Mühendislik-Mimarlık Fakültesi Dergisi, c. 33, sayı. 1, ss. 87-96, Mar. 2018, doi:10.21605/cukurovaummfd.420675

[3] A. Altıntaş , "Üç Fazlı Transformatör Tasarımı İçin Bir Arayüz Programı", Afyon Kocatepe Üniversitesi Fen Ve Mühendislik Bilimleri Dergisi, c. 8, sayı. 2, ss. 37-45, Ara. 2008

[4] Özden, S. , Sırav Aral, B. , Canseven Kurşun, A. G. & Seyhan, N. (2020). Measurement and Risk Assessment of Extremely Low Frequency Magnetic Fields around Transformers in a Working Place . Erzincan University Journal of Science and Technology , 13 (2) , 857-867 . DOI: 10.18185/erzifbed.637570

[5] Özçelik, M. A. & Aycan, A. (2017). Manyetik Olarak Etkileşen Bobinlerin Alternatif ve Doğru Akımda İncelenmesi . Kahramanmaraş Sütçü İmam Üniversitesi Mühendislik Bilimleri Dergisi , 20 (4) , 172-180 . DOI: 10.17780/ksujes.356588

[6] D. Aşkın , İ. İskender ve A. Mamızadeh , "Farkli Yapay Sinir Ağlari Yöntemlerini Kullanarak Kuru Tip Transformatör Sargisinin Termal Analizi", Gazi Üniversitesi Mühendislik Mimarlık Fakültesi Dergisi, c. 26, sayı. 4, ss. 0, Şub. 2013

[7] G. Kaymaz, Ö. , Kalkan, G. , Başaran, T. & Erek, A. (2015). Bir Dilim Transformatör Radyatöründe Akiş Ve Isi Transferinin Farkli Yağ Tipleri Kullanilarak İncelenmesi . Mühendis ve Makina , 56 (666) , 53-63 https://dergipark.org.tr/tr/pub/muhendismakina/issue/54330/736101

[8] N. A. Karademir ve M. K. Eker , "Transformatör T-Bağlantı Yapısının Çekirdek Kayıplarına Etkisi", Politeknik Dergisi, c. 19, sayı. 4, ss. 389-397, Ara. 2016

[9] Georgilakis P.S., “Spotlight on modern transformer design”, Springer, London (2009).

[10] Kulkarni S.V., Khaparde S.A., “Transformer Engineering Design, Tecnology, and Diagnostics”, CRC Press, (2013).

[11] H. Dirik ve C. Gezegin , "Yük Altında Çalışan Tek-Fazlı Transformatörlerin Demir ve Bakır Kayıplarının İzlenmesi", Düzce Üniversitesi Bilim ve Teknoloji Dergisi, c. 7, sayı. 3, ss. 2116-2127, Tem. 2019, doi:10.29130/dubited.551316

BIOGRAPHIES

Mehmet Ali Özçelik received B.S., M.S., and PhD Degrees in Electrical Education/Electrical and Electronics Engineering from Marmara University/Harran University, Istanbul/Şanlıurfa and Electrical & Electronics Engineering, Kahramanmaras Sutcu Imam University, Turkey, in 1999, 2006, and 2015 respectively. He has been in Center for Future Energy Systems at the Rensselaer Polytechnic Institute, New York as a visiting/post-doc researcher from 2018 to 2020. He is currently an Assoc.Prof.Dr at the Department of Electric and Energy, Gaziantep University, Turkey. His field of interest includes PV systems, Microgrids and Smart lighting systems. He is an IEEE Senior Member.

Ahmet Aycan received B.S., and M.S. degrees in Electrical Education from Gazi University, Ankara, Türkiye, in 1990 and 1996, respectively. He is currently an Instructor at the department of Electric and Energy, Gaziantep University, Turkey. His field of interest includes Power Electronics and Electrical Machines.

European Journal of Technique

journal homepage: https://dergipark.org.tr/en/pub/ejt

Vol.12, No.2, 2022

Energy and Exergy Analysis of Hydrogen Production on Co-Gasification of Municipal Solid Waste and Coal

Abdulkadir Kocer[1*], Ercument Aksoy[2], Ismet Faruk Yaka[3] and Afsin Gungor[4]

[1*]Vocational School of Technical Sciences, Akdeniz University, 07070, Antalya, Turkey. (e-mail: akocer@akdeniz.edu.tr).
[2] Vocational School of Technical Sciences, Akdeniz University, 07070, Antalya, Turkey. (e-mail: ercumentaksoy@akdeniz.edu.tr).
[3] Department of Mechanical Engineering, Akdeniz University, 07070, Antalya, Turkey. (e-mail: ismetfarukyaka@hotmail.com).
[4] Department of Mechanical Engineering, Akdeniz University, 07070, Antalya, Turkey. (e-mail: afsingungor@hotmail.com).

ARTICLE INFO

Received: Feb., 09. 2022
Revised: Dec., 09. 2022
Accepted: Dec, 27. 2022

Keywords:
Hydrogen production
Co-gasification
Municipal solid waste
Energy
Exergy

Corresponding author: *Abdulkadir KOCER*

ISSN: *2536-5010* | e-ISSN: *2536-5134*

DOI: https://doi.org/10.36222/ejt.1070804

ABSTRACT

Hydrogen energy is considered one of the cleanest sources of energy due to its high efficiency. The only combustion product of hydrogen is water. Gasification can be used for the conversion of wastes into other fuels, and it presents an engaging renewable replacement for fossil fuels. This study aims to produce hydrogen as a result of the co-gasification of municipal solid waste (MSW) with coal to generate energy during its disposal. The importance of the system has been emphasized by making energy and exergy analyses. Gasification performance and the importance of hydrogen production of municipal solid blended with coal at different ratios (10%, 30%, 50%, 70%, and 90%) were also determined. A numerical model was developed for the co-gasification system. At the end of the study, a reduction in HHV can be seen as the coal concentration is increased. Also, with an increase in coal content of the MSW, it was found that the exergy values in syngas composition decreased. This study implies that gasification can be used for the evaluation of coal with the disposal of MSW and conversion of these wastes into energy, without harming the environment.

1. INTRODUCTION

In recent years, municipal solid waste (MSW) disposal has been one of the most important environmental problems for all countries. MSW is a system that includes social, economic, and environmental factors [1]. Generating energy in the process of waste disposal is important for the economy. In the last decade, the amount of MSW in Turkey increased by 32% with population growth [2]. MSW is divided into two categories; organic and inorganic. The composition of municipal solid waste in Turkey is given in Table 1. These wastes consist of organic wastes in the range of 40%-65% [3].

Commonly, MSW is disposed of as open dumping and sanitary landfilling. According to the Turkish State Statistical Institute's 2018 database [2], 67% of MSW is disposed of as sanitary landfilling. Recovery and composting are other disposal methods. MSW disposal is also applied in thermal methods such as pyrolysis, incineration, and gasification.

Gasification can be used for the conversion of wastes into other fuels, and it presents an engaging renewable replacement for fossil fuels. It is also an effective method for the disposal of waste. Most of the hydrogen gas formed is produced by physicochemical processes.

TABLE 1
COMPOSITION OF MSW IN TURKEY [3]

Components	Range (%) in weight
Organics	40–65
Paper/cardboard	7–18
Plastics	5–14
Metal	1–6
Glass	2–6
Others	7–24

However, these processes are not economical and are not preferred as they require external energy sources [4]. Thermochemical and biological processes can also be applied practically to produce hydrogen gas [5]. The greatest advantage of gasification is its effects on the environment. It can have a significant role in the reduction of landfill disposal. Besides, the emission tests for gasification confirm its acceptance [6].

Xydis et al. analyzed the electricity produced exergetically, from a landfill in the area of Volos, Greece, and discussed how

the extension of the landfill influences electricity production. They also reported that the exergy efficiency of the operation is at a level of 33% [7].

Cabuk et al. investigated the effect of fuel blend composition on hydrogen yield in the co-gasification of coal and non-woody biomass. The authors reported that the yields of hydrogen depend on the volatile content of raw biomass, in the co-gasification of lignite with biomass. Also, it was reported that hydrogen yields of 84 and 75 mol/kg fuel were obtained from lignite and torrefied biomass, respectively [8].

Gai et al. reported that the steam gasification of hydrochar obtained from sewage sludge produced a higher hydrogen yield than direct steam gasification of sewage sludge under the same conditions. They also reported that hydrothermal carbonization effectively pretreated sewage sludge to produce hydrogen-rich gas via steam gasification [9].

Seyitoglu et al. conducted energy and exergy analyses to investigate system performances for different coal types and they reported that the overall energy and exergy efficiencies of the entire system became 41% and 36.5%, respectively [10].

The study aims to produce hydrogen gas as a result of the co-gasification of MSW with coal to generate energy during its disposal. The importance of the system has been evaluated by energy and exergy analyzes. Gasification performance and the importance of hydrogen production of municipal solid blended with coal at different ratios (10%, 30%, 50%, 70%, and 90%) were also determined. In this study, it is discussed whether coal can be disposed of without harming the environment by gasification and whether these wastes can be converted into energy.

2. MATERIALS AND METHODS

A two-stage water gas shift (WSG) reactor was used to obtain the syngas from a gasifier and a bypass line was used to control the composition of syngas at the exit of the cascade reactor as shown in Figure 1.

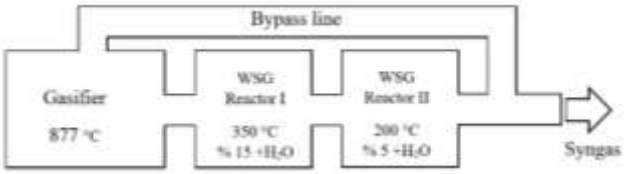

Figure 1. Schematic view of the cascade WGS reactor system

The properties of coal and municipal solid waste used in the study are given in Table 2. A numerical model was developed for the gasification system. Then, an optimum working condition was defined for H_2/CO ratio, which is equal to 2, at the gasification system exit. In the model, a combined relaxation Newtone Raphson method is used, using Visual Basic Net. The flowchart of the computations in the model is presented in Figure 2.

TABLE 2
PROPERTIES OF COAL AND MUNICIPAL SOLID WASTE [11], [12]

	MSW	Coal
C (%)	47.90	41.81
H (%)	6.00	4.28
O (%)	32.90	8.09
N (%)	1.20	2.16
Moisture (%)	30.00	13.51

It is quite difficult to obtain the best synthesis gas composition for H_2 production from MSW. For a reliable gasification model, the parameters and reactions of the gasification process should be well-determined. In this study, a co-gasification model was developed based on seven simultaneous reactions (Table 3). Equals show the reactions used in the model. The equilibrium constants of these reactions are given in Table 4.

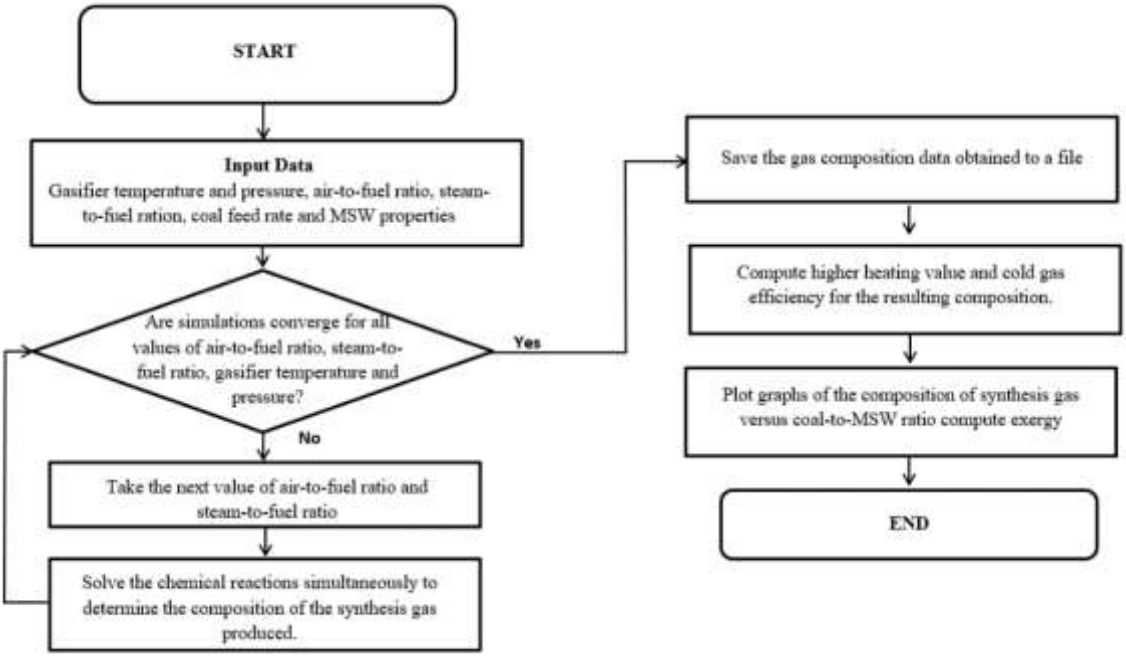

Figure 2. Flowchart of MSW gasification model.

TABLE 3
CHEMICAL REACTIONS INVOLVED IN THE GASIFICATION SYSTEM [13]

No	Reactions	Equals
1	Oxidation I	$C+O_2=CO_2$ (−394.5 kJ/mol)
2	Oxidation II	$C+12O_2=CO$ (−111.5 kJ/mol)
3	Steam gasification	$C+H_2O=CO+H_2$ (+131.4 kj/mol)
4	Boudouard reaction	$C+CO_2=2CO$ (+172.6 kj/mol)
5	Methanation reaction	$C+2H_2=CH_4$ (−74.9 kJ/mol)
6	Steam reforming reaction	$CH_4+H_2O=CO+3H_2$ (+206.2 kj/mol)
7	Water-gas shift reaction	$CO+H_2O=CO_2+H_2$(−41.2 kJ/mol)

TABLE 4
EQUILIBRIUM CONSTANTS USED IN THE MODEL

Temperature (K)	$K_{p,w}$ Eq. (5)	$K_{p,b}$ Eq. (6)	$K_{p,m}$ Eq. (7)
400	$7.7x10^{-11}$	$5.2x10^{-14}$	$2.99x10^{5}$
600	$5.1x10^{-5}$	$1.9x10^{-6}$	$9.24x10^{1}$
800	$4.4x10^{-2}$	$1.1x10^{-2}$	$1.34x10^{0}$
1000	$2.62x10^{0}$	$1.90x10^{0}$	$9.6x10^{-2}$
1500	$6.08x10^{2}$	$1.62x10^{3}$	$2.5x10^{-3}$

TABLE 5
VARIATION OF THE EQUILIBRIUM CONSTANT, $K_{P,S}$ WITH TEMPERATURE FOR THE WGS REACTION [14]

Temperature (K)	$K_{p,s}$
400	4050.00
600	27.00
800	4.04
1000	1.38
1500	0.37

2.1. Modeling and validation

The model requires syngas composition to be known at the beginning of the calculation and after entering the operation parameters such as steam/fuel ratios, air/fuel ratios, and reactor temperatures. The model performs calculations for the H_2/CO ratio. If the calculations converge to a solution, the program saves the results to a file and stops. Otherwise, perform the following operations; updating the values of the H_2/CO ratio and giving an initial value to the bypass ratio, the WGS reaction is solved to get a syngas composition. As a final step, the desired H_2/CO ratio is checked. If this ratio satisfies the criteria, the program computes the higher heating value (HHV) of the resulting syngas composition and, hot and cold gas efficiencies of the system.

The developed model was confirmed by experimental data for the co-gasification of pelletized wood residues in the literature [15], and the hydrogen gas content produced by the model is less than 2.77%.

It is emphasized in the literature that the gasifier temperature should be in the range of 700-850 °C. At lower temperatures, the gasification efficiency decreases, and the tar content increases [16]. The gasifier temperature of the model developed is 877 ° C (1150 K).

2.2. Energy and exergy analysis

To analyze the production of syngas from the co-gasification of MSW and coal, and to be able to make an assessment of the efficiency of the process, an energy and exergy analysis was performed.

Energy analysis is the main method to study gasification systems. System efficiency can be calculated according to the sum of H_2, CO, and CH_4 ratios that can be used from the syngas components resulting from gasification. The exergy rate can be expressed as the sum of the physical exergy and chemical exergy rates [17].

$$Ex = Ex_{ph} + Ex_{ch} \tag{1}$$

$$Ex_{ph} = \sum_i n_i \left[(h - h_0) - T_0(s - s_0)\right] \tag{2}$$

$$Ex_{ch} = \sum_i n_i \left(e_{0_i} + RT_0 \ln \frac{n_i}{\sum n_i}\right) \tag{3}$$

where "n_i" is the molar yield of gas component (mol/kg), "R" is the ideal gas constant and "e_{0i}" is the standard chemical exergy of a pure chemical compound, "s" is entropy and "h" is enthalpy, these values are for the given temperatures. Also, specific enthalpy (h_0) and entropy (s_0) values of the system at ambient temperature (25 °C) and pressure (1 atm) are given in Table 6.

TABLE 6
SPECIFIC ENTHALPY, ENTROPY, AND STANDARD CHEMICAL EXERGY VALUES OF SOME GASES [6].

Gas	h_0 (kJ/kmol)	s_0 (kJ/kmol K)	e_{0i} (kJ/kmol)
H_2	8468	130.574	236 100
CO	8669	197.543	275 100
CO_2	9364	213.685	19 870
H_2O (g)	9904	188.72	9500
CH_4	-	-	831 650

Exergy values of solid carbon, methane, and hydrogen gases in coal were taken into account while making exergy calculations. The specific heat value of solid carbon was calculated from the equation given below by Abbott and Van Ness [18];

$$c_{p_C} = 17.166 + 4.271\frac{T}{1000} - \frac{8.79 * 10^5}{T^2} \tag{4}$$

$$h - h_0 = \int_{T_0}^{T} c_p dT \tag{5}$$

$$s - s_0 = \int_{T_0}^{T} \frac{C_p}{T} dT - R \ln \frac{P}{P_0} \tag{6}$$

where c_p is the constant pressure-specific heat capacity which can be calculated by the equations given in Table 7.

TABLE 7
VARIATION OF SPECIFIC HEAT VALUES (C_P) AT CONSTANT PRESSURE WITH TEMPERATURE [14].

Gas	$c_p = \frac{kJ}{kmolK}, \theta = \frac{T(Kelvin)}{100}$
N_2	$c_p = 39.060 - 512.79\theta^{-1.5} + 1072.7\theta^{-2} - 820.40\theta^{-3}$
O_2	$c_p = 37.432 + 0.020102\theta^{1.5} - 178.57\theta^{-1.5} + 236.88\theta^{-2}$
H_2	$c_p = 56.505 - 702.74\theta^{-0.75} + 1165.0\theta^{-1} - 560.70\theta^{-1.5}$
CO	$c_p = 69.145 - 0.70463\theta^{0.75} - 200.77\theta^{-0.5} + 176.76\theta^{-0.75}$
H_2O	$c_p = 143.05 - 183.54\theta^{0.25} + 82,751\theta^{0.5} - 3.6989\theta$
CO_2	$c_p = -3.7357 + 30.529\theta^{0.5} - 4.1034\theta + 0.024198\theta^2$
CH_4	$c_p = -672.87 + 439.74\theta^{0.25} - 24.875\theta^{0.75} + 323.88\theta^{-0.5}$

3. RESULT AND DISCUSSION

During the first stage, syngas from the gasifier was fed into the system and mixed with steam at the WGS Reactor 1. Some portion of the syngas from the gasifier was mixed with the exiting stream via a bypass line connecting inlet and outlet streams. During the second stage, syngas at the exit of WGS Reactor 1 was mixed with a second stream of steam. Syngas at the exit of WGS reactor 2 was mixed with a bypass stream to produce the resulting composition.

The result in Figure 3 shows that a decrease in the H_2 gas content in syngas composition can be observed with an increase in the coal content of the MSW. The main reason for this is that MSW has a high moisture content. At the same conditions, CH_4 content was observed to increase. The CO content was seen to decrease negligibly. As shown in Figure 4, a decrease in HHV can be observed with an increase in the coal content.

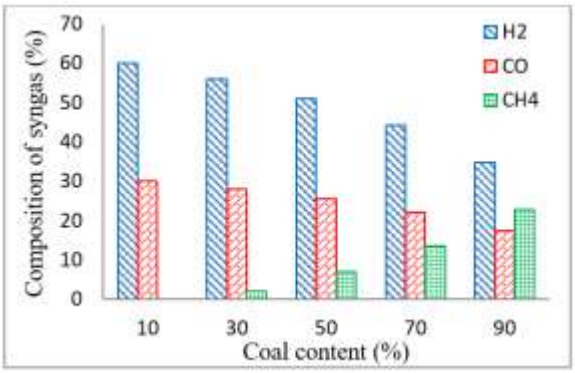

Figure 3. Effect of coal content in the composition of syngas (H_2, CO, CH_4) from co-gasifier with MSW

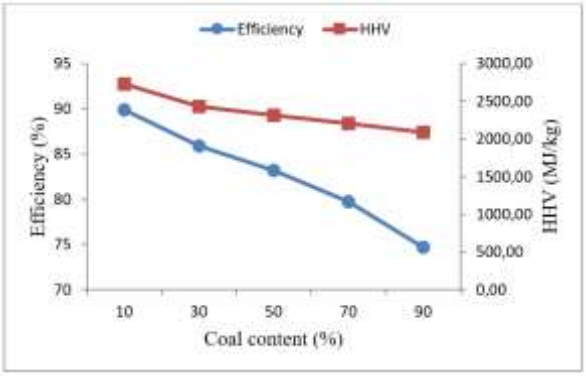

Figure 4. Effect of coal content on efficiency and HHV from co-gasifier with MSW

Figure 5 illustrates the effect of coal content on syngas exergy values from the co-gasifier with MSW. According to Zhang et al. [17], exergy values are determined by their temperature and yield. Also, a decrease in the exergy values in syngas composition was observed with an increase in the coal content of the MSW.

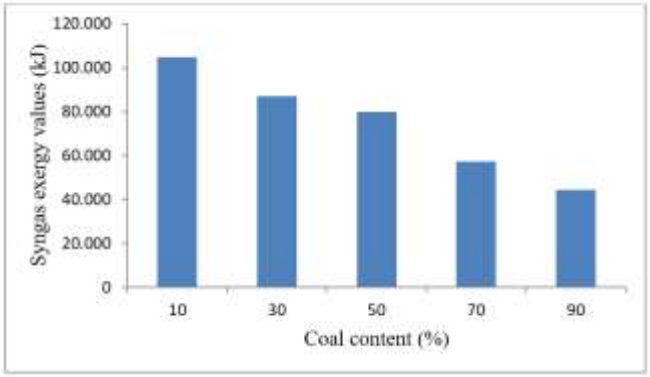

Figure 5. Effect of coal content on syngas exergy values from co-gasifier with MSW

4. CONCLUSION

Hydrogen production is important in terms of the energy economy. MSW and coal potentials are reliable sources of energy in hydrogen production. Gasification is important to evaluate the existing coal without harming the environment. It is also important for the disposal of MSW and conversion of it into energy.

In the present study, energy and exergy analyses of hydrogen production on the co-gasification of MSW and coal were evaluated. Also, gasification performance and the importance of hydrogen production of municipal solid blended with coal at different ratios (10%, 30%, 50%, 70%, and 90%) were determined. A numerical model was developed for the co-gasification system.

The results produced from the study showed that hydrogen gas can be used for the evaluation of coal with the disposal of MSW and conversion of these wastes into energy, without harming the environment.

REFERENCES

[1] C. Zhou, D. Hu, R. Wang, and J. Liu, "Exergetic assessment of municipal solid waste management system in south Beijing," *Ecological Complexity*, vol. 8, no. 2, pp. 171–176, Jun. 2011, doi: 10.1016/J.ECOCOM.2011.01.006.

[2] TUIK, "Turkish Statistical Institute Databases," 2019.

[3] N. G. Turan, S. Çoruh, A. Akdemir, and O. N. Ergun, "Municipal solid waste management strategies in Turkey," *Waste Management*, vol. 29, no. 1, pp. 465–469, Jan. 2009, doi: 10.1016/j.wasman.2008.06.004.

[4] A. Tawfik, M. El-Qelish, and A. Salem, "Efficient Anaerobic Co-Digestion of Municipal Food Waste and Kitchen Wastewater for Bio-Hydrogen Production," *International Journal of Green Energy*, vol. 12, no. 12, pp. 1301–1308, Dec. 2015, doi: 10.1080/15435075.2014.909357.

[5] M. Ni, D. Y. C. Leung, M. K. H. Leung, and K. Sumathy, "An overview of hydrogen production from biomass," *Fuel Processing Technology*, vol. 87, no. 5, pp. 461–472, May 2006, doi: 10.1016/j.fuproc.2005.11.003.

[6] N. Couto, V. Silva, E. Monteiro, and A. Rouboa, "Exergy analysis of Portuguese municipal solid waste treatment via steam gasification," *Energy Conversion and Management*, vol. 134, pp. 235–246, Feb. 2017, doi: 10.1016/J.ENCONMAN.2016.12.040.

[7] G. Xydis, E. Nanaki, and C. Koroneos, "Exergy analysis of biogas production from a municipal solid waste landfill," *Sustainable Energy Technologies and Assessments*, vol. 4, pp. 20–28, Dec. 2013, doi: 10.1016/J.SETA.2013.08.003.

[8] B. Cabuk, G. Duman, J. Yanik, and H. Olgun, "Effect of fuel blend composition on hydrogen yield in co-gasification of coal and non-

woody biomass," *International Journal of Hydrogen Energy*, vol. 45, no. 5, pp. 3435–3443, Jan. 2020, doi: 10.1016/J.IJHYDENE.2019.02.130.

[9] C. Gai, Y. Guo, T. Liu, N. Peng, and Z. Liu, "Hydrogen-rich gas production by steam gasification of hydrochar derived from sewage sludge," *International Journal of Hydrogen Energy*, vol. 41, no. 5, pp. 3363–3372, Feb. 2016, doi: 10.1016/j.ijhydene.2015.12.188.

[10] S. S. Seyitoglu, I. Dincer, and A. Kilicarslan, "Energy and exergy analyses of hydrogen production by coal gasification," *International Journal of Hydrogen Energy*, vol. 42, no. 4, pp. 2592–2600, Jan. 2017, doi: 10.1016/J.IJHYDENE.2016.08.228.

[11] A. Gungor, M. Ozbayoglu, C. Kasnakoglu, A. Biyikoglu, and B. Z. Uysal, "Determination of Air/Fuel and Steam/Fuel Ratio for Coal Gasification Process to Produce Synthesis Gas," *Journal of Environmental Science and Engineering*, vol. 5, pp. 799–804, 2011.

[12] H. Topal, "Plasma Gasification Technology For Solid Waste Disposal," *Journal of the Faculty of Engineering and Architecture of Gazi University*, vol. 30, no. 4, pp. 733–741, Dec. 2015, doi: 10.17341/gummfd.26834.

[13] A. Kocer, I. F. Yaka, and A. Gungor, "Evaluation of greenhouse residues gasification performance in hydrogen production," *International Journal of Hydrogen Energy*, vol. 42, no. 36, pp. 23244–23249, Sep. 2017, doi: 10.1016/j.ijhydene.2017.05.110.

[14] P. Basu, *Combustion and gasification in fluidized beds*, 1st Editio. CRC press, 2006. doi: https://doi.org/10.1201/9781420005158.

[15] C. A. Alzate, F. Chejne, C. F. Valdés, A. Berrio, J. D. la Cruz, and C. A. Londoño, "CO-gasification of pelletized wood residues," *Fuel*, vol. 88, no. 3, pp. 437–445, Mar. 2009, doi: 10.1016/j.fuel.2008.10.017.

[16] X. L. Yin, C. Z. Wu, S. P. Zheng, and Y. Chen, "Design and operation of a CFB gasification and power generation system for rice husk," *Biomass and Bioenergy*, vol. 23, no. 3, pp. 181–187, Sep. 2002, doi: 10.1016/S0961-9534(02)00042-9.

[17] Y. Zhang, B. Li, H. Li, and B. Zhang, "Exergy analysis of biomass utilization via steam gasification and partial oxidation," *Thermochimica Acta*, vol. 538, pp. 21–28, Jun. 2012, doi: 10.1016/J.TCA.2012.03.013.

[18] M. Abbott, H. Van Ness, and J. Casas, *Theory and problems Thermodynamics*, JV Casas. McGraw-Hill, 1972.

BIOGRAPHIES

Abdulkadir Kocer was born in Bolvadin, Afyonkarahisar in 1981. He graduated from the Mechanical Education Department of Gazi University Technical Education Faculty in 2002. In 2005, he obtained his MSc degree from the Mechanical Education Department of Gazi University in Ankara, Turkey. In 2018, he obtained his Ph.D. degree from the Farm Machinery Department of Akdeniz University. He is also an Assistant Professor at Vocational School of Technical Sciences of Akdeniz University. His main research fields are gasification, solar energy, computer programming, and biomass energy.

Ercument Aksoy obtained his BSc degree in geodesy and photogrammetry engineering from Yildiz Technical University in 1993. He received the MSc. diploma in Geology Engineering from the Akdeniz University in 2016. His research interests are remote sensing, geographic information systems, environmental information systems and İmage processing. In 1997 he joined the Vocational School of Technical Sciences, Akdeniz University as a lecturer.

Ismet Faruk Yaka obtained his BSc degree in mechanical engineering from Sakarya University in 2014. He received the BSc., and MSc. diploma in Mechanical Engineering from the Akdeniz University in 2017. His research interests are gasification, solar energy and heat enhancement. In 2019 he joined the Faculty of Engineering, Akdeniz University as a research assistant.

Afsin Gungor received his Ph.D. in mechanical engineering (Istanbul Technical University) in 2006. He is presently professor of mechanical engineering at Akdeniz University, Antalya TURKEY. Prof Gungor has edited 15 books, has published more than 260 proceedings, and published more than 110 papers in peer-reviewed international journals, in addition to more than 30 book chapters. In the last 2 years, Prof. Gungor has applied for patents for 3 innovative projects. Prof Gungor was the founder and Dean of Bucak Technology Faculty, Burdur Mehmet Akif Ersoy University, Burdur, TURKEY, his research interests include New and Renewable Energy Sources, Nanotechnology, Energy Conversion and Management, Simulation and Modeling of Energy Systems, Combustion and Gasification of Coal and Biomass in Fluidised Beds, Hydrogen Production and Purification in Gasification of Coal and Biomass, Solar Thermal Applications.

European Journal of Technique

journal homepage: https://dergipark.org.tr/en/pub/ejt

Vol.12, No.2, 2022

Power Quality Analysis for Power Led Drives

Secil Genc [1], Okan Ozgonenel [2], Orkut Onat Yildiz [3] and İbrahim Hakki Kilic [3]

[1*]Ondokuz Mayis University, Electrical and Electronic Engineering Department, 55200, Samsun, Istanbul, Turkiye. (e-mail: secil.yilmaz@omu.edu.tr).
[2] Ondokuz Mayis University, Electrical and Electronic Engineering Department, 55200, Samsun, Istanbul, Turkiye. (e-mail: okanoz@omu.edu.tr).
[3]BORSAN, OSB Organize Sanayi Boulvard, Samsun, Tekkeköy, Samsun, Turkiye. (e-mail: orkutonatyildiz@borsan.com.tr).
[4] BORSAN, OSB Organize Sanayi Boulvard, Samsun, Tekkeköy, Samsun, Turkiye. (e-mail: ibrahimkilic@borsan.com.tr).

ARTICLE INFO

Received: Dec., 08. 2022
Revised: Dec., 22. 2022
Accepted: Dec, 23. 2022

Keywords:
Power quality
EMI
Conducted emissions
Harmonics

Corresponding author: *Okan Ozgonenel*

ISSN: *2536-5010* | e-ISSN: *2536-5134*

DOI: https://doi.org/10.36222/ejt.1216165

ABSTRACT

DC micro grids have grown increasingly popular in the energy grid in recent years, as distributed generation has increased. Distributed generation refers to small or large-scale renewable energy that is linked to the main power system. Renewable energy sources like solar and wind power help the local grid, but their output is inherently intermittent and unpredictable, interfering with regular grid operation. Some of these issues can be mitigated by using energy storage in conjunction with renewable energy. Renewable energy is often linked to the grid using power electronic converters.

The goal of this research is to simulate and evaluate transmitted emissions in the time and frequency planes using IEEE 1459 to investigate the impacts of DC / DC converters on DC lines, particularly for renewable energy generation. While there are standards and norms for frequencies up to 2 kHz and beginning at 150 kHz, the frequency range 2-150 kHz only has suggested techniques and propagation restrictions. As a result, the emission conveyed in the frequency range of 2-150 kHz is a subject that must be comprehended. The structure of the generation model, as well as the idea of power quality in electricity generating models, will be investigated using data collected through experimental and computer simulations on a medium-scale hybrid network connected to the grid. The technological advances acquired will subsequently be utilized to evaluate the power quality of various DC and AC single/three phase power systems (such as computer servers, airplanes, and so on).

1. INTRODUCTION

With the rise of distributed generation in recent years, DC microgrids have become increasingly widespread in the electrical grid. Distributed generation refers to small or large-scale renewable energy that links to the power grid. Wind energy, solar energy, geothermal energy, and biomass energy are all popular forms of renewable energy [1-6]. Photovoltaic cells generate direct voltage and current. Because the output of a solar cell varies depending on the weather, the regulation of such generation is done with the assistance of a DC-DC converter to regulate the power flow and voltage levels in microgrids. In a DC microgrid, DC-DC converters connect generation, energy storage, and loads, which are frequently externally networked via AC-DC converters.

There are several voltage levels of DC distribution lines. Power generating and diverse and distinct power sources (photovoltaic systems, micro turbines, wind farms, etc.), energy storage facilities (railways, subways, tram lines having various energy storage devices, roadside and on-board) (such as supercapacitors and batteries). They are all linked to a DC mains network of the same voltage level or, via converters, to a different voltage level. Furthermore, as renewable energy sources are integrated into the grid, interest in DC-DC and bidirectional AC-DC converters is growing. The usage of PWM-based converters is becoming more common as the utilization of renewable energy and battery technology grows. Aside from PWM-based converters, the growing usage of non-linear devices, electronic and electrical equipment such as SMPS, motors, fluorescent lights, electronic data processors, and power supply switches generates additional electromagnetic noise. This may have an impact on the system's stability. A DC microgrid's frequency range can range from extremely low (below 9 kHz) to very high (such as 9-150 kHz and 150 kHz-30 MHz) [7]. The increased use of DC-DC converters, which are frequently operated at higher switching frequencies, might result in electromagnetic interference (EMI) in the system. Above 2 kHz, these disruptions are referred to as "high frequency distortion" [8]. These conducted emissions have an impact on the AC mains side as well. The two primary implications of power quality problems on a distribution system are a power quality problem and the unfavorable impact on equipment (electrical loads) from power factor reduction induced by specific forms of harmonics. The Electrical Power Research Institute (EPRI) has suggested an end-user-centered definition of "power quality problem" as any power problem caused by voltage, current, or frequency variations that causes customer equipment to malfunction or misoperate. The emissions

produced by power converters used in distributed generation vary substantially not just along the time axis or in amplitude, but also across the frequency spectrum. All these components manifest as harmonics/high frequency interferences with varying amplitudes and consequences. These harmonics usually disrupt or destroy the operation of converters and other micro grid-connected devices [4], [9]. Currently, no limits are imposed by electrical distribution companies on transmitted radiated switching voltage sources, ballasts, or other equipment. However, it is apparent that emissions in this high frequency band have an impact on grid-connected devices [8]. Simultaneously, considering the EMI of the device at the original design phase will allow designers to meet electromagnetic compatibility at a reasonable cost before discovering it [10]. As a result, the power quality of these transmitted emissions should be investigated. While there are standards and norms for frequencies up to 2 kHz and beginning at 150 kHz, there are only suggested techniques and propagation limitations for frequencies between 2 and 150 kHz. As a result, new methods for frequencies in this range must be developed, or methods from other frequency ranges must be adapted [3]. There isn't enough research on the effect of high frequency disruptions on networks in the literature, it's been discovered. When the broadcasts are analyzed, it is discovered that there are insufficient research on the impact of transmitted emissions on the network. Ensini et al. [6] evaluated the effect of conducted emissions emanating from a single-phase DC-DC converter on the DC mains side in their study on the influence of transmitted emissions on the grid. Webling et al. [11] proposed a method for measuring the differential and differential mode transmitted emissions from switched-mode power sources. Jettanasen et al. investigated the nano-grid road lighting system's emitted emissions [4]. In general, power electronics switching topology in power electronics settings and electromagnetic waves propagating to the environment at MHz levels are stressed based on the transmitted propagation. Upper harmonic power quality issues have not been addressed since no study has been undertaken on the influence of released emissions into our country's grid. The strongest motivations for working in this sector have been the increased impacts of transmitted emissions on the grid and the absence of any limits, especially with the widespread use of electric cars, which is one of the development goals.

The behavior of DC and AC systems (microgrids, lines, inverter/converter equipment, etc.) that will serve as a model for power quality studies will be described in this project. In contrast to the literature, a full overview of single-phase and three-phase DC and AC systems will be offered. The goal of this project is to improve power quality and solve electromagnetic compatibility issues in DC-DC and DC/AC alternating grid connections, particularly with the increased usage of electric cars. Recommendations for measuring, analyzing, and mitigating high frequency conducted emissions will be made. Methods and methods for exact dispersion analysis will be developed. Separate analyses will be performed on the common and difference mode conducted emissions reflected on the network.

This project aims to interpret computer simulation findings and provide reports. By standardizing the higher frequencies, it is intended to help to the optimization of the Turkish energy grid, the reduction of losses, and the enhancement of power quality. In this regard, TEİAŞ released in 2021 the technical standards for the grid connection of electricity storage facilities, their monitoring using SCADA, and their usage as supplementary services. However, the influence of high-frequency disturbances on the grid induced by power converters employed in between is overlooked in this regulation. With this project, awareness of power quality issues emerging from conducted emissions that will emerge as a result of the battery's integration into the grid will be promoted, and ideas for the diversification of quality indices will be developed. In other words, awareness will be promoted regarding the development of additional laws and the standardization of the new EPDK regulation.

2. RELATED WORKS

The process of collecting, evaluating, and interpreting measurable electrical signal data is known as power quality monitoring. During the data acquisition step, voltage and current are continually measured during a specific process. Experts assist in the analysis and interpretation process. Intelligent systems may be built and deployed using breakthroughs in signal processing and artificial intelligence to automatically transform and interpret measurable data into meaningful information with minimum human interaction. Current and voltage sensors are used to measure both AC and DC systems (measuring transformers, etc). Although DC/AC metering configurations are not the primary goal of this proposed project, the best metering setups for the most efficient power quality study/research will be offered. Measurement errors induced by measurement devices, as well as connecting points, will be investigated in terms of the idea of DC power quality.

Khilnani et al. conducted a power quality assessment of emissions from a microgrid-based DC/DC converter at 0-2kHz steady state and transient loading situations within the scope of prior research. They used the quick Fourier transform to assess the experimental data (FFT). To assess DC power quality, they employed the low frequency sinusoidal distortion index (percent LFSD) and the amplitude probability distribution (APD) of voltage and current [2]. Ensini et al. investigated conducted emissions between 9 and 150 kHz in terms of DC power quality as measured by DFSB, ripple index, and APD. They compared LFSD and APD findings using CISPR 15, CISPR 14, EN50065, and EN50160 standards at various intervals [6]. Webling et al. [11] proposed a method for calculating emissions from switched-mode power sources. The rising usage of non-linear technologies has created 'power harmonics,' resulting in worse power quality. Electromagnetic noise is produced by electronic and electrical equipment such as SMPS, motors, fluorescent lamps, electronic data processors, and power supply switches. The emission produced by the device under test (DUT) will be determined not only by its internal source (electronics), but also by the quality of the incoming AC mains power. Mahesh et al. investigated how voltage harmonics impact the conducted propagation caused by DUT. Based on the experimental data, they concluded that the existence of voltage harmonics at the LISN input has a considerable impact on the DUT propagations [13]. Larrson et al. took measurements in an apartment by filtering the conducted emissions from a fluorescent bulb lighting system for a set amount of time. To minimize the harmonic content of the current, almost all fluorescent lights with high frequency ballasts employ active power factor correction (PFC) circuits. When the filtered signal is inspected, it is discovered that the converter with active PFC oscillates because of its failure to manage the current near to zero crossover. These oscillations have frequencies ranging from a few kilohertz to more than ten kHz. A three-dimensional linear scale based on short time

Fourier transform (STFT) analysis is utilized to better understand where the energy of this high frequency oscillating signal is focused [12]. Spadacini et al. suggested a circuit model for conducting emission analysis of all subsystems of an electric vehicle powertrain that can reflect both functional, low-frequency behaviour and high-frequency impacts (battery, inverter, motor). It is linked to the interface established in LISN CISPR 25 between the battery and the DC power bus. The "current-probe method" and the voltage approach were compared in CISPR 25. They stressed the importance of probe location in the CISPR current-probe approach when very high-frequency components of conducted emissions (over 30MHz) are present [14]. Spadacini et al. also evaluated the influence of difference mode (DM) and common mode (CM) currents delivered from the inverter in electric vehicle engines on the EMI's lithium-ion batteries. DM and CM currents can enter batteries via AC cables, DC wires, and ground, affecting battery performance. They developed a SPICE model of the power drive system as well as a test platform to assess the effect of the power drive system's EMI on lithium-ion batteries. They demonstrated in their experiments that the voltage fluctuation range of an unfiltered battery is greater than that of a filtered battery owing to DM and CM currents [15]. Mutoh et al. concentrated on the 1 MHz or higher frequency transient EMI noise of common mode currents produced during switching operations in electric vehicle drive systems. The fast Fourier transform was used to evaluate high frequency voltage and current data. Control strategies for reducing EMI sounds have been presented [16]. Shall and Kadi assessed the electric vehicle charger's emitted and conducted emissions in the frequency range of 150 kHz to 108 MHz in accordance with CISPR 25 IEC:2008 guidelines [17]. Korth et al. used a high frequency modelling technique to achieve a more exact estimate of the battery's voltage response owing to a high frequency current surge [18]. When the studies are analyzed, LISN is the first instrument utilized to filter the conducted emissions. The LISN is a low-pass filter that is connected between the AC or DC power source and the DUT and offers a port for creating a certain impedance and monitoring radio frequency (RF) noise. Simultaneously, the signals are seen using an EMI receiver/spectrum analyzer or data capture card. Furthermore, EMI receivers use frequency scanning or, at very high frequencies, an FFT-based time domain scan. The spectrum of the input signal is measured and analyzed by these EMI receivers [19-20]. The harmonic spectrum of the signals may be determined when the signal is delivered to the computer utilizing data capture cards for better analysis using different analysis methods [21-22]. While the EMI receiver is using FFT, the signal sent to the computer environment may be examined and compared using STFT, wavelet transforms, and Fourier transforms with different window functions. Because unstable signals in the 2-150 kHz frequency range shift over time owing to their nature, an analytical technique is necessary. As a result, the disturbances must be examined not only in the frequency domain, but also in the time-frequency domain. Because the measured value is voltage, it is represented in µV. This unit must be represented in logarithmic form, namely dBµV, and compared to the limitations in the standard in order for the limits in the frequency spectrum and test standards to be more understood. The standards used for emissions in the 2-150 kHz frequency range are: CISPR 11, which sets the mandatory limit for emission from high performance scientific, medical, or industrial equipment, and electrical lighting systems, which set the same emission limits as the CISPR 11 standard but are a very common source of broadband upper harmonic disturbance. CISPR 15, which also specifies emission limits for active supply converters, IEC TS 62578, which describes the operating conditions and typical characteristics of active supply converters, EN50065 general and EN50065 industrial (the latter two differ after 100 kHz) power line communication standards, and Standard EN 50160, which expresses low voltage, medium voltage, and high voltage supply characteristics, voltage events, and variations [3].

3. MEASUREMENT of CONDUCTED EMISSIONS

3.1. Simulation works

Fig. 1 depicts a flowchart for observing the propagation transmitted from a DC-DC buck converter with 48 V output voltage used in DC power systems. The simulation was performed in the MATLAB™ environment in order to compare it to the actual mechanism that will be implemented in the future. For comparison, the low frequency sinusoidal distortion index (percent LFSDI), ripple index, and amplitude probability distribution of DC voltage and current were determined. To restrict the transmitted emissions, IEC TS 62578, CISPR 11-15, EN50065, and EN 50160 standards were applied in this investigation. Because there is currently no standard for determining if LFSDI and APD levels are acceptable, the transmitted emissions were tested for variable input voltage and load. Wavelet transform and discrete wavelet transform methods with varied window functions, which are among the approaches proposed in related studies, have been tested for 2-150 kHz EMI band range.

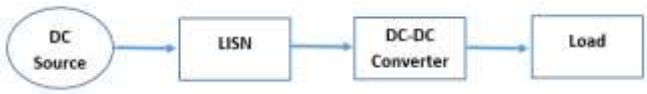

Figure 1. Flowchart of the system

MATLAB simulation circuit for power quality analysis of conducted emissions from DC-DC buck converter with varying input voltage and 48 V output voltage is given in Fig. 2. Simulation parameters are given as follows.

• Total simulation time=0.5 sec for enough the system reached steady state.

• Bandwidth: The frequency resolution has been taken as 5 ms for the collection of the signal in 200 Hz bands recommended by the EN 55065-1standard.

• Number of windows=Total time (0.5 sec)/ bandwidth (0.005 sec)=100

• Total number of samples=250000

• Number of samples in the window = Total number of samples (25000) / number of windows (100) = 2500

A time frame of 200msec is recommended by the IEC 61000-4-7 standard (5Hz frequency resolution). This scenario, however, is unsuitable for the processing of high frequency signals. As a result, the time window length for signal gathering in the 200Hz bands indicated by the EN 55065-1 standard and the standards covering frequency ranges below 150 kHz was set to 5msec.

This unit is given in logarithmic form, namely db µV, to make the restrictions in the frequency spectrum and test standards more accessible.

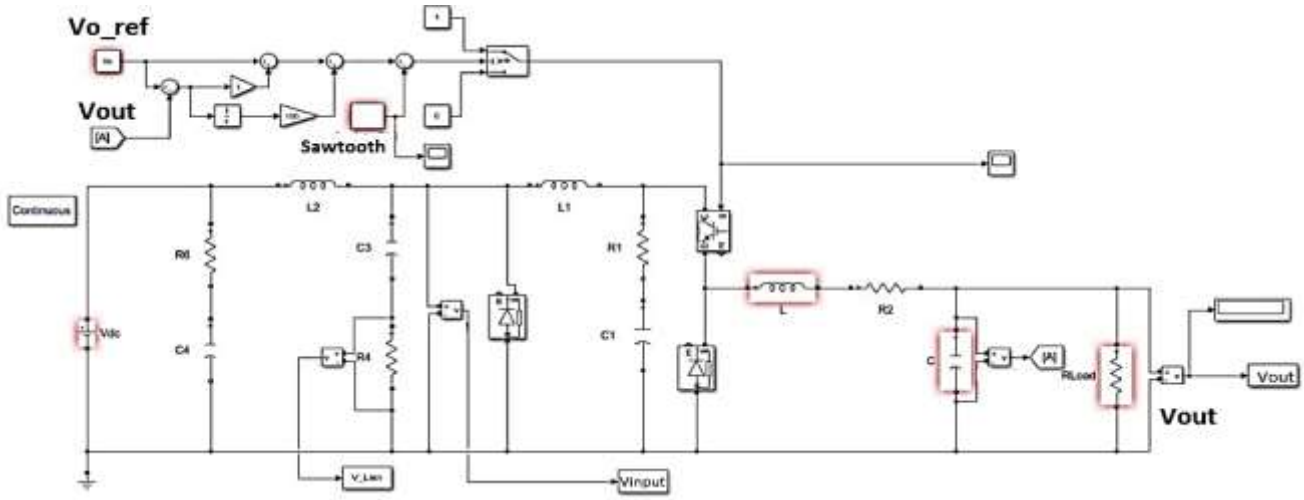

Figure 2. MATLAB simulation circuit for power quality analysis of conducted emissions from DC-DC converter

$$\mathrm{dbV} = 20\log(V) \quad (1)$$

$$db\mu V = 20\log(V) \times 10^{6} \quad (2)$$

Fig. 3 shows the input and output voltages of the DC-DC converter, as well as the voltages measured over the LISN communicated to the network side when a 2900W load is attached, when the converter input voltage is 410V and the output voltage is 48V.

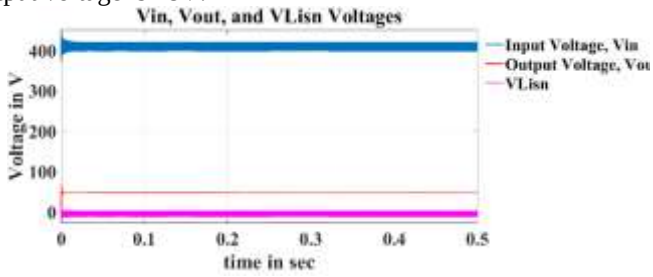

Figure 3. MATLAB simulation circuit for power quality analysis of conducted emissions from DC-DC converter

STFT analysis was done on the signal taken from the LISN output for 0.5 sec using 5msec time frames. Fig. 4 depicts the signal investigated in the 0-5msec time region. The Fourier analysis shows that, depending on the switching frequency of the converter, 20kHz and its multiples can be detected. The switching frequencies are only visible when samples are obtained above 6kHz (ignoring the transient).

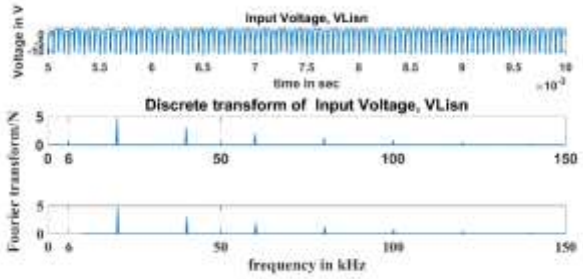

Figure 4. Amplitude variation of LISN voltage in time and frequency axis

3.2. Evaluation of conducted emission in terms of power quality indexes in DC systems

3.2.1. Distortion index

The frequency of the DC's fundamental component is zero. Instead of harmonic and internal harmonic components, Equation 3 expresses the overall effective value of low frequency sinusoidal disorder (DFSB). In Equation 3, Q[0] represents the steady-state DC value; Q[k] represents the frequency spectrum recorded for samples of q[n] over a particular time period (rms).

$$\mathrm{D} = \left[\sum_{k>0}^{k_{max}} (\mathrm{Q[k]/Q[0]})^2\right]^{1/2} \quad (3)$$

3.2.2. Ripple index

Equations 4,5 and 6 are used to compute the ripple index of DC-DC input voltage. Here, X_DC represents the mean DC component, X_i represents the time history sign, and X(e) represents the deviation from the mean. Due to the transient situation, samples after the first half of the 0.5sec total simulation time (after 0.25sec) were evaluated.

$$\mathrm{X_{DC}} = \frac{1}{N}\sum_{i=1}^{N} \mathrm{X_i} \quad (4)$$

$$\mathrm{X_e} = \sqrt{\frac{1}{N}\sum_{i=1}^{N} (\mathrm{X_i} - \mathrm{X_{DA}})^2} \quad (5)$$

$$\mathrm{X_e} = \frac{\mathrm{X_E}}{\mathrm{X_{DC}}} \quad (6)$$

3.2.3. Amplitude Probability Distribution (APD)

APD represents the likelihood that the interference will have a given amplitude value or more. Equation 7 calculates the APD value of the LISN output voltage. APD is the amplitude probability distribution, and FR(r) is the additive distribution function.

$$\mathrm{X_{DC}} = \frac{1}{N}\sum_{i=1}^{N} \mathrm{X_i} \quad (7)$$

4. INTRODUCTION EVALUATION of RESULTS for DC-DC BUCK CONVERTER

In simulation studies, samples obtained for 0.5sec in the simulation were evaluated by scrolling through 5msec frames. The signal's assessment in the 5-10msec time frame is shown in Figs. 5 and 6. Fig. 5, shows CE under varying load conditions. According to the result, for this window length CE exceeds the limit for EN50065 standard and increase with the load. The APD analysis depicts the probable magnitude increase from the steady state for DC voltage. As seen in Fig. 6, APD also increases with the load.

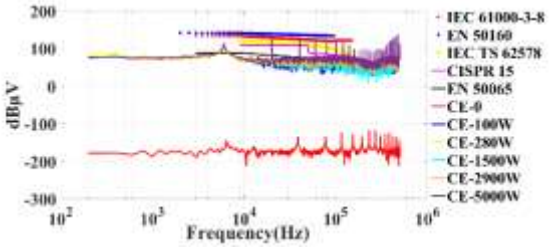

Figure 5. Variation of conducted emissions depending on load in case of 5-10msec window length, 410V input voltage

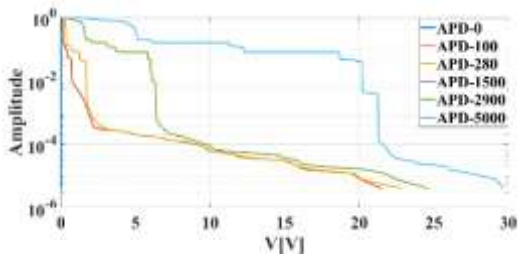

Figure 6. Change of APD depending on load in case of 5-10msec window length, 410V input voltage

Table 1. 5-10 ms Window interval, LFSD-9, LFSD-150 and variation of ripple depending on load in case of 410V input voltage.

TABLE I
POWER QUALITY RESULTS FOR VARYING LOAD CONDITION

LFSD-9	LFSD-150	Ripple	Load (W)	Voltage (V)
7E-15	7E-15	1E-15	0	410
0.79	0.79	6E-5	100	410
0.49	0.49	1E-5	280	410
0.82	0.82	9E-5	1500	410
0.83	0.83	1E-4	2900	410
0.69	0.69	0.03	5000	410

The following figures are obtained in the case of 5kW load condition.

Fig. 7 shows APD variation under varying input voltage. As seen in Fig. 7, the variation of APD decrease with the voltage. Adversely, as illustrated in Fig. 8, CE variation rises with input voltage.

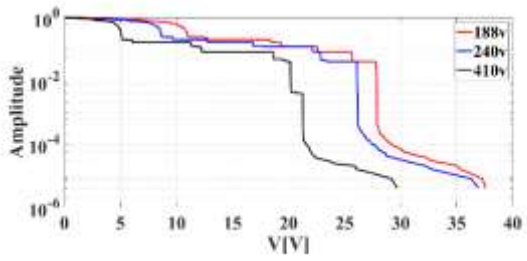

Figure 7. 5-10msec window length, variation of APD depending on input voltage at 5000W load

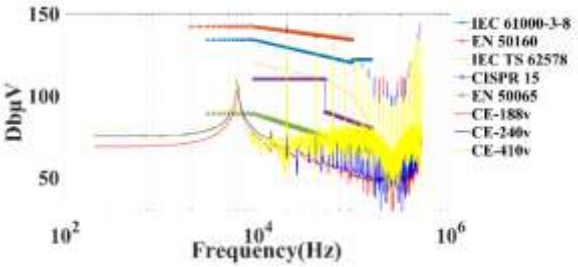

Figure 8. 5-10msec window length, variation of transmitted emissions depending on input voltage at 5kW load

Table 2. Variation of LFSD-9, LFSD-150 and ripple depending on load in case of different input voltage in case of 5-10msec window interval and 5kW load.

TABLE II
POWER QUALITY RESULTS FOR VARYING SUPPLY CONDITION

LFSD-9	LFSD-150	Ripple	Load (W)	Voltage (V)
0.69	0.69	0.12	5000	188
0.86	0.87	0.08	5000	240
0.69	0.69	0.03	5000	410

5. SPECTOGRAM

The spectrogram generates a feature vector that shows the energy change of the harmonic in the frequency bands over time and allows you to see where the major signal energy is focused. Fig. 9 depicts the spectrogram of the STFT-based signal. The use of a spectrogram is necessary since it was unclear if a 6 kHz harmonic signal is transient or not. According to the result, the harmonic can be observed only at the first energizing moment and not at subsequent sampling times. Depending on the switching frequency, harmonics of 20kHz and their multiples are observed during switching frequency.

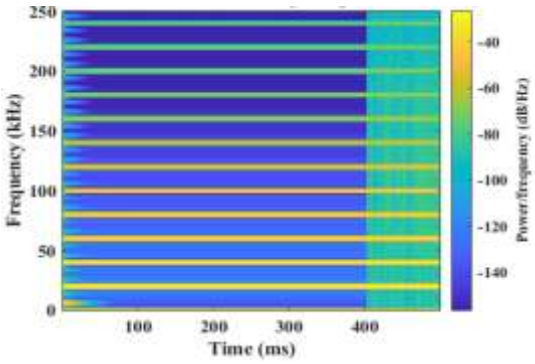

Figure 9. Spectrogram of EMI signals

6. WAVELET ANALYSIS

6.1. Discrete wavelet transform

Because STFT has a fixed frequency resolution, it poses problems. A wide window improves frequency resolution but degrades temporal resolution. A small window provides excellent temporal resolution but poor frequency resolution. These are known as narrow-gap transformations and wide-range transformations, respectively. Wavelet packet decomposition of the digitized signal is an alternative to the STFT-based technique. Instead of a discrete number of frequency components as in the Fourier transform, the wavelet transform separates the signal into numerous frequency ranges.

Figure 10 shows the discrete wavelet transform. Because the sampling frequency is 500kHz and the upper frequency is 250kHz due to the Nyquist theorem, the high and low frequency components are shown in Fig. 13. Normally, this iterative procedure is repeated until the number of samples remains constant. The application's criterion is based on achieving the best answer with the aid of 'entropy.'

$$k = \log_2 N \tag{8}$$

where N is the number of sampled signals and k is the resolution level. Since each window contains 2500 samples, the resolution level that may be reduced, k, is determined to be 11. When the 11th level of Mallat's wavelet tree (Fig. 13) is inspected, it offers the resolution of frequencies less than 50 Hz. Table 3 shows MDL findings for the sampled signal at 5-10 ms time intervals with an input voltage of 410V and a load of 1500W. When wavelet families were evaluated within themselves, the most suitable families were determined to be db20 from the Daubechies family, sym3 from the Symlets family, coif2 from the Coiflet family, bior5.5 from the biorthogonal family, reverse biortogonal rbio2.6, dmey from the discrete Meyer family, and fk22 from the Fejér-Korovkin filter family. Among the wavelet families, db20 with the lowest MDL was picked as the best fit.

TABLE III
VARIATION OF RIPPLE DEPENDING ON DIFFERENT WINDOW STATES IN CASE OF 410 V INPUT VOLTAGE

Filter	MDL	Filter	MDL	Filter	MDL	Filter	MDL
db1	52.8	sym2	49.6	coif1	51.6	rbio1.1	52.8
db2	49.6	**sym3**	**47.5**	**coif2**	**51.1**	rbio1.3	53.8
db3	47.5	sym4	48.9	coif3	50.8	rbio1.5	52.8
db4	48.2	sym5	50.9	coif4	50.5	rbio2.4	49.7
db5	46.4	sym6	50	coif5	50.3	**rbio2.6**	**48.7**
db6	44.5	sym7	52.5	bior1.1	52.8	rbio2.8	49.762
db7	44.8	sym8	49.1	bior1.3	52.1	rbio3.3	45.2
db8	44.5	sym9	50.3	bior1.5	50.6	rbio3.5	44.1
db9	42.5	sym10	49.8	bior2.4	55.6	rbio3.7	45.2
db10	42.3	sym11	49.3	bior2.6	53.9	rbio3.9	44.1
db11	43.2	sym12	49.4	bior2.8	54.2	rbio4.4	50.9
db12	40.9	sym13	49	bior3.3	59	rbio5.5	50.5
db13	40.7	sym14	50	bior 3.5	56.1	rbio6.8	51.1
db14	41.9	sym15	50.2	bior3.7	55.7	dmey	49.8
db15	39.2	sym16	48.8	bior4.4	54.3	fk4	53.5
db16	39.8	sym17	49.8	**bior5.5**	**50.2**	fk6	48.04
db17	40.2	sym18	50.1	bior6.8	52.7	fk8	48.05
db18	37.9	sym19	50.7			fk14	47.2
db19	38.2	sym20	48.5			**fk22**	**44.7**
db20	**38.1**						

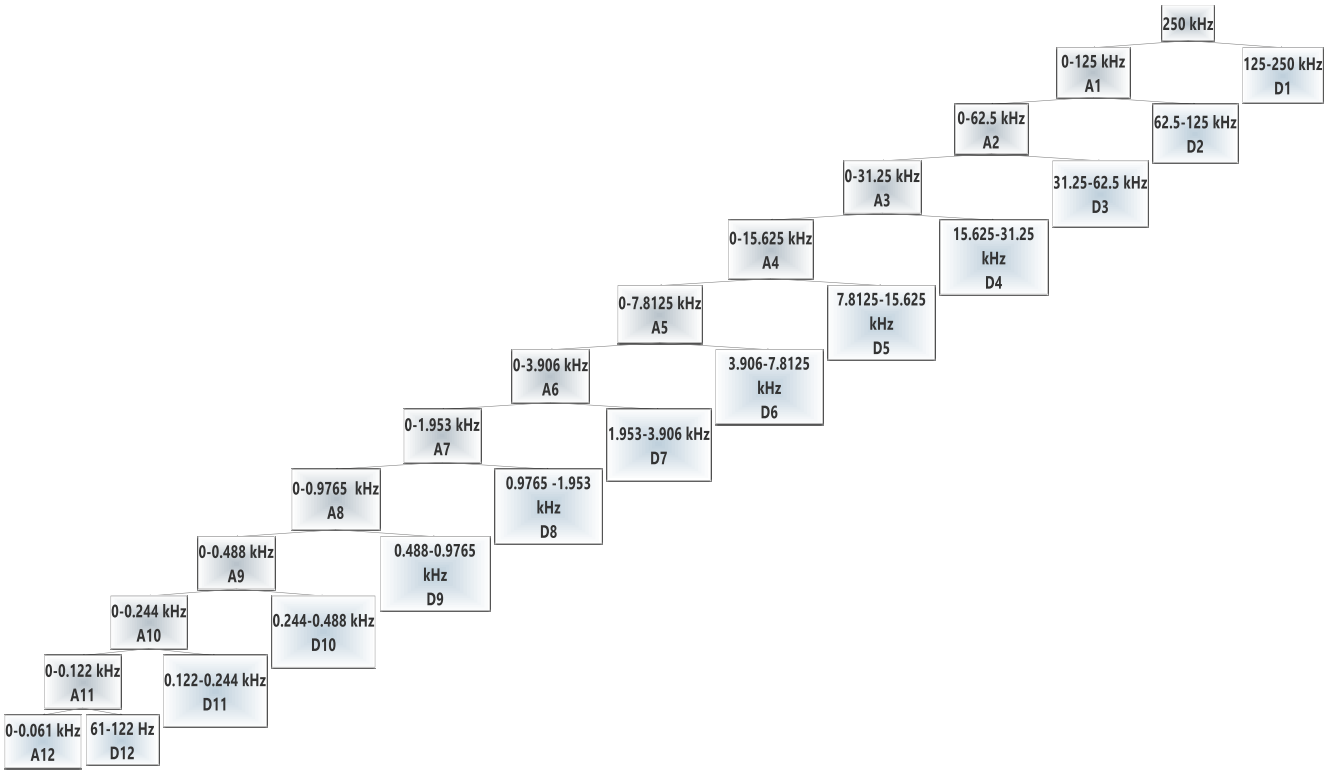

Figure 10. Approximation and detail coefficients of the analyzed signal and their frequency ranges

The appropriate decomposition level of the multiple resolution analysis was determined using Shannon entropy. This function computes the entropy of each resolution level. The level is determined by the point at which the approach and detail coefficients reverse direction. When the entropy curve in Fig. 11 is inspected, the approximation and detail coefficients for db20 change direction at the fourth level. Because we want to observe 50Hz in our research and our data load is not too high, we will need to go down to the 4th level for data load applications. As a result, it was requested to descend to the 11th floor and observe the 50Hz indicator.

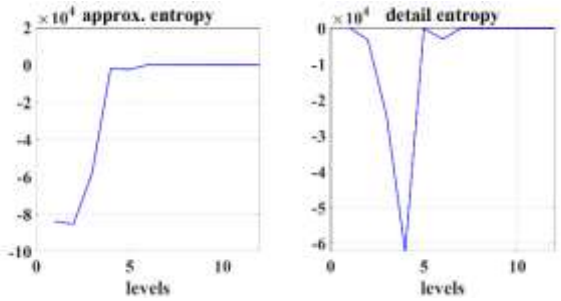

Figure 11. Calculation of the optimal decomposition level of Db20 wavelet families

Fig. 12 shows the energy levels of approximation and detail coefficients depend on db20 wavelet family.

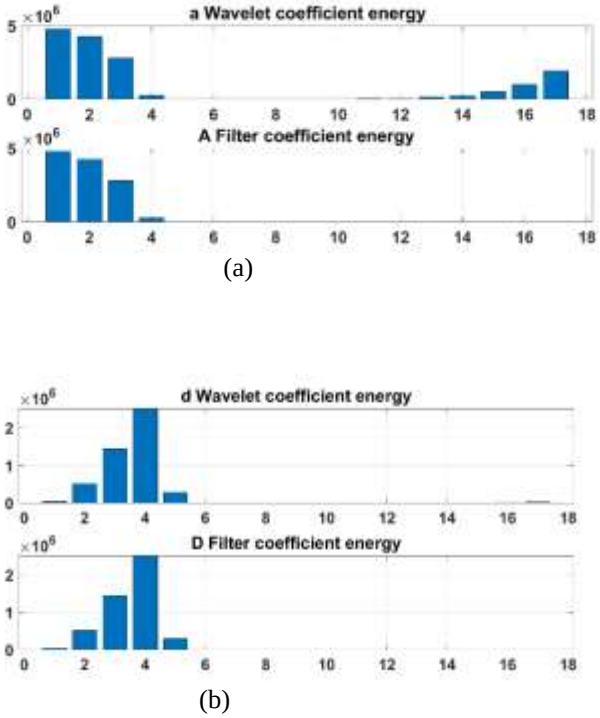

Figure 12. Energy levels of coefficients

The energy of the d wavelet coefficients suited for high frequency analysis is crucial in this study. When the energy of the d coefficients shown in Fig. 12 (b) is analysed, the d4 wavelet encompassing 20 kHz, which is the switching frequency, has the maximum energy. The switching signal d3 at 40kHz corresponds to the frequency range covered by the wavelet coefficient, 60kHz to the range covered by d2, and 6kHz to the range covered by d5 and d6. Because d5 has a larger frequency range, its energy stays greater than d6. Because the LISN device did not pass the 50 Hz low frequency signal, the d11 energy was insufficient

When using the 'multiresolution analyzer' toolbar from MATLAB™ tools. The energy of the signal obtained in wavelet transform 4th level analysis is approximately half of the energy of the whole signal. The influence of the filter coefficients will be especially important in filter designs to reduce harmful interference of EMI signals.

6.2. Multi-resolution analysis

The wavelet packet spectrum comprises the absolute values of the coefficients from the binary wavelet packet tree's frequency sorted end nodes. In wavelet packet transform, terminal nodes give the highest level of frequency resolution. J denotes the wavelet packet transformation level, while Fs is the sampling frequency. Equation 9 is used to compute the width of the band to the end nodes. The wavelet packet spectrum comprises the absolute values of the coefficients from the binary wavelet packet tree's frequency sorted end nodes. In wavelet packet transform, terminal nodes give the highest level of frequency resolution. J denotes the wavelet packet transformation level, while Fs is the sampling frequency. The width of the band to the end nodes is calculated by equation 9 [23].

$$\left[\frac{nFs}{2^{j+1}}, \frac{(n+1)Fs}{2^{j+1}}\right] \quad n = 0,1,2,3,\dots 2^{j} - 1 \tag{9}$$

Fig. 13 shows an example of a 2nd level wavelet tree structure in which the same logic decomposes at further levels to make the wavelet packet tree more accessible.

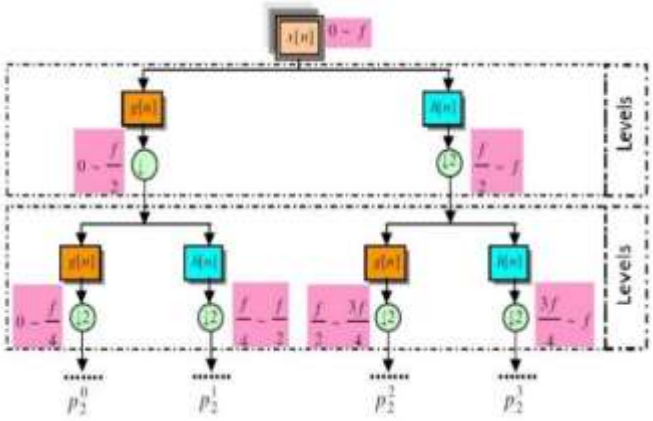

Figure 13. Energy change of the harmonic in the relevant frequency range according to the resolution level

Fig. 13 shows 2nd level multi-resolution analysis and its associated frequency ranges. Suppose that x(t) signal has N = 2^L samples and decomposed up to s. level packet analysis. In this case, here will be 2^s nodes/packets or frequency bands, and there are $2^{(L-s)}$ or N / 2^s wavelet packet coefficients in each level band. For m=0,1…..,2^s-1, wavelet packet coefficients of m node and k level is expressed as $p_s^{2m}[k]$ and calculated as follow:

$$X_{RMS}^{m} = \sqrt{\frac{1}{N}\sum_{k=1}^{N/2^s}\{p_s^m[k]\}^2} \tag{10}$$

When the wavelet tree analysis is done using the db20 family, which was chosen based on the Shannon entropy result, the effective value of the wavelet coefficients of each node is

determined using equation 10. Analysis up to level 6 is necessary to meet the frequency range criteria (above 2kHz). However, in the sixth level, the switching frequency corresponds to a signal with a frequency range of 27.344 - 31.250kHz and the greatest amplitude given in Fig. 14. The switching frequency is more readily noticed at the 11th level for the comparative assessment of wavelet packet analysis with STFT since there are nodes with a band gap of 122.0703 Hz. As a result, the switching frequency falls within the range of 29.785 - 29.907.

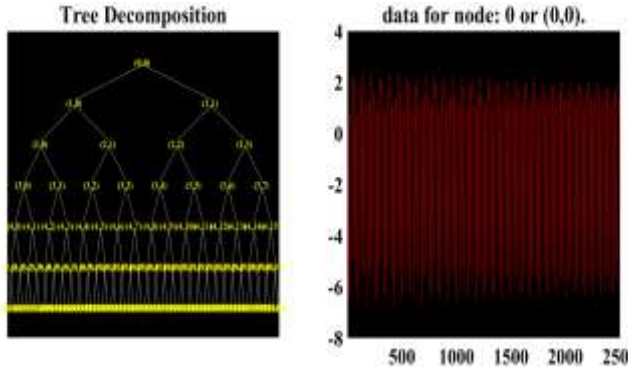

(a)

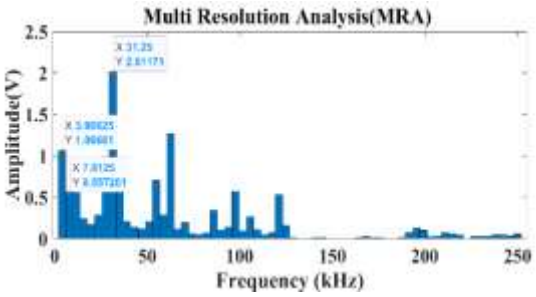

(b)

Figure 14. Energy change of the harmonic in the relevant frequency range according to the resolution level

In summary, discrete wavelet transform gives harmonics a wider band. MRA was used to harmonic analysis detailed to evaluate whether harmonic leakage exists. Wavelet analysis has performed an alternative for STFT. However, because wavelets cover a wide frequency range, they are inadequate for emissions investigation.

7. EMI FILTER for BUCK CONVERTER

It is necessary to utilize filters to reduce high-frequency noise because filters are frequently situated and created to satisfy standard criteria. Filtering makes a product less susceptible to any existing high-frequency noise in the environment while also preventing the product from causing high-frequency interference. Early design consideration of EMI could assist designers in efficiently meeting EMC regulations prior to implementation. To reduce design process and costs, EMI forecast should be properly taken care of by precise design. In this section in PSIM software environment suppression of noise was simulated and given in Fig. 17. PI controller of output voltage and LISN are seen in Fig. 15 and Fig. 16. Also, output voltage of converter is given in Fig. 18.

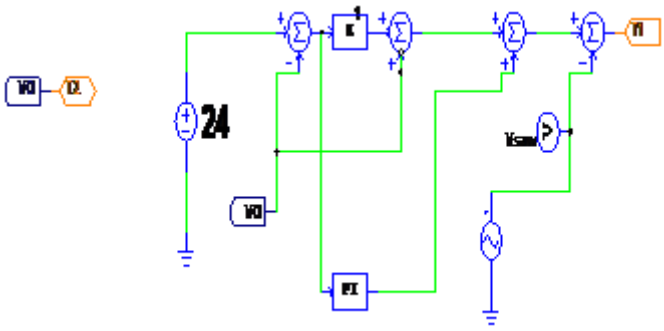

Figure 15. PI controller of buck converter

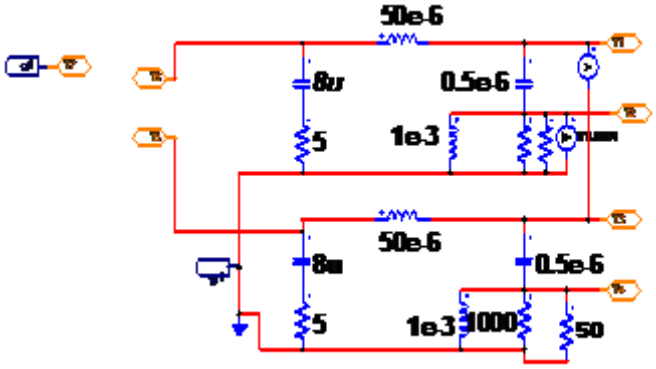

Figure 16. LISN device of buck converter

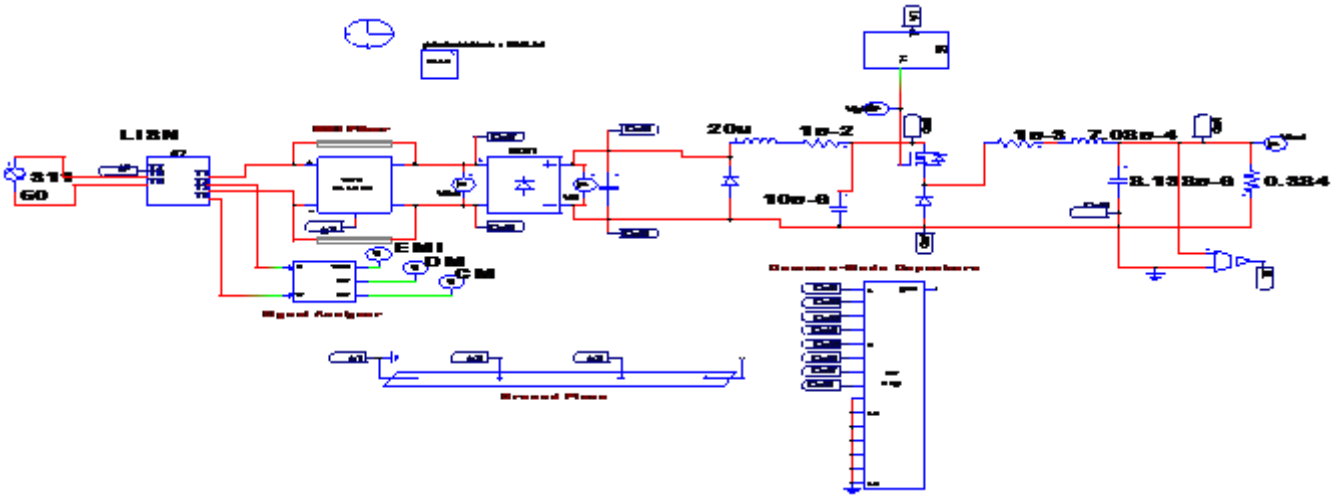

Figure 17. EMI Filter Design of Buck Converter (CISPR 22 Class-B)

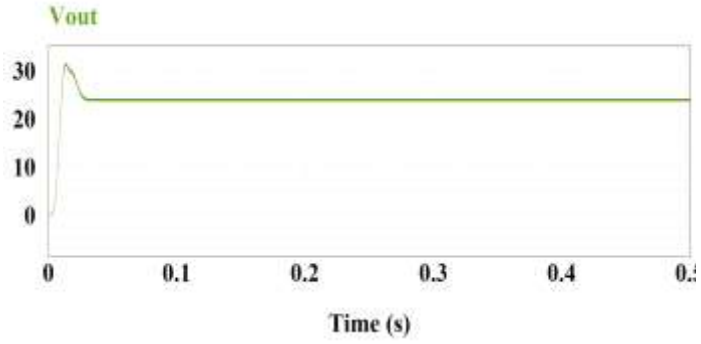

Figure 18. Output voltage of Converter

EMI, DM, and CM signals are obtained through 'signal analyzer' in the simulation and shown in Fig. 19.

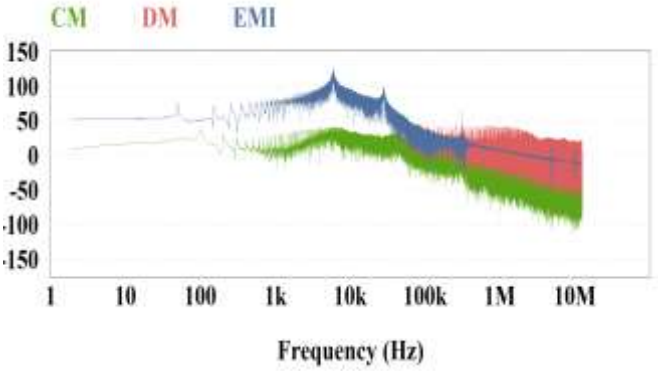

Figure 19. EMI, DM, and CM signals

For suppression of noise EMI filter parameters given in Table IV. When these filter parameters used for EMI filter, suppression of noise is supported with Fig. 20.

TABLE IV
EMI FILTER PARAMETERS

	Parameter	Value
EMI Filter	Filter enable	0
	Filter type	0
	Num. stage	1
	Cx	6.13nF
	R_Cx	0
	L_Cx	1.2µH
	Cy	2.04 nF
	R_Cy	0
	L_Cy	15.78 µH
	k_leakage_cm	0.05
	R_cm	0.1mΩ
	C_cm	0
	R_dm	0.1mΩ
	Cd	0
	R_Cd	0
Common Mode EMI	freq_cm_EMI	59.9kHz
	Amp_cm_EMI	55
	Amp_cm_EMI_Std	36.8
Differential Mode EMI	freq_dm_EMI	59.5kHz
	Amp_dm_EMI	128.6
	Amp_dm_EMI_Std	36.8
Common Mode Capacitance	Ccm1,Ccm2	500pF
	Ccm3,Ccm4, Ccm7,Ccm8	50pF
	Ccm5,Ccm6	100pF

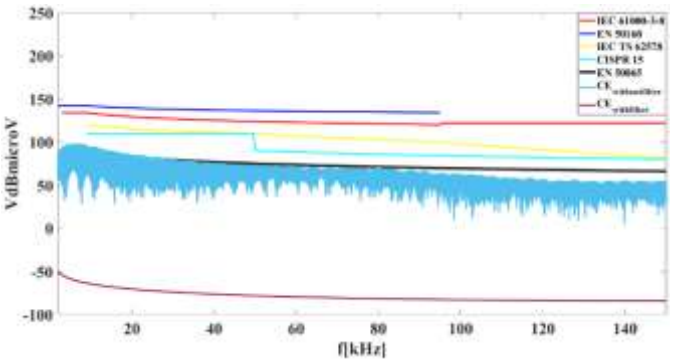

Figure 20. Suppression of noise

8. CONCLUSION

The goal of this project was to emphasize the importance of CEs, which will become more widespread as the use of electric vehicles and led driver grows in general. In this study power quality analysis of conducted emissions was performed for buck converter in MATLAB and PSIM software environments. The solution approach to reduce the power quality problem based on this converter is explained. Reducing CE with EMI filter design is difficult for power electronics applications, particularly inverters. Because a filter's design is unique to the circuit, it is necessary to construct a noise model of the circuit. In this research also, spectrum of the signals was calculated using the STFT technique in MATLAB™ tools for the evaluation of disturbances The intended result could not be attained using db20, the most appropriate wavelet family for the signal among the standard wavelet families. The EMI requirements for converters because of international standards are discussed. It has been demonstrated that conducted emissions are higher in the case of nonfilter buck converter situation. As a result, the CE attenuation was preserved this buck converter system in PSIM. Another results are summarized as below:

• Power quality evaluation of DC-DC converter performed in Matlab simulation environment in terms of emissions.

• LFSD increased in loaded condition compared to unloaded condition. Considering the last half-time of the sampling time, which is out of the transient state, generally the CE to the grid side increases depending on the load increase.

• APD and ripple index decreased as the input voltage increased.

• CE and DFSB increase as the input voltage increases.

• While the DFSB index decreases in the last window intervals of the sampled time compared to the first time intervals, the fluctuation remains constant.

• When the spectrogram of the signal (analysis that gives the energy of the frequency dependent on time) of the 6 kHz frequency other than the switching frequency in the analysis with STFT is examined, it has been observed that this frequency does not occur during the entire sampling frequency, but during the temporary period. However, in wavelet transform, both low and high frequency analysis can be performed at the same time. At the same time, the change in frequency over time can be observed. For this purpose, when the discrete wavelet transform analysis was performed first, it

was seen that the energy of the relevant frequency range and the amplitude responses of the frequencies in the STFT were compatible. In order to make a more detailed and comparison, spleen packet analysis was performed by choosing the most suitable family from the traditional wavelet family. At the same time, the amplitude of the harmonics corresponding to the frequency range at the nodes was calculated to evaluate for the standard limits. However, since the response of the harmonics is incompatible with the STFT, it was thought that the analysis with the 'Vaidyanathan filter' used in the amplitude response of the harmonics in the wavelet packet analysis would be more appropriate.

ACKNOWLEDGEMENT

This work was supported in part by Ondokuz Mayis University under Projects PYO.MUH.1904.21.011 and PYO.MUH.1906.21.002

REFERENCES

[1] D D. Ritzmann, et al.,"Comparison of measurement methods for 2–150-kHz conducted emissions in power networks", IEEE Transactions on Instrumentation and Measurement,vol 70, pp. 1-10, 2020.

[2] A. D. Khilnani, et al. "Power quality analysis (0-2kHz) in DC/DC converters under steady state and transient conditions", presented at the International Symposium on Electromagnetic Compatibility-EMC EUROPE, Amsterdam, Netherlands, Aug. 2-5,27-30 2018.

[3] K. Niewiadomski, et al., "Time-domain assessment of data transmission errors in systems with multiple DC/DC converters", presented at the 2020 International Symposium on Electromagnetic Compatibility-EMC EUROPE, Rome, Italy, Sep. 23-25, 2020.

[4] A. Onur et al., "Determination of the optimum Hybrid renewable power system: a case study of Istanbul Gedik University Gedik Vocational School", Balkan Journal of Electrical and Computer Engineering, vol. 7, no.4, pp. 456-463, 2019.

[5] E. Aykut, et al. "Techno-economic and environmental analysis of grid connected hybrid wind/photovoltaic/biomass system for Marmara University Goztepe campus", International Journal of Green Energy, vol. 17, no.15, pp. 1036-1043, 2020.

[6] L. Ensini, et al. 2018. "Conducted emissions on DC power grids", presented at the 2018 International Symposium on Electromagnetic Compatibility (EMC EUROPE), Amsterdam, Netherlands, Aug, 27-30, 2018.

[7] D. Kumar, et al., "DC microgrid technology: system architectures, AC grid interfaces, grounding schemes, power quality, communication networks, applications, and standardizations aspects", IEEE Access, vol. 5, pp. 12230-12256,2017.

[8] F. Leferink, "Conducted interference, challenges and interference cases", IEEE Electromagnetic Compatibility Magazine, vol. 4, no. 1, pp. 78-85, 2015.

[9] A. Mariscotti, "Discussion of power quality metrics suitable for DC power distribution and smart grids", presented at the Proc. 24th IMEKO TC4 Int. Symp, Sep. 17-20, Xi'an, China, 2019.

[10] M., Miloudi, et al.,"Common and differential modes of conducted electromagnetic interference in switching power converters", Rev. Roum. des Sci. Tech. Ser. Electrotech. Energ., vol. 62, no. 3, pp. 246–251, 2017.

[11] S. Weßling and S. Dickmann, "Prediction of conducted emissions produced by a DC-DC-converter using component parasitics and partial inductances", presented at the 2013 International Symposium on Electromagnetic Compatibility, Brugge, Belgium, Sep. 2-6,2017.

[12] E.A. Larsson, et al., "Measurements of high-frequency (2–150 kHz) distortion in low-voltage networks", IEEE Transactions on Power Delivery, vol. 25, no. 3, pp. 1749-1757, 2010

[13] F. Krug and P. Russer, "Quasi-peak detector model for a time-domain measurement system." IEEE Transactions on Electromagnetic Compatibility, vol. 47, no.2, pp. 320-326, 2005.

[14] G. Spadacini, et al., "Conducted emissions in the powertrain of electric vehicles", presented at the 2017 IEEE International Symposium on Electromagnetic Compatibility & Signal/Power Integrity (EMCSI), Washington, DC, USA, Aug 7-11, 2017.

[15] G. Spadacini, et al., "SPICE simulation in time-domain of the CISPR 25 test setup for conducted emissions in electric vehicles", presented at the 2015 Asia-Pacific Symposium on Electromagnetic Compatibility (APEMC), Taipei, Taiwan, May 26-29, 2015.

[16] A. Larrson, and M. Bollen “A proposal for emission and immunity of equipment including power-line communication.” [Online]. Available: https://www.arbenelux.com/wp-content/uploads/2017/11/Tekbox-TBOH01-LISN.pdf. [Accessed: 7-Dec-2022].

[17] N. Mutoh, et al., "Control methods for EMI noises appearing in electric vehicle drive systems", presented at the Twentieth Annual IEEE Applied Power Electronics Conference and Exposition, Austin, TX, USA, Mar, 6-10, 2015.

[18] H. Shall and M. Kadi, "Study of the radiated emissions of an electric vehicle battery charger during the charge cycle", presented at the 2015 IEEE 12th International Multi-Conference on Systems, Signals & Devices (SSD15), Mahdia, Tunisia,Mar 16-19,2015.

[19] P.K.P. Ferraz, et al., "A high frequency model for predicting the behavior of lithium-ion batteries connected to fast switching power electronics", Journal of Energy Storage, vol. 18, pp. 40-49,2018.

[20] T. Karaca, et al., "EMI-receiver simulation model with quasi-peak detector", 2015 IEEE International Symposium on Electromagnetic Compatibility, Dresden, Germany, Aug 16-22, 2015.

[21] T. Sonmezocak et al., "High performance adaptive high performance adaptive active harmonic filter design for nonlinear led loads", Light & Engineering, vol. 30, no.1, 2022.

[22] S. Dursun, et al., "Comparative analysis of lighting elements’ effects on electric system", European Journal of Technique (EJT), vol. 11, no. 2, pp. 153-164, 2021.

[23] V. Fahri, "RMS and power measurement using the dual-tree complex wavelet transform", Scientific Research and Essays, vol. 5, no. 18 pp. 2645-2655, 2010.

BIOGRAPHIES

Secil GENC was born in Elazıg in 1992. She received her B.Sc degree from Firat University in 2014 and M.Sc. degree from Ondokuz Mayis University in 2018. She is currently pursuing Ph.D. degree in Electrical and Electronics Engineering Department at Ondokuz Mayis University, Samsun, Turkiye. She is also a research assistant at Ondokuz Mayis University. Her research interests include power electronics, electromagnetic interference, renewables and machine learning.

Okan OZGONENEL was born in Samsun in 1967. He worked for Goztepe SSK Hospital as an engineer from 1989 to 1991. Then he received a special grant and promoted as Lecturer in Amasya Technical and Vocational Higher School by means of World Bank Second Industrial Training Project. He has worked there for 10 years and then joined Ondokuz Mayis University, Electrical & Electronic Engineering Department in 2002. He was promoted as full Professor in 2014 and since then he has been working for Ondokuz Mayis University where he is full time Professor. He joined The University of Nottingham many times for his post-doctoral studies.
His main research includes power system modeling, protection, and renewables.

Orkut Onat YILDIZ graduated from Karadeniz Technical University's Electrical Department in 2002 and He graduated from Anadolu University's Faculty of Economics in 2019. He worked as a laboratory supervisor at Borsan Kablo from 2006 to 2010, as a Quality Manager from 2010 to 2018, and as an R&D manager since 2019.

İbrahim Hakkı KILIÇ received his bachelor's degree in Materials Science and Ceramics Engineering from Dumlupnar University in 2011, and he is currently pursuing my master's degree in the Textile Engineering Department at Istanbul Technical University. He worked as a production manager at Işıldar Aydınlatma between 2013 and 2017, and as of 2019, He worked as a lighting group R&D and quality manager at Borsan Kablo ve Lighting. His specialties include 3D modeling and automation systems.
.

European Journal of Technique

journal homepage: https://dergipark.org.tr/en/pub/ejt

Vol.12, No.2, 2022

Analysis and Characterization of the Soteria Mosaic in the Antakya Museum with Archeometric Techniques

Hülya IŞIK[1] and Abdulkadir LEVENT[2*]

[1] Batman University, Archeometric Department, Batman, Turkey. (72hulyaisik@gmail.com).
[2*]Batman University, Chemistry Department, Batman, Turkey.(leventkadir@hotmail.com).

ARTICLE INFO

Received: Aug., 11. 2022
Revised: Sep., 07. 2022
Accepted: Sep, 10. 2022

Keywords:
Power systems
Smart grid
Harmonics
Fourier series
Newton Raphson

Corresponding author: *Abdulkadir Levent*

ISSN: *2536-5010* | e-ISSN: *2536-5134*

DOI: https://doi.org/10.36222/ejt.1160995

ABSTRACT

Mosaic, like all other branches of art, is one of the most important aesthetic ties that human beings establish with the world. When we look at the mosaic, we can see the changing traces of the past and relive the time that has been forgotten for a long time. Mosaic is an eternal art that has endured natural conditions such as wind and rain and has survived to the present day with slight damages.

This study was carried out in three stages. First, the stone tessera of the Soteria mosaic were color analyzed using the portable Color Detector X-Rite CAPSURE precision color measuring instrument. The tesserae were then analyzed using the Energy Dispersive Portable X-Ray Fluorescence Spectrometer device, which is a non-destructive method for quantitative analysis of its elements. In the next stage, petrographic analysis was performed in laboratory environment to determine the rock type and minerals of 10 stone tessera belonging to the Soteria mosaic.

As a result, the examination of the qualities and contents of the materials used in the mosaics; By establishing a connection between the past, present and future, it will be able to make important contributions in revealing the reasons why the mosaics have survived to the present day.

1. INTRODUCTION

For the first time in human history, the concept of art began to emerge with the figures of the mother goddess shaped by hand from the earth and the murals made in the caves, and has come down to the present day as a serious activity put forward by humanity for centuries. Understanding of art; It has shown different characteristics due to the different lifestyles of human communities and their being in different geographies, which has led to an artistically rich accumulation [1]

Mosaic is the technique of lining up small pieces of different types (wood, metal, glass, etc.) side by side and flattening them by embeding them in mortar. Unlike many arts, mosaic is not a high-cost art, but even an art in which waste materials are re-evaluated [2]. As Vasari said, "Mosaic is an eternal art. The things that best resist the blows of wind and water are those made with color" [3]. Mosaic art has become a form of expression of the traces and forgotten time experienced in the past [4].

Hatay is the place where civilizations, ideas and art come together between East and West. Since it has a very important place in terms of mosaics, you can see some of the most distinguished mosaics of the world in Hatay Museum.

In this study, the Soteria mosaic, one of the most important mosaic works in the Hatay Archaeological Museum, was discussed (Figure 1). Soteria Mosaic is one of the most important mosaic works exhibited in Hatay Archaeological Museum. This mosaic belonging to the Roman period is dated to the 5th century a.d. It was found as the flooring of a bathroom in Narlıca village of Antakya. In the very center of the Soteria Mosaic, which is in an octagonal form, there is a bust of a woman and inscriptions around it. At the beginning of the mosaic, a wreath of leaves is depicted as a full-bodied woman carrying a necklace in Byzantine style on her chest. The perimeter of the mosaic is decorated with geometric patterns [5].

According to the bibliography research, we can summarize the studies on the structural analysis and characterization of mosaics as follows. In the study titled "Analysıs of Materials Used in Mosaic Machig", first of all, the definition of mosaic was made, its development in the historical process was included and then the use of the mosaic in the structure and the performance characteristics expected from the material were discussed [6]. In the study titled "Characterization of the Mosaic Mortars of the Ancient City of Perge", information was given about the characterization, qualities and construction technologies of

mortars and plasters with important functions such as stone, brick, wood and iron in historical buildings [7]. In the study titled "Painting Analysis of the Mosaics of Antioch and Zeugma", based on the mosaics in Zeugma, they concluded that the importance given to mosaic construction in this city about 1800 years ago was probably the workshops and a mosaic school in the city. In their studies, they stated that mythological stories gained weight as subjects in Zeugma mosaics[8]. (Şahin, 2010). They analyzed the metal, mortar and mosaic samples unearthed in the Maltepe Rescue Excavation with the Energy Dispersed Portable X-Ray Fluorescence Spectrometer (P-EDXRF)[9].

According to our bibliography research, it was not found that the structure of Soteria mosaic was evaluated qualitatively and quantitatively using archaeometric techniques. In the light of this information, the Soteria mosaic, one of the most important mosaic works in the Hatay Archaeological Museum, was discussed in this study. In order to characterize the structure of the Soteria mosaic qualitatively and quantitatively, 21 stone tessera samples were examined. First of all, color analysis was performed with the portable Color Detector X-Rite CAPSURE precision color measuring device. After the color analysis, chemical analysis was performed on the tessera belonging to Soteria mosaic with the P-EDXRF method, which is a non-destructive method. Thanks to the properties in the P-EDXRF device, it is used in the characterization studies of the elemental composition of archaeological and artistic materials [10]. The P-EDXRF device has significant advantages over other analytical techniques with its easy to use, fast results and analysis feature without destroying the material, especially with the possibility of on-site analysis. In addition, petrographic analysis was performed to determine the color, rock type, minerals, hardness and texture of 10 stone tessera belonging to the Soteria mosaic taken from the museum in the laboratory environment.

Figure 1. The places where the Soteria mosaic exhibited in the Hatay museum is analyzed.

2. MATERIAL and METHOD

A total of 20 stones belonging to the Soteria mosaic were examined with permission from the Hatay museum for tessera analysis. Places marked in blue (1-10) are taken for laboratory environment. Places marked in red (11-20) were analyzed on-site at the Hatay Museum (Figure 1). The tesserae selected for the laboratory environment were deformed from the edges of the mosaic in a way not to damage the pattern of the mosaic, and broken tessera were preferred. In order for the selected samples to give healthy results, they are soaked in pure water and softened, and the dust and dirt on them are cleaned with the help of soft-tipped brushes and scalpels.

For the archaeometric analysis of stone tessera, the following operations were carried out, respectively.

1. Analysis was performed with the P-EDXRF device, which is a non-destructive method to determine which compounds or elements (CaO, MgO, SiO2, Fe2O3, Al2O3, etc.) are present in the chemical structure of the tesserae (Figure2). Samples 1-20 were analyzed with the geochem mode of the P-EDXRF instrument, while sample 21 was analyzed with soil mode (Figure 3-4).

Figure 2. The process of analyzing samples with the P-EDXRF instrument.

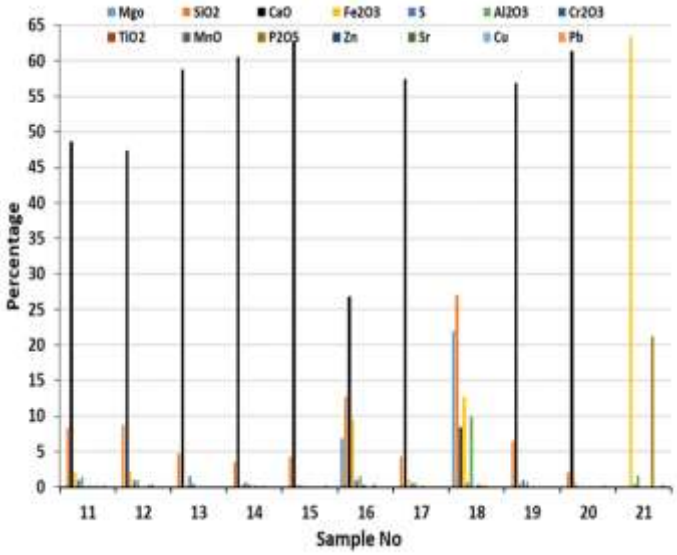

Figure 3. Distribution of P-EDXRF Analysis Results of MgO, SiO2, CaO, Fe2O3, Al2O3, Cr2O3, As, TiO2, MnO, P2O5, S, Zn, Sr, Cu and Pb in Taş Tessera(1-10).

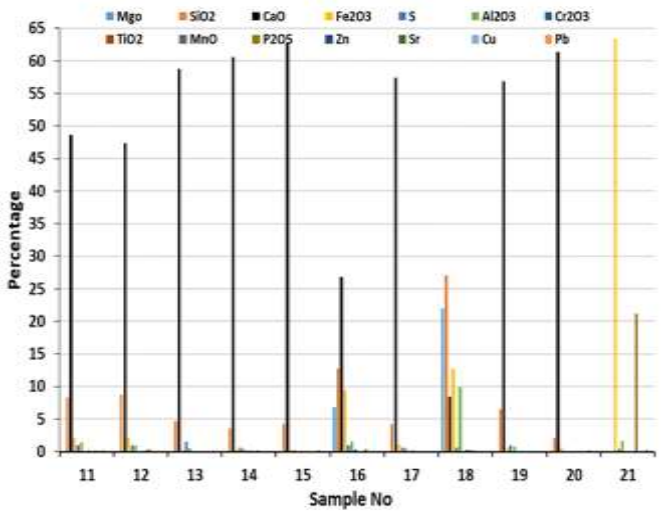

Figure 4. Distribution of P-EDXRF analysis results of MgO, SiO2, CaO, Fe2O3, Al2O3, Cr2O3, As, TiO2, MnO, P2O5, S, Zn, Sr, Cu and Pb in Taş Tessera (11-21).

2. Color analysis was performed for 10 samples (Example-11-20) examined on-site in Hatay museum to determine the code of the color of the tessera in the munsell catalog, using the portable Color Detector X-Rite CAPSURE precision color measuring device (Figure 5). According to the color code obtained as a result of the analysis, equivalent color was determined from Munsell Color Catalog (Table 1)[11].

Figure 5. X- Color analysis with Rite CAPSURE device

3. Petrographic Analysis was performed to determine the Rock Type, Hardness, Texture, Rock and Minerals of 10 stone tessera (Example 1-10) taken for laboratory environment. The Stone Tessera was photographed with the Leica DFC280 digital camera (Figure 5) and evaluated with the Leica Qwin digital imaging program (Table 2). Petrographic descriptions of thin sections are given in detail in table 3.

Table 1. Color analysis results according to the Munsell catalogue of stone tessera.

Sample No	Y(Yellow), G(Green), R(Red)	Colour	Munsell Cat. Equivalent Color
11	5 YR 4/4	Brown	
12	5 GY 4/1	Green	
13	2.5 H 8/2	White	
14	10 YR 6/4	Yellow	
15	10 YR 4/1	Brown	
16	5 YR 2.5/1	Black	
17	2.5 H 7/2	White	
18	N4.25	Dark Grey	
19	5 YR 4/2	Red	
20	10 R 5/1	Brown	

Table 2. The results of color analysis of stone tessera.

S. No	L	a	b	Colour	Eq. Color
1	11,0197	1,2029	-0,3462	black	
2	19,2067	1,3607	-0,9680	black	
3	16,3326	2,8304	2,5137	black	
4	15,8228	0,4961	3,1370	black	
5	49,1020	2,9112	18,8351	Cream	
6	45,5402	0,0859	22,8356	Yellow	
7	52,5901	3,3480	9,7531	white	
8	46,6333	5,1693	10,6312	white	
9	40.2910	4,2228	11,7770	white	
10	18,8053	6,5806	8,3087	Brown	

L: 0/100; White/Black, **A:** 0/-60; Green and 0/+60; Red, **b:** 0/-60; Blue and 0/+60; Yellow

Table 3. Petrographic properties of Hatay Soteria Mosaic tessera specimens.

No	Rock Type	Tissue	Mohs	Rocks and Minerals
1-4	Serpentinite	Sieve	5–5.5	Its structure, which contains mainly antigolite, includes a small proportion of chrysotil, chromite, hematite and magnetite.
5	Breschic Limestone	Breschic	2.5 - 3	Its structure, which mainly contains calcite, includes limestone, limonite, hematite, fossil and fossil shells.
6-7	Crystallized Limestone	Crystallized	2.5 - 3	In its structure, which mainly contains calcite, aragonites are seen in places.
8	Biosparitic Limestone	Sparitic	2.5 - 3	Its structure, which mainly contains calcite, includes fossils (nummulites and alveolina species) and fossil shells.
9	Biomicritical Limestone	Micritical	2.5 - 3	Its structure, which mainly contains calcite, includes aragonite and fossil and fossil shells.
10	Listvenit	Crystallized	4.5– 5	In the cavities in the structure where a high degree of carbonation is seen, quartz, hematite, limonite, calcite and clay accumulation and silicization in structural fractures / cracks are included.

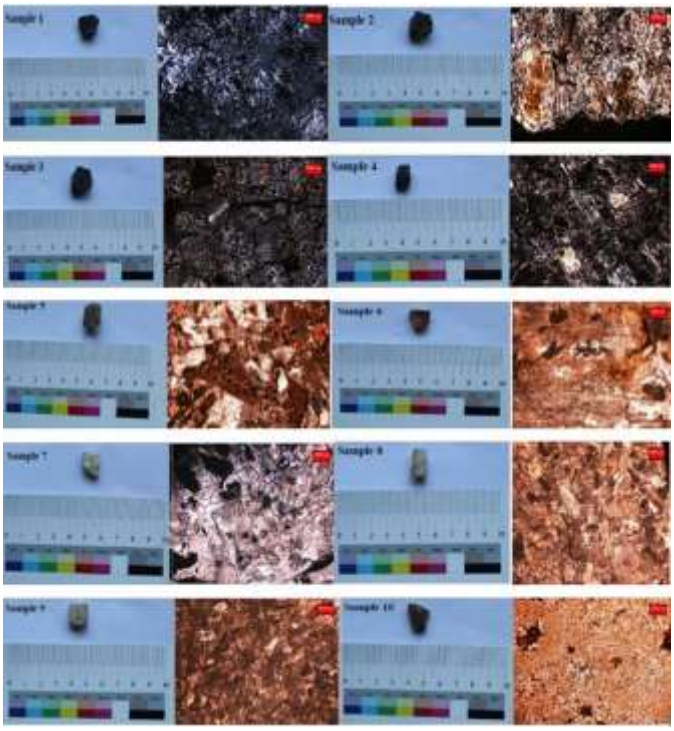

Figure 6. General and thin section images of samples

3. DISCUSSION and CONCLUSION

In the presented study, the qualitative and quantitative analysis of Stone Tessera was performed with Color Detector X-Rite, P-EDXRF and petrographic techniques.

As a result of color analysis of the Stone Tessera (Examples 1-4), it was determined that the samples were black as shown in Table 2. When Figure 3-4 was examined in detail, as a result of the analysis of these tesserae with P-EDXRF, SiO 2, MgO, CaO and Fe2O3 compounds were detected at a higher rate than the other components. Petrographic analysis was performed to support the analyzes and to determine the rock structure in the structure of the mosaics. According to the results of the analysis, it was determined that these stone tesserae (Table 3) belonged to the serpentite rock species (Figure 6). The mineral contents of this rock species, mainly antigoride, include a small percentage of chrysotyll, chromite, hematite and magnetite. Serpentine is dark green, black or red black [12]. In addition to having a wide range of mineral contents, the serpentinite rock type usually has a chemical composition of Mg2(Si2O5).(OH)4 species[13]. According to the results of petrographic analysis, P-EDXRF based on the minerals and chemical composition of the serpentite rock species supported the compound ratios (MgO, SiO2 and CaO) obtained as a result of the analysis. In addition, due to the hematite and chromite it contains, it is estimated that the Fe2O3 compound is seen and the color comes from this compound.

According to the color analysis result of Sample 5 (Table 2), the P-EDXRF chemical analysis of the sample, which was determined to be a cream-colored stone tessera, determined that the ratio of CaO compound was very high compared to other chemical components as shown in Figure 3-4. As a result of the thin section analysis (Figure 6), it was determined that this rock species was Breşik limestone and that limestone, limonite, hematite, fossil and fossil cavals were determined in the structure containing calcite in this rock type. According to the results of petrographic analysis and P-EDXRF analysis, the high incidence of CaO compound is estimated to be due to the calcite mineral contained in Breşik limestone (Table 3).

According to the color analysis results of Sample 6-7 (Table 2), CaO, SiO2 and MgO compounds were found to be higher than other chemical components in the chemical structure of these samples as shown in Figure 3-4 as a result of P-EDXRF chemical analysis of the samples determined to be yellow and white colored stone tessera. According to the results of the thin section analysis (Figure 6), it was determined that the rock type of the 6 and 7 samples were crystallized limestone. In this rock species, it was determined that aragonites were included in its structure, which mainly contains calcite (Table 3). As a result of P-EDXRF analysis, the high incidence of CaO compound is estimated to be due to CaCO3, the chemical composition of Calcite and Aragonite [14].

According to the color analysis result (Table 2), the sample (example 8), which was determined to be white colored Stone Tessera, was determined at a higher rate than other chemical components as shown in Figure 3-4 as shown in Figure 3-4 as a result of P-EDXRF chemical analysis. According to the results of the thin section analysis (Figure 6), the rock type of the sample is estimated to be Biosparitic limestone (Table 3). In this rock species, the main calcite-containing structure includes fossils (numulites and alyeoline species) and fossil cavities The high incidence of CaO compound as a result of P-EDXRF analysis is estimated to be due to CaCO3, the chemical composition of calcite[15].

According to the results of color analysis in Table 2, the P-EDXRF chemical analysis of sample 9, which was determined to be a white stone tessera, determined the CaO compound at a higher rate than other chemical components as shown in Figure 3-4. According to the results of the thin section analysis (Figure 6) it is estimated that the rock type of the sample is Biomicritical limestone. In this rock species, the structure containing mainly calcite includes aragonite and fossil/fossil cavities in places (Table 3). As a result of P-EDXRF chemical analysis, the high incidence of CaO compound is estimated to be due to CaCO 3 compound, which is the chemical composition of Calcite and Aragonite[15].

According to the color analysis result (Table 2), the P-EDXRF chemical analysis of the sample-10, which was determined to be brown colored Stone Tessera, determined at a higher rate than the other chemical components as shown in Figure 3-4. According to the results of the thin section analysis (Figure 6), it was determined that the rock type of the sample was Listvenit (Table 3). In this rock type, there is a high degree of carbonation in the cavities in its structure with quartz, hematite, limonite, calcite and clay accumulation and silicifications in structural fractures / cracks. Listvenites are defined as carbonated and various proportionally silicized equivalents of serpentined ultramafic rocks in ophiolithic complexes[16]. As a result of petrographic analysis, the chemical composition of CaO and Quartz is SiO 2, and the appearance of CaO, MgO andSiO 2 compounds as a result of P-EDXRF analysis shows that the analysis supports each other.

Color Detector X-Rite CAPSURE device analyzes the remaining samples (Sample 11-20) and their colors are determined and shown in Table 1. As a result of the analyzes, 3 Brown, 2 White, Yellow, Black, Dark Gray, Red and Green colors were determined. According to the results of P-EDXRF

chemical analysis (Figure 3-4), it is seen that CaO and SiO2 compounds are higher than other chemical components. It is estimated that the presence of TiO2 (Figure 3-4) compound in very few samples made in the Hatay museum is seen as a trace element because the back of the mosaic is covered with cement mortar. As a result of P-EDXRF chemical analysis performed in Soil mode in the region of cement mortar (Figure 3-4), CaO and TiO 2 compounds are seen at a high rate because the top is covered with lime. The detection of TiO2 as a trace element in the samples examined on site without taking a tessera sample from the mosaic in the Buda Hatay Museum supports this result.

When Figure 3-4 is examined in detail, according to the results of P-EDXRF chemical analysis, CaO, SiO 2, MgO and Fe2O3 chemical compounds with color-determining properties were detected at a high rate. In thin section analysis, the detection of limestones in general supported the P-EDXRF chemical component analysis.

When the geological structure of Hassa district of Hatay is investigated [17]; In the Amanos Mountains, Serpentinite, Limestone, Limestone, Limestone, Sandstone, Quartzite and Pebble are seen intensively. Based on this study, it has strengthened the opinion that the tessera belonging to the Soteria mosaic, which is exhibited in the Hatay Museum and which we have discussed, may have been procured from the Hatay region when evaluated according to the results of the analyzes.

As a result of these archaeometric analyzes and evaluations; the fact that the mosaics have survived to the present day shows how durable materials were used in their construction. In addition, it shows that this study may shed light on the studies to be carried out in this field in the future scientific studies as well as guiding the selection of materials during the restoration and conservation works that can be done.

REFERENCES

[1] Anonymous, Art and Design, Mosaic Analysis, Ministry of National Education, Ankara, 3-5, 2015.

[2] A.C. Üstüner, Mosaic Art, Engin Matbaacılık, Istanbul, 2002.

[3] A. Courtille, Konstantinopolis Mozaikçisi, Menekşe Tokyay, Doğan Kitapçılık, İstanbul, 2004.

[4] D. Tabanlı, Examination of Roman Period Mosaics on the Example of Ephesus, Master's Thesis, Dokuz Eylül University Institute of Fine Arts, Department of Ceramics, Izmir.

[5] Hatay Archeology Museum House of Mosaics, 2015, https:// www.rotasenin. com/ hatay-arkeoloji-muzesi (Date of Access: 24.07.2022). 2007.

[6] N. Efe, Analysıs of Materıals Used In Mosaic Makıng, Master's Thesis, İstanbul Technıcal University Instıtute of Scıence and Technology, İstanbul, 2009.

[7] T. Uğur, Characterization of mosaic mortars belonging to the ancient city of Perge, Istanbul University / Institute of Social Sciences / Department of Conservation and Restoration of Movable Cultural Assets. 2011.

[8] M. Sahin, Mosaic Art Antakya and Zeugma Mosaics Painting Analysis, Master's Thesis, Anadolu University Institute of Fine Arts. Eskisehir, 2010.

[9] M. Aydın, A. Zararsız and S. Demirci, Archaeometric Studies on Some Finds Obtained from the Late Roman-Early Byzantine Period Ankara Maltepe Rescue Excavation, 26. Archaeometry Excavation Results Meeting, Istanbul, 2010.

[10] M. Adın, Ensuring the Return of the Stolen Original Golden-Winged Seahorse (Hippocampus) to Turkey by Portable X-Ray Fluorescence Spectrometry Method, Turkish Academy of Sciences Journal of Archaeology (TÜBA-AR), 20, 147-157. 2017.

[11] Digital Archaeological Archive of Comparative Slavery, 2019, (https://www. Daacs.org/about-the-database/database-structure/context-table/) History of Agriculture. 24.07.2022.

[12] N. Rajakaruna, RS. Boyd, Serpentine Soils. In: Oxford Bibliographies in Ecology. Ed. David Gibson, Oxford University Press, New York. 2014.

[13] E. Özdemir, B.G. Özbey, L. Kurt, A. Bölükbaşı, Serpentine Ecology And Contributions To The Serpentine Flora Of Turkey, Journal Of Soil Science And Plant Nutrition, 5 (1), Ankara, 22-33. 2017.

[14] M. Önal, K. Karaman, Faculty of Engineering Department of Mining Engineering, Minarets, (https://slideplayer.biz.tr/slide/292.

[15] G. Buisson, M. Leblanc, Gold-bearing listwaenites (carbonatized ultramafic rocks) from ophiolite complexes. In Metallogeny of Basic and Ultrabasic Rocks, Gallagher JM, Ixer RA, Neary CR (eds). Transactions - Institution of Mining and Metallurgy: London; 121–132. 1986.

[16] A. Atasoy, Soil Geography of Hassa District (Hatay), International Journal of Social Research, 10 (48), 256-257. 2017.

BIOGRAPHIES

Hülya Işık received her BSc and MSc degrees in 2015 and 2019, respectively, from Department of Archeometric, Faculty of Science, Batman University (Batman, Turkey). Her research interest focuses on archaeometry and cultural heritage preservation and restoration.

Abdulkadir Levent received his BSc, MSc and PhD degrees in 1998, 2001 and 2007, respectively, from Department of Chemistry, Faculty of Science, Yüzüncü Yıl University (Van, Turkey). Then, he joined Batman University (Batman, Turkey) in 2010. He became Associate Professor in 2012 and full professor in 2016 at the same university. His research interest comprises the development new electrochemical sensors for the determination of a wide range of organic compounds of pharmaceutical, environmental, biological and clinical interest, and spectrometric and chromatographic methods.

European Journal of Technique

journal homepage: https://dergipark.org.tr/en/pub/ejt

Vol.12, No.2, 2022

Comparison of Simulation Results for 25 kW Power Output Rooftop PV System

Taner Dindar[1*], Vedat Esen[2], Ali Samet Sarkın[3]

[1*]Ankara University, Nallıhan Vocational High School, Nallıhan, Türkiye. (e-mail: tdindar@ankara.edu.tr).
[2] Istanbul Topkapı University, Electrical and Electronics Engineering Department, 34087, Istanbul, Türkiye. (e-mail: vedatesen@topkapi.edu.tr).
[3] Osmaniye Korkut Ata University, Kadirli Vocational School of Higher Education, Osmaniye, Türkiye. (e-mail: sametsarkin@osmaniye.edu.tr)

ARTICLE INFO

Received: Sep., 14. 2022
Revised: Nov., 05. 2022
Accepted: Nov, 29. 2022

Keywords:
Photovoltaic
Solar energy
PV simulation
Solarius
PVsyst
PVGIS
PV*SOL

Corresponding author: *Taner Dindar*

ISSN: *2536-5010* | e-ISSN: *2536-5134*

DOI: https://doi.org/10.36222/ejt.1175023

ABSTRACT

The use of electrical energy from renewable energy sources has increased considerably in recent years. Photovoltaic (PV) solar energy, which is one of the renewable energy sources, takes its source from the sun, which is considered an unlimited source. With the widespread use of photovoltaic systems, some legal regulations by governments have been made for their installation. Simulation programs are used for the design, layout, technical and economic analysis of PV systems.

In this study, the design is made using the PVsyst, PV*SOL, Solarius programs, and the PVGIS website used in PV systems. The projects are designed to have an output power of 25 kW. According to the simulation results, the PVGIS website provides approximate data since technical details cannot be entered. In the results of PVGIS and all simulation programs, it has been calculated that the system can produce 42-48 MWh of electrical energy annually. Power Ratio (PR) results of the system were in the range of 78-85%. Annual electrical energy production per installed kW has been calculated to be 1436-1635 kWh/year. It is stated that the annual saved CO^2 will be 18.66-22.226 tons /year. When the simulation results are analysed monthly, the differences between the months are remarkable. The reason for these deviations can be explained by the annual solar radiation (kWh/m^2) data and databases used by the programs. It has been observed that the simulation programs consider the monthly average temperatures and sunshine durations of the region.

It is thought that there is a need to compare real-time data with simulation results in future studies. It is considered that this study will be helpful for future studies.

1. INTRODUCTION

It is predicted that global warming will lead to an increase in the average temperature of the world by more than 1.5°C after 2030 [1]. One of the causes of global warming is the fossil resources used in the production of electrical energy. With the Paris Convention, many countries have made agreements to abandon fossil resources and switch to renewable energy sources for electricity generation [2]. Countries are interested in renewable energy in line with their regulations and energy policies. The renewable energy sector has become an important shareholder and market area to meet global electricity energy in the last 20 years. The leading energy sources in the field of renewable energy are solar and wind energy. Solar and wind energy have advantages such as the absence of fossil fuels in energy production, the absence of waste, and the fact that their operation is easier and less costly than conventional sources, except for the first installation. Generating electrical energy from these renewable sources has benefits such as reducing environmental pollution, reducing greenhouse gas emissions, and preventing global warming [3]. Software or tools are used for design and simulation purposes in areas where electricity will be produced from wind energy and solar energy. Simulation programs provide users with advantages such as estimated electricity production, system performance, return on investment payback period, and layout design of the installation site. With these advantages, the investment cost can be determined at first by saving time and cost with the design of an area.

It cannot be expected that solar power plants will realize their annual electrical energy production exactly according to their installation power. Over time, due to technical reasons such as humidity, dusting, pollution, and degradation in panel power output, the annual electrical energy production estimate varies according to the installed region. The annual degradation rate is 0.5% and the annual maintenance cost is 1% of the total investment amount [4, 5]. Various anti-reflection coating techniques are used to prevent degradation

caused by dusting and reflection [6]. The altitude, latitude, solar radiation intensity, wind speed, air temperature and humidity averages of the region to be installed will affect the electrical energy production values [7]. Production in Photovoltaic (PV) systems varies daily and seasonally, depending on the time of day, meteorological conditions, and solar radiation. Spatial interpolation and solar radiation modeling are used in modeling and prediction studies [8]. It is estimated based on meteorological data of previous years to estimate the expected electrical energy production compared to the installed capacity. In addition to meteorological data, sunshine-based, cloud-based, temperature-based, and hybrid meteorological parameter-based models are used in modeling [9]. In this on-grid-middle voltage level design study, meteorological solar radiation modeling was used.

Meteorological databases that are widely used in design and simulation are Meteonorm, NASA SSE, NCEP, GIS Solar Data, HelioClim, and World Radiation Data Center. Software programs and interface websites which are used in solar energy simulations are PVsyst (pvsyst.com), PV*SOL (valentin-software.com), Solarius (accasoftware.com), BlueSol (bluesolpv.com), Homer (homerenergy.com), PVCase (pvcase.com), Easy-PV (easy-pv.co.uk), PV F-Chart (fchartsoftware.com/fchart), SolarGIS (solargis.info), Global Solar Atlas (globalsolaratlas.info), Helio Scope (helioscope.com), System Advisor Model (SAM) (sam.nrel.gov), and PV-GIS (re.jrc.ec.europa.eu/pvg_tools/en/). Some of the software programs provide very comprehensive design and analysis capabilities, while others allow easy use and quick results. With simulation programs, small-scale, off-grid or grid-connected(on-grid) PV systems can be designed, and technical-economic analyses can be performed.

Among these programs, which are also used by commercial enterprises, PV*SOL and PVsyst programs are the most frequently used for more technical details [10]. Homer program can be used to design and analyze hybrid systems such as wind-solar-biomass and is often used for techno-economic evaluations [11]. In a study conducted in the PV*SOL program, simulation results and real-time data were compared, and up to 94.33% similarity was observed between real data and simulation data [12]. When the studies on the roof-top PV system are examined, in the application on the roof of a university building, the available roof area for PV applications has been determined by defining the limitations. These limitations have been determined by considering factors such as PV panel temperature co-efficiency and shading. PV*SOL software was used, and it was seen that university buildings have the potential to produce 5,389.2 MWh/year of electrical energy. According to the simulation results, it is calculated that the annual electricity generation per kWp will be 1,336.6 kWh/kWp. When the environmental analysis is performed, this utilization can save 63,727.05 tons of CO_2, 1.89 tons of CH_4, 0.27 tons of N_2O, 970.05 tons of SO_2, and 590.12 tons of NO emissions in 25 years if the PV system is applied [13].

In a study in which PV system data with an installed power of 7.8 kWp was simulated with the Homer program, it was revealed that the simulation data has an annual error margin of 1.7% from the real data [14]. The annual average Performance Ratio (system utilization rate) (PR)(Eq.1) of an off-grid system simulated with PVsyst was simulated as 72.8%. It was simulated that the highest PR was in December and the lowest PR was in April [15]. A rooftop hybrid system with a wind turbine and a PV system on the roof of a university building was designed with Homer. For a roof area of 400 m^2, the optimum PV power is simulated as 30 kW and the optimum wind turbine power is simulated as 22.5 kW. According to the simulation results, it is seen that 55% of the annual energy demand of the building can be met, with 23% PV panels and 32% with wind turbines [16]. In a study simulating the PVGIS interface and comparing the results with the real electrical energy production values, it was seen that the simulation results were realized with a 5% error from the actual production results [17]. A simulation study was performed with PVsyst on the roof of a university campus building with 30 kWp and 38 kWp installed power. It has been seen that as a result of simulation the Performance Ratio (PR) for 30 kWp power is 76.1%, the annual electrical energy production is 49.80 kWh and the annual carbon dioxide emission of 42 tons will be saved [18]. The simulation of the 301 kWp application on a roof of a hotel in Jordan was done with PVGIS and PVsyst. According to the calculation result, the daily average electrical energy production will be 4.93 kWh/kWp/day. It has been calculated that the system will have a PR of 82.8% and it has been calculated that the system will have a PR of 82.8% and will be able to produce an average of 541 MWh of electrical energy annually. According to the country's electricity tariff prices and the costs of the simulation period, the amortization period of 4.1 years has been revealed [19].

In this study, simulator programs used in PV systems were investigated first. Then, the simulators used in roof-type designs were studied in the literature and the most frequently used programs were surveyed. Using PV*SOL, PVsyst, Solarius, and PVGIS programs, a comparison of technical analysis and simulation results was made for a rooftop PV system with an installed power of 29.4 kWp, including a system loss of 15%, which can be a power output of 25 kW.

2. MATERIAL AND METHOD

There are programs used in the calculation of simulation, technical analysis, and amortization periods used in the design of solar PV systems. These programs were investigated from literature studies. As the location, Osmaniye Korkut Ata University Kadirli Vocational School of Higher Education building in Kadirli district in Osmaniye region of Türkiye was selected and a 25 kW roof-top type fixed angle PV system was designed. The reason why it is designed as 25 kW is the legal upper limit of the allowed installed power in roof-top type PV systems by the Ministry of Energy and Natural Resources of Türkiye [20]. Solarius by Acca, PVsyst, and PV*SOL programs, and the PVGIS database were used in the design. The simulations were designed in the same conditions as each other. In this study, attention was paid to the differences in technical results rather than the economic and investment analysis of the design, and the consistency of the results was desired to be discussed.

The building location is at the coordinates 37.39'N, 36.07'E, at an altitude of 114 m, in the direction of 167° South, and with non-slope. There is not any obstacle like a tree or building that can lead to shadowing around the structure. The height of the roof from the ground is 10 meters. The dimensions of the designed area are 17 meters wide and 40 meters long. All systems are designed with a power output of 25 kW, with a loss of 15%, and a total of 29.4 kWp. PV panels were selected with a power output of 545 Wp, 21% efficiency,

Voc 48 V, Isc 13.9 A, Vm 41.08 V, Im 13.04 A, and monocrystalline cell panel type. Inverters are selected as 27 kWp AC 3-phase 380 Volt. The operating voltage range of the inverters is 580-850 Volts.

In the Solarius simulation, the data were taken from the Meteonorm 7.1 database. In the PVGIS database, the calculation was made with the SARAH2 database. SARAH2 database takes measurements with an accuracy of 0.05x0.05° and gives the average data between 2005-2020. In the PVsyst simulation, the data were taken from the Perez and Meteonorm databases. Hofmann and Hay&Davies techniques were used in PV*SOL simulation. The installation area and view are given in Fig. 1.

Figure 1. The location and satellite image of the building

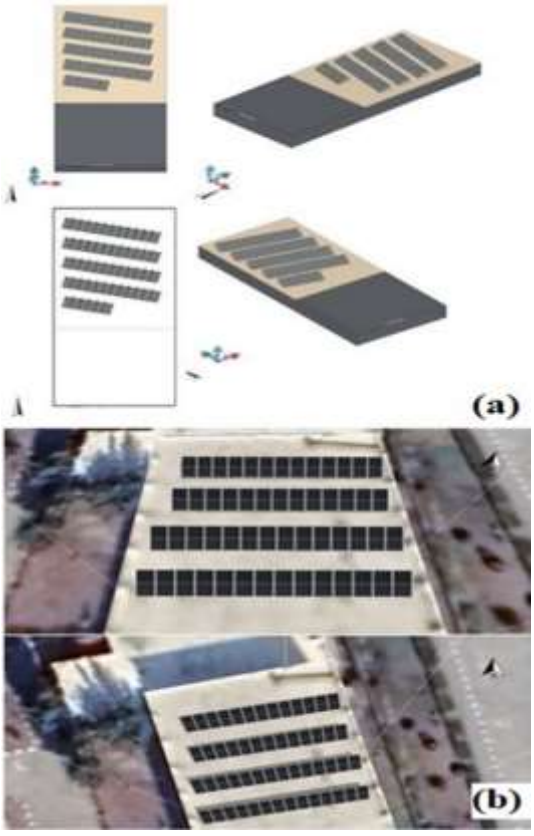

Figure 2. Design and layout prepared with Solarius(a) and PV*SOL(b)

According to the design, 54 PV panels with a 29.43 kWp total power were placed on an installation area of 140 m^2. PV panels are connected as 3 strings and 18 PV panels in each string are connected in series. Thus, inverter input is adjusted to 600-650 Volt-40 Ampere voltage and current values when the panel surface is 50°C under sunny day conditions. The design was made considering that the efficiency of the PV panel decreases between 0.25-0.5% with each 1°C increase in temperature [21]. The 3D design and layout designs of the roof-top type PV system designed with Solarius and PV*SOL program, which can output 25 kW of power, are as in Fig. 2.

3. RESULTS

The parameters considered in PV system designs are the solar radiation of the region, the ambient temperature, the temperature coefficient of the PV panel, the inverter efficiency, the maximum power that can be obtained under standard test conditions (STC), and the number of PV panels [22]. Although these parameters vary according to the modeling, they are common parameters used in the literature. In the design, these parameters were considered in the simulations. Since it is known that different databases are used in simulation calculations, the annual global horizontal irradiation (GHI) (kWh/m^2) solar radiation data of the region divided by months are given in Table 1. When the annual solar radiation data are compared, they are close to each other, except for the PV*SOL program.

TABLE I
ANNUAL SOLAR RADIATION (KWH/M^2)

Months	PV*SOL	Solarius	PVsyst	PVGIS
January	67.3	58.5	69.1	73.59
February	77.02	94.905	81.8	85.97
March	116.62	130.51	125.7	120.37
April	148.38	177.6	153.5	164.74
May	177.38	169.57	189.7	208.8
June	189.96	201.3	211.8	211.94
July	195.42	233.12	220.1	228.12
August	189.13	214.83	203.1	208.98
September	151.44	171	167.1	165.73
October	108.43	133.61	121.3	137.62
November	73.17	94.2	83.5	87.43
December	60.32	59.21	69.1	75.41
Total	1,554.57	1,738.355	1,695.8	1,768.7

In the Solarius program, daily and annual solar radiation data are taken from the Photovoltaic Geographical Information System (GIS) database. When the data of the same region is studied in the PVGIS system, it is seen that it is not exactly the same. According to the Solarius program, the annual solar radiation was 1,738.355 kWh/m^2, 1,695.8 kWh/m^2 according to the PVsyst program, 1,768.7 kWh/m^2 according to the PVGIS interface, and 1,554.57 kWh/m^2 according to the PV*SOL program in the region selected for the installation.

The average monthly temperatures and sunshine durations of the region for the last 24 years are given in Fig. 3. According to the records taken between 1987-2021, the region is a temperate region with an average temperature of 18.7°C for 24 years and the average annual sunshine duration is 5.1 hours. Considering the annual average of 4.5-5 hours of sunshine duration per day, where the average is 6 hours in the summer season in Turkey, it is considered that the annual average of 5.1 hours is quite high.

PVGIS calculated annual electrical energy production as 43,750 kWh/year, electrical energy production per kW as 1,486 kWh/kWp/year, and Power Ratio (PR) as 85%, but there is no data about CO_2 emissions. PV*SOL program estimated annual electricity generation according to location is 42,234 kWh/year, energy production per kW is 1,436 kWh/kWp/year, Power Ratio is 78%, and the saved amount of CO_2 is 19.8 tons/year. In the Solarius program, the prevented emission of CO_2 equivalent is 22.226 tons/year, the total annual amount of electrical energy is 48,053 kWh/year, 1,632 kWh/kWp/year electrical energy production rate, and the Power Ratio is 85%. As a result of the simulation in the PVsyst program, the Power Ratio is 84.54%, 48,130 kWh/year of total electrical energy production, 1,635 kWh/kWp of electrical energy production per kW and 18.66 tons of CO_2 prevented from being released in a year. The self-consumption of the electrical energy consumed by the system components in all simulations is 8 kWh/year. This consumption power is approximately 0.2% of the annual electrical energy produced by the systems and is a small power that can be ignored. The results of the simulations are given in Table 2.

TABLE II
OVERVIEW OF SIMULATIONS

Months	PV*SOL	Solarius	PVsyst	PVGIS
Annual Electrical Energy Production (kWh/year)	42,234	48,053	48,130	43,750
Power Ratio (%)	78	85	84,54	85
Annual Electrical Energy Production per kW(kWh/year) (kWh/kWp/year)	1,436	1,632	1,635	1,486
Saved CO_2 (tons/year)	19.8	22.226	18.66	n/a

According to the results shown in Table 2., it is predicted that an average of 20 tons of CO_2 emissions will be prevented per year. There is no data on carbon emissions in the PVGIS interface. According to the simulation results, the CO_2 equivalent prevented per kW is approximately 1 ton per year. The PR was given 78% in PV*SOL and 85% in others, which resulted in a difference in the expected electrical energy from the designed system.

$$PR = \frac{P_{real}}{P_{ref}}.100 \quad (1)[24]$$

$$P_{ref} = \text{GlobInc} \times P_{ins} \quad (2)[24]$$

Where:

PR : Power Ratio
P_{real} : Real Power (supplied to grid)(kWh)
P_{ref} : Reference Power (simulated) (kWh)
GlobInc : Global Incident (kWh/m^2)
P_{ins} : Installed Power (kWp)

To determine the Real power exactly, the total electrical energy value produced during at least 1 year must be measured. However, the actual PR value can be expressed after that, but the PR value changes every year due to solar radiation varying from one year to the next. P_{real} value in simulations changes with factors such as pollution, reflection, aging of the PV panel, and wiring quality. For this reason, the PR value given in each simulation gives an approximate expression. The parameter with the highest probability of error in the simulations is the error rate in taking the P_{real} value in the PR calculation.

In the annual electrical energy production prediction given in Fig. 4, when separated by months, the PV*SOL program simulated more electrical energy production than the Solarius program in January, May, and December, although the total electrical energy production result was less than the other simulation results. It estimated less electrical energy in all months than the PVsyst program. In the PVGIS simulation in January, May, and December, higher electrical energy estimates were given than Solarius results. The reason why the Solarius program gives lower estimations than PVGIS and PV*SOL simulations in January, May, and December is that it shows lower solar radiation data in January, May, and December as can be seen in the solar radiation values in Table 1.

Figure 3. Annual average temperature and sunshine duration of Osmaniye province [23]

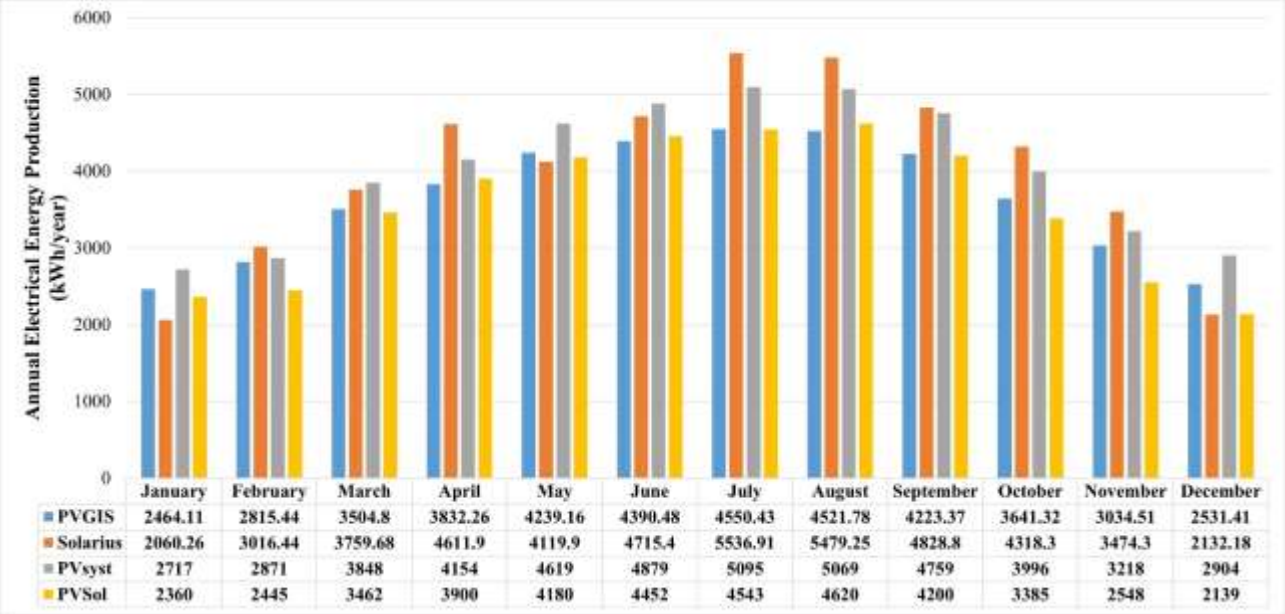

	January	February	March	April	May	June	July	August	September	October	November	December
PVGIS	2464.11	2815.44	3504.8	3832.26	4239.16	4390.48	4550.43	4521.78	4223.37	3641.32	3034.51	2531.41
Solarius	2060.26	3016.44	3759.68	4611.9	4119.9	4715.4	5536.91	5479.25	4828.8	4318.3	3474.3	2132.18
PVsyst	2717	2871	3848	4154	4619	4879	5095	5069	4759	3996	3218	2904
PVSol	2360	2445	3462	3900	4180	4452	4543	4620	4200	3385	2548	2139

Figure 4. Prediction of Annual electrical energy production (kWh)

A very high difference in the electrical energy production was observed between the Solaris simulation in April, July, and August, and the other estimates. These results do not seem to be consistent with the solar radiation in Table 1. For this reason, it has been evaluated that the deviation in the annual electrical energy production data is very high in the Solarius program. Although the total annual electrical production estimate is close to other predictions, the reliability of the data seems doubtful when studied month by month.

When the results of PV*SOL and PVGIS in Table 1., Table 2. and Fig. 4. are examined, the annual total solar radiation of PVGIS is higher than that shown in PV*SOL, but the annual electrical energy production is closer to each other. The expected PR of 78% in the PV*SOL program is effective for this result.

It has been seen that knowing the annual solar radiation data, the meteorological data of the region, and the geographical conditions reduce the error rate in simulation results. Although databases based on long-term data are used, situations such as climate change, temperature change during the year, sunshine duration, and unexpected shading depending on the geographical conditions of the region increase the error rate in the results.

4. DISCUSSION AND CONCLUSION

In this study, the factors affecting the result have been examined by comparing the simulation results in a grid-connected or off-grid roof-top PV system to be installed in any region. A system with an installed power of 29.4 kWp and maximum output power of 25 kW due to a loss of 15% is designed. PV*SOL, Solarius, and PVsyst design and simulation programs, which are frequently used in PV systems, and the PVGIS website is used. According to the results, considering the annual solar radiation data, temperature, and sunshine duration of the 25 kW output power, it has been revealed that there is an annual electricity generation potential of 42-48 MW in the region.

It has also been determined that the use of renewable energy will prevent and save an average of 20 tons of CO_2 equivalent emissions per year. Considering that 70% of Turkey's greenhouse gas emissions occur from energy production, the environmental impact of producing electrical energy from renewable sources will be very important [25].

It is thought that photovoltaic solar energy systems will gain more importance in the future considering the high market share it has achieved in recent years among other renewable energy systems, the increase in efficiency with progressing semiconductor technology, and the decrease in overall system losses. The system is designed grid-connected and doesn't have a storage system so all electrical energy produced can be transferred to the grid. Nevertheless, there is a need to compare the simulation data with the real and long-term data in connection with the grid. In future studies, attention will be paid to comparing simulation results by measuring real-time data.

REFERENCES

[1] Hoegh-Guldberg O. et. al., "Impacts of 1.5°C global warming on natural and human systems", Intergovernmental Panel on Climate Change (IPCC), France, 2022.

[2] United Nations – the United Nations Framework Convention on Climate Change, "The Paris Agreement", (2015). Accessed: Nov. 16, 2022. [Online]. Available: https://unfccc.int/sites/default/files/english_paris_agreement.pdf

[3] Gorgulu S., Ekren N., Energy saving in lighting system with fuzzy logic controller which uses light-pipe and dimmable ballast, *Energy and Buildings*, 61 (2013), pp. 172-176. https://doi.org/10.1016/j.enbuild.2013.02.037

[4] Battle C. et. al., Regulatory design for RES-E support mechanisms: learning curves, market structure and burden-sharing, *Energy Policy, 41* (2012), pp. 212-220. DOI: 10.1016/j.enpol.2011.10.039

[5] Jordan D.C., Kurtz S.R., Photovoltaic degradation rates-an analytic review. *Progress Photovoltaics, 21* (2013), pp. 12–29. https://doi.org/10.1002/pip.1182

[6] Ekren N., Researches on Anti-reflection coating (ARC) methods used in PV systems, *Balkan Journal of Electrical and Computer Engineering*, 6 (2018), pp. 42-46. https://doi.org/10.17694/bajece.402004

[7] Saglam S. et. al., Measurement of meteorological parameter effects on photovoltaic energy production, *International Journal of Circuits, Systems and Signal Processing*, 9 (2015), pp. 240-246.

[8] Cervantes-Ortiz C.A. et. al., The effect of parameters and irradiance estimation techniques on PV potential quantification: The case of Mexico, *Sustainable Energy Technologies and Assessments, 45* (2021), pp.101131 DOI:10.1016/j.seta.2021.101131

[9] Besharat F. et. al., Empirical models for estimating global solar radiation: a review and case study, *Renew. Sustain. Energy. Rev., 21* (2013), pp.798–821 doi.org/10.1016/j.rser.2012.12.043

[10] Kanters, J. et. al., Tools and methods used by architects for solar design, *Energy and Buildings, 68* (2014), pp. 721–731 DOI:10.1016/j.enbuild.2012.05.031

[11] Aykut E., Terzi Ü. K., Techno-economic and environmental analysis of grid connected hybrid wind/photovoltaic/biomass system for Marmara University Goztepe campus, *International Journal of Green Energy*, 17 (2020), 15, pp. 1036-1043 https://doi.org/10.1080/15435075.2020.1821691

[12] Ozcan, H. G. et. al., A comprehensive evaluation of PV electricity production methods and life cycle energy-cost assessment of a particular system, *Journal of Cleaner Production, 238* (2019), pp. 117883 DOI:10.1016/j.jclepro.2019.117883

[13] Ahmed A. et. al., Investigation of PV utilizability on university buildings: A case study of Karachi, Pakistan, *Renewable Energy, 195* (2022), pp. 238-251 doi.org/10.1016/j.renene.2022.06.006

[14] Anang N. et. al., Performance analysis of a grid-connected rooftop solar PV system in Kuala Terengganu, Malaysia, *Energy & Buildings, 248* (2021), pp. 111182 doi.org/10.1016/j.enbuild.2021.111182

[15] Kumar R. et. al., Design and simulation of standalone solar PV system using PVsyst Software: A case study, *Proceedings*, (Dwivedi G., Verma P.), MaterialsToday: Proceedings, International Conference on Innovations in Clean Energy Technologies (ICET2020), Madhya Pradesh, India, 2020, Vol. 46, pp. 5322-5328

[16] Akar O. et. al., Determination of the optimum hybrid renewable power system: a case study of Istanbul Gedik University Vocational School, Balkan Journal of Electrical and Computer Engineering, 7 (2019), 4, pp. 456-463. https://doi.org/10.17694/bajece.623632

[17] Haydaroglu, C., Gumus, B., Examination of Web-Based PVGIS and SUNNY Design Web Photovoltaic System Simulation Programs and Assessment of Reliability of the Results, *Journal of Engineering and Technology, 1* (2017), pp. 32-38.

[18] Barua S. et. al., Rooftop solar photovoltaic system design and assessment for the academic campus using PVsyst software, *J. Electr. Electron. Eng., 5* (2017), 1, pp. 76–83

[19] Al-Zoubi H. et. al., Design and feasibility study of an on-grid photovoltaic system for green electrification of hotels: a case study of Cedars hotel in Jordan, *International Journal of Energy and Environmental Engineering, 12* (2021), pp. 611–626 doi.org/10.1007/s40095-021-00406-z

[20] Enerji Piyasası Düzenleme Kurumu (EPDK), "25 KW'a Kadar Güneş Enerjisine Dayalı Elektrik Üretim Tesisler İçin Usul Ve Esaslar", (2022). Accessed: Nov. 15, 2022. [Online]. Available: https://www.epdk.gov.tr/Detay/Icerik/3-0-92/elektriklisanssiz-uretim

[21] Ahmad E.Z. et. al., Outdoor performance evaluation of a novel photovoltaic heat sinks to enhance power conversion efficiency and temperature uniformity, *Case Studies in Thermal Engineering, 31* (2022), pp. 101811 https://doi.org/10.1016/j.csite.2022.101811

[22] Lara E.G., Garcia F.S., Review on viability and implementation of residential PV-battery systems: Considering the case of Dominican Republic, *Energy Reports, 7* (2021), pp. 8868-8899, doi.org/10.1016/j.egyr.2021.11.208

[23] Türkiye Meteoroloji Genel Müdürlüğü, "Resmi İstatistikler". (2022). Accessed: Nov. 15, 2022. [Online]. Available: https://mgm.gov.tr/veridegerlendirme/il-ve-ilceler-istatistik.aspx?k=A&m=OSMANIYE

[24] Sarniak M.T., Researches of the Impact of the Nominal Power Ratio and Environmental Conditions on the Efficiency of the Photovoltaic System: A Case Study for Poland in Central Europe, *Sustainability, 12* (2020), 15, pp. 6162; https://doi.org/10.3390/su12156162

[25] Türkiye İstatistik Kurumu (TÜİK), "Greenhouse Gas Emission Statistics-1990-2020". (2022). Accessed: Nov. 15, 2022. [Online]. Available: https://data.tuik.gov.tr/Bulten/Index?p=Sera-Gazi-Emisyon-Istatistikleri-1990-2020-45862

BIOGRAPHIES

Taner Dindar was born on February 6, 1987. He graduated BSc from Kocaeli University Electrical Engineering in 2021. He recevied MSc degree in 2012 from Marmara University in Türkiye. He is doing a Ph.D. in Energy Systems Engineering at Kocaeli University. He is currently working as a lecturer at Ankara University Nallıhan Vocational School.

Vedat Esen was born on June 30, 1982 in İstanbul, Türkiye. He graduated from Yıldız Technical University, Faculty of Electrical and Electronics, İstanbul, and received MS and PhD degrees from Marmara University, Institute of Pure and Applied Sciences, in Istanbul, Turkey, in 2011 and 2020 respectively. He is currently an assistant professor in Engineer Faculty Electrical and Electronics Engineering Department at İstanbul Topkapı University in Türkiye. His current interests are power systems and renewable energy systems.

Ali Samet Sarkın was born in İstanbul, 1987. He received the BSc. and MSc. degrees in electrical education from Marmara University, İstanbul, in 2010 and 2013 respectively. He received a Ph.D. degree in electrical and electronics engineering from Marmara University, Istanbul, Türkiye, in 2022. Since 2014, he has been working as a Lecturer at Osmaniye Korkut Ata University. His research interests include identification systems including RFID, renewable energy systems, photovoltaic systems, and their applications.

.

European Journal of Technique

journal homepage: https://dergipark.org.tr/en/pub/ejt

Vol.12, No.2, 2022

SARS-CoV-2 Virus RNA Sequence Classification and Geographical Analysis with Convolutional Neural Networks Approach

Selçuk YAZAR[1*],

[1*]Kırklareli University, Software Engineering Department, 39000, Kırklareli, Turkey. (e-mail: selcukyazar@klu.edu.tr).

ARTICLE INFO

Received: Mar., 27. 2022
Revised: Sep., 24. 2022
Accepted: Oct, 25. 2022

Keywords:
Deep Learning
Bioinformatics
Artificial Intelligence
Computer Vision
Pattern Recognition

Corresponding author: *Selçuk Yazar*

ISSN: *2536-5010* | e-ISSN: *2536-5134*

DOI: https://doi.org/10.36222/ejt.1094218

ABSTRACT

Covid-19 infection, which spread to the whole world in December 2019 and is still active, caused more than millions of deaths in the world today. Research on this subject has been focused on analyzing the genetic structure of the virus, developing vaccines, the course of the disease, and its source. In this study, RNA sequences belonging to the SARS-CoV-2 virus are transformed into gene motifs with two basic image processing algorithms and classified with the convolutional neural network (CNN) models.

The CNN models achieved an average of 98% Area Under Curve(AUC) value was achieved in RNA sequences classified as Asia, Europe, America, and Oceania. The resulting artificial neural network model was used for phylogenetic analysis of the variant of the virus isolated in Turkey. The classification results reached were compared with gene alignment values in the GISAID database, where SARS-CoV-2 virus records are kept all over the world. Our experimental results have revealed that now the detection of the geographic distribution of the virus with the CNN models might serve as an efficient method

1. INTRODUCTION

Artificial intelligence practices and particularly deep learning studies are a widely used discipline in many research fields, including medicine and bioinformatics. The CNN models, especially in the field of medical imaging, are very successful in lesions and disease diagnosis. In addition to the success of deep learning methods in the fields of image processing, natural language processing, also has a lot of usage on a time scale with approaches such as Long-Short Term memory. In deep learning practices, low-level features such as DNA sequence, pathology images, and tomography scans can be learned from the data, by largely eliminating the need for engineering applications. Another important feature of the deep learning technique is that the intermediate values and weights obtained during training can be used in other related applications.

Deep learning approaches are frequently used in the processing of large-scale genetic data, especially in the field of bioinformatics. Today, the size of these datasets exceeds the size of 10 million [1]. Studies in this area are concentrated in the analysis and classification of DNA and RNA sequences. By using certain machine learning algorithms such as Support Vector Machines, Random Trees, it is aimed to reveal certain or undetermined structures in the genetic sequence with the developed methods. Apart from the classical approaches, the proposed deep learning methods can be used in areas such as metagenomics and proteomics (protein research) as it has been shown. In these studies, deep learning models were used to analyze splice junction information and gene structures of RNA of viruses and to determine variants. For example, deep learning model variables allow a secondary RNA structure which has been detected, can be used to detect another microRNA insertion lasso [2].

There are several publications about phylogenetic RNA–seq analysis using distinct deep learning algorithms. Applications that investigate the patristic distance (distance from the ancestor) of the RNA sequences obtained and differentiated from various virus variants and the structure of the tree structures are popular. In the CNN methods used in this type of paper here, the MultiDimensional Scaling approach was used and classical methods such as SVM were compared [3]. Another study focuses on the classification of insertion points in RNA-seq matches. In the mentioned paper Homo sapiens Splice Sites Database (HS3D) has been used to classify and variant estimates on mRNA (messenger RNA) using CNN models and compared with other common LSTM and SVM algorithms [4]. In another study, Single-cell RNA-seq analysis used the Encode-Decoder approach, which is utilized for today to reduce noise in deep learning applications [5]. The encoder-

decoder approach used in deep learning applications is based on the coding strategy that the network can process before sending data to the artificial neural network. In Encoder-Decoder applications, input data is reduced in the bottleneck layer and then reproduced for further processing. Another area where such studies are concentrated in cancer research [6]. Auto Encoder method was used to classify cancer-causing genes.

The SARS-CoV-2 [7] outbreak poses the biggest global health and socioeconomic threat since the Second World War. Phylogenetic studies have gained increasing importance with regard to the Covid-19 virus, which is currently watching horizontally but is concerned about the epidemic again in the coming days. The geographical spread of the virus and the monitoring of the mutations it undergoes also constitute the basis of the vaccine studies to be produced against the virus. The creation of phylogenetic trees of viruses and bacteria plays a key role in understanding the structures of these pathogens.

In this study, we took the RNA data of the SARS-Cov-2 virus from the databases that published it internationally for researchers to use. We have collected this data in four groups: Asia, Europe, America, and Australia. In the data obtained, we used RNA sequences with an average length of more than 29,000 characters. Then, we aimed to classify the sequences by using the model created based on the DenseNet-121 artificial neural network, using the midpoint circle and Smallest Univalue Segment Assimilating Nucleus (SUSAN) [8] algorithms. We compared the classification results from the models we created with gene alignment counts from viruses isolated in Turkey, Spain, Italy, Iran, and India.

2. MATERIAL VE METHODS

2.1. Dataset

The data of the RNA sequences we used in the study were provided from two databases. Since it was isolated in December 2019, GISAID [9] and the National Center for Biotechnology Center (NCBI Virus) [10] databases provide analysis of SARS-CoV-2 RNA records worldwide. During the study, we obtained the Asian-tagged series from the NCBI Virus database and the others via GISAID. The data stored and published in these repositories are kept in FASTA [11] file format. In this file format, the date, location, quality, and publication information of the researchers are available when the virus's RNA sequence is isolated. Since the quality of RNA sequences is also mentioned in these repositories, we did not prefer the sequences that are incomplete or have low safety in the classification model we created. Today, more than 16 thousand complete or partial genomic sequences are published on GISAID. In the NCBI (Virus) database, more than 2 thousand sequences are published complete or partially tagged. The total number of complete gene sequences obtained from these two databases is 3754. The distribution of the numbers for the examples here is Europe 1402, America 1226, Asia 858, and Australia 268. The distribution of the data is shown in Figure 1. The quantities that determine the quality and completeness of the data in these repositories are that the base pair number is more than 29,000 and the unsolved amino acid value is less than 5%. These features, which we have listed here, have created the motifs of the RNA information that we have collected so that all of the amino acid values are displayed correctly. Although we tried to select fully isolated gene sequences, in some cases we inevitably had to use sequences containing spaces as "N" due to the low number of data.

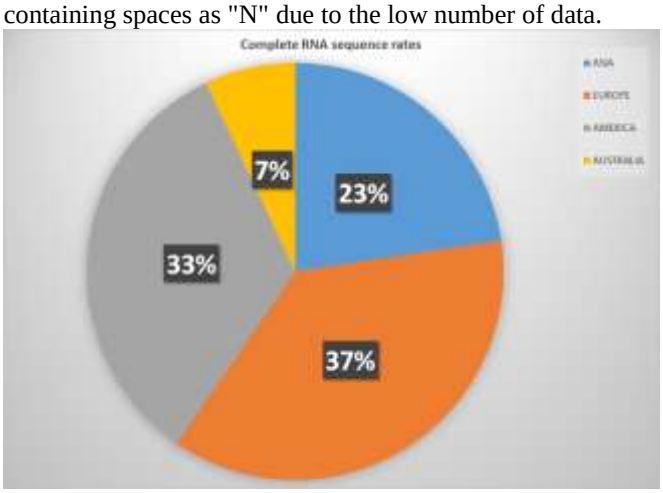

Figure 1. Distribution of complete genome sequences counts by continents used for our training dataset.

2.2. Creating RNA motifs with Mid-point circle algorithm

While converting the RNA sequences of the SARS-CoV-2 virus into visual motifs, we took advantage of an analogy and expressed them as circles. An RNA sequence contains four basic nucleobases, A(denine), C(ytosine), G(uanine) and T(hymine) [12]. While expressing these nucleobases, color codes are also used. Generally, these bases are found in pairs on DNA, but these molecules are not found in pairs on RNA. This is called the open helix RNA sequence. This is one of the main differences between DNA and RNA sequences. The color codes of these nucleobases are shown in Table 1.

TABLE I
NUCLEOBASES IN DNA AND RNA AND THEIR COLOR CODES [12].

Nucleobase	Color
Adenine	Yellow
Cytosine	Blue
Guanine	Green
Thymine	Red

The midpoint circle drawing algorithm [13] is an algorithm used to determine the points required to pixelate a circle shape. In the flow of the algorithm, to find the perimeter points of a circle, first the points in the parts divided into eight are determined, then the points in the remaining octant are determined. When determining any point (x, y) around the circle, the next pixel value is (x, y + 1) or (x-1, y + 1). We used this algorithm to fill the circle we obtained for using the RNA data that we translated into the character array. We obtained in this way with the motifs and converted the RNA sequences to 200x200 size and 3 channels into pictures. Since the gene sequences that we use in the study are not the same length, and we determined that this is the optimum dimension in our circle drawing algorithm. While creating the motifs, we used the missing and remaining pixels as white color to complete the circle. Note that a linear flat is noticeable on the right side of the circle. In terms of artificial neural networks, these pictures correspond to 200x200x3 matrices. The RNA motif that we obtained as a result of the algorithm is shown in Figure 2.

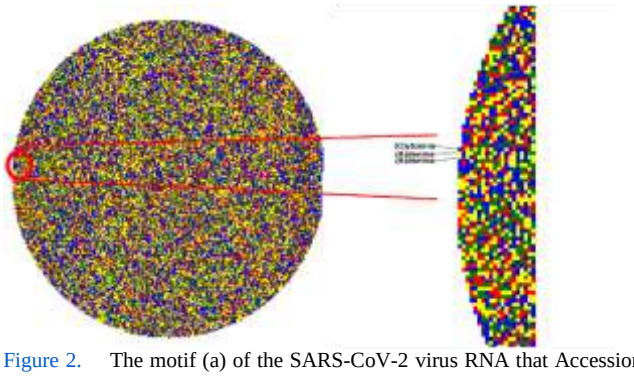

Figure 2. The motif (a) of the SARS-CoV-2 virus RNA that Accession ID EPI_ISL_425685; was isolated in Scotland in March 2020, and the nucleobase equivalents (b) of the pixels within the motif.

Before obtained the images here, we used the FASTA files we obtained from datasets to convert them into motifs by separating them into RNA sequences with an application we developed with C#.

2.3. The SUSAN Filter

When watching the motif files we obtained from our work, and we clearly saw that some parts of it repeat. We evaluated these repetitions that we inspected may be indicative and certain patterns in the RNA structure of the virus are preserved and some parts of them are mutated. For the classification model to work correctly, identifying these patterns is important in finding mutations that differ by geographic regions. In addition, we evaluated the detection of these patterns would be beneficial in forming the phylogenetic tree structure of the newly acquired RNA sequences or in finding similarities with the previously analyzed sequences. One of the main approaches used in visual information processing such as image segmentation and pattern recognition is the edge detection method. There are many algorithms developed for edge detection today. However, low-level applications were developed at the beginning of the image processing paradigm in general and today it has been moved to higher levels. In order to detect repetitive patterns in the motif files we obtained and preferred the low-level SUSAN edge detection algorithm.

SUSAN was proposed by Smith in 1997, which was a new approach to low-level image processing. SUSAN filter consists of three main parts. These can be listed as EDGE, CORNER detections, and filtering. The mask used in SUSAN's algorithm is circular, unlike other convolution masks. The main idea of the SUSAN method is to relate each pixel of the image to a small adjacent pixel area with a brightness similar to the central pixel. The central part, called the Univalue Segment Assimilating Nucleus (USAN), is the part that conveys the most important information about the structure of the image. To summarize, the SUSAN algorithm is basically a combination of a gauss filter and a linear filter that prevents image degradation. Linear filters, in general, tend to blur more image details than most non-linear filters [14]. As a result of our applying of the SUSAN filter to the motifs we obtained, the RGB pictures were converted into grayscale. However, the dimensions of the pictures are still stored here as 200x200x3.

We also conducted tests with semantic segmentation methods to determine the patterns in the motifs we obtained during the study. But, since unsupervised segmentation methods gave different results in each motif image we obtained, we did not prefer this approach since it requires parameter adjustment for 3754 images in total. At this stage, in the SUSAN filter we used for edge detection, we found that we can mark repeating patterns in all images for the same parameters. Our results are shown in Figure 3.

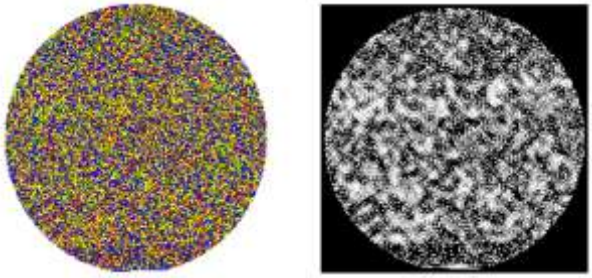

Figure 3. SUSAN filtered results for a sample motif file. The white areas in (b) show similarly repeating patterns in all motifs obtained.

2.4. Building the model

The creation of a CNN model in deep learning is the starting step, especially for classification success and prediction. Determining weights by building a neural network from scratch is basically a working process based on trial and error. Another criterion for the success of the models is the number and variety of data to be studied. As in this study, if the number of data is low, previously trained artificial neural network models are used. The neural networks such as Vgg16, Vgg19, Xception that have previously performed high in classification are preferred in such cases. We used a version of the DenseNet pre-trained neural network to classify the motifs we produced from this study [15]. DenseNet neural networks differ from classical convoluted networks in terms of interlayer connections. In conventional convolutional networks, there are N layers and N connections, and after applying a process combination, it connects the output of the layer to the next layer. However, there are N (N + 1) / 2 direct connections between layers in DenseNet networks. In these connections, the output feature maps of the layers are not collected, but they are combined. The connections between the layers are made in the form of feedforward. The DenseNet is divided into the DenseBlocks, where the dimensions of the feature maps remain constant within a block but the number of filters varies between them. These layers between them are called Transition Layers and are involved in sub-sampling by applying a batch normalization, 1x1 convolution, and 2x2 pooling layers. Important advantages of the DenseNet networks can be said as reducing the number of parameters and strengthen feature propagation. Apart from visual classification and clustering applications, the DenseNet neural networks are preferred in many areas such as signal processing and speech recognition [16, 17].

If the number of objects in the dataset is low in the training of artificial neural networks, a transfer learning method is applied. This method is often preferred especially in applications such as the classification and generation of medical images. The typical way to transfer learning with deep neural networks is to fine-tune a pre-trained model on the source task using data from the target task. The transfer learning method has been preferred in computer vision applications for a long time such as domain adaptation methods. In transfer learning strategies, a modification method is used in the final layers using the ImageNet pre-trained network or its weights [18]. The learning weights of such a feed-forward network are transferred to the layers added later, resulting in higher rates of success.

CNN's architectures typically consist of different layer types, including convolution, pooling, and fully connected layers, and apply regularization for the data that has been examined. There are three main concepts in the CNN topology. These are spatial and temporal sampling, sharing weights, and receptive fields. Each convolutional layer in the CNN is made up of small kernels used to determine high-level features. The last convolutional layer in the neural network supports fully connected layers. Less connection and easy learning are provided during learning with the parameter reduction method, which is the principle of operation of the CNNs. in the first layers in the CNN, Low levels of meaningful properties such as edges, corners, textures, and lines are obtained. The kernel matrices used in this process are in the n x n dimension, and the process is carried out by advancing the number of steps called stride on the picture. The pooling layer on CNN expresses a number of fully connected layers. In this layer, high-dimensional matrices received in the previous layers are reduced to one-dimensional arrays. At the last stage, there is a stage or layer called the detector stage. In these layers, generally non-linear functions such as Softmax, ReLu, tanh are used and complex models are learned.

In this study, the weight values taken from the DenseNet-121 network were transferred to an AveragePooling layer at first. In the next step, we dropped the values from this layer to the neural network connections by 50% dropout to prevent overfitting during learning. Thanks to the dropout process, some network cells are removed from the model so that the overfitting of the neural network is prevented. At the last stage, we sent the RNA sequences to the 4 dimensional fully connected layer that will be used for the four classes we will classify. We chose the non-linear function we used in this layer as SoftMax. This function takes a vector of K real numbers as input and normalizes it to a distribution of K probabilities proportional to the exponents of the input numbers. The softmax function is expressed as

$$(x_i) = \frac{\exp(x_i)}{\sum_j (x_j)} \qquad (1)$$

In this way, we have obtained more than eight million parameters in the neural network model we created in this paper. However, 83.000 of these parameters are non-trainable. We used the categorical cross-entropy function for the loss function. This function is one of the common functions used for single label categorization. It indicates that only one class is applicable for each data point. The categorical cross-entropy function is defined as in Equation (2).

$$L(x, \hat{x}) = -\sum_{j=0}^{m}\sum_{i=0}^{n}\left(x_{ij} * \log\left(\hat{x}_{ij}\right)\right) \qquad (2)$$

where m, n are the numbers of entries, i and j indicates iteration, and xˆ indicates the predicted label. We preferred the optimization method and used for training as RMSProp (Root Mean Square Propagation). Optimization functions are used to determine the learning speed of the artificial neural network. We set the Learning Rate value in the optimization function to 0.001. As a result of all these values, the model and input data we obtained are shown in Figure 4.

We run this model on Google Colab for 75 epochs. This number is the optimum value we have obtained in our trials. Training the neural network for more epochs caused over-fitting in the data

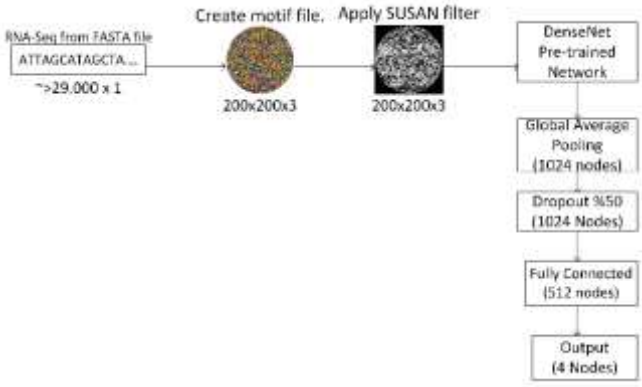

Figure 4. The stages of preparing motif files and model architecture.

3. RESULTS AND DISCUSSION

We desire to evaluate the results and obtained in this study under two headings. Overall, the success of a classification problem is evaluated by the confusion matrix and the Receiver Operating Characteristic (ROC) curve analysis. In our experiment, DenseNet-121 based one of the models we applied for the classification of four classes yielded 93% accuracy. This result is a satisfactory level of success in terms of classification. We could not achieve this level of success in the model we developed using the Vgg19 pre-trained neural network. The advantage of the DenseNet network is that although the number of parameters that can be trained by using convolution blocks increases in total, these parameters between the blocks are transferred to the next blocks, thus achieving more successful results. As a result of the filter we applied to the motif images we obtained from the RNA sequence, it is clear that this type of artificial neural network approach seems more appropriate. Our motif files have pixel sections that can be counted as noise. To generate feature maps of these pixels, they need to be subjected to a high amount of convolution and pooling. In another respect, DenseNet based models are known to give successful results in medical image classification applications today [19-21]. The visuals we obtain by applying the filter are obviously similar to medical images. The training results that we performed for the three versions of the DenseNet network together with the Vgg19 model we implemented in our first trials are shown in Table 2.

As can be seen in Table 2, the sensitivity of the four classes we obtained, Recall and f1 score values are quite good for the DenseNet-121 network. The training and validation performance plot of the model we trained with the DenseNet-121 network is also shown in Figure 5. Here we found the highest validation rate as 94%. However, on average, we measured the accuracy rate of our model as 93.6%. These model trainings were performed on the Google Colab platform. The validation results obtained with the experiments are 0.9374 (total time: 1 hour, 56 minutes), 0.9334 (total time: 3 hours, 12 minutes), 0.9335 (total time: 47 minutes), 0.9387 (total time: 49 minutes), and 0.9414 (total time: 1 hour, 32 minutes) respectively.

Notably during the training of our model, although the number of data belonging to Australia is quite low, the classification success is high in the DenseNet-121 network. In such cases caused by a lack of data, the general approach is to

use the augmentation method to increase model success. If we pay attention to Table 2, this model is not healthy even though the precision of the Australian class is 1.00 in the model we train in the DenseNet-169 network. This value indicates the data which is over-fitting. Moreover, although the value of Australia was such a great value in DenseNet-169, we did not get a successful result for this class in the predict we made later. In our comparison with later bioinformatics data, we chose not to evaluate the results of this model. According to the results listed in Table 2, the confusion matrix of our DenseNet-121 model, where we obtained the most optimum results, is shown in Figure 6.

TABLE II
CLASSIFICATION RESULTS FOR FOUR DIFFERENT CNN MODELS. THE MODEL WE CREATED USING DENSENET-121 HAS OPTIMUM RESULTS.

Model	Epochs	Region/Class	Precision	Recall	f1-score
Vgg19	130	ASIA	0.69	0.74	0.72
		EUROPE	0.88	0.85	0.86
		AMERICA	0.90	0.83	0.87
		AUSTRALIA	0.68	0.90	0.78
DenseNet-121	75	ASIA	0.88	0.83	0.86
		EUROPE	0.93	0.95	0.94
		AMERICA	0.98	0.98	0.98
		AUSTRALIA	0.84	0.88	0.86
DenseNet-169	75	ASIA	0.87	0.87	0.87
		EUROPE	0.93	0.95	0.94
		AMERICA	0.97	0.98	0.98
		AUSTRALIA	1.00	0.83	0.91
DenseNet-201	75	ASIA	0.88	0.79	0.83
		EUROPE	0.90	0.96	0.93
		AMERICA	0.98	0.98	0.98
		AUSTRALIA	0.87	0.83	0.85

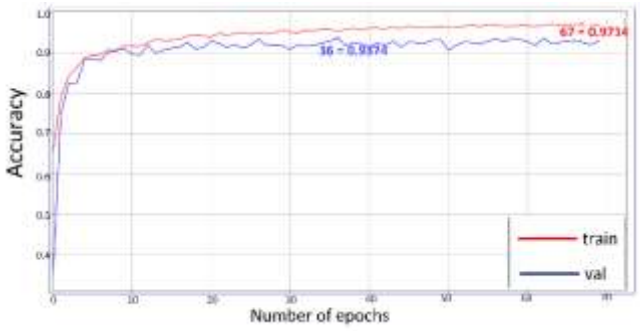

Figure 5. The plot of training and verification performance of the model.

As can be seen from the confusion matrix, a high degree of classification success is seen in our motif files. Although the incorrect values are small, considering the relationship of the data that is linked as a result of mutation, such as virus RNA, it may show their connection. Since this will be a controversial title, we consider it an issue to be emphasized. The claim that the error matrix also shows these distinctions requires a lot of research since there is no 100% geographical difference in virus mutations.

Another quantity that indicates classification success is the AUC value. In general, ROC values are defined as a probability curve in classification studies. AUC, on the other hand, expresses the degree or extent of class separability within these possibilities. The higher the AUC value, the higher the classification predictions of the model used. Here, when explaining the AUC results, values that are close to one are evaluated as the random classification of a positive sample higher than a random negative sample. The AUC values we obtained during the model training are shown in Figure 7. We classified the gene sequences that we divided into four classes into 97%, 98%, 99%, and 98% rates, respectively. These results showed us that RNA sequence information can be separated from each other by the method we use.

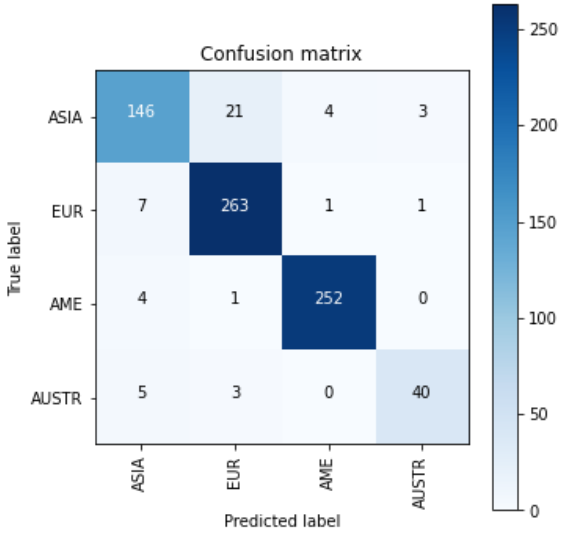

Figure 6. Confusion matrix was obtained in the training of four classes.

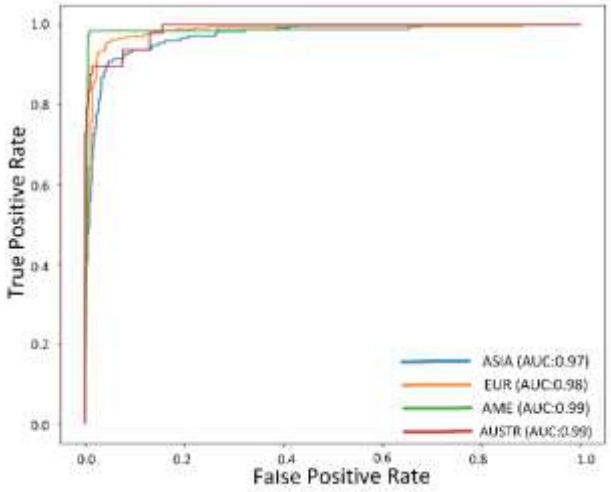

Figure 7. AUC plot of classification result for DenseNet-121.

Another issue that we would like to draw attention to in our study is the difficulties in automatic pattern recognition that are still studied today. Repetitive patterns can be described as inverse of complexity. It tells us that the information obtained as a result of the observation is characterized or a name can be given to it. Examples of such patterns are fingerprints, human faces, a specific form of handwriting, or a pure signal during the speech. The two main approaches in this regard are supervised classification, which defined as discriminant examination, and unsupervised classification called clustering. In the pre-tests we conducted during this study, we tried to

identify the repetitive patterns that can be easily noticed by an observer in the motif files we created with semantic segmentation. While the method we used gave good results for the object, animal, etc. encountered in daily life, it did not achieve successful results in the motif files we created. Obviously, this is because the images used to obtain weights in artificial neural networks developed for such approaches represent everyday objects. The patterns we encounter are low-level templates that can only be noticed by a human observer. In this regard, we were able to detect these repetitive unknown patterns in motif images using a low-level filter such as SUSAN. Also, another problem here was that in our dataset of approximately 3700 images, the parameters we used for semantic segmentation were only successful for one image. In this case, as many different parameters as the number of images would be required. As we have just mentioned, the image of the motif formed is a picture that contains a lot of noise.

TABLE III

COMPARISON OF THE NUMERICAL RATES OF VIRUS LOCATIONS MATCHED IN THE GISAID DATASET AND THE CLASSIFICATION RATES OBTAINED FROM THE CNN MODEL. SINCE THE ALIGNMENT RATES WERE NOT SHARED IN THE DATABASE, WE COULD ONLY COMPARE NUMERICALLY. STAR NOTED SEQUENCES DIRECTLY SUBMITTED GISAID.

Nu.	Accession Id	Location	GISAID- EpiCov Results(Alignment counts)	Our Proposal (Labels came from NN model)	Author(s)
1	EPI_ISL_424366	Turkey	Asia 20 Europe 4 America 3 Australia 3	ASIA 100%	Pavel et al.*
2	EPI_ISL_429864	Turkey	Asia 8 Europe 18 America 3 Australia 1	ASIA: 98.826% EUR: 0.051% AME: 0.001% AUSTR: 1.121%	Bayrakdar et al.*
3	EPI_ISL_429866	Turkey	Asia18 America 12	ASIA: 98.988% EUR: 0.049% AME: 0.001% AUSTR: 0.962%	Bayrakdar et al.*
4	EPI_ISL_429869	Turkey	Asia 20 America 10	ASIA: 98.478% EUR: 0.051% AME: 0.001% AUSTR: 1.469%	Bayrakdar et al.*
5	EPI_ISL_429870	Turkey	Asia 10 Europe 16 America 2 Australia 2	ASIA: 98.837% EUR: 0.050% AME: 0.001% AUSTR: 1.111%	Bayrakdar et al.*
6	EPI_ISL_429872	Turkey	Asia 25 Australia 4	ASIA: 98.082% EUR: 0.051% AME: 0.001% AUSTR: 1.867%	Bayrakdar et al.*
7	EPI_ISL_412973	Italy	Asia 7 Europe 18 America 5	ASIA: 7.254% EUR: 92.219% AME: 0.017% AUSTR: 0.509%	Zehender et al.[26]
8	EPI_ISL_414598	Spain	Asia 1 Europe28 America 1	EUR: 100%	Eiez-Fuertes et al. [27]
9	EPI_ISL_413522	India	Asia 20 Europe 1 America 9	ASIA: 100%	Yadav et al.[28]
10	EPI_ISL_424349	Iran	Asia 15 America 15	AME 100%	Zeinali et al.*
11	EPI ISL 415155	Belgium	Asia 2 Europe 18 America 3 Australia7	ASIA: 0.300% EUR: 99.691% AME: 0.001% AUSTR: 0.008%	A. Bal et al. [29]

This type of pixel, normally expressed as noise, has turned into really important points in this study. In nature, a single change in any gene sequence has very different consequences. With the fixed parameters we determined in the SUSAN filter, we obtained the desired result for all images in the dataset. An example result between the two methods is shown in figure 8. For segmentation, the parameters we use here are the number of convolution layers, the number of iterations, the number of channels, and the number of labels to separate. Their values also vary according to each image in our database.

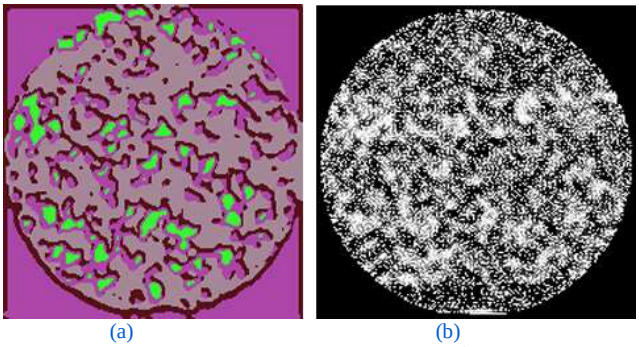

(a) (b)

Figure 8. Semantic segmentation result (a) and SUSAN filter comparison (b) we obtained for the motif file.

Another topic that we would like to evaluate is the comparison of our classification results with a phylogenetic analysis of the isolated RNA sequences in the world. For this, we compared our classification result with the first six RNA sequences that isolated in Turkey at the GISAID EpiCoV database, which we obtained on April 30, 2020. In addition, we compared our classification results with other virus RNA data isolated in Italy, Spain, Iran, and India, where the epidemic was effective and research was published. We have interpreted these comparisons statistically.

It is an important issue to specify the date when comparing. Because virus RNA information isolated from this date is not available in our artificial intelligence model training set. In the literature, Phylogenomic analysis methods examine the properties of 3 types of proteins to investigate the structure of these types of viruses. In particular, these classifications are important for the evolution of the S-pike protein of SARS-CoV-2, which originates from the name "Corona" and produces crown-like structures on its surface. In addition, protein regions, which are generally responsible for the formation of certain structures of viruses, have distinctions called S, V, and G clade. Making predictions and classifications for the future of a virus is possible by examining these distinctions. In studies related to the SARS-CoV-2 virus, the characteristic of S, V, and G clades reflects 69% of the virus. In addition, S-clade value indicates 72% of viruses in America and G-clade 74% of those in Europe [22]. In studies on the gene structure of the virus, which has been found is widespread episome groups according to different geographical regions such as China, Europe, and America. Although the numbers obtained from the isolation are limited, it has been shown and the classification resulting from the protein structures that we mentioned also can be grouped according to the continents [23-25]. The results obtained from these studies have shown us the visual classification study that we use here is a viable approach. However, since we did not make a comparison in the context of the V-S-G clade in this study, we only discussed our results numerically. In our comparison method, we used the proportions of the counts on four continents of the top 30 matching gene sequences of the virus analysis in the GISAID. For instance, if there are five Asian samples in 30 alignments, we accepted their numerical ratio as 16%. Unfortunately, the data we obtained from these public datasets do not have information about how many matches are in percentage. We showed our results in Table 3. Examples of the virus isolated in Turkey, not some scientific announcements, which have been mentioned links with Australia. In the results we obtained here, we observed the results confirming this connection.

In the results in Table 3, although the 7th sample is an Australian connection according to the results we find, this alignment does not appear in GISAID. However, the access numbers of EPI_ISL_428878, EPI_ISL_428915, EPI_ISL_428908, EPI_ISL_428915, EPI_ISL_428908, which are included in the top 30 alignments, have a connection with Australia. We think that we indirectly found a relationship, although it is not directly related due to the complex nature of virus RNA sequence variations. However, this claim needs to be supported by more detailed studies.

4. CONCLUSION

When examining the overall results, we can say that the model we created is successful in terms of classification. The results showed us, thanks to the motif images that we created and the filter we used, RNA sequences can be separated according to certain classes. In half of the RNA sequences that we excluded from the CNN model training and examined the results of the comparison, we reached conclusions that could provide preliminary information about the geographic regions of the virus gene information. Here we can say that with the help of the motif of the RNA sequence we created, we have developed a method that can contribute to detecting understandable biomarkers that can be used in metagenomics studies. The succession of classification and the partial success in phylogenetic analysis is due to the need for a better filter that can be applied to the motifs we create.

Another issue to be discussed in the results that we find by obtaining a new RNA sequence of the SARS-Cov-2 virus every day, the genome alignment structure can change. Since it is still a very new field of research today, the values we find as a result of the classification can change their weight over time. Due to the random mutations of viruses, some of the RNA segments may have been randomly matched. Nevertheless, according to the information we have obtained from our motifs, certain parts of the virus RNA sequences isolated from all over the world are repeating. Although not the subject of this study, these common patterns found will contribute to the development of the drug or vaccine, against the virus.

ACKNOWLEDGEMENT

The GISAID and NCBI(Virus) researchers did not participate in the analysis or writing of this report. The source codes and data of the research were shared on github.com/covidcnn web address.

REFERENCES

[1] M. Wainberg, D. Merico, A. Delong, and B. J. Frey, "Deep learning in biomedicine," Nature Biotechnology, vol. 36, no. 9, pp. 829-838, 2018/10/01 2018.

[2] Y. Lu, Y. Zhou, W. Qu, M. Deng, and C. Zhang, "A Lasso regression model for the construction of microRNA-target regulatory networks," Bioinformatics, vol. 27, no. 17, pp. 2406-2413, 2011.

[3] D. Fioravanti et al., "Phylogenetic convolutional neural networks in metagenomics," BMC Bioinformatics, vol. 19, no. 2, p. 49, 2018/03/08 2018.

[4] Y. Zhang, X. Liu, J. MacLeod, and J. Liu, "Discerning novel splice junctions derived from RNA-seq alignment: a deep learning approach," BMC Genomics, vol. 19, no. 1, p. 971, 2018/12/27 2018.

[5] G. Eraslan, L. M. Simon, M. Mircea, N. S. Mueller, and F. J. Theis, "Single-cell RNA-seq denoising using a deep count autoencoder," Nature Communications, vol. 10, no. 1, p. 390, 2019/01/23 2019.

[6] P. Danaee, R. Ghaeini, and D. A. Hendrix, "A DEEP LEARNING APPROACH FOR CANCER DETECTION AND RELEVANT GENE IDENTIFICATION," (in eng), Pacific Symposium on Biocomputing. Pacific Symposium on Biocomputing, vol. 22, pp. 219-229, 2017.

[7] L. L. M. Poon and M. Peiris, "Emergence of a novel human coronavirus threatening human health," Nature Medicine, vol. 26, no. 3, pp. 317-319, 2020/03/01 2020.

[8] S. M. Smith and J. M. Brady, "SUSAN—A New Approach to Low Level Image Processing," International Journal of Computer Vision, vol. 23, no. 1, pp. 45-78, 1997/05/01 1997.

[9] Y. Shu and J. McCauley, "GISAID: Global initiative on sharing all influenza data - from vision to reality," Euro Surveill, vol. 22, no. 13, Mar 30 2017.

[10] E. L. Hatcher et al., "Virus Variation Resource–improved response to emergent viral outbreaks," Nucleic acids research, vol. 45, no. D1, pp. D482-D490, 2017.

[11] W. R. Pearson and D. J. Lipman, "Improved tools for biological sequence comparison," (in eng), Proceedings of the National Academy of Sciences of the United States of America, vol. 85, no. 8, pp. 2444-2448, 1988.

[12] I. Miko and L. LeJeune, Essentials of Genetics. Cambridge, MA: NPG Education, 2009.

[13] J. Bresenham, "A linear algorithm for incremental digital display of circular arcs," Communications of the ACM, vol. 20, no. 2, pp. 100-106, 1977.
[14] R. Chokshi, D. Israni, and N. Chavda, "An efficient deconvolution technique by identification and estimation of blur," in 2016 IEEE International Conference on Recent Trends in Electronics, Information & Communication Technology (RTEICT), 2016, pp. 17-23: IEEE.
[15] G. Huang, Z. Liu, L. Van Der Maaten, and K. Q. Weinberger, "Densely connected convolutional networks," in Proceedings of the IEEE conference on computer vision and pattern recognition, 2017, pp. 4700-4708.
[16] C. Y. Li and N. T. Vu, "Densely Connected Convolutional Networks for Speech Recognition," in Speech Communication; 13th ITG-Symposium, 2018, pp. 1-5.
[17] J. Rubin, S. Parvaneh, A. Rahman, B. Conroy, and S. Babaeizadeh, "Densely connected convolutional networks and signal quality analysis to detect atrial fibrillation using short single-lead ECG recordings," in 2017 Computing in Cardiology (CinC), 2017, pp. 1-4.
[18] M. Long, Y. Cao, J. Wang, and M. I. Jordan, "Learning transferable features with deep adaptation networks," arXiv preprint arXiv:1502.02791, 2015.
[19] R. D. Gottapu and C. H. Dagli, "DenseNet for Anatomical Brain Segmentation," Procedia Computer Science, vol. 140, pp. 179-185, 2018/01/01/ 2018.
[20] V. Gupta et al., "Performance of a Deep Neural Network Algorithm Based on a Small Medical Image Dataset: Incremental Impact of 3D-to-2D Reformation Combined with Novel Data Augmentation, Photometric Conversion, or Transfer Learning," Journal of Digital Imaging, vol. 33, no. 2, pp. 431-438, 2020/04/01 2020.
[21] X. Xu, J. Lin, Y. Tao, and X. Wang, "An Improved DenseNet Method Based on Transfer Learning for Fundus Medical Images," in 2018 7th International Conference on Digital Home (ICDH), 2018, pp. 137-140.
[22] X.-L. Qiang, P. Xu, G. Fang, W.-B. Liu, and Z. Kou, "Using the spike protein feature to predict infection risk and monitor the evolutionary dynamic of coronavirus," Infectious Diseases of Poverty, vol. 9, no. 1, p. 33, 2020/03/25 2020.
[23] R. Lu et al., "Genomic characterisation and epidemiology of 2019 novel coronavirus: implications for virus origins and receptor binding," The Lancet, vol. 395, no. 10224, pp. 565-574, 2020.
[24] L. Zhang, J.-R. Yang, Z. Zhang, and Z. Lin, "Genomic variations of SARS-CoV-2 suggest multiple outbreak sources of transmission," medRxiv, p. 2020.02.25.20027953, 2020.
[25] X. Tang et al., "On the origin and continuing evolution of SARS-CoV-2," National Science Review, 2020.
[26] G. Zehender et al., "Genomic characterization and phylogenetic analysis of SARS-COV-2 in Italy," Journal of Medical Virology, vol. n/a, no. n/a, 2020/03/29 2020.
[27] F. Díez-Fuertes et al., "Phylodynamics of SARS-CoV-2 transmission in Spain," bioRxiv, p. 2020.04.20.050039, 2020.
[28] P. Yadav et al., "Full-genome sequences of the first two SARS-CoV-2 viruses from India," Indian Journal of Medical Research, Original Article vol. 151, no. 2, pp. 200-209, February & March 1, 2020 2020.
[29] A. Bal et al., "Molecular characterization of SARS-CoV-2 in the first COVID-19 cluster in France reveals an amino-acid deletion in nsp2 (Asp268Del)," bioRxiv, p. 2020.03.19.998179, 2020.

BIOGRAPHIES

Selçuk YAZAR Received the B.S. degree in engineering physics from the Ankara University in 1997. From 1998 to 2010, he worked as DevOps engineer and software developer. He received the M.S. and Ph.D. degrees in computer engineering from the Trakya University. His research interest include Internet of Things, Deep Learning and Virtualization.

European Journal of Technique

journal homepage: https://dergipark.org.tr/en/pub/ejt

Vol.12, No.2, 2022

PLL-Less Active/Reactive Power Control of Photovoltaic Energy Source with Applying *pq*-Theory in Single-Phase Grid System

Mehmet Büyük[1*]

[1*]Adıyaman University, Electrical-Electronics Engineering Department, 02040, Adıyaman, Türkiye (e-mail:mbuyuk@adiyaman.edu.tr).

ARTICLE INFO

Received: Jun., 10. 2022
Revised: Jul., 22. 2022
Accepted: Oct, 05. 2022

Keywords:
Renewable energy systems
Grid-connected inverter
PLL-less control
pq-theory
Reactive power support

Corresponding author: *Mehmet Büyük*

ISSN: *2536-5010* | e-ISSN: *2536-5134*

DOI: https://doi.org/10.36222/ejt.1129083

ABSTRACT

Converter systems are applied to manage active/reactive power control of photovoltaic (PV) source during integration with the electric grid system. The control algorithm of the conventional converter system consists of a reference generation unit, a dc-link voltage control loop, two power control loops and a phase lock loop (PLL) system. PLL unit is used to lock in phase angle of the electric grid, and to perform the coordinate transformation for calculations of the active/reactive powers. However, the control algorithm has a slow dynamic response because of utilisation of a PLL structure. In addition, additional complex mathematical computations are required with the use of a PLL algorithm. Furthermore, the interaction of the PLL and the power control loops may lead power oscillation problems under weak grid, and also result in instability of the PV system. In this study, to avoid the aforementioned issues and to enhance the power flow capability of the grid-connected PV panels, a PLL-less control algorithm in *pq*-theory is studied for the active/reactive power management and the grid synchronization. In addition, the mathematical formulations of the current control algorithm are presented in detail. To show the effectiveness of the PLL-less controller, a PV system model with using real PV panel groups is designed and constructed in a simulation environment. The proposed control method is tested under various operation cases such as dynamic environmental conditions, reactive power support and voltage variations. The proposed method shows efficient performance under applications of the different operation situations.

1. INTRODUCTION

Due to decreasing fossil fuels and rising demand for electrical energy, the use of renewable energy sources (RESs) in the electric grid system has increased dramatically around the world recently. Expanding the use of renewable energy sources is critical for supplying electricity and meeting future demand [1]. Once the RESs are used in expanded points in the electric grid system, they are referred to as distributed energy systems (DESs). With a growing demand for clean energy resources like as photovoltaic (PV), wind turbine (WT), and fuel cell technology, the word DESs is becoming increasingly often used (FC) [2]. PV systems have become into prominent among DESs owing to their wide advantages such as cheaper, robustness and easy installation [3]. In addition, PV system application has the potential to improve the electric network in terms of energy supply, power control, and system stability in this way. [4, 5]. Furthermore, by reducing the amount of power flowing through the distribution system, the electric grid's safety can be enhanced [1]. Moreover, the application of PV sources has contributed for efficient power utilization requirements in electric network system, particularly in low-voltage level applications [6, 7].

In electric grid system, the integration of PV units has been implemented in single-phase or three-phase configurations for the grid connection. A PV power structure needs proper power electronic converters for suitable power conversion during coupling with the electric grid [8, 9]. Two different stages, namely dc-dc converter and dc-ac converter, are usually applied for grid-connected RESs to control power flow and to provide a high quality power for the electric grid [10]. The main objective of the dc-dc converter is to ensure tracking of maximum power point (MPP) with an appropriate dc-link voltage level for the dc-ac converter [11]. Differently, a dual controller can be applied in PV system to achieve operation under mode change [12]. And the dc-ac converter is used to convert the dc power into ac power, and it is the key technology for the integration of PV panels into the utility grid. A convenient control algorithm is requested for the dc-ac inverter in order to satisfy the power management and reliable operation during the electric grid connection [13, 14]. Thus, the controller of the inverter should meet the requirements of the electric grid interconnection determined via regional and international standards.

In grid-connected PV system applications, control mechanism is used to satisfy the control of the dc-ac inverter,

and thus ensures the adjustment of the amount of the active and reactive powers supplied by the inverter system [15, 16]. The control algorithm of the dc-ac inverter usually consists of a dc-link voltage controller, a current/power controller, a reference generation unit and a phase lock loop (PLL) system. However, the main disadvantage of the inverter control algorithm is a slow dynamic tracking of the grid voltage due to using a PLL algorithm [17]. The application of the PLL requires extra heavy mathematical computations. Furthermore, some harmonic issues may occur under weak electric network due to the interaction of the PLL algorithm with the current/power control loop. This interaction may also lead to instability of the overall system [18]. Therefore, the calculation cost of the control algorithm can be lowered, and system stability can be improved during weak grid operation, by eliminating the necessity for the PLL system [19].

In literature, several PLL-less control algorithms are offered for the grid-connected PV systems to prevent the drawbacks of PLL application in the control loop. PLL-less control methods are examined for the single-phase [20, 21] and three-phase [22, 23] grid connected PV systems. Despite the fact that there have been some studies on PLL-less control algorithms for three-phase systems, the majority of researchers/academicians have focused on single-phase DES architectures. In [20], a PLL-less control system is suggested for a single stage grid-connected PV system. The rms quantity of the electric network voltage is needed to obtain the sinus and cosine functions for the coordinate transformation. However, when calculating the grid voltage rms value, there is a signal period delay, which influences the response time. In [24] and [25], different PLL-less control algorithm is suggested for using in active and reactive power management in PV source. However, an extra peak detector is applied to perform the synchronization capability. On the other hand, Khan et al. propose a dual loop controller in parallel without PLL need. [26, 27], in which two modulation parameters are acquired as a results of the proposed technique. Besides, the modulation parameters are summed to compute the reference modulation value, which brings about complicated switching modulation. Different from previous methods, advanced PLL-less control methods are reported by applying sliding mode control in Ref. [28] and nonlinear input-to-state-stability theory in Ref. [29]. In Ref. [30], a vector control based PLL-less method is applied for PV system, in which d-q vectors are used in control algorithm. However, aforementioned algorithms require more complex mathematical calculations to ensure PLL-less controller.

In this paper, a pq-theory control method without need of PLL algorithm is proposed for a single-phase grid-connected PV system to supply active/reactive power and to synchronize the electrical grid under a kind of operation cases. In this context, orthogonal signals of voltage and current signals are generated for active and reactive power calculation. Second-order generalized integrator (SOGI) function is preferred in this study to get the orthogonal components. The mathematical formulation of the SOGI function is provided in s-domain. To verify the effectiveness of the PLL-less control method, a single-phase grid-connected PV model has been designed and constructed in a simulation program environment. The proposed controller is tested under dynamic conditions such as temperature and irradiance changes. In addition, a reactive support case is examined to observe the response of the proposed technique. Moreover, the effectiveness of the proposed control is also tested under variations of the grid voltage. The proposed method has a remarkable response under voltage variations such as voltage sag and swell.

The rest of the paper is as follows; In Section 2, the configuration and design of the proposed system are described in detail. In Section 3, the PLL-less approach in pq-theory for the single-phase grid-tied PV system is presented. In addition, a comparison with the existing methods for single-phase PV sources is given in this section. The verification and assessment of the PLL-less method under various case studies are introduced in Section 4. And the conclusions are presented in Section “Conclusions”.

2. CONFIGURATION AND DESIGN OF THE PROPOSED SYSTEM

In this section, the power system configuration and system design of the single-phase grid-connected PV panels are conducted. By this way, the power system topology for a single-phase electrical system is illustrated. In addition, the design procedure of the proposed power system is briefly demonstrated.

2.1. Power circuit configuration of the grid-connected PV system

The block scheme of the proposed system configuration is demonstrated in Fig. 1. The proposed system is a single-phase electrical system that involves PV panel group, converter interface unit and the electric grid. PV source panels are able to supply active power for the electrical grid. Additionally, the converter system consists of a dc/dc converter and dc/ac inverter for interfacing the PV system with the electric network. Three-lag dc-dc boost converter topology is preferred in the current study to obtain lower ripple harmonic current. The boost converter controls the active power injected by PV units. On the other hand, the single-phase inverter system consists of a dc-link capacitor, an H-bridge inverter, an LCL ripple filter and a control algorithm. The dc-link capacitor maintains a stable dc voltage at the dc-link bus. The inverter performs the conversion of dc voltage into ac voltage. The control algorithm satisfies the control of active/reactive powers, dc voltage regulation and synchronization to the electrical grid. Besides, the LCL filter is used to interface the inverter to the electrical grid and to effectively reduce the high frequency ripple harmonics generated from the inverter.

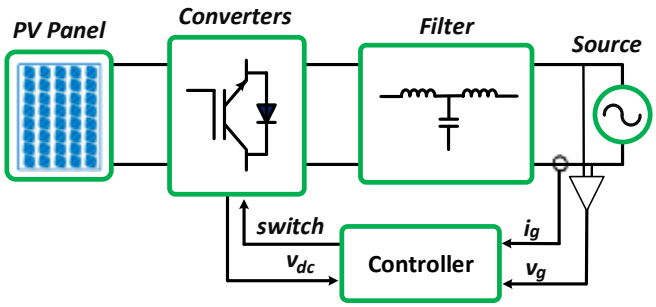

Figure 1. Power system structure of the single-phase grid-tied PV source

In the grid-connected PV systems, the conversion of the electrical energy and the control of the active/reactive powers are performed via the inverter system. The supplied active/reactive power amount is obtained by specifying the injected current amplitude and the phase angle with respect to the network phase voltage. The phase voltage and the supplied current from the inverter system are determined by equations (1) and (2).

$$v_g(t) = V_g \cos(wt + \emptyset_v) \quad (1)$$

$$i_g(t) = I_g \cos(wt + \emptyset_i) \quad (2)$$

where, V_g and I_g define the magnitudes of the electrical network voltage and the grid-side current of the inverter. Besides, $\emptyset_v$ and $\emptyset_i$ are the phase angles of the grid voltage and the current used for synchronization and power control.

The phase voltage magnitude and angle value are dependent to the electrical grid situations. Besides, the grid-side current amplitude and phase angle are calculated with the active power produced by PV energy amount and the reference reactive power value. The relationship of the injected active/reactive powers with the grid voltage, current and phase angles are given as Eq. (3). The voltage phase angle is usually selected as the reference angle during synchronization.

$$\left.\begin{aligned} P_{inj} &= \frac{1}{2}(V_g I_g \cos(\emptyset_v - \emptyset_i)) \\ Q_{inj} &= \frac{1}{2}(V_g I_g \sin(\emptyset_v - \emptyset_i)) \end{aligned}\right\} \quad (3)$$

where, the supplied active power is approximately equal to the power of PV source, ($P_{inj} \approx P_{pv}$). In addition, the reactive power is chosen according to the reference active power, in which the system controller decides according to power factor value, ($Q_{inj} = Q_{ref}$).

2.2. Design procedure of power circuit

In the grid-connected PV system, the design of the overall system consists of the design two systems: one is the design of PV panels with interfacing system, and the other is the inverter system design. Since the first one is out of scope of this study, the design of the inverter system is only presented in this section.

In this study, a single-phase inverter system is applied for interfacing PV units with the electrical grid. The overall design of the single-phase inverter system comprises the designs of the H-bridge inverter, the dc-link capacitor and the output LCL filter. The design of the inverter is related to the selection of the switching components (i.e. MOSFETs or IGBTs). The selection of the components is mainly decided according to the rated values of the system operating voltage, current and frequency variables. Thus, considering these parameters, the optimal components could be chosen from the electronic market.

On the other side, the dc-link capacitor is selected in terms of the system power, switching frequency, dc-link voltage and voltage ripple [31]. Thus, the dc-link capacitance is chosen according to the Eq. (4).

$$C_{dc} \geq \frac{0.15 S_N}{V_{dc} \Delta V_{dc} f_s} \quad (4)$$

where, S_N is the rated power of the inverter system. V_{dc} and ΔV_{dc} are the rated dc-link voltage and its allowable ripple ratio. f_s is the modulation frequency of the inverter.

The other design of the inverter system is the output LCL filter. This filter type includes two inductors and one capacitor. In design of the filter, the components are chosen by taking account the modulation index, the injected current ripple, the resonance frequency of the filter, voltage drop caused by inductances and power factor ratio in addition to the rated current and voltage values [2, 32]. The inductances/capacitance values are obtained by using the equations (5-7).

$$C_f \leq \frac{0.05 S_N}{3 w_0 V_N^2} \quad (5)$$

$$\frac{2V_{dc}(1 - m_i)m_i}{4 I_N \Delta I_{max} f_s} \leq L_1 + L_2 \leq \frac{3 V_g^2}{10 w_0 S_N} \quad (6)$$

$$L_2 = r L_1 \quad (7)$$

where, I_N and ΔI_{max} are the rated current value and its maximum ripple ratio. m_i determines the modulation index. Besides r is the split ratio between the inverter-side inductance (L_1) and the grid-side inductance (L_2). The split ratio is selected to be equal or higher than 1 [32].

In addition to these parameters, the selected values must satisfy the resonance frequency (w_r) range as (8). The resonance frequency should be higher than 10 times of the grid frequency and lower than half of the switching frequency.

$$10 w_0 \leq w_r \leq 0.5 w_s \quad (8)$$

where, $w_r = \sqrt{\frac{L_1 + L_2}{L_1 L_2 C_f}}$

According to the design criteria mentioned above, the entire system parameters are given in Table 1. The frequency response of the LCL filter according to the parameters in Table 1 is illustrated in Fig. 2. It can be seen the resonance frequency is dropped in the range determined in Eq. (8).

TABLE I
THE SYSTEM PARAMETERS OF THE PROPOSED SYSTEM

Electrical Grid	
Grid voltage (V_g)	311 V
Grid frequency (w_0)	100π rad/s
Inverter System	
Rated power (S_N)	5 kVA
DC-link voltage (V_{dc})	380 V
DC-link capacitor (C_{dc})	2.4 mF
Switching frequency (f_s)	7.5 kHz
LCL-filter	L_1 = 1 mH L_2 = 1 mH C_f = 50 µF

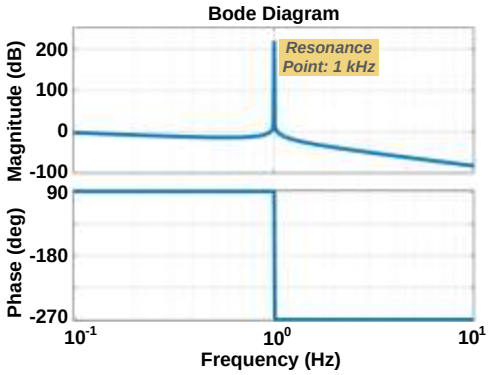

Figure 2. Frequency response of LCL filter applied in the system

3. PLL-LESS CONTROL METHODOLOGY IN PQ-THEORY

In this section, the PLL-less control mechanism in pq-theory is introduced for application in single-phase grid-connected PV sources. Moreover, to show the advantages of the proposed method, an illustrative table of the current literature is presented at the end of the section.

Figure 3 shows the detailed electrical circuit model of the single-phase grid-connected PV system. A three-lag dc-dc boost converter is applied between the PV panels and the inverter. Moreover, the details for the single-phase inverter

system are conducted in the previous section. Thus, the PLL-less control scheme in pq-theory for the inverter system is presented in detail in this section. The control algorithm of the inverter system is shown in Fig. 4. The control algorithm includes only three controller units; a dc-link controller and active/reactive power controllers. A PI controller is exploited for both the dc-link controller and power controllers.

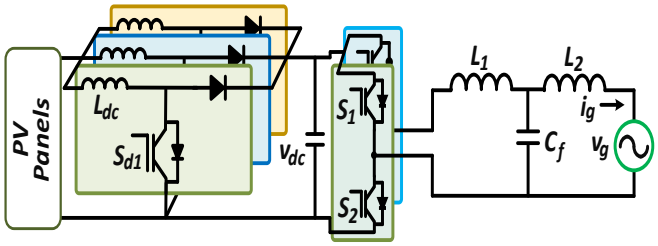

Figure 3. The detailed circuit diagram of the single-phase grid-connected PV system topology

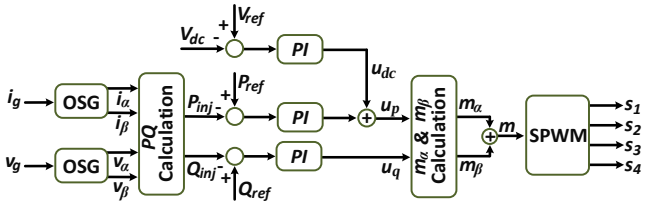

Figure 4. The control mechanism of the single-phase grid-connected PV source

The first step in control mechanism is to obtained orthogonal signals of voltage and current signals. Orthogonal signal generator (OSG) is applied for voltage and current to get the orthogonal signals. The OSG is a type of band-pass filter. The orthogonal signals (X_α-X_β) in s-domain are acquired as Eqs. (9) and (10).

$$X_\alpha(s) = \frac{kw_0 s}{s^2 + kw_0 s + {w_0}^2} X_g(s) \tag{9}$$

$$X_\beta(s) = \frac{k{w_0}^2}{s^2 + kw_0 s + {w_0}^2} X_g(s) \tag{10}$$

where, X implies the voltage signal V or current signal I. k is the coefficient for the controlling the response time and bandwidth. A phase delay is produced via the band-pass filter to generate the β component of voltage or current [9]. The frequency response of transfer functions for the α and β components are plotted in Fig. 5. It is obvious that the both signals are unity at 50 Hz frequency. Besides, α component has zero phase delay during the phase delay of β component is 90 degree. The waveforms of the generated α and β components of the signal X are illustrated in Fig. 6. As shown in Fig. 6, the grid signal X_g equals to X_α signal, and V_β signal is obtained by a 90^o phase delay to the α component.

After generation of the orthogonal signals of the voltage and current components, the active and reactive power are computed for power control. The injected active and reactive powers by the inverter system are obtained by the orthogonal signals as Eqs. (11-12).

$$P_{inj} = {}^1\!/_2\,(v_\alpha i_\alpha + v_\beta i_\beta) \tag{11}$$

$$Q_{inj} = {}^1\!/_2\,(v_\beta i_\alpha - v_\alpha i_\beta) \tag{12}$$

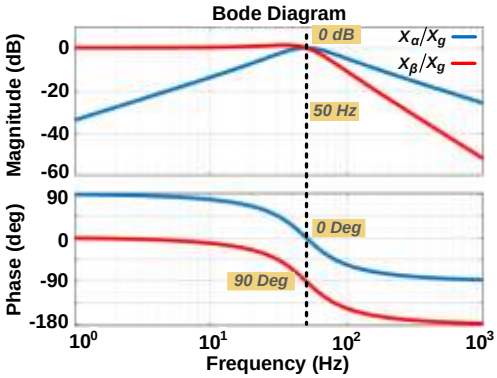

Figure 5. The frequency responses of the transfer functions for α and β components

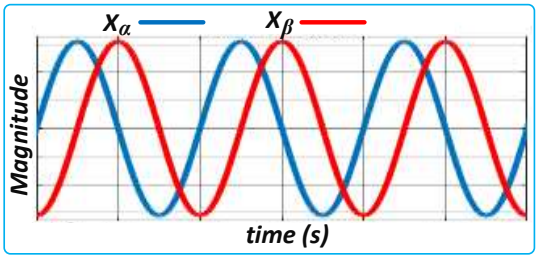

Figure 6. The waveforms of α and β components generated from OSG function

To control the power amount, the injected powers are extracted from the reference active and reactive power values to obtain power errors. Then, the error signals are curbed via the PI controllers for generating active and reactive reference components. The reference components are obtained as Eqs. (13-14).

$$u_p = k_p P_{err} + k_i \int P_{err} dt + u_{dc} \tag{13}$$

$$u_q = k_p Q_{err} + k_i \int Q_{err} dt \tag{14}$$

where, $P_{err} = P_{ref} - P_{inj}$ and $Q_{err} = Q_{ref} - Q_{inj}$. k_p and k_i are the PI parameters for the power controllers. P_{ref} is determined via MPPT controller and Q_{ref} is defined according to reactive power requirement by the electric grid. u_{dc} is the reference signal for the dc-link voltage fluctuations, in which it is determined as Eq. (15).

$$u_{dc} = k_{p,dc}(V_{ref} - V_{dc}) + k_{i,dc} \int (V_{ref} - V_{dc}) dt \tag{15}$$

where, $k_{p,dc}$ and $k_{i,dc}$ are proportional and integrator coefficients, respectively.

After that, the orthogonal modulation indices (m_α and m_β) can be derived by the Eqs. (16-17) as follows.

$$m_\alpha = \frac{(u_p + v_{\alpha\beta}^2)}{v_{dc}} v_\alpha + \frac{u_q}{v_{dc}} v_\beta \tag{16}$$

$$m_\beta = \frac{(u_p + v_{\alpha\beta}^2)}{v_{dc}} v_\beta - \frac{u_q}{v_{dc}} v_\alpha \tag{17}$$

The actual modulation signal is obtained via addition of the both orthogonal indices given in Eqs. (16) and (17), $m = m_\alpha + m_\beta$. v_{dc} and $v_{\alpha\beta}^2$ are the mean of the dc-link voltage and the square of the grid voltage amplitude, respectively. $v_{\alpha\beta}^2$ is calculated as follows.

$$v_{\alpha\beta}^2 = v_\alpha^2 + v_\beta^2 \quad (18)$$

The modulation signal is then compared with a triangle wave having 7.5 kHz frequency. The switches S_1 and S_4 are triggered once the reference is higher, and S_2 and S_3 are switched vice versa.

In addition, sinus and cosine function can be generated to apply for signal transformations. This can be achieved by dividing α and β components to the voltage amplitude as given in (19).

$$cos\theta = v_\alpha / v_{\alpha\beta}$$
$$sin\theta = v_\beta / v_{\alpha\beta} \quad (19)$$

Furthermore, to illustrate the benefits of the proposed control algorithm, a comparison of the single-phase grid-connected PV systems is presented in Table 2 through investigating several methods in literature in terms of the reference generation frame, PLL usage, and number and types of controllers.

TABLE II
A COMPARISON OF THE PROPOSED SYSTEM WITH THE SINGLE-PHASE GRID-CONNECTED INVERTER SYSTEMS

Ref. No	Reference Generation	PLL Usage	# of Controller			Modulation Method
			P/PI	PR	Others	
[33]	pq-theory	Yes	3	1	-	SPWM
[7]	pq-theory	Yes	1	2	-	SPWM
[34]	SRF	NA	3	-	-	SPWM
[35]	pq-theory	Yes	1	-	2 MPC	SPWM
[26]	SRF	No	3	-	-	SPWM
[36]	SRF	Yes	2	-	-	Hysteresis
[37]	SRF	Yes	2	-	-	SPWM
[38]	pq-theory	Yes	2	-	-	Hysteresis
Current Study	pq-theory	No	2	-	-	SPWM

(NA: Not Available, SRF: Synchronous Reference Frame, MPC: Model Predictive Control)

4. CASE STUDIES AND ASSESSMENT

In this section, the proposed control algorithm scheme is evaluated for a single-phase grid-tied PV units under various case studies. To examine the effectiveness of the proposed method, a grid-connected PV system is designed and constructed in a simulation environment. The rated power of the PV panels is constructed to apply a maximum 4.27 kW under optimal environmental situations. The PV modules are selected from SunPower manufacturer with SPR-305E-WHT-D model code, where each panel has 305 W maximum power generation rating. In accordance, seven series with two parallel string array is connected to acquire the rated power from the PV units.

The control algorithm is firstly examined under different voltage conditions, as illustrated in Fig. 7, in order to demonstrate the capability of the proposed method for the generation of the sinus and cosine functions. In the figure, the waveforms of the grid voltage, sinus function and cosine function are shown. A voltage sag and a voltage swell cases are constituted to examine the response of the proposed technique. The grid voltage drops to 0.7 pu from 1 pu between 1.1s and 1.2s. And it increases to 1.2 pu from 1 pu between 1.3s and 1.4s. Besides, it is unity at the other time intervals. It can be seen from the figure that the cosine and sinus functions are not affected during the voltage sag and swell cases.

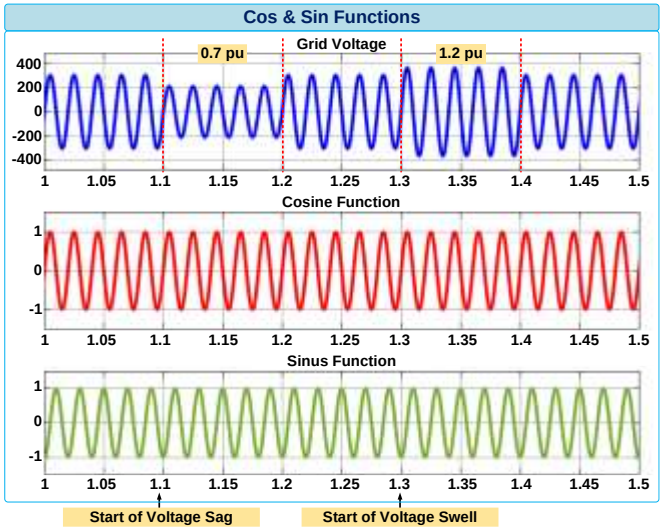

Figure 7. Generation of sinus and cosine functions under voltage sag and swell conditions

The proposed control algorithm with the designed system is investigated and verified under three different cases: (1) Dynamic operation conditions, (2) Reactive power support and (3) Voltage sag and swell.

4.1. Case 1: Dynamic operation conditions

The proposed method is investigated under a dynamic operation case in order to provide reliable and efficient operation of the proposed method for the grid-connected PV system. By this way, the proposed method is investigated under different temperature and irradiance values. Moreover, the proposed algorithm can be applied for other distributed sources such as FC unit under temperature changes and wind energy under various wind speed values.

Figure 8 shows the changes in the temperature and irradiance between 0.5s and 3s time intervals for verifying the proposed control method in dynamic operation condition. It is clear from the figure a temperature change is applied between 1s-2s time interval by increasing to 31 ^{0}C from 25 ^{0}C. In addition, the irradiance varies from 1000 W/m^2 to 600 W/m^2.

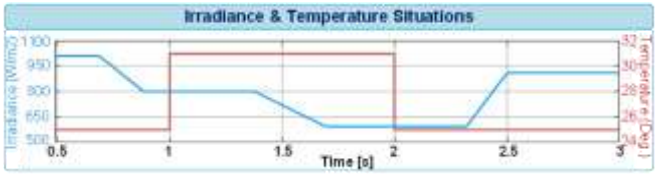

Figure 8. Irradiance and temperature situations for dynamic operation case

The response of the proposed method under the temperature and irradiance variations in Fig. 8 is demonstrated in Fig. 9. The grid voltage, grid current, dc-link voltage and the injected active power are given in Fig. 9. It can be seen that the grid current, the dc-link voltage and the injected active power have smooth responses with the proposed method under the dynamic temperature and irradiance changes. The dc-link voltage has almost 2-3 V oscillation during the condition changes. Besides, the injected current and active power have effective transient responses under the dynamic operation case.

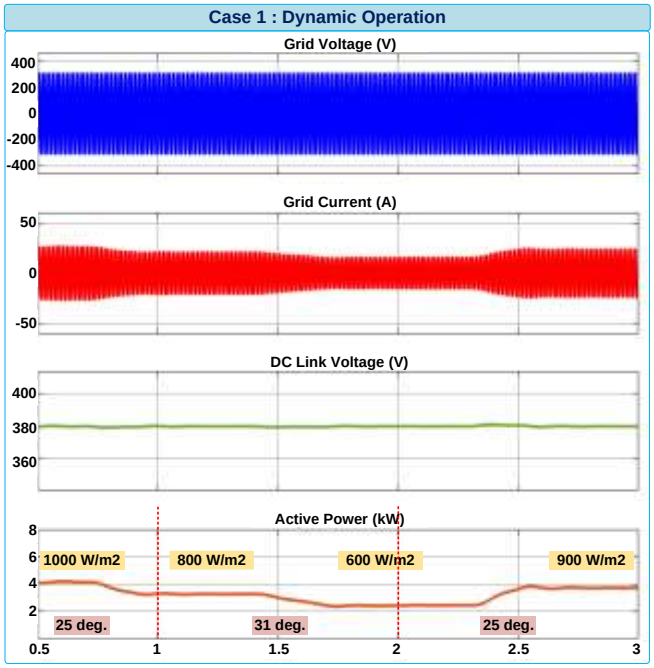

Figure 9. Response of the proposed method under changes of irradiance and temperature

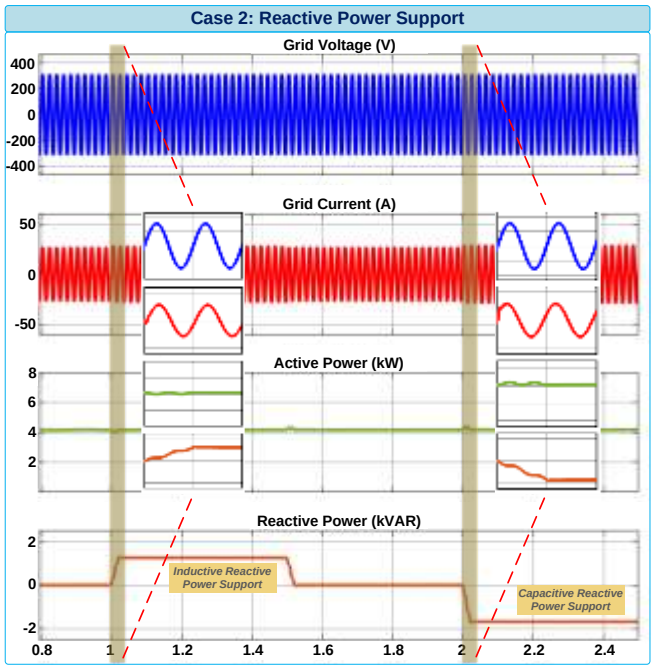

Figure 10. Injection of inductive and capacitive reactive powers to support the electrical grid

4.2. Case 2: Reactive power support

The proposed control approach is also examined by consideration of a reactive power support operation case. In this context, both capacitive reactive power and inductive reactive power support cases are performed with the proposed method. The injection of inductive reactive power and capacitive reactive power cases to support the electrical grid is indicated in Fig. 10. In the figure, the grid voltage, the grid current, the active power and the reactive power are presented. The inductive reactive power support is performed between 1s-1.5s time intervals by 30 % rating of the injected active power. Besides, a capacitive power support of forty percent of the injected active power is provided at 2s-2.5s time interval. It is obvious that the proposed method has a remarkable performance during both inductive and capacitive reactive power support events.

4.3. Case 3: Voltage sag/swell situations

In order to demonstrate the robustness of the proposed control algorithm, both sag and swell conditions of the grid voltage are evaluated in this case via varying the grid voltage amplitude. Figure 11 illustrates the waveforms of the grid voltage, the grid current, the dc-link voltage and the injected active power for both voltage sag and voltage swell situations.

The voltage sag and the voltage swell are performed by 30 % and 20 %, respectively. The voltage sag case starts at 1.1s, and lasts for five periods, as shown in Fig. 11 (a). It is clear that the proposed controller ensures a good stability performance during the occurrence of the voltage sag. The injected power is set to its stable condition at 0.06s. Moreover, the dc-link voltage has low voltage oscillation (almost 5 V), once the voltage sag occurs.

On the other side, the voltage swell case is performed at 1.3s, and similar to the voltage sag, it continues five periods, as demonstrated in Fig. 11 (b). The proposed control algorithm also shows efficient response under the voltage swell. In this case, the injected power is set to its stable situation at 0.08s. Furthermore, almost 4V oscillation is observed when the voltage amplitude arises.

5. CONCLUSIONS

In this paper, a PLL-less control algorithm in pq-theory is performed for single-phase grid-connected PV system. The PLL usage is not required with the control method in the current study. Thus, the calculation complexity of the PLL application is avoided in this study, which results in low computation burden. In addition, the instabilities that may arise from the usage of a PLL are prevented by this method. The mathematical background of the PLL-less control mechanism in pq-theory is introduced in detail. In the current controller scheme, orthogonal signals of the grid voltage and inverter current are generated by SOGI function to obtain injected powers and then calculate modulation indices. Moreover, only two controllers without dependence on a PLL application are needed in the proposed control technique.

To observe the ability of the control technique in this study, a single-phase grid-connected PV system is designed and built in the simulation environment. The performance of the control scheme in the generation of alpha and beta functions is firstly validated under weak grid operation such as voltage sag and voltage swell conditions. It is shown that the both functions do not have any impact from the occurrences of the voltage sag and swell. The control scheme is also tested for three difference scenario cases in the constructed simulation model. These cases consist of the conditions of a dynamic operation, reactive power support and voltage sag/swell, respectively. The proposed method is tested under %30 voltage sag and %20 voltage swell situations. In addition, a reactive power support with 30 percentage of the active power is supplied both for inductive and capacitive cases. The robustness and effective performance of the proposed method are verified for applications of the different temperature and irradiance values for dynamic operation case, inductive and capacitive reactive power supports in the second case, and occurrences of 30 % voltage sag and 20 % voltage swell in the third case.

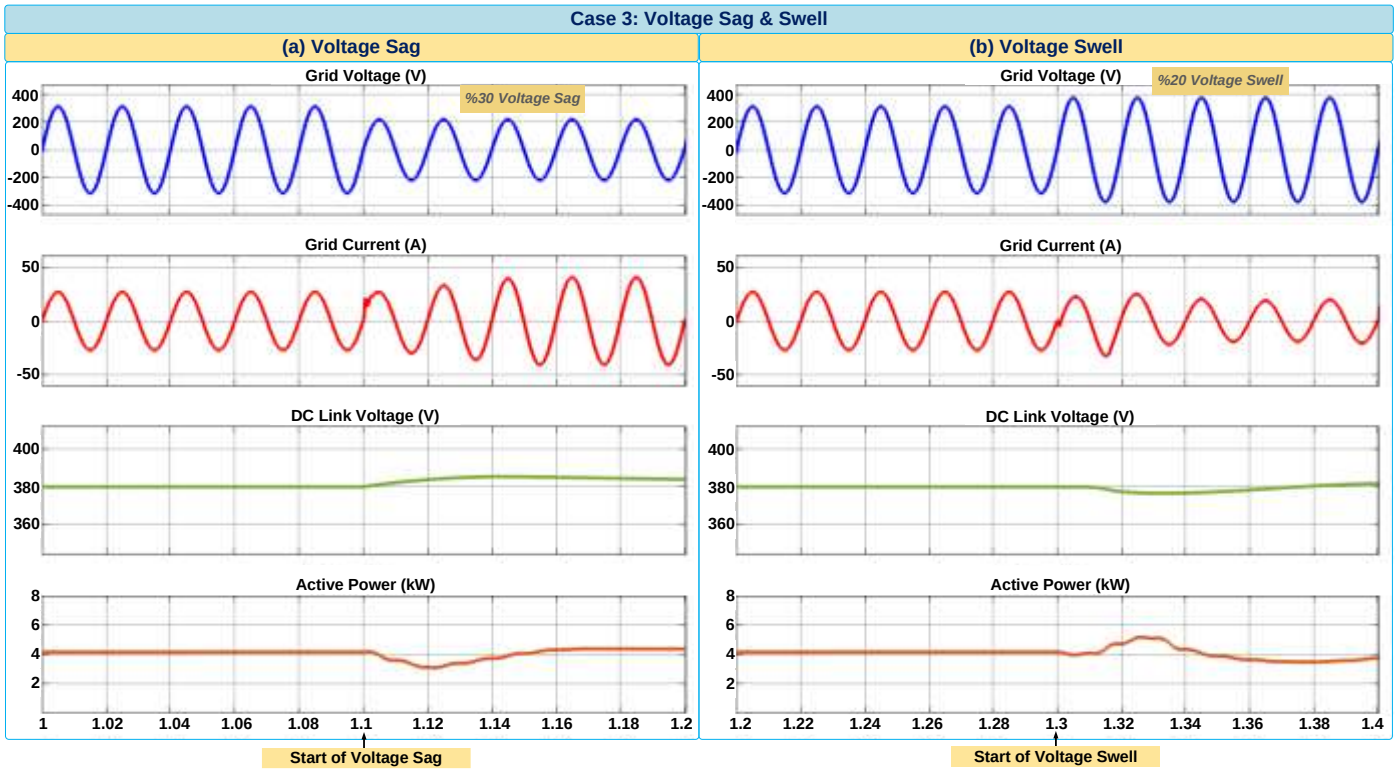

Figure 11. The response of the proposed method under (a) voltage sag and (b) voltage swell cases

REFERENCES

[1] R. Sharma and S. Mishra, "Dynamic Power Management and Control of a PV PEM Fuel-Cell-Based Standalone ac/dc Microgrid Using Hybrid Energy Storage," *IEEE Transactions on Industry Applications*, vol. PP, pp. 1-1, 09/22 2017.

[2] M. Büyük, A. Tan, M. Tümay, and K. Ç. Bayındır, "Topologies, generalized designs, passive and active damping methods of switching ripple filters for voltage source inverter: A comprehensive review," *Renewable and Sustainable Energy Reviews*, vol. 62, pp. 46-69, 2016/09/01/ 2016.

[3] K. Brecl, J. Ascencio-Vásquez, and M. Topič, "Performance of PV systems in Slovenia with the help of typical daily profiles and automatic detection of orientation and inclination angles," *Solar Energy*, vol. 236, pp. 870-878, 2022/04/01/ 2022.

[4] M. Bornapour, R.-A. Hooshmand, A. Khodabakhshian, and M. Parastegari, "Optimal coordinated scheduling of combined heat and power fuel cell, wind, and photovoltaic units in micro grids considering uncertainties," *Energy*, vol. 117, pp. 176-189, 2016/12/15/ 2016.

[5] M. A. Hannan, S. Y. Tan, A. Q. Al-Shetwi, K. P. Jern, and R. A. Begum, "Optimized controller for renewable energy sources integration into microgrid: Functions, constraints and suggestions," *Journal of Cleaner Production*, vol. 256, p. 120419, 2020/05/20/ 2020.

[6] E. Kabalcı, "Review on novel single-phase grid-connected solar inverters: Circuits and control methods," *Solar Energy*, vol. 198, pp. 247-274, 2020/03/01/ 2020.

[7] B. Liu, Z. Zhang, G. Li, D. He, Y. Chen, Z. Zhang, *et al.*, "Integration of power decoupling buffer and grid-tied photovoltaic inverter with single-inductor dual-buck topology and single-loop direct input current ripple control method," *International Journal of Electrical Power & Energy Systems*, vol. 125, p. 106423, 2021/02/01/ 2021.

[8] G. Liu, T. Caldognetto, P. Mattavelli, and P. Magnone, "Suppression of Second-Order Harmonic Current for Droop-Controlled Distributed Energy Resource Converters in DC Microgrids," *IEEE Transactions on Industrial Electronics*, vol. 67, pp. 358-368, 2020.

[9] C. Xie, K. Li, X. Zhao, J. C. Vasquez, and J. Guerrero, *Reduced Order Generalized Integrators with Phase Compensation for Three-Phase Active Power Filter*, 2017.

[10] P. Verma, T. Kaur, and R. Kaur, "Power control strategy of an integrated PV system for active power reserve under dynamic operating conditions," *Sustainable Energy Technologies and Assessments*, vol. 45, p. 101066, 2021/06/01/ 2021.

[11] J. P. Roselyn, C. P. Chandran, C. Nithya, D. Devaraj, R. Venkatesan, V. Gopal, *et al.*, "Design and implementation of fuzzy logic based modified real-reactive power control of inverter for low voltage ride through enhancement in grid connected solar PV system," *Control Engineering Practice*, vol. 101, p. 104494, 2020/08/01/ 2020.

[12] Y. Wang, B. Ren, and S. Liyanage, "Unified control scheme for a dual-stage grid-connected PV system with mode change," *Solar Energy*, vol. 239, pp. 88-101, 2022/06/01/ 2022.

[13] D. Çelik and M. E. Meral, "A novel control strategy for grid connected distributed generation system to maximize power delivery capability," *Energy*, vol. 186, p. 115850, 2019/11/01/ 2019.

[14] M. M. Savrun and M. İnci, "Adaptive neuro-fuzzy inference system combined with genetic algorithm to improve power extraction capability in fuel cell applications," *Journal of Cleaner Production*, vol. 299, p. 126944, 2021/05/25/ 2021.

[15] S. Gu, X. Du, Y. Shi, Y. Wu, P. Sun, and H. Tai, "Power control for grid-connected converter to comply with safety operation limits during grid faults," in *2016 IEEE Energy Conversion Congress and Exposition (ECCE)*, 2016, pp. 1-5.

[16] A. Q. Al-Shetwi, M. A. Hannan, K. P. Jern, M. Mansur, and T. M. I. Mahlia, "Grid-connected renewable energy sources: Review of the recent integration requirements and control methods," *Journal of Cleaner Production*, vol. 253, p. 119831, 2020/04/20/ 2020.

[17] P. Rodríguez, A. Luna, I. Candela, R. Mujal, R. Teodorescu, and F. Blaabjerg, "Multiresonant Frequency-Locked Loop for Grid Synchronization of Power Converters Under Distorted Grid Conditions," *IEEE Transactions on Industrial Electronics*, vol. 58, pp. 127-138, 2011.

[18] B. Wen, D. Boroyevich, R. Burgos, P. Mattavelli, and Z. Shen, "Analysis of D-Q Small-Signal Impedance of Grid-Tied Inverters," *IEEE Transactions on Power Electronics*, vol. 31, pp. 675-687, 2016.

[19] Y. Gui, X. Wang, F. Blaabjerg, and D. Pan, "Control of Grid-Connected Voltage-Source Converters: The Relationship Between Direct-Power Control and Vector-Current Control," *IEEE Industrial Electronics Magazine*, vol. 13, pp. 31-40, 2019.

[20] K. M. Tsang, W. L. Chan, and X. Tang, "PLL-less single stage grid-connected photovoltaic inverter with rapid maximum power point tracking," *Solar Energy*, vol. 97, pp. 285-292, 2013/11/01/ 2013.

[21] K. S. R. Sekhar and M. A. Chaudhari, "Reactive Power Enhancement of a PLL less PV inverter for AC Micro-grids," in *2020 IEEE First International Conference on Smart Technologies for Power, Energy and Control (STPEC)*, 2020, pp. 1-6.

[22] S. Dedeoglu and G. C. Konstantopoulos, "PLL-Less Three-Phase Droop-Controlled Inverter with Inherent Current-Limiting Property," in *IECON 2019 - 45th Annual Conference of the IEEE Industrial Electronics Society*, 2019, pp. 4013-4018.

[23] P. Patel, U. Mali, and G. Patel, "PLL less strategy for grid tied inverter with different load conditions," in *2017 Third International Conference on Advances in Electrical, Electronics, Information, Communication and Bio-Informatics (AEEICB)*, 2017, pp. 251-254.

[24] X. Li and R. S. Balog, "PLL-less robust active and reactive power controller for single phase grid-connected inverter with LCL filter," in *2015 IEEE Applied Power Electronics Conference and Exposition (APEC)*, 2015, pp. 2154-2159.

[25] S. Deo, C. Jain, and B. Singh, "A PLL-Less Scheme for Single-Phase Grid Interfaced Load Compensating Solar PV Generation System," *IEEE Transactions on Industrial Informatics*, vol. 11, pp. 692-699, 2015.

[26] A. Khan, M. Hosseinzadehtaher, and M. B. Shadmand, "Single Stage PLL-less Decoupled Active and Reactive Power Control for Weak Grid Interactive Inverters," *IFAC-PapersOnLine*, vol. 53, pp. 12390-12395, 2020/01/01/ 2020.

[27] A. Khan, M. Easley, M. Hosseinzadehtaher, M. B. Shadmand, H. Abu-Rub, and P. Fajri, "PLL-less Active and Reactive Power Controller for Grid-Following Inverter," in *2020 IEEE Energy Conversion Congress and Exposition (ECCE)*, 2020, pp. 4322-4328.

[28] E. Heydari, A. Y. Varjani, and D. Diallo, "Fast terminal sliding mode control-based direct power control for single-stage single-phase PV system," *Control Engineering Practice*, vol. 104, p. 104635, 2020/11/01/ 2020.

[29] G. C. Konstantopoulos, Q. Zhong, and W. Ming, "PLL-Less Nonlinear Current-Limiting Controller for Single-Phase Grid-Tied Inverters: Design, Stability Analysis, and Operation Under Grid Faults," *IEEE Transactions on Industrial Electronics*, vol. 63, pp. 5582-5591, 2016.

[30] K. S. Raja Sekhar, M. A. Chaudhari, and T. Davi Curi Busarello, "A PLL-less Vector Control technique for the single-phase Grid connected inverters," *International Journal of Electrical Power & Energy Systems*, vol. 142, p. 108353, 2022/11/01/ 2022.

[31] R. Chen, "DC Capacitor Minimization of Single Phase Power Conversion and Applications," PhD, Michigan State University., 2016, PhD Thesis.

[32] H. Cha and T. Vu, "Comparative analysis of low-pass output filter for single-phase grid-connected Photovoltaic inverter," in *2010 Twenty-Fifth Annual IEEE Applied Power Electronics Conference and Exposition (APEC)*, 2010, pp. 1659-1665.

[33] Ö. Çelik, A. Tan, M. İnci, and A. Teke, "Improvement of energy harvesting capability in grid-connected photovoltaic micro-inverters," *Energy Sources, Part A: Recovery, Utilization, and Environmental Effects*, pp. 1-25, 04/24 2020.

[34] C. Kalavalli, P. Meenalochini, P. Selvaprasanth, and S. Syed Abdul Haq, "Dual loop control for single phase PWM inverter for distributed generation," *Materials Today: Proceedings*, vol. 45, pp. 2216-2219, 2021/01/01/ 2021.

[35] M. Talha, S. R. S. Raihan, and N. A. Rahim, "PV inverter with decoupled active and reactive power control to mitigate grid faults," *Renewable Energy*, vol. 162, pp. 877-892, 2020/12/01/ 2020.

[36] S. Roy, P. Kumar Sahu, S. Jena, and A. Kumar Acharya, "Modeling and control of DC/AC converters for photovoltaic grid-tie micro-inverter application," *Materials Today: Proceedings*, vol. 39, pp. 2027-2036, 2021/01/01/ 2021.

[37] L. Hassaine and B. Mohamed Rida, "Control technique for single phase inverter photovoltaic system connected to the grid," *Energy Reports*, vol. 6, 11/01 2019.

[38] M. İnci, "Active/reactive energy control scheme for grid-connected fuel cell system with local inductive loads," *Energy*, vol. 197, p. 117191, 2020/04/15/ 2020.

BIOGRAPHIES

Mehmet Büyük received his BSc and MSc degrees in Electrical-Electronics Engineering from Çukurova University, in 2012 and 2015. He received the PhD degree in Electrical-Electronics Engineering from Çukurova University, 2019. He is currently Researcher at the department of Electrical-Electronics Engineering, Adıyaman University. His research areas are custom power devices, power quality, vehicle-to-grid (V2G) systems and wireless power transfer.

European Journal of Technique

journal homepage: https://dergipark.org.tr/en/pub/ejt

Vol.12, No.2, 2022

Estimation through ANN of Voltage Drop Resulting from Overloads on Power Transformers

Onur Akar[1*]

[1*]Marmara University, Department of Electronics and Automation, Istanbul, Türkiye. (e-mail: onur.akar@marmara.edu.tr).

ARTICLE INFO

Received: Oct., 17. 2022
Revised: Dec., 05, 2022
Accepted: Dec, 07. 2022

Keywords:
Voltage Drop
Power Transformers
Artificial Neural Network
Electrical Energy Quality

Corresponding author: *Onur Akar*

ISSN: *2536-5010* | e-ISSN: *2536-5134*

DOI: https://doi.org/10.36222/ejt.1190240

ABSTRACT

Along with the increasing population, technological developments and industrialization in the world, the need for electrical energy shows rapid increase day by day. For that reason, it is very important to ensure permanence in the process from the generation of electrical energy to its transmission to consumers. One of the most significant components of power systems is the power transformer, and it plays an important role in the process of energy transmission and distribution. Thus, continuous operation of the power transformers should be ensured for the quality and reliability of the power systems. Despite the institutions in charge of electric power generation, transmission and distribution carry out inspections for the continuous operation of the power transformers, failures resulting from voltage drop arise due to overloads. In this study, the estimation through Artificial Neural Network (ANN) of voltage drop resulting from overloads was performed using the data of power transformers of different quality. It was observed that the values obtained as the result of estimations through ANN were correct with a rate of 99%. It is considered that this study will set an example for other studies in the field.

1. INTRODUCTION

Electrical energy is one of the essential requirements of our lives along with today's technological developments. The quality of electrical energy is a significant issue that concerns the producer and distributor companies as well as the consumers in the competitive energy market. In general, quality of energy is important in terms of problems causing changes in current, voltage and frequency that can result in misoperation or failure of consumers' devices [1,2]. Low quality energy is able to cause problems on the electronic devices as well as the electrical home appliances. Sensitive devices such as computers and televisions are greatly affected especially from voltage and frequency changes. The quality of electrical energy also affects the production quality and efficiency at industrial facilities. The electrical appliances cannot show the required performance when they are fed with interrupted energy, or with an energy different than the required values. For such reasons, the quality of energy is important at all points of consumption of electrical energy and at all kinds of voltage levels. In addition, the harmonics, overvoltage and undervoltage are among the most frequently encountered problems. The voltage drop is defined as short-term reductions in the voltage amplitude. According to IEEE Std 1159-1995, the voltage drop remains between 10% and 90% of the nominal voltage, and the period of drop is able to change between half a period and one minute. The voltage drop's waveform and range is as shown in Fig. 1 [3-6].

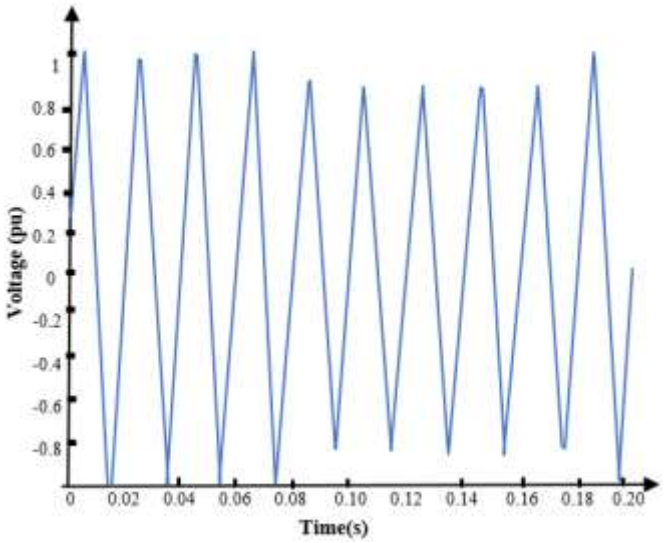

Figure 1. Waveform of voltage drop

Short-term voltage drops affects sensitive loads in industrial distribution systems. In addition, the voltage drop is also relevant to balanced and unbalanced failures in distribution systems, location, and different transformer connection groups [3,4,7]. In principle, the root cause of voltage drop is all the circumstances causing current increase in the system. Three main causes are indicated for the occurrence of voltage

drop. These are short circuit, failures occurring superficially in the systems, and high current drawn during commissioning of high power motors and of power transformers, respectively [8-10]. The power transformer is one of the most significant parameters constituting the energy transmission and distribution system. Smooth operation of power transformers is a very important criterion in ensuring the continuity and stability of demand guarantee in the energy system. The power transformers encounter different types of failures, and the repair and elimination of such failures are being highly expensive and time-consuming [11,12]. But the transformers' lifetime is able to be extended up to 60 years through proper maintenance and monitoring. But knowing the effect of voltage drops caused by such failures in transmission and distribution systems on large industrial loads and on engines provides great ease regarding the characteristics of short-term voltage drops in distribution systems [13,14]. It was observed that the transformers reach saturation following the occurrence of voltage drop. It is known that the root cause of transformers' saturation is the magnetizing current 10-20 times the nominal current drawn by the transformer from the mains in spike occurring following the finalization of voltage drop. Magnetizing current is at very high levels and causes harmonic distortion during energizing of transformer as unloaded or under low load. In some cases, similar magnetizing current occurs through return of voltage to its normal value following voltage drop, and in other cases, it occurs as the result of high amplitude harmonic distortion due to saturation of the transformer [15-19].

In the studies performed, methods based on measurement with respect to voltage drop against loading of power transformers were examined. In this study, it was intended to estimate voltage drop of transformers under full load through the ANN model developed by the use of specific input variables of the transformers. In this manner, the estimation through ANN of voltage drops resulting from overloads on transformers was performed.

2. MATERIAL AND METHOD

2.1. Transformers' Data

In this study, the values of power, rated voltage, idle leakage current, loss at full load, idle loss, short circuit voltage, voltage drop at full load, and efficiency at full load of power transformers with different characteristics were used as specified in Table I [20].

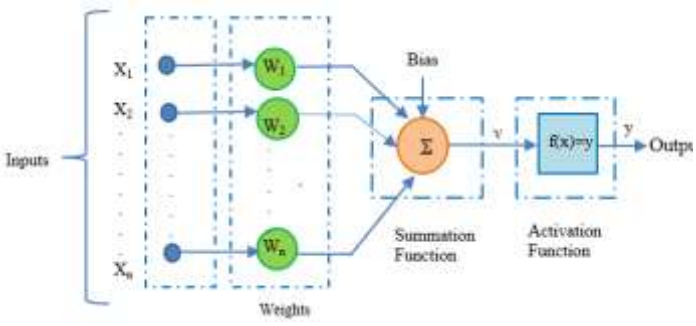

Figure 2. Structure of artificial neuron

TABLE I

TECHNICAL SPECIFICATIONS OF POWER TRANSFORMERS

Power (kVA)	*Rated Voltage (kV)*	*Idle Current (% Io)*	*Loss at Full Load (W)*	*Idle Loss (W)*	*Short Circuit V(%Uk)*	*V. Drop at full Load(%)*	*Efficiency at Full Load (%)*
25	6.3	2.5	550	65	4	3.773	9.02
25	10.5	2.5	550	65	4	3.773	97.02
25	15.8	2.5	550	65	4	3.773	97.02
25	33	3.15	700	110	4.5	4.360	96.11
40	6.3	2.4	650	80	4	3.512	97.77
40	10.5	2.4	650	80	4	3.512	97.77
40	15.8	2.4	650	80	4	3.512	97.77
40	33	2.92	900	135	4.5	4.153	96.87
50	6.3	2.3	750	90	4	3.446	97.94
50	10.5	2.3	750	90	4	3.446	97.94
50	15.8	2.3	750	90	4	3.446	97.94
50	33	2.76	1050	160	4.5	4.086	97.06
63	6.3	2.25	900	110	4	3.407	98.04
63	10.5	2.25	900	110	4	3.407	98.04
63	15.8	2.25	900	110	4	3.407	98.04
63	33	2.62	1225	195	4.5	4.012	97.26
80	6.3	2.2	1050	125	4	3.342	98.20
80	10.5	2.2	1040	125	4	3.342	98.20
80	15.8	2.2	1050	125	4	3.342	98.20
80	33	2.5	1400	225	4.5	3.913	97.52
100	6.3	2.1	1250	145	4	3.306	98.29
100	10.5	2.1	1250	145	4	3.306	98.29
100	15.8	2.1	1250	145	4	3.306	98.29
100	33	2.27	1600	270	4.5	3.859	97.66
125	6.3	2	1475	175	4	3.264	98.38
125	10.5	2	1475	175	4	3.264	98.38
125	15.8	2	1475	175	4	3.264	98.38
125	33	2.14	1900	330	4.5	3.787	97.82
160	6.3	1.9	1700	210	4	3.193	98.53
160	10.5	1.9	1700	210	4	3.193	98.53
160	15.8	1.9	1700	210	4	3.193	98.53
160	33	2	2150	390	4.5	3.686	98.05
200	6.3	1.9	2025	255	4	3.162	98.58
200	10.5	1.9	2025	255	4	3.162	98.58
200	15.8	1.9	2025	255	4	3.162	98.58
200	33	1.9	2575	470	4.5	3.652	98.10
250	6.3	1.6	2350	300	4	3.117	98.69
250	10.5	1.6	2350	300	4	3.117	98.69
250	15.8	1.6	2350	300	4	3.117	98.69
250	33	1.8	3000	550	4.5	3.600	98.26
315	6.3	1.5	2800	365	4	3.084	98.76
315	10.5	1.5	2800	365	4	3.084	98.76
315	15.8	1.5	2800	365	4	3.084	98.76
315	33	1.7	3575	670	4.5	3.559	98.34
400	6.3	1.5	3250	430	4	3.034	98.86
400	10.5	1.5	3250	430	4	3.034	98.86
400	15.8	1.5	3250	430	4	3.034	98.86
400	33	1.7	4150	790	4.5	3.498	98.48
500	6.3	1.4	3950	520	4	3.020	98.89
500	10.5	1.4	3950	520	4	3.020	98.89
500	15.8	1.4	3950	520	4	3.020	98.89
500	33	1.6	4850	950	4.5	3.455	98.56
630	6.3	1.4	4600	600	4	2.980	98.98
630	10.5	1.4	4600	600	4	2.980	98.98
630	15.8	1.4	4600	600	4	2.980	98.98
630	33	1.6	5500	1100	4.5	3.392	98.71
800	6.3	1.3	6000	650	4	4.264	98.98
800	10.5	1.3	6000	650	4	4.264	98.98
800	15.8	1.3	6000	650	4	4.264	98.98
800	33	1.50	7000	1300	4.5	4.350	98.72
1000	6.3	1.20	7600	770	4	4.271	98.96
1000	10.5	1.20	7600	770	4	4.271	98.96
1000	15.8	1.20	7600	770	4	4.271	98.96
1000	33	1.40	8900	1450	4.5	4.360	98.72
1250	6.3	1.20	9500	950	4	4.271	98.97
1250	10.5	1.20	9500	950	4	4.271	98.97
1250	15.8	1.20	9500	950	4	4.271	98.97
1250	33	1.40	11500	1750	4.5	4.810	98.69
1600	6.3	1.10	12000	1200	4	4.264	98.98
1600	10.5	1.10	12000	1200	4	4.264	98.98
1600	15.8	1.10	12000	1200	4	4.264	98.98
1600	33	1.30	14500	2200	4.5	4.371	98.71
2000	6.3	1.10	15000	1450	4	4.264	98.98
2000	10.5	1.10	15000	1450	4	4.264	98.98
2000	15.8	1.10	15000	1450	4	4.264	98.98
2000	33	1.20	18000	2700	4.5	4.367	98.72
2500	6.3	1.00	18500	1750	4	4.257	99.00
2500	10.5	1.00	18500	1750	4	4.250	99.00
2500	15.8	1.00	18500	1750	4	4.250	99.00

2.2. Artificial Neural Network (ANN)

The artificial neural networks consist of artificial neurons indicated in Fig. 2. The artificial neurons are the data processing technology formed by simulating the biological nervous system as being inspired from the information processing technique of human brain and real neurons. ANN is a method frequently used in the solution of complex problems [21-25].

In artificial neural networks, the data is given to the network from the input layer. The information reaching the network as being processed in interlayers is converted to output by the use of network's weight values. For the network to be able to generate the correct outputs for the inputs, it is required for the weights to have correct values. The operation of determining the correct weights is called network training. The required number of value items in input and output layers is determined considering the problem. There is no method indicating the required number of items in each layer along with the number of interlayers. In general, it is found with the trial and error method [26-28].

In order to be able to make estimation with ANN, it is first required to train the ANN to be formed. In this study, the variables used for ANN training were input (weight) values, and output (target) values. These values are shown in Table II. As ANN's input values, the values of power, rated voltage, idle leakage current, loss at full load, idle loss, short circuit voltage, voltage drop at full load, and efficiency at full load of power transformer were used. The transformer's voltage drop at full load (%) was assigned as ANN's output value.

TABLE II
ANN INPUT AND OUTPUT VALUES

Inputs	Weight and Target Data	Max.Values	Min. Values
X1	Transformer Power(kVA)	2500	25
X2	Rated Voltage(kV)	33	6.3
X3	Idle Current(%Io)	3.15	1
X4	Loss at full Load (W)	22500	550
X5	Idle Load (W)	3200	65
X6	Short Circuit Voltage (%Uk)	4.5	4
X7	Efficiency at Full Load (%)	99	96.11
Y1	Voltage Drop at Full Load (%)	4810	2980

3. IMPLEMENTATION

The input (weight) and output (target) values of the ANN model formed in order to estimate the transformers' voltage drop at full load are shown in Fig. 3. In ANN, it is required to convert the verbal data to digital data. Without the conversion, it will not be possible for us to introduce these values to ANN. The operation of making the training of ANN more efficient by subjecting the weight and target data, to be used in the training of network, to specific operations is called the normalization operation. In this study, the training data was reduced to the range of (0, 1) by the use of min.-max. Equation 2 was used to reduce the training data to this interval. The data obtained as the result of normalization is as shown in Table III [29-31].

$$X' = \frac{(X_i - X_{min})}{(X_{max} - X_{min})} \qquad (1)$$

In the Equation;

X' is the normalized value,
X_i is the input value of ANN,
X_{min} is the smallest value of input value,
X_{max} is the greatest value of input value

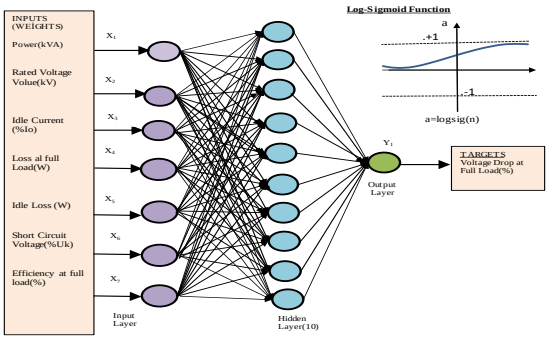

Figure 3. Weight and target values of the ANN model for the estimation of transformer voltage drop

TABLE III
NORMALIZED WEIGHT AND TARGET VALUES USED IN ANN TRAINING

Inputs	Weight and Target Data	Max.Values	Min. Values
X1	Transformer Power(kVA)	1	0
X2	Rated Voltage(kV)	1	0
X3	Idle Current(%Io)	1	0
X4	Loss at full Load (W)	1	0
X5	Idle Load (W)	1	0
X6	Short Circuit Voltage (%Uk)	1	0
X7	Efficiency at Full Load (%)	1	0
Y1	Voltage Drop at Full Load (%)	1	0

The graphs between the normalized data and transformer's voltage drop are shown in the part from Fig. 4 to Fig. 10.

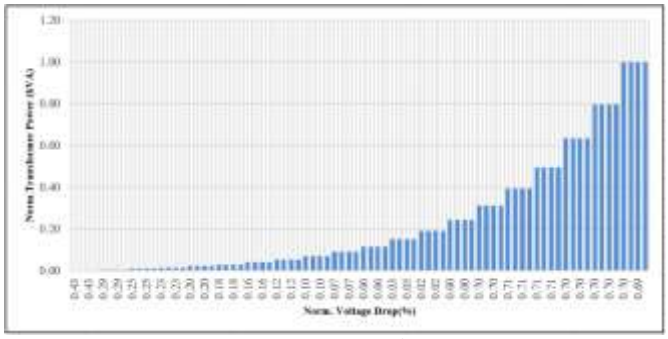

Figure 4. Graph between Norm.Transformer Power (kVA) and Norm.Transformer Full Load Voltage drop (%)

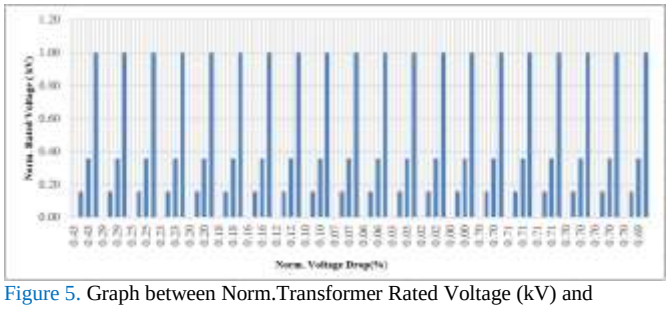

Figure 5. Graph between Norm.Transformer Rated Voltage (kV) and Norm.Transformer Full Load Voltage drop (%)

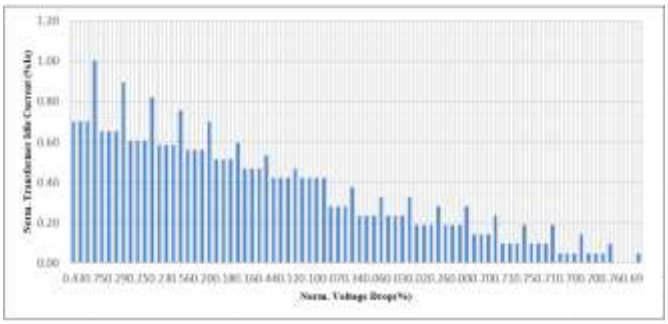

Figure 6. Norm. Transformer No-load Current (%Io) and Norm. Graph between transformer Voltage drop (%) at full

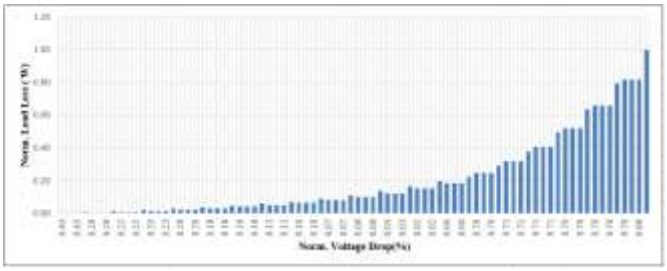

Figure 7. Graph between Norm.Transformer Load Loss (W) and Norm.Transformer Full Load Voltage Drop (%)

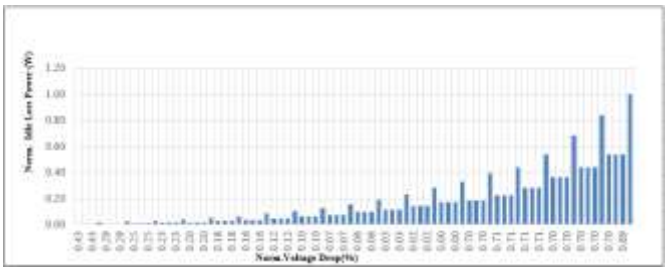

Figure 8. Norm. Graph between the No-load Loss power (W) of the transformer and the Norm.Transformer full load voltage drop (%)

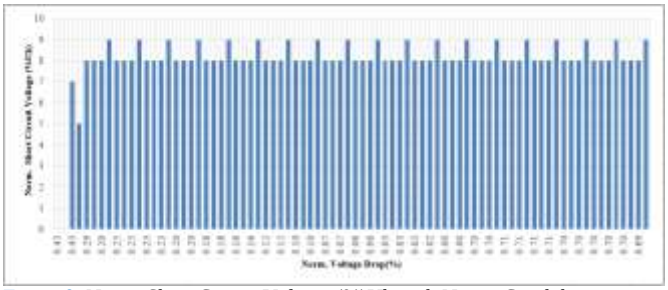

Figure 9. Norm. Short Circuit Voltage (%)Uk with Norm. Graph between transformer Voltage drop (%) at full load

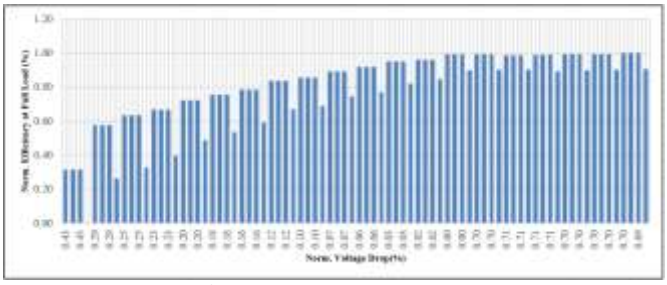

Figure 10. Norm. Transformer Full Load Voltage Drop (%) and Norm. Graph between Transformer Efficiency (%) at full load

In the defined model, feed-forward back propagation was selected as ANN model for the estimation of the transformer's voltage drop at full load. As seen in Table IV, TRAINLM was selected as the training function, and LEARNGDM was selected as the adaptive learning function. The MSE (Mean Squared Error) specified in equation (2) was used as the performance function. LOGSIG (Log-Sigmoid Transfer Function) was used as the transfer function.

$$MSE = \frac{1}{n}\sum_{i=1}^{n}\frac{(y_1 - y_2)^2}{n} \quad (2)$$

In the Equation;

n is the number of data points

y_1 represents observed values

y_2 represents predicted values

TABLE IV
FUNCTIONS AND DATA SELECTED IN THE ANN TRAINING

Network Properties		
Network Type	:	Feed-Forward backpropagation
Training function	:	TRAINLM
Adaption learning function	:	LEARNGDM
Performance function	:	MSE
Number of layers	:	2
Properties for	:	Layer 1
Tranfer Function	:	LOGSIG

The functions and data used in ANN training were as shown in Table 4. In Fig. 11.a, ANN model having 7 input values and 1 output value is shown. During the development of the model formed for ANN estimation, technical information of 560 transformers according to 7 different input variables was used. In Fig. 11.b., the percentages of data used in ANN trainings are shown.

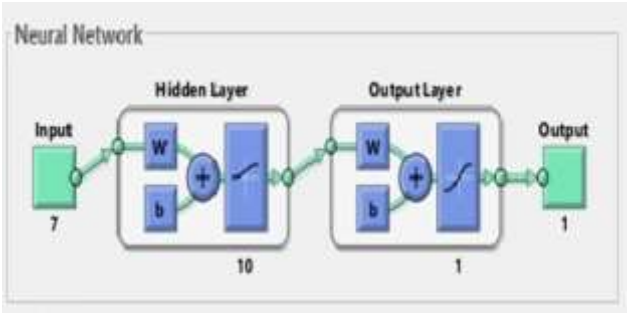

(a)

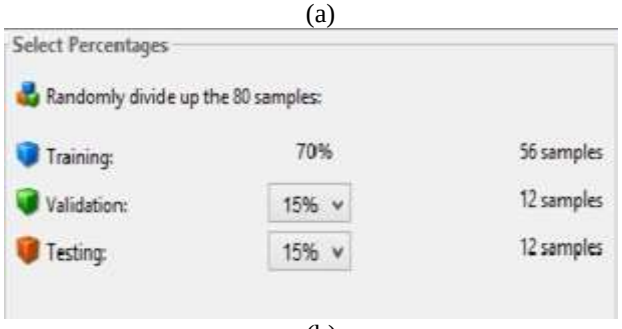

(b)

Figure 11. Defined ANN values and percentages

In the ANN training, the closest value was obtained in about the 114th iteration. As the result of this training, the values of training were found to be correct at a rate of 99.605%. It was observed that the validation values were correct at a rate of 98.651%, and that it was correct at a rate of 99.351% in ALL. As the correlation value

was equal to one, it was observed that there was perfect similarity between network output and target output.

After the completion of the training, it was observed that the known values and estimated values completely correspond with each other, and that they verify the requested estimation at a rate of 99%. There are also shown with Fig. 12 (a) column and Fig. 12 (b) line graphs.

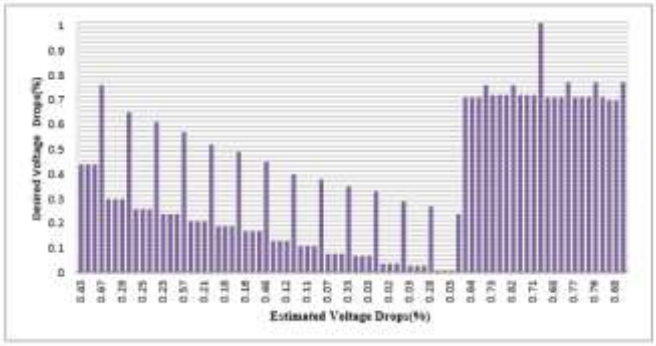

(a)

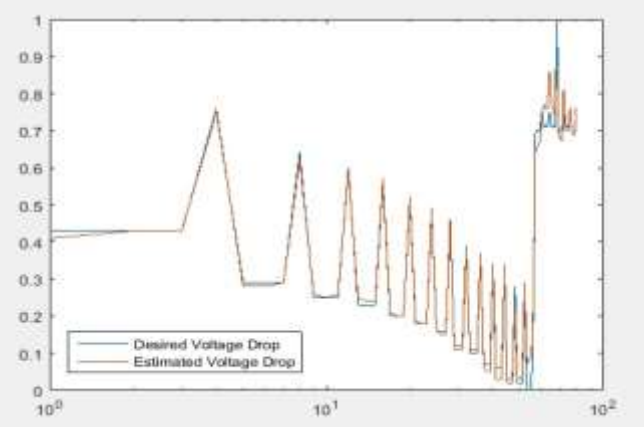

(b)

Figure 12. Graphs showing that Desired Voltage Drop values and Estimated Voltage Drops overlap in (a) and (b) graphs.

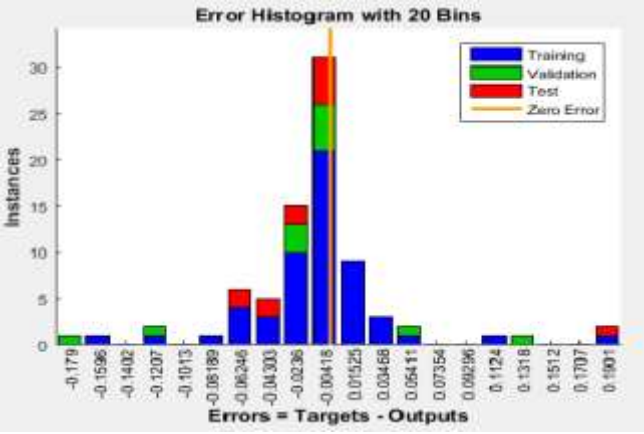

Figure 13. Error rate graph resulting from estimation

In Fig. 13, it is observed that the error rate between the estimations made with ANN after entry of the weight and target values in ANN, and the required values is about 1%.

4. CONCLUSION AND SUGGESTIONS

In this study, it was intended to show that it is possible to estimate the voltage drops through ANN as an alternative to theoretical and applied methods with respect to power transformers' voltage drop. It was observed that the ANN's estimation results and the known data were very close with an acceptable tolerance. In addition, in this study, less mathematical statements were used without having preliminary information regarding the system by the use of estimation method through ANN, and it was ensured to reach post-training results as faster and more accurately. By this study, it was observed that the real values and estimated values were very close, and that they were close to 1. It is considered that this will set a model for future similar studies.

REFERENCES

[1] Demirci, A., Akar, O., Terzi, U.K., Sonmezocak, T., Investigation of International Harmonic Standards in Power Systems, 4th International Mardin Artuklu Scientific Research Congress, 7-8 August 2020, Mardin, Turkey, pp.97-110.

[2] Das. J.C., Effects of Momentary Voltage Dips on the Operation of Induction and Synchronous Motors, IEEE Trans. on Industry Applications, Vol. 26, (1990), Issue. 4, pp. 711-717, https://doi.org/10.1109/28.55998

[3] Wang Y., Pahalawaththa, N.C., Powver System Load Modelling, POWERCON '98. 1998 International Conference on Power System Technology. Proceedings (Cat. No.98EX151), Beijing, China, 18-21 August 1998, pp.677-682. https://doi.org/10.1109/IECON.2007.4459952

[4] Taylor C. W., *Power System Voltage Stability*, Electric Power Research Institute - EPRI, McGraw-Hill, New York, NY, 1994

[5] Esen, V., Oral, B., Akıncı, T.Ç., The determination of short circuits and grounding faults inelectric power systems using time frequency analysis, Journal of Energy in Southern Africa, vol. 26, (2015), No. 2, pp. 123–132.

[6] IEEE Standards Association, IEEE Std 1159-2019, IEEE Power and Energy Society, USA, pp.1-96 https://ieeexplore.ieee.org/servlet/opac?punumber=8866826

[7] Meyer, F.J., Lee, K.Y., Improved Dynamic Load Model for Power System Stability Studies, IEEE Power Engineering Review, Vol. Per-2, (1982), No.9. pp.49-50. https://doi.org/10.1109/MPER.1982.5519488

[8] Sauer, P.W., Pai, M.A., *Power System Dynamics and Stability*, Department of Electrical and Computer Engineering, The University of Illinois at Urbana-Champaign, 1406 W. Green St., Urbana, IL 61801, 2006. Online available: (24.08.2022) https://courses.engr.illinois.edu/ece576/sp2018/Sauer%20and%20Pai%20book%20-%20Jan%202007.pdf

[9] Styvaktakis, E., Bollen, M.H.J., Gu, I.Y.H., Classification of Power System Events: Voltage Dips, Ninth International Conference on Harmonics and Quality of Power. Proceedings (Cat. No. 00EX441), IEEE, 2000, 2 pp.745-750. https://doi.org/10.1109/ICHQP.2000.897771

[10] Yun, S.-Y., Kim, J.-C., An Evaluation Method of Voltage Sag using a Risk Assessment Model in Power Distribution Systems, Elsevier Science LTD, Electrical Power and Energy Systems, 25, (2003), 10, pp. 829-839. https://doi.org/10.1016/S0142-0615(03)00063-2

[11] Akar, O., Terzi, U.K., Ozgonenel, O., Location of transformers during the extension of an electricity distribution network, Electric Power Systems Research, Vol.211, (2022), No.1, pp.1-10. https://doi.org/10.1016/j.epsr.2022.108189

[12] Ozgonenel O, Decreasıng The Effect Of The Second Harmonıc Component For Power Transformer Protectıon, Journal of Polytechnic, Vol. 5, (2002), No: 3, pp. 221-225.

[13] Mirzai, M., Gholami, A., Aminifar, F., Failures Analysis and Reliability Calculation for Power Transformers, Journal of Electrical System, Vol.2, (2006), No.1, pp.1-12.

[14] Wang, M., Vandemaar, A.J., Srivastava, K.D., Review of condition assessment of power transformers in service, IEEE Electrical Insulation Magazine, Vol. 18, (2002), No. 6., pp. 12-25, https://doi.org/10.1109/MEI.2002.1161455

[15] Şengül M., Öztürk S., Arsoy A.B, at.al., Gerilim Düşmesi Süresinin Transformatör Mıknatıslanma Akımı Üzerindeki Etkileri, Academia, Accelerating the world's research, pp.1-5. Online available: (24.08.2022), https://academia.edu

[16] Campbell A., McHattie R., Backfilling the Sinewave – A Dynamic Voltage Restorer Case Study,IEE Power Engineering Journal, Vol. 13, (1999), No. 3, pp. 153-158.

https://doi.org/10.1049/pe:19990309

[17] Bollen M.H., *Understanding Power Quality Poblems, Voltage Sags and Interruptions*, Wiley-IEEE Press, New York ,2000.

[18] Styvaktakis E., Bollen M.H.J., Transformer Saturation after a Voltage Dip, IEEE Power Engineering Review ,Vol. 20, (2000), No.4, pp. 62-63.

[19] Guasch L., Pedra J., Effects of Symmetrical Voltage Sags on Three-Phase Three-Legged Transformers, IEEE Transactions on Power Delivery, Vol. 19, (2004), No.2, pp. 875-883. https://doi.org/10.1109/TPWRD.2004.825306

[20] Maksan, Online available: (24.08.2022) https://www.doganates.com/userfiles/images/maksan.pdf

[21] Akpinar, K.N., Ozgonenel, O., Optimization of Artificial Neural Network for Power Quality Disturbances Detection, 2019 7th International Istanbul Smart Grids and Cities Congress and Fair (ICSG) IEEE,Istanbul, Turkey, 2019, pp. 95-98. https://doi.org/10.1109/SGCF.2019.8782429

[22] Kalogirou S.A., Applications of Artificial Neural Networks in Energy Systems a Review, Energy Conversion and Management, 40,(1999), 10, pp.1073-1087. https://doi.org/10.1016/S0196-8904(99)00012-6

[23] Jin L.V., Summary of Artificial Neuron Model Research. Industrial Electronics Society, 33rd Annual Conference of the IEEE Industrial Electronics Society, Taipei, Taiwan, 5-8 Nov.2007, pp.677-682 https://doi.org/10.1109/IECON.2007.4459952

[24] Ozgonenel, O., Wavelet based ANN approach for transformer protection, International Journal of Electronics and Communication Engineering, Vol. 2, (2008), No.6, pp. 1277-1284.

[25] Freeman, J.A., Skapura, D.M., *Neural Networks: Algorithms, Applications, and Programming Techniques*, Addison-Wesley Publishing Company, 1991.

[26] Micheletti N., Chandler J.H., Lane S.N., Investigating the geomorphological potential of freely available and accessible structure-from-motion photogrammetry using a smartphone, Earth Surf. Proc. Land. 40, (2015), 4, pp.473-486. https://doi.org/10.1002/esp.3648

[27] Saglam, S. Akar, O., Oral, B., Estimation of Solar Radiation Using Artificial Neural Network with Meteorological Data of Marmara University Goztepe Campus, International Conference on Science and Technology, Vol.1 Prizren, Sırbistan, 05-09 Eylül 2018, pp.695-704

[28] Arslan A., Ince R, The neural network approximation to the size effect in fracture of cementitious materials, Engineering Fracture Mechanics, Vol.54, (1996), No.2, pp. 249-261 https://doi.org/10.1016/0013-7944(95)00140-9

[29] Fausett, V.L., *Fundamentals of Neural Network:Architectures, Algorithms* And Applications, Prentice-Hall, 1994.

[30] Ozgonenel, O. Terzi, U.K, Akar, O., Kurt, U., Discrimination of magnetizing inrush and internal fault currents based on stockwell transform and ANN approach for transformer protection ", 2019 11th International Conference on Electrical and Electronics Engineering (ELECO) IEEE, Appl. (CIC), Bursa, Turkey, 2019, pp. 96–100. https://doi.org/10.23919/ELECO47770.2019.8990377

[31] Davarci Ok, Z., Sahin, M., Akar, O., "Estimation by ANN of Luminous Efficacy of Lamps Used for Lighting",Balkan Journal of Electrical and Computer Engineering, Vol. 10, (2022), No.2, pp. 187–197, https://doi.org/10.17694/bajece.1022960

BIOGRAPHIES

Onur AKAR was born in 1981 in Giresun. He received his undergraduate, graduate and doctorate degrees from Marmara University in 2005, 2011 and 2020, respectively. He worked as a lecturer at Istanbul Gedik University between 2010-2020. He served as the Head of Electricity Program at Istanbul Gedik University between 2012-2015. He served as the Head of the Department of Electricity and Energy between 2021-2022 as an assistant professor in the Department of Electricity and Energy of the same university. He is still working as an Assistant Professor Marmara University, Vocational School of Technical Sciences. His research interests include Control Systems, Renewable Energy Systems, Power Systems and Lighting Systems.

European Journal of Technique

journal homepage: https://dergipark.org.tr/en/pub/ejt

Vol.12, No.2, 2022

Application of Heuristic Assembly Line Balancing Methods to Lighting Automation Industry

Yelda Karatepe Mumcu[1*]

[1*]Marmara University, Department of Electricity and Energy, Istanbul, Türkiye. (e-mail: ykaratepe@marmara.edu.tr).

ARTICLE INFO

Received: Oct., 18. 2022
Revised: Dec., 07. 2022
Accepted: Dec, 10. 2022

Keywords:
Assembly Line Balancing
Heuristic Assembly Line Balancing Methods
Hoffman Method
Comsoal Method
Lighting Automation Manufacturing

Corresponding author: *Yelda Karatepe Mumcu*

ISSN: *2536-5010* | e-ISSN: *2536-5134*

DOI: https://doi.org/10.36222/ejt.1191203

ABSTRACT

The assembly line balancing problem is an important issue for every manufacturing company. A balanced assembly line ensures that a product is produced in the optimum time, and as a result of this effect, less machinery, materials and labour are used during this production. In this article, theoretical information about assembly line balancing has been given, and then the data needed for assembly line balancing has been obtained by making a time study of the production of Downlight Luminaire. With these data obtained, assembly line balancing was done and compared by using Hoffman and Comsoal methods. The aim of this study is to investigate the applicability of Hoffman and Comsoal methods, which are one of the heuristic assembly line balancing methods, in the assembly lines of the companies producing in the lighting sector.

1. INTRODUCTION

Assembly lines, whose main feature is to transfer work pieces from one station to another, are places where product parts and components are put together and processed in different ways [1].

Assembly line balancing, which is also defined as the allocation of work pieces to operating systems, is also expressed as providing the processes needed during product formation to assembly stations in order to reduce lost time [2].

Assembly line balancing methods according to the way they are produced; it is divided into three groups as single model, multi model and mixed model assembly lines [3-5].

Assembly line balancing methods-based solution approaches are threefold: Heuristic methods, analytical methods and simulation techniques [6].

The heuristic methods in the literature are given in the Table I. [7-10].

In this study, time studies of Downlight Luminaire production which are examined in assembly line balancing are carried out and the data which are necessary for balancing are obtained.

With the parallel of these obtained data, assembly line balancing studies are performed by heuristic methods which are called Hoffman Method and Comsoal Method. The results which are obtained by applying heuristic method after studies of assembly line balancing is given.

When the studies on this subject are examined, very few studies have been found in the literature.

In his study, Ling examined the Cold Cathode Fluorescent Lamp assembly production line and achieved more stability, increased efficiency and satisfactory results in the production line [11].

In his study, Yao examined bottleneck workstations on the lamp assembly line and issues affecting line production capacity, such as redundant capacity. To overcome these shortcomings, he proposed a new line balancing scheme [12].

Saptari and colleagues conducted a case study on the assembly line of an electrical accessory manufacturer in Malaysia. The productivity of the existing assembly line has been examined. They proposed an assembly line setup based on the Line Balancing Method [13].

The aim of this study is to create assembly lines which have the highest line efficiency and to reveal the applicability of heuristic assembly line balancing method on lighting automation manufacturing assembly line.

2. EXPERIMENTAL STUDY

In this research Downlight Luminaire is analysed. All the necessary data and measurements within the scope of the study were obtained from the company X, which produces

downlight Luminaire. The model of the analysed Downlight Luminaire is shown in Fig. 1.

Figure 1. Model of Downlight Luminaire

TABLE I
HEURISTIC METHODS

Ranked Positional Weight Method (Helgeson-Birnie)
Hoffman Method
Enumeration Method (Jackson)
Moddie-Young Method
Basic Heuristic Method
Related Activity Method (Agrawal)
Raouf-Tsui-Elsayed Method
Shortest Path Method (Klein-Gutjahr)
Grouping Method (Tonge)
Probabilistic Assembly Line Balancing Method (Elsayed-Boueher)
Candidate Matrix Method (Salveson)
Kilbridge-Wester Method
Comsoal Method
Dynamic Programming Method (Karp-Held-Shareshian)

The Downlight Luminaires production which is shown above consists of 3 main parts including body, frame and power supply. The Downlight Luminaire is produced when parts are treated in appropriate machines according to operation order. Fig. 2. shows production flow that is necessary for producing the Downlight Luminaire.

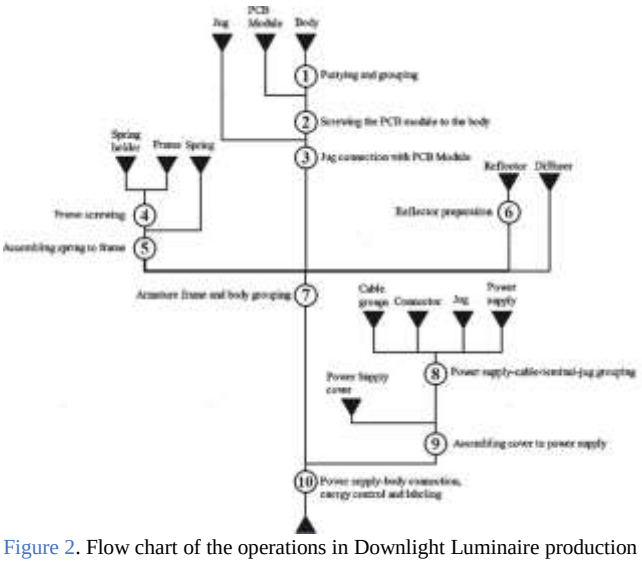

Figure 2. Flow chart of the operations in Downlight Luminaire production

2.1. Time Study and Assembly Line Balancing Studies

Time study provides needed information to design, to plan, to organize and to control the production process [14].
The most widely technique among time study techniques used in the companies is the time study, in other words it is called the stopwatch technique.
All operation durations are measured by using stopwatch to determine the standard time of production of Downlight Luminaire.

As these measurements are being done, the data on how many measurements are necessary to be done for each operation are provided by means of the formula given below. These measurements are repeated by considering the data which are generated. In this statistical method, several pre-observations (n^1) are conducted firstly. Afterwards the formula given Eq. 1 is solved for 95.45 security level and ± 5% error margin [15].

$$n = \left(\frac{40\sqrt{n^1 \sum x^2 - (\sum x)^2}}{\sum x} \right)^2 \quad (1)$$

Where;

n is Actual Sample Size, n^1 is number of pre-observations, x is measured time.
Afterwards the standard time is calculated for each operation by using formula shown Eq. 2.

$$ST = MT \cdot R + MT \cdot R \cdot t \quad (2)$$

Where;

ST is standard time (minute), MT is measured time (minute), R is performance (%), t is tolerance (%) [16].
The durations obtained as a result of the measurements which are done for each operation by considering tolerance share, performed performance assessments, the arithmetic mean of performance rates in terms of PM which are measured by using stopwatch are shown in Table II. As it is shown in Table II, Downlight Luminaire production in assembly line involve in 10 operations and total production duration of Downlight Luminaire is 4.802 minutes.
Assembly line balancing studies are carried out according to Downlight Luminaire production which consists of 10 operations which are shown in Fig. 3 with its diagram. The operation time which belongs to Downlight Luminaire production, machines which are used during this operation and previous operations are shown in Table II.

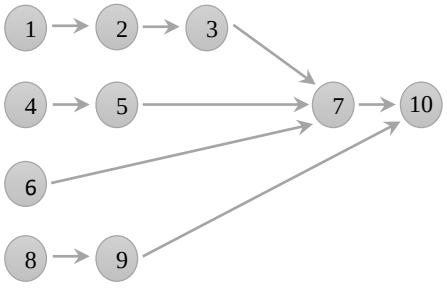

Figure 3. Priority diagram for Downlight Luminaire

Loss of balance of assembly lines, their efficiency and their daily total production amount is estimated by using formulas which are given Eq. 3,4 and Eq. 5.

$$LB = \left[\frac{(nC - \sum C_0)}{nC} \cdot 100 \right] \quad (3)$$

$$LE = (1 - LB) \cdot 100 \quad (4)$$

$$PA = \frac{T}{C} \quad (5)$$

Where;

LB is Loss of Balance (%), *LE* is Line Efficiency (%), *C* is Cycle Time (minute), *n* is Total Number of Work Stations (number-unit), C_o is Average of Work Station Time (minute), *PA* is Daily Total Production Amount (unit) and *T* is Daily Total Production Time (minute) [10].

In all assembly line balancing studies which are carried out within the scope of this study, it is supposed that handwork operations are done by all operators on condition that operations are done by same type of machines.

TABLE II

OPERATION TIMES, USED MACHINE TYPES AND PREVIOUS OPERATIONS FOR DOWNLIGHT LUMINAIRE

Ope. No.	*Operations*	*Machine Type*	*Ope. Times (min.)*	*Prev. Ope.*
1	Puttying and grouping	Hand-made	0.477	-
2	Screwing the PCB module to the body	Electric screwdriver	0.405	1
3	Jug connection with PCB module	Hand-made	0.444	2
4	Frame screwing	Electric screwdriver	0.711	-
5	Assembling spring to frame	Hand-made	0.683	4
6	Reflector preparation	Hand-made	0.416	-
7	Armature frame and body grouping	Electric screwdriver	0.594	3-5-6
8	Power supply – cable – terminal – jug grouping	Hand-made	0.489	-
9	Assembling cover to power supply	Hand-made	0.183	8
10	Power supply – body connection, testing and labelling	Hand-made	0.400	7-9
		Total Time	**4.802**	

2.2.1. Hoffman Method

Before the method can be applied; if i precedes j, 1 is written at the intersection of the columns (i and j) of the matrix, otherwise, the priority matrix is developed by giving the value 0 to all the rest. So that the priority item can be used to generate all possible work item permutations, each column of the matrix is summed together to form a row matrix called "code numbers". The originally obtained sequence of code numbers (row matrix) has as many elements as the number of work items, at least one of which is zero. The next steps are explained in detail on the example of line balancing work for downlight luminaire [1].

Firstly, priority matrix is designed as assembly line is being constituted by using Hoffman Method (Table III-a). There are 4 operations (1, 4, 6 and 8) which have rate 0 in code number array. The operation numbered 1 which is the first one among them is assigned to 1st work station. The cycle time is 1.35 minute. As the time of the first operation is 0.477 minute, remaining work station time is calculated as C-t_1 = 1.35 - 0.477 = 0.873 minute. The time of second operation which have rate 0 (the operation numbered 4) is 0.711 minute. It is shorter than remaining time of 1st work station and the operation numbered 4 can be assigned to 1st work station.

To make an assignment to 2nd work station, a new priority matrix is obtained by crossing out line and column numbered 1 and 4 in priority matrix (Table III-b).

The first rate 0 which is left to right in code number array can be seen in operation numbered 2. As this operation cannot be assigned to 1st work station it is assigned to 2nd work station. Remaining time of 2nd work station is calculated as C-t_2 = 1.35 - 0.405 = 0.945 minute.

The time of the second operation which has rate 0 (operation numbered 5) is 0.683 minute. As it is shorter than remaining time of 2nd work station, the operation numbered 5 is assigned to 2nd work station. The remaining time of 2nd work station is calculated as C-t_5 = 0.945 - 0.683 = 0.262 minute.

To make an assignment to 3rd work station a new priority matrix is designed by crossing out lines and columns numbered 2 and 5 in the priority matrix (Table III-c).

The first rate 0 which is left to right in code number array can be seen in operation numbered 3. As this operation cannot be assigned to 1st and 2nd work station it is assigned to 3nd work station. Remaining time of 3nd work station is calculated as C-t_3 = 1.35 - 0.444 = 0.906 minute.

The time of the second operation which has rate 0 (operation numbered 6) is 0.416 minute. As it is shorter than remaining time of 3nd work station, the operation numbered 6 is assigned to 3nd work station. The remaining time of 3nd work station is calculated as C-t_6 = 0.906 - 0.416 = 0.490 minute.

The time of the third operation which has rate 0 (operation numbered 8) is 0.489 minute. As it is shorter than remaining time of 3nd work station, the operation numbered 8 is assigned to 3nd work station. The remaining time of 3nd work station is calculated as C-t_8 = 0.490 - 0.489 = 0.001 minute.

To make an assignment to 4rd work station a new priority matrix is designed by crossing out lines and columns numbered 3, 6 and 8 in the priority matrix (Table III-d).

The first rate 0 which is left to right in code number array can be seen in operation numbered 7 (0.594 minute). As this operation cannot be assigned to 1st, 2nd and 3rd work station it is assigned to 4th work station. Remaining time of 4nd work station is calculated as C-t_7 = 1.35 - 0.594 = 0.756 minute.

The second rate 0 which is left to right in code number array can be seen in operation numbered 9. As this operation cannot be assigned to 1st work station it is assigned to 3nd work station. Remaining time of 2nd work station is calculated as C-t_9 = 0.262 - 0.183 = 0.079 minute.

To make an assignment a new priority matrix is designed by crossing out lines and columns numbered 7 and 9 in the priority matrix (Table III-e).

The time of second operation which have rate 0 (the operation numbered 10) is 0.400 minute. It is shorter than remaining time of 1st work station. It is longer than remaining time of 1st, 2nd and 3rd work station and the operation numbered 10 can be assigned to 4st work station.

TABLE III

SOLUTION MATRIX

Op.	1	2	3	4	5	6	7	8	9	10
1	0	1	0	0	0	0	0	0	0	0
2	0	0	1	0	0	0	0	0	0	0
3	0	0	0	0	0	1	0	0	0	0
4	0	0	0	0	1	0	0	0	0	0
5	0	0	0	0	0	1	0	0	0	0
6	0	0	0	0	0	0	1	0	0	0
7	0	0	0	0	0	0	0	1	0	0
8	0	0	0	0	0	0	0	0	1	0
9	0	0	0	0	0	0	0	0	0	1
10	0	0	0	0	0	0	0	0	0	0
Code No	0	1	1	0	1	0	3	0	1	2

(a)

Op.	2	3	5	6	7	8	9	10
2	0	1	0	0	0	0	0	0
3	0	0	1	0	0	0	0	0
5	0	0	0	1	0	0	0	0
6	0	0	0	0	1	0	0	0
7	0	0	0	0	0	1	0	0
8	0	0	0	0	0	0	1	0
9	0	0	0	0	0	0	0	1
10	0	0	0	0	0	0	0	0
Code No	0	1	0	0	0	1	0	2

(b)

Op.	3	6	7	8	9	10
3	0	0	1	0	0	0
6	0	0	1	0	0	0
7	0	0	0	0	1	0
8	0	0	0	0	1	0
9	0	0	0	0	0	1
10	0	0	0	0	0	0
Code No	0	0	2	0	1	2

(c)

Op.	7	9	10
7	0	0	1
9	0	0	1
10	0	0	0
Code No	0	0	2

(d)

Op.	10
10	0
Code No	0

(e)

As it can be seen in the assignment example which is done for 1st, 2nd, 3rd and 4th work station, one can achieve a solution. The solution results according to designing assembly line by using Hoffman Method are shown Table IV.

TABLE IV

LINE BALANCING RESULTS

Workstation No	Ope. No	Machine Type	Time (min.)	Total Time for Workstation (x)	Remaining Time (C-x)
1	1	Hand-made	0.477		
	4	Electric screwdriver	0.711	1.188	0.162
2	2	Electric screwdriver	0.405		
	5		0.683	1.271	0.079
	9	Hand-made	0.183		
		Hand-made			
3	3	Hand-made	0.444		
	6	Hand-made	0.416	1.349	0.001
	8	Hand-made	0.489		
4	7	Electric screwdriver	0.594		
	10		0.400	0.994	0.356
		Hand-made			
Total Time			***4.802***	***4.802***	***0.598***

As it can be deduced from Table IV, the assembly line is designed according to having 1.35 minute cycle time with 4 work stations. Loss of balance and assembly line efficiency of designed assembly line are shown Eq. 6 and 7.

$$LB = \left[\frac{(4 \cdot 1.35) - (4.802)}{(4 \cdot 1.35)}\right] \cdot 100 = 11.074\% \qquad (6)$$

$$LE = (1 - 0.11074) \cdot 100 = 88.925\% \qquad (7)$$

2.2.3. COMSOAL Method

To be able to apply this method, the table which is shown below must be designed (Table 5-a). In the first column of the table, operation numbers are shown. In the second column, the Amounts of the Previous Operation (APO) are shown. In the third column, Operation Without Previous Operation (OWPO) takes place.

While assignments for work stations are being made, first operation among the operations which is written in 3rd column is chosen respectively. The selected operation is deleted from 1st column and table is created again. Factors which immediate the chosen operation and haven't other factors that follow them are added to 3rd column. This procedure continues until cycle time at the station and work factors runs short and they are not able to assign new factors. After then it is started to make assignments to next stations.

In Table V, the all of steps of applying the method are given as in the example.

TABLE V

SOLUTION STAGES OF PROBLEM USING OF COMSOAL METHOD

Op. No	APO	OWPO
1	0	1
2	1	4
3	1	6
4	0	8
5	1	
6	0	
7	3	
8	0	
9	1	
10	2	

(a)

Op. No	APO	OWPO
2	0	2
3	1	4
4	0	6
5	1	8
6	0	
7	3	
8	0	
9	1	
10	2	

(b)

Op. No	APO	OWPO
3	0	4
4	0	6
5	1	8
6	2	
7	3	
8	0	
9	1	
10	2	

(c)

Op. No	APO	OWPO
4	0	4
5	1	6
6	0	8
7	2	
8	0	
9	1	
10	2	

(d)

Op. No	APO	OWPO
5	1	6
6	0	8
7	2	
8	0	
9	1	
10	2	

(e)

Op. No	APO	OWPO
6	0	8
7	2	
8	0	
9	1	
10	2	

(f)

Op. No	APO	OWPO
9	0	9
10	1	

(g)

Op. No	APO	OWPO
10	0	10

(h)

In the Table V which is schemed while applying the method, the operation numbered 1 which is written in 3rd column is selected for first work station assignment. Number 1 operation is assigned to the 1st work station. Remaining time of the 1st work station is calculated as C-t_1 = 1.35 - 0.477 = 0.873 minute.

In the Table V-b the operation numbered 2 (0.405 minute) in 3rd column is selected. The time of the operation is shorter than the residual time of 1st work station (0.873 minute) and can be assigned to 1st work station. Remaining time of the 1st work station is calculated as C-t_2 = 0.873 - 0.405 = 0.468 minute.

In the Table V-c the operation numbered 3 (0.444 minute) in 3rd column is selected. The time of the operation is shorter than the residual time of 1st work station (0.468 minute) and can be assigned to 1st work station. Remaining time of the 1st work station is calculated as C-t_3 = 0.468 - 0.444 = 0.024 minute.

In the Table V-c the operation numbered 4 (0.711 minute) in 3rd column is selected. The time of the operation is longer than the residual time of 1st work station (0.024 minute) and cannot be assigned to 1st work station and it is assigned to the 2nd station. Remaining time of the 2nd work station is calculated as C-t_4 = 1.35 - 0.711 = 0.639 minute.

In the Table V-d the operation numbered 5 (0.683 minute) in 3rd column is selected. Since the time of the operation is longer than the residual time of 1st and 2nd work station (0.024 minute - 0.639 minute) and cannot be assigned to 1st and 2nd work stations it is assigned to the 3rd station. Remaining time of the 3rd work station is calculated as C-t_5 = 1.35 - 0.683 = 0.667 minute.

This procedure continues until cycle time at the station and work factors runs short and they are not able to assign new factors. After then it is started to make assignments to next stations.

TABLE VI

LINE BALANCING RESULTS

Workstation Number	Ope. No	Machine Type	Time (min.)	Total Time for Workstation (x)	Remaining Time (C-x)
1	1	Hand-made	0.477	1.326	0.024
	2	Electric screwdriver	0.405		
	3		0.444		
		Hand-made			
2	4	Electric screwdriver	0.711	1.310	0.040
	6		0.416		
	9	Hand-made	0.183		
		Hand-made			
3	5	Hand-made	0.683	1.277	0.073
	7	Electric screwdriver	0.594		
4	8	Hand-made	0.489	0.889	0.461
	10	Hand-made	0.400		
	Total Time		***4.802***	***4.802***	***0.598***

As it can be deduced from Table VI, the assembly line is designed according to having 1.35-minute cycle time with 4 work stations. Loss of balance and assembly line efficiency of designed assembly line are shown Eq. 8 and 9.

$$LB = \left[\frac{(4 \cdot 1.35) - (4.802)}{(4 \cdot 1.35)}\right] \cdot 100 = 11.074\% \qquad (8)$$

$$LE = (1 - 0.11074) \cdot 100 = 88.925\% \qquad (9)$$

3. RESULTS

In this study, Downlight Luminaire production line balancing was done by using Hoffman and Comsoal methods, one of the heuristic assembly line balancing methods.

The results of the assembly line studies which are carried out by using Heuristic Methods are shown in the table below (Table VII). As can be seen from the table, line balancing was carried out with 4 workstations in the assembly line balancing work performed with both methods. When both methods are examined in terms of line efficiency, high line efficiency has been achieved with both methods.

When Table VII is examined, it is seen that the difference between the methods is due to the operation assignments made to the two workstations. In the Hoffman method, 2 operations were assigned to the 1st work station, while 3 operations were assigned in the Comsoal method. Likewise, 3 operations are assigned to the 3rd workstation in the Hoffman method, while 2 operations are assigned to the Comsoal method. This difference arises due to the uniqueness of the methods.

TABLE VII
RESULTS OF STUDIES FOR ASSEMBLY LINE BALANCING

	Assembly Line Balancing Methods			
Work-station	**Hoffman**		**Comsoal**	
	Op.	**Eff. (%)**	**Op.**	**Eff. (%)**
1	1 4	88.00	1 2 3	98.22
2	2 5 9	94.14	4 6 9	97.03
3	3 6 8	99.92	5 7	94.59
4	7 10	73.62	8 10	65.85
Line Eff. (%)	**88.925**		**88.925**	

4. CONCLUSION

The aim of this study is to examine the applicability of heuristic assembly line balancing methods to design the highest performing assembly lines in lighting automation companies.

Within the scope of the study, a line balancing study was carried out in a company that produces Downlight Luminaire with the methods of Hoffman and Comsoal, one of the heuristic methods. As a result of the line balancing work performed with both assembly line balancing methods, a high line efficiency of 89% was achieved. This has led to the conclusion that high efficiency production can be made with less labour, less time and therefore less cost. The results also showed that both methods can be used in lighting automation companies.

When the two methods are compared with each other, it is seen that the difference between them consists of the operations distributed to the workstations and there is no difference in terms of line efficiency.

This study also revealed that all companies operating in the electricity sector can achieve high line efficiency by using these methods in the production of different products.

With further studies on this subject, it will shed light on the applicability of the results that will emerge as a result of the application of the other Heuristic Methods, especially for researchers and manufacturers.

REFERENCES

[1] Kayar, M., Production and Productivity - Basic Principles and Applications, Ekin Press, Bursa, Turkey, 2012

[2] Erel, E., Sabuncuoglu, I., Aksu, B.A., Balancing of U-Type Assembly Systems Using Simulated Annealing, International Journal of Production Research, Taylor & Francis Ltd., 39 (2001), 13, pp. 3004-3015

[3] Acar, N., Estas, S., Kesikli Seri Üretim Sistemlerinde Planlama ve Kontrol Çalışmaları, Milli Prodüktivite Merkezi Yayınları, No:309, Ankara 3. Basım, Türkiye, 1991

[4] Scholl, A., Becker, C., A Survey on Problems and Methods in Generalized Assembly Line Balancing, European Journal of Operational Research, 168(2006), 3, pp. 694-715

[5] Scholl, A., Becker, C., State-of-the-Art Exact and Heuristic Solution Procedures for Simple Assembly Line Balancing, European Journal of Operational Research, 168 (2006), 3, pp. 666-693 https://doi.org/10.1016/j.ejor.2004.07.022

[6] Suresh, G., Vinod, V.V., Sahu, S., A Genetic Algorithm for Assembly Line Balancing, Production Planning and Control, 7 (1996), 1, pp. 38–46 https://doi.org/10.1080/09537289608930323

[7] Cengiz, K., An Application with Assembly Line Balancing and Simulation Approach on Discrete Manufacturing Flow Systems, MSc Thesis, Yıldız Teknik University, Istanbul, Türkiye, 2002

[8] Seber, S., Study of Line Balancing Application and Simulation Approach in a make-to-order Company, MSc Thesis, Yıldız Teknik University, Istanbul, Türkiye, 2004

[9] Karademir, H., Simulation Approach to Production Line Balancing and an Application, MSc Thesis, Yıldız Teknik University, Istanbul, Türkiye, 2005

[10] Kayar, M., Study of the Causes of Unproductiveness in Apparel Companies and Fieldwork Analysis for Their Solution, PhD Thesis, Marmara University, Istanbul, Turkey, 2008

[11] Ling, Z., Research on assembly line balancing based on electronic products, Proceedings of the 2015 International Conference on Mechatronics, Electronic, Industrial and Control Engineering, 2015, 1290-1293 https://doi.org/10.2991/meic-15.2015.294

[12] Yao, W., Study on Line Balancing for a Type of Lamp Assembling, Applied Mechanics and Materials, 63-64 (2011), pp 751-754 doi:10.4028/www.scientific.net/AMM.63-64.751

[13] Saptaria, A., Xin, LJ., Mohammad, NA., Optimizing Assembly Line Production through Line Balancing: A Case Study, Applied Mechanics and Materials, 761 (2015), pp. 104-108 10.4028/www.scientific.net/AMM.761.104

[14] Prokopenko, J., Productivity Management: A Practical Handbook, 2nd Edition, International Labour Office, Geneva, 1992

[15] Kanawaty, G., Introduction to Work Study, International Labour Office (ILO), 4th Edition, Geneva, 1992

[16] Türkmen, A., Yeşil Y., Kayar M., Heuristic production line balancing problem solution with MATLAB software programming, International Journal of Clothing Science and Technology, 28 (2016), 6, pp. 750-779

BIOGRAPHIES

Yelda KARATEPE MUMCU obtained her bachelor degree in Electricity Education Technology from the University of Marmara, Department of Electricity Education. She obtained MSc. degree in Electricity Education from the University of Marmara Institute of Pure and Applied Science in 2001. She obtained Ph.D. degree in Electricity Education from the University of Marmara Institute of Pure and Applied Science in 2006. She is working as an Assist. Prof.Dr. in University of Marmara, Vocational School of Technical Sciences, Department of Electricity and Energy. She has authored many publications in SCI Index Journals, national scientific journals and international conference proceedings. Her research interests include: Electrical and Electronics Engineering, Energy, Power System Analysis, Electric Power Transmission, Distribution and Protection, Artificial Neural Network.

European Journal of Technique

journal homepage: https://dergipark.org.tr/en/pub/ejt

Vol.12, No.2, 2022

Power Quality Analysis for Power Led Drives

Secil Genc [1], Okan Ozgonenel [2], Orkut Onat Yildiz [3] and İbrahim Hakki Kilic [3]

[1*]Ondokuz Mayis University, Electrical and Electronic Engineering Department, 55200, Samsun, Istanbul, Turkiye. (e-mail: secil.yilmaz@omu.edu.tr).
[2] Ondokuz Mayis University, Electrical and Electronic Engineering Department, 55200, Samsun, Istanbul, Turkiye. (e-mail: okanoz@omu.edu.tr).
[3]BORSAN, OSB Organize Sanayi Boulvard, Samsun, Tekkeköy, Samsun, Turkiye. (e-mail: orkutonatyildiz@borsan.com.tr).
[4] BORSAN, OSB Organize Sanayi Boulvard, Samsun, Tekkeköy, Samsun, Turkiye. (e-mail: ibrahimkilic@borsan.com.tr).

ARTICLE INFO

Received: Dec., 08. 2022
Revised: Dec., 20. 2022
Accepted: Dec, 23. 2022

Keywords:
Power quality
EMI
Conducted emissions
Harmonics

Corresponding author: *Okan Ozgonenel*

ISSN: *2536-5010* | e-ISSN: *2536-5134*

DOI: https://doi.org/10.36222/ejt.1216165

ABSTRACT

DC micro grids have grown increasingly popular in the energy grid in recent years, as distributed generation has increased. Distributed generation refers to small or large-scale renewable energy that is linked to the main power system. Renewable energy sources like solar and wind power help the local grid, but their output is inherently intermittent and unpredictable, interfering with regular grid operation. Some of these issues can be mitigated by using energy storage in conjunction with renewable energy. Renewable energy is often linked to the grid using power electronic converters.

The goal of this research is to simulate and evaluate transmitted emissions in the time and frequency planes using IEEE 1459 to investigate the impacts of DC / DC converters on DC lines, particularly for renewable energy generation. While there are standards and norms for frequencies up to 2 kHz and beginning at 150 kHz, the frequency range 2-150 kHz only has suggested techniques and propagation restrictions. As a result, the emission conveyed in the frequency range of 2-150 kHz is a subject that must be comprehended. The structure of the generation model, as well as the idea of power quality in electricity generating models, will be investigated using data collected through experimental and computer simulations on a medium-scale hybrid network connected to the grid. The technological advances acquired will subsequently be utilized to evaluate the power quality of various DC and AC single/three phase power systems (such as computer servers, airplanes, and so on).

1. INTRODUCTION

With the rise of distributed generation in recent years, DC microgrids have become increasingly widespread in the electrical grid. Distributed generation refers to small or large-scale renewable energy that links to the power grid. Wind energy, solar energy, geothermal energy, and biomass energy are all popular forms of renewable energy [1-6]. Photovoltaic cells generate direct voltage and current. Because the output of a solar cell varies depending on the weather, the regulation of such generation is done with the assistance of a DC-DC converter to regulate the power flow and voltage levels in microgrids. In a DC microgrid, DC-DC converters connect generation, energy storage, and loads, which are frequently externally networked via AC-DC converters.

There are several voltage levels of DC distribution lines. Power generating and diverse and distinct power sources (photovoltaic systems, micro turbines, wind farms, etc.), energy storage facilities (railways, subways, tram lines having various energy storage devices, roadside and on-board) (such as supercapacitors and batteries). They are all linked to a DC mains network of the same voltage level or, via converters, to a different voltage level. Furthermore, as renewable energy sources are integrated into the grid, interest in DC-DC and bidirectional AC-DC converters is growing. The usage of PWM-based converters is becoming more common as the utilization of renewable energy and battery technology grows. Aside from PWM-based converters, the growing usage of non-linear devices, electronic and electrical equipment such as SMPS, motors, fluorescent lights, electronic data processors, and power supply switches generates additional electromagnetic noise. This may have an impact on the system's stability. A DC microgrid's frequency range can range from extremely low (below 9 kHz) to very high (such as 9-150 kHz and 150 kHz-30 MHz) [7]. The increased use of DC-DC converters, which are frequently operated at higher switching frequencies, might result in electromagnetic interference (EMI) in the system. Above 2 kHz, these disruptions are referred to as "high frequency distortion" [8]. These conducted emissions have an impact on the AC mains side as well. The two primary implications of power quality problems on a distribution system are a power quality problem and the unfavorable impact on equipment (electrical loads) from power factor reduction induced by specific forms of harmonics. The Electrical Power Research Institute (EPRI) has suggested an end-user-centered definition of "power quality problem" as any power problem caused by voltage, current, or frequency variations that causes customer equipment to malfunction or mis operate. The emissions

produced by power converters used in distributed generation vary substantially not just along the time axis or in amplitude, but also across the frequency spectrum. All these components manifest as harmonics/high frequency interferences with varying amplitudes and consequences. These harmonics usually disrupt or destroy the operation of converters and other micro grid-connected devices [4], [9]. Currently, no limits are imposed by electrical distribution companies on transmitted radiated switching voltage sources, ballasts, or other equipment. However, it is apparent that emissions in this high frequency band have an impact on grid-connected devices [8]. Simultaneously, considering the EMI of the device at the original design phase will allow designers to meet electromagnetic compatibility at a reasonable cost before discovering it [10]. As a result, the power quality of these transmitted emissions should be investigated. While there are standards and norms for frequencies up to 2 kHz and beginning at 150 kHz, there are only suggested techniques and propagation limitations for frequencies between 2 and 150 kHz. As a result, new methods for frequencies in this range must be developed, or methods from other frequency ranges must be adapted [3]. There isn't enough research on the effect of high frequency disruptions on networks in the literature, it's been discovered. When the broadcasts are analyzed, it is discovered that there are insufficient research on the impact of transmitted emissions on the network. Ensini et al. [6] evaluated the effect of conducted emissions emanating from a single-phase DC-DC converter on the DC mains side in their study on the influence of transmitted emissions on the grid. Webling et al. [11] proposed a method for measuring the differential and differential mode transmitted emissions from switched-mode power sources. Jettanasen et al. investigated the nano-grid road lighting system's emitted emissions [4]. In general, power electronics switching topology in power electronics settings and electromagnetic waves propagating to the environment at MHz levels are stressed based on the transmitted propagation. Upper harmonic power quality issues have not been addressed since no study has been undertaken on the influence of released emissions into our country's grid. The strongest motivations for working in this sector have been the increased impacts of transmitted emissions on the grid and the absence of any limits, especially with the widespread use of electric cars, which is one of the development goals.

The behavior of DC and AC systems (microgrids, lines, inverter/converter equipment, etc.) that will serve as a model for power quality studies will be described in this project. In contrast to the literature, a full overview of single-phase and three-phase DC and AC systems will be offered. The goal of this project is to improve power quality and solve electromagnetic compatibility issues in DC-DC and DC/AC alternating grid connections, particularly with the increased usage of electric cars. Recommendations for measuring, analyzing, and mitigating high frequency conducted emissions will be made. Methods and methods for exact dispersion analysis will be developed. Separate analyses will be performed on the common and difference mode conducted emissions reflected on the network.

This project aims to interpret computer simulation findings and provide reports. By standardizing the higher frequencies, it is intended to help to the optimization of the Turkish energy grid, the reduction of losses, and the enhancement of power quality. In this regard, TEİAŞ released in 2021 the technical standards for the grid connection of electricity storage facilities, their monitoring using SCADA, and their usage as supplementary services. However, the influence of high-frequency disturbances on the grid induced by power converters employed in between is overlooked in this regulation. With this project, awareness of power quality issues emerging from conducted emissions that will emerge as a result of the battery's integration into the grid will be promoted, and ideas for the diversification of quality indices will be developed. In other words, awareness will be promoted regarding the development of additional laws and the standardization of the new EPDK regulation.

2. RELATED WORKS

The process of collecting, evaluating, and interpreting measurable electrical signal data is known as power quality monitoring. During the data acquisition step, voltage and current are continually measured during a specific process. Experts assist in the analysis and interpretation process. Intelligent systems may be built and deployed using breakthroughs in signal processing and artificial intelligence to automatically transform and interpret measurable data into meaningful information with minimum human interaction. Current and voltage sensors are used to measure both AC and DC systems (measuring transformers, etc). Although DC/AC metering configurations are not the primary goal of this proposed project, the best metering setups for the most efficient power quality study/research will be offered. Measurement errors induced by measurement devices, as well as connecting points, will be investigated in terms of the idea of DC power quality.

Khilnani et al. conducted a power quality assessment of emissions from a microgrid-based DC/DC converter at 0-2kHz steady state and transient loading situations within the scope of prior research. They used the quick Fourier transform to assess the experimental data (FFT). To assess DC power quality, they employed the low frequency sinusoidal distortion index (percent LFSD) and the amplitude probability distribution (APD) of voltage and current [2]. Ensini et al. investigated conducted emissions between 9 and 150 kHz in terms of DC power quality as measured by DFSB, ripple index, and APD. They compared LFSD and APD findings using CISPR 15, CISPR 14, EN50065, and EN50160 standards at various intervals [6]. Webling et al. [11] proposed a method for calculating emissions from switched-mode power sources. The rising usage of non-linear technologies has created 'power harmonics,' resulting in worse power quality. Electromagnetic noise is produced by electronic and electrical equipment such as SMPS, motors, fluorescent lamps, electronic data processors, and power supply switches. The emission produced by the device under test (DUT) will be determined not only by its internal source (electronics), but also by the quality of the incoming AC mains power. Mahesh et al. investigated how voltage harmonics impact the conducted propagation caused by DUT. Based on the experimental data, they concluded that the existence of voltage harmonics at the LISN input has a considerable impact on the DUT propagations [13]. Larrson et al. took measurements in an apartment by filtering the conducted emissions from a fluorescent bulb lighting system for a set amount of time. To minimize the harmonic content of the current, almost all fluorescent lights with high frequency ballasts employ active power factor correction (PFC) circuits. When the filtered signal is inspected, it is discovered that the converter with active PFC oscillates because of its failure to manage the current near to zero crossover. These oscillations have frequencies ranging from a few kilohertz to more than ten kHz. A three-dimensional linear scale based on short time

Fourier transform (STFT) analysis is utilized to better understand where the energy of this high frequency oscillating signal is focused [12]. Spadacini et al. suggested a circuit model for conducting emission analysis of all subsystems of an electric vehicle powertrain that can reflect both functional, low-frequency behaviour and high-frequency impacts (battery, inverter, motor). It is linked to the interface established in LISN CISPR 25 between the battery and the DC power bus. The "current-probe method" and the voltage approach were compared in CISPR 25. They stressed the importance of probe location in the CISPR current-probe approach when very high-frequency components of conducted emissions (over 30MHz) are present [14]. Spadacini et al. also evaluated the influence of difference mode (DM) and common mode (CM) currents delivered from the inverter in electric vehicle engines on the EMI's lithium-ion batteries. DM and CM currents can enter batteries via AC cables, DC wires, and ground, affecting battery performance. They developed a SPICE model of the power drive system as well as a test platform to assess the effect of the power drive system's EMI on lithium-ion batteries. They demonstrated in their experiments that the voltage fluctuation range of an unfiltered battery is greater than that of a filtered battery owing to DM and CM currents [15]. Mutoh et al. concentrated on the 1 MHz or higher frequency transient EMI noise of common mode currents produced during switching operations in electric vehicle drive systems. The fast Fourier transform was used to evaluate high frequency voltage and current data. Control strategies for reducing EMI sounds have been presented [16]. Shall and Kadi assessed the electric vehicle charger's emitted and conducted emissions in the frequency range of 150 kHz to 108 MHz in accordance with CISPR 25 IEC:2008 guidelines [17]. Korth et al. used a high frequency modelling technique to achieve a more exact estimate of the battery's voltage response owing to a high frequency current surge [18]. When the studies are analyzed, LISN is the first instrument utilized to filter the conducted emissions. The LISN is a low-pass filter that is connected between the AC or DC power source and the DUT and offers a port for creating a certain impedance and monitoring radio frequency (RF) noise. Simultaneously, the signals are seen using an EMI receiver/spectrum analyzer or data capture card. Furthermore, EMI receivers use frequency scanning or, at very high frequencies, an FFT-based time domain scan. The spectrum of the input signal is measured and analyzed by these EMI receivers [19-20]. The harmonic spectrum of the signals may be determined when the signal is delivered to the computer utilizing data capture cards for better analysis using different analysis methods [21-22]. While the EMI receiver is using FFT, the signal sent to the computer environment may be examined and compared using STFT, wavelet transforms, and Fourier transforms with different window functions. Because unstable signals in the 2-150 kHz frequency range shift over time owing to their nature, an analytical technique is necessary. As a result, the disturbances must be examined not only in the frequency domain, but also in the time-frequency domain. Because the measured value is voltage, it is represented in µV. This unit must be represented in logarithmic form, namely dBµV, and compared to the limitations in the standard in order for the limits in the frequency spectrum and test standards to be more understood. The standards used for emissions in the 2-150 kHz frequency range are: CISPR 11, which sets the mandatory limit for emission from high performance scientific, medical, or industrial equipment, and electrical lighting systems, which set the same emission limits as the CISPR 11 standard but are a very common source of broadband upper harmonic disturbance. CISPR 15, which also specifies emission limits for active supply converters, IEC TS 62578, which describes the operating conditions and typical characteristics of active supply converters, EN50065 general and EN50065 industrial (the latter two differ after 100 kHz) power line communication standards, and Standard EN 50160, which expresses low voltage, medium voltage, and high voltage supply characteristics, voltage events, and variations [3].

3. MEASUREMENT of CONDUCTED EMISSIONS

3.1. Simulation works

Fig. 1 depicts a flowchart for observing the propagation transmitted from a DC-DC buck converter with 48 V output voltage used in DC power systems. The simulation was performed in the MATLAB™ environment in order to compare it to the actual mechanism that will be implemented in the future. For comparison, the low frequency sinusoidal distortion index (percent LFSDI), ripple index, and amplitude probability distribution of DC voltage and current were determined. To restrict the transmitted emissions, IEC TS 62578, CISPR 11-15, EN50065, and EN 50160 standards were applied in this investigation. Because there is currently no standard for determining if LFSDI and APD levels are acceptable, the transmitted emissions were tested for variable input voltage and load. Wavelet transform and discrete wavelet transform methods with varied window functions, which are among the approaches proposed in related studies, have been tested for 2-150 kHz EMI band range.

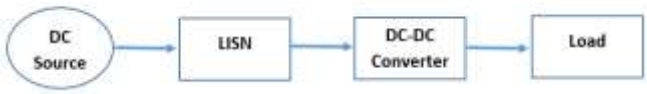

Figure 1. Flowchart of the system

MATLAB simulation circuit for power quality analysis of conducted emissions from DC-DC buck converter with varying input voltage and 48 V output voltage is given in Fig. 2. Simulation parameters are given as follows.

• Total simulation time=0.5 sec for enough the system reached steady state.

• Bandwidth: The frequency resolution has been taken as 5 ms for the collection of the signal in 200 Hz bands recommended by the EN 55065-1standard.

• Number of windows=Total time (0.5 sec)/ bandwidth (0.005 sec)=100

• Total number of samples=250000

• Number of samples in the window = Total number of samples (25000) / number of windows (100) = 2500

A time frame of 200msec is recommended by the IEC 61000-4-7 standard (5Hz frequency resolution). This scenario, however, is unsuitable for the processing of high frequency signals. As a result, the time window length for signal gathering in the 200Hz bands indicated by the EN 55065-1 standard and the standards covering frequency ranges below 150 kHz was set to 5msec.

This unit is given in logarithmic form, namely db µV, to make the restrictions in the frequency spectrum and test standards more accessible.

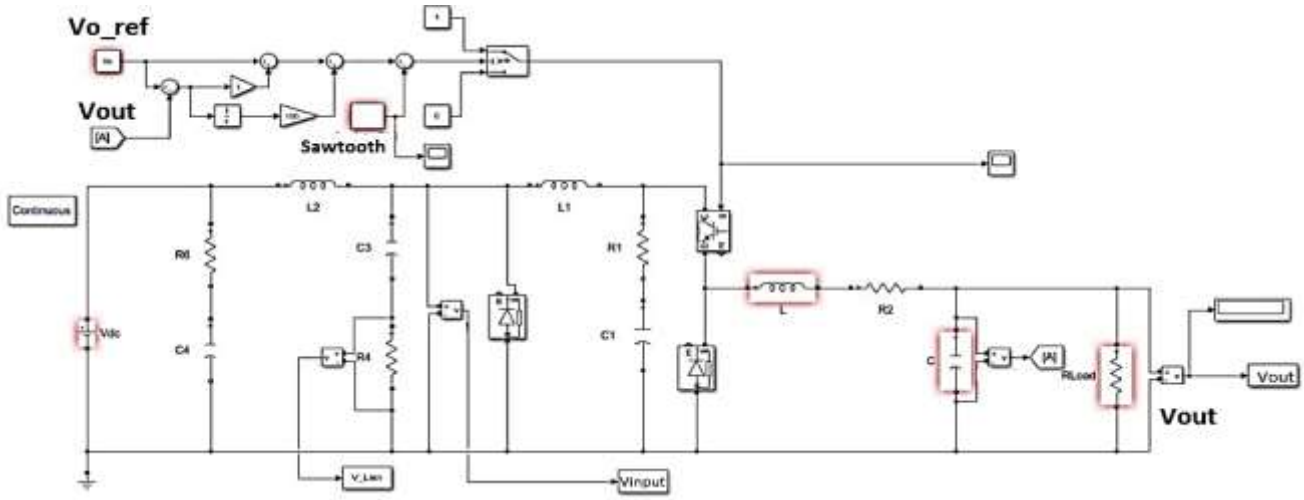

Figure 2. MATLAB simulation circuit for power quality analysis of conducted emissions from DC-DC converter

$$\mathrm{dbV} = 20\log(\mathrm{V}) \quad (1)$$

$$db\mu V = 20\log(V) \times 10^{6} \quad (2)$$

Fig. 3 shows the input and output voltages of the DC-DC converter, as well as the voltages measured over the LISN communicated to the network side when a 2900W load is attached, when the converter input voltage is 410V and the output voltage is 48V.

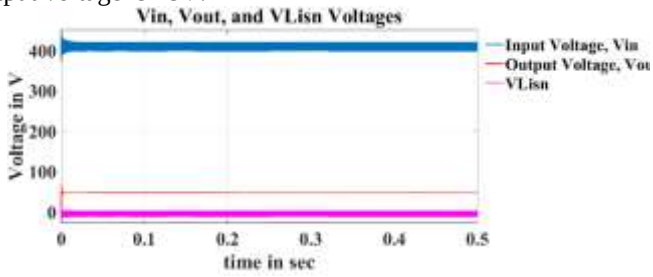

Figure 3. MATLAB simulation circuit for power quality analysis of conducted emissions from DC-DC converter

STFT analysis was done on the signal taken from the LISN output for 0.5 sec using 5msec time frames. Fig. 4 depicts the signal investigated in the 0-5msec time region. The Fourier analysis shows that, depending on the switching frequency of the converter, 20kHz and its multiples can be detected. The switching frequencies are only visible when samples are obtained above 6kHz (ignoring the transient).

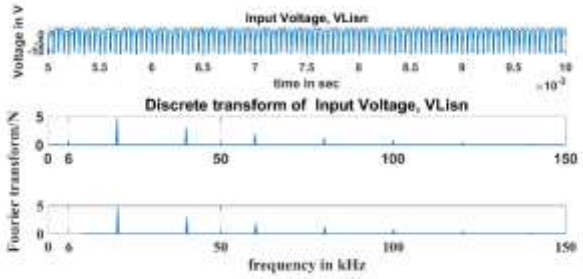

Figure 4. Amplitude variation of LISN voltage in time and frequency axis

3.2. Evaluation of conducted emission in terms of power quality indexes in DC systems

3.2.1. Distortion index

The frequency of the DC's fundamental component is zero. Instead of harmonic and internal harmonic components, Equation 3 expresses the overall effective value of low frequency sinusoidal disorder (DFSB). In Equation 3, Q[0] represents the steady-state DC value; Q[k] represents the frequency spectrum recorded for samples of q[n] over a particular time period (rms).

$$\mathrm{D} = \left[\sum_{\mathrm{k}>0}^{\mathrm{k_{max}}} (\mathrm{Q[k]/Q[0]})^2\right]^{1/2} \quad (3)$$

3.2.2. Ripple index

Equations 4,5 and 6 are used to compute the ripple index of DC-DC input voltage. Here, X_DC represents the mean DC component, X_i represents the time history sign, and X(e) represents the deviation from the mean. Due to the transient situation, samples after the first half of the 0.5sec total simulation time (after 0.25sec) were evaluated.

$$\mathrm{X_{DC}} = \frac{1}{N}\sum_{i=1}^{N} \mathrm{X_i} \quad (4)$$

$$\mathrm{X_e} = \sqrt{\frac{1}{N}\sum_{i=1}^{N} (\mathrm{X_i} - \mathrm{X_{DA}})^2} \quad (5)$$

$$\mathrm{X_e} = \frac{\mathrm{X_E}}{\mathrm{X_{DC}}} \quad (6)$$

3.2.3. Amplitude Probability Distribution (APD)

APD represents the likelihood that the interference will have a given amplitude value or more. Equation 7 calculates the APD value of the LISN output voltage. APD is the amplitude probability distribution, and FR(r) is the additive distribution function.

$$\mathrm{X_{DC}} = \frac{1}{N}\sum_{i=1}^{N} \mathrm{X_i} \quad (7)$$

4. INTRODUCTION EVALUATION of RESULTS for DC-DC BUCK CONVERTER

In simulation studies, samples obtained for 0.5sec in the simulation were evaluated by scrolling through 5msec frames. The signal's assessment in the 5-10msec time frame is shown in Figs. 5 and 6. Fig. 5, shows CE under varying load conditions. According to the result, for this window length CE exceeds the limit for EN50065 standard and increase with the load. The APD analysis depicts the probable magnitude increase from the steady state for DC voltage. As seen in Fig. 6, APD also increases with the load.

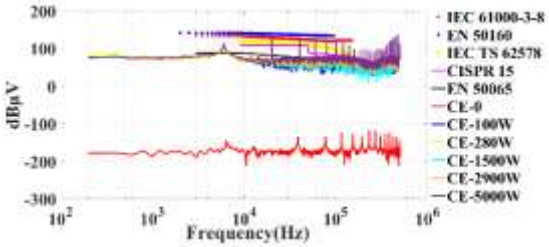

Figure 5. Variation of conducted emissions depending on load in case of 5-10msec window length, 410V input voltage

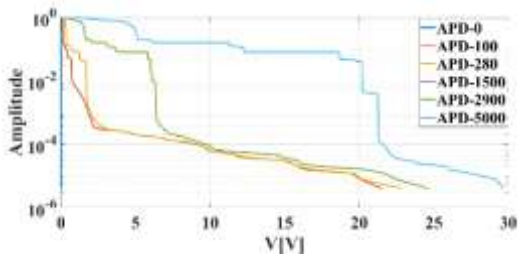

Figure 6. Change of APD depending on load in case of 5-10msec window length, 410V input voltage

Table 1. 5-10 ms Window interval, LFSD-9, LFSD-150 and variation of ripple depending on load in case of 410V input voltage.

TABLE I
POWER QUALITY RESULTS FOR VARYING LOAD CONDITION

LFSD-9	LFSD-150	Ripple	Load (W)	Voltage (V)
7E-15	7E-15	1E-15	0	410
0.79	0.79	6E-5	100	410
0.49	0.49	1E-5	280	410
0.82	0.82	9E-5	1500	410
0.83	0.83	1E-4	2900	410
0.69	0.69	0.03	5000	410

The following figures are obtained in the case of 5kW load condition.

Fig. 7 shows APD variation under varying input voltage. As seen in Fig. 7, the variation of APD decrease with the voltage. Adversely, as illustrated in Fig. 8, CE variation rises with input voltage.

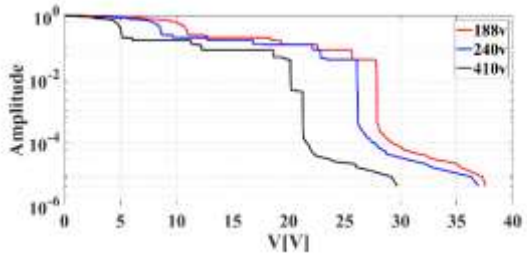

Figure 7. 5-10msec window length, variation of APD depending on input voltage at 5000W load

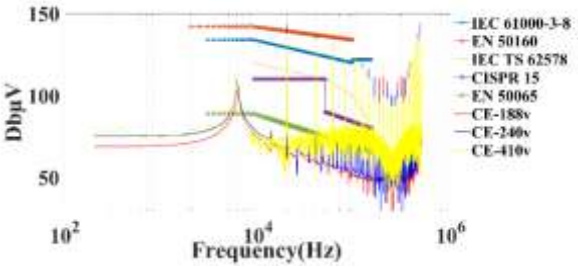

Figure 8. 5-10msec window length, variation of transmitted emissions depending on input voltage at 5kW load

Table 2. Variation of LFSD-9, LFSD-150 and ripple depending on load in case of different input voltage in case of 5-10msec window interval and 5kW load.

TABLE II
POWER QUALITY RESULTS FOR VARYING SUPPLY CONDITION

LFSD-9	LFSD-150	Ripple	Load (W)	Voltage (V)
0.69	0.69	0.12	5000	188
0.86	0.87	0.08	5000	240
0.69	0.69	0.03	5000	410

5. SPECTOGRAM

The spectrogram generates a feature vector that shows the energy change of the harmonic in the frequency bands over time and allows you to see where the major signal energy is focused. Fig. 9 depicts the spectrogram of the STFT-based signal. The use of a spectrogram is necessary since it was unclear if a 6 kHz harmonic signal is transient or not. According to the result, the harmonic can be observed only at the first energizing moment and not at subsequent sampling times. Depending on the switching frequency, harmonics of 20kHz and their multiples are observed during switching frequency.

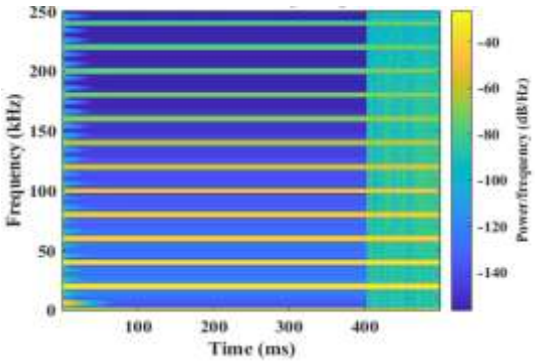

Figure 9. Spectrogram of EMI signals

6. WAVELET ANALYSIS

6.1. Discrete wavelet transform

Because STFT has a fixed frequency resolution, it poses problems. A wide window improves frequency resolution but degrades temporal resolution. A small window provides excellent temporal resolution but poor frequency resolution. These are known as narrow-gap transformations and wide-range transformations, respectively. Wavelet packet decomposition of the digitized signal is an alternative to the STFT-based technique. Instead of a discrete number of frequency components as in the Fourier transform, the wavelet transform separates the signal into numerous frequency ranges.

Figure 10 shows the discrete wavelet transform. Because the sampling frequency is 500kHz and the upper frequency is 250kHz due to the Nyquist theorem, the high and low frequency components are shown in Fig. 13. Normally, this iterative procedure is repeated until the number of samples remains constant. The application's criterion is based on achieving the best answer with the aid of 'entropy.'

$$k = \log_2 N \tag{8}$$

where N is the number of sampled signals and k is the resolution level. Since each window contains 2500 samples, the resolution level that may be reduced, k, is determined to be 11. When the 11th level of Mallat's wavelet tree (Fig. 13) is inspected, it offers the resolution of frequencies less than 50 Hz. Table 3 shows MDL findings for the sampled signal at 5-10 ms time intervals with an input voltage of 410V and a load of 1500W. When wavelet families were evaluated within themselves, the most suitable families were determined to be db20 from the Daubechies family, sym3 from the Symlets family, coif2 from the Coiflet family, bior5.5 from the biorthogonal family, reverse biortogonal rbio2.6, dmey from the discrete Meyer family, and fk22 from the Fejér-Korovkin filter family. Among the wavelet families, db20 with the lowest MDL was picked as the best fit.

TABLE III
VARIATION OF RIPPLE DEPENDING ON DIFFERENT WINDOW STATES IN CASE OF 410 V INPUT VOLTAGE

Filter	MDL	Filter	MDL	Filter	MDL	Filter	MDL
db1	52.8	sym2	49.6	coif1	51.6	rbio1.1	52.8
db2	49.6	**sym3**	**47.5**	**coif2**	**51.1**	rbio1.3	53.8
db3	47.5	sym4	48.9	coif3	50.8	rbio1.5	52.8
db4	48.2	sym5	50.9	coif4	50.5	rbio2.4	49.7
db5	46.4	sym6	50	coif5	50.3	**rbio2.6**	**48.7**
db6	44.5	sym7	52.5	bior1.1	52.8	rbio2.8	49.762
db7	44.8	sym8	49.1	bior1.3	52.1	rbio3.3	45.2
db8	44.5	sym9	50.3	bior1.5	50.6	rbio3.5	44.1
db9	42.5	sym10	49.8	bior2.4	55.6	rbio3.7	45.2
db10	42.3	sym11	49.3	bior2.6	53.9	rbio3.9	44.1
db11	43.2	sym12	49.4	bior2.8	54.2	rbio4.4	50.9
db12	40.9	sym13	49	bior3.3	59	rbio5.5	50.5
db13	40.7	sym14	50	bior 3.5	56.1	rbio6.8	51.1
db14	41.9	sym15	50.2	bior3.7	55.7	dmey	49.8
db15	39.2	sym16	48.8	bior4.4	54.3	fk4	53.5
db16	39.8	sym17	49.8	**bior5.5**	**50.2**	fk6	48.04
db17	40.2	sym18	50.1	bior6.8	52.7	fk8	48.05
db18	37.9	sym19	50.7			fk14	47.2
db19	38.2	sym20	48.5			**fk22**	**44.7**
db20	**38.1**						

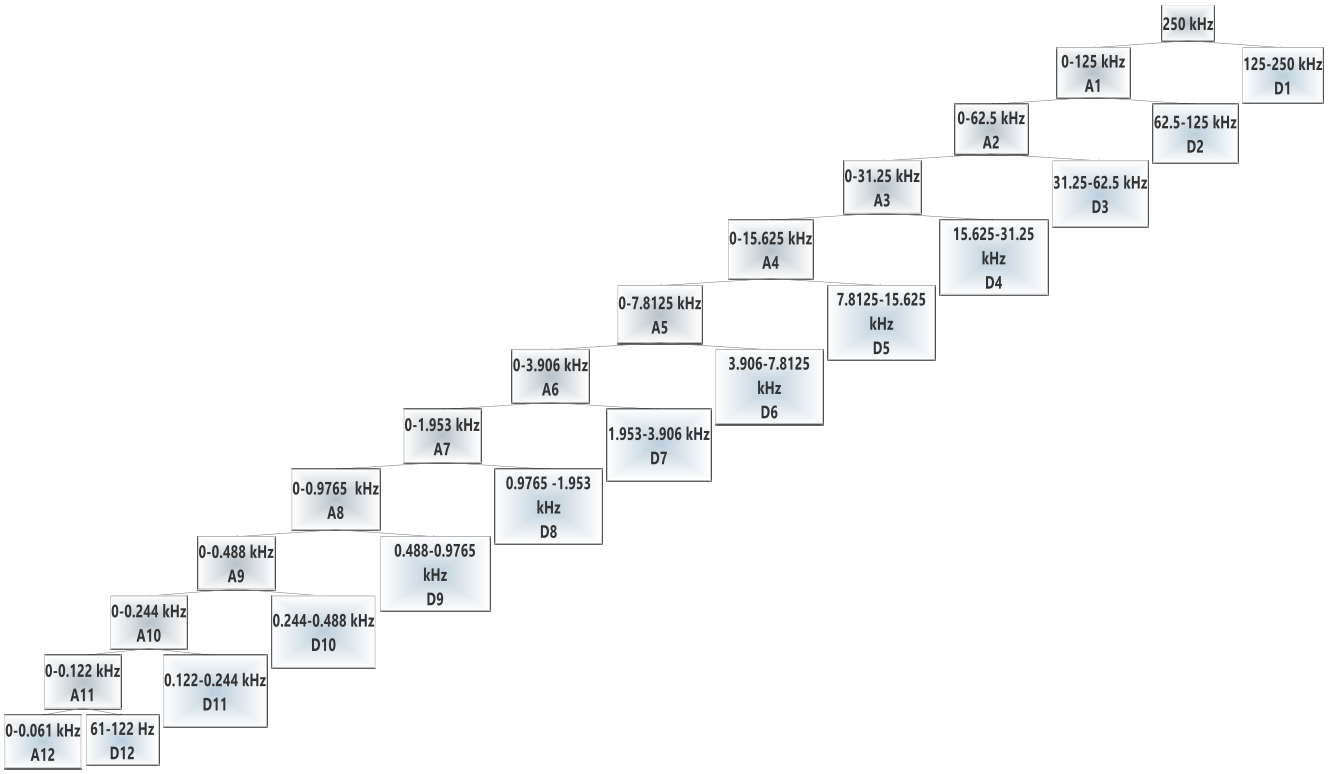

Figure 10. Approximation and detail coefficients of the analyzed signal and their frequency ranges

The appropriate decomposition level of the multiple resolution analysis was determined using Shannon entropy. This function computes the entropy of each resolution level. The level is determined by the point at which the approach and detail coefficients reverse direction. When the entropy curve in Fig. 11 is inspected, the approximation and detail coefficients for db20 change direction at the fourth level. Because we want to observe 50Hz in our research and our data load is not too high, we will need to go down to the 4th level for data load applications. As a result, it was requested to descend to the 11th floor and observe the 50Hz indicator.

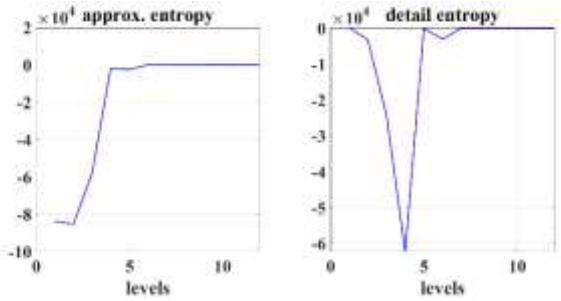

Figure 11. Calculation of the optimal decomposition level of Db20 wavelet families

Fig. 12 shows the energy levels of approximation and detail coefficients depend on db20 wavelet family.

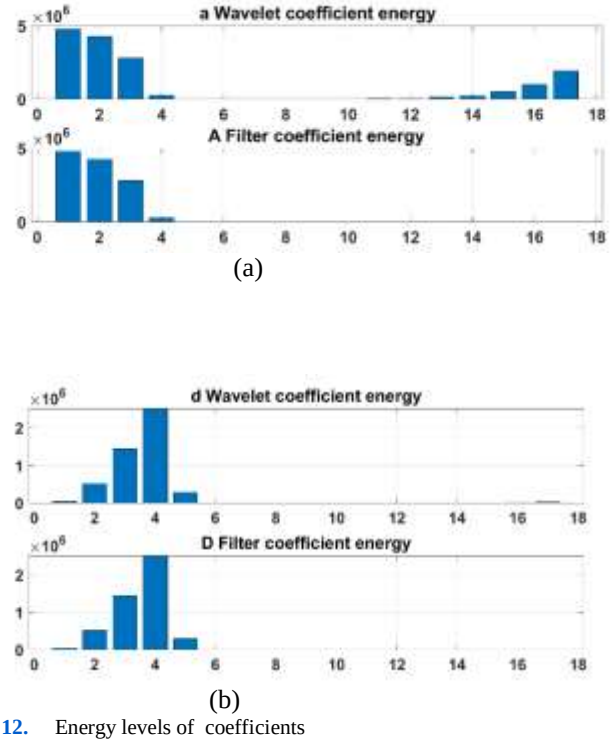

Figure 12. Energy levels of coefficients

The energy of the d wavelet coefficients suited for high frequency analysis is crucial in this study. When the energy of the d coefficients shown in Fig. 12 (b) is analysed, the d4 wavelet encompassing 20 kHz, which is the switching frequency, has the maximum energy. The switching signal d3 at 40kHz corresponds to the frequency range covered by the wavelet coefficient, 60kHz to the range covered by d2, and 6kHz to the range covered by d5 and d6. Because d5 has a larger frequency range, its energy stays greater than d6. Because the LISN device did not pass the 50 Hz low frequency signal, the d11 energy was insufficient

When using the 'multiresolution analyzer' toolbar from MATLAB™ tools. The energy of the signal obtained in wavelet transform 4th level analysis is approximately half of the energy of the whole signal. The influence of the filter coefficients will be especially important in filter designs to reduce harmful interference of EMI signals.

6.2. Multi-resolution analysis

The wavelet packet spectrum comprises the absolute values of the coefficients from the binary wavelet packet tree's frequency sorted end nodes. In wavelet packet transform, terminal nodes give the highest level of frequency resolution. J denotes the wavelet packet transformation level, while Fs is the sampling frequency. Equation 9 is used to compute the width of the band to the end nodes. The wavelet packet spectrum comprises the absolute values of the coefficients from the binary wavelet packet tree's frequency sorted end nodes. In wavelet packet transform, terminal nodes give the highest level of frequency resolution. J denotes the wavelet packet transformation level, while Fs is the sampling frequency. The width of the band to the end nodes is calculated by equation 9 [23].

$$\left[\frac{nFs}{2^{j+1}}, \frac{(n+1)Fs}{2^{j+1}}\right] \quad n = 0,1,2,3,\dots 2^{j} - 1 \tag{9}$$

Fig. 13 shows an example of a 2nd level wavelet tree structure in which the same logic decomposes at further levels to make the wavelet packet tree more accessible.

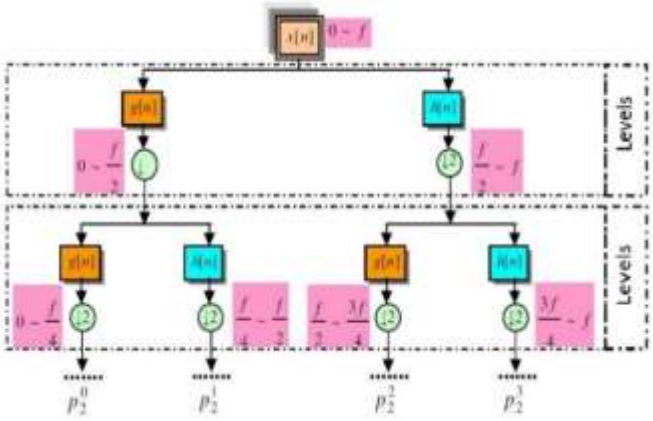

Figure 13. Energy change of the harmonic in the relevant frequency range according to the resolution level

Fig. 13 shows 2nd level multi-resolution analysis and its associated frequency ranges. Suppose that x(t) signal has N = 2^L samples and decomposed up to s. level packet analysis. In this case, here will be 2^s nodes/packets or frequency bands, and there are $2^{(L-s)}$ or N / 2^s wavelet packet coefficients in each level band. For m=0,1…..,2^s-1, wavelet packet coefficients of m node and k level is expressed as $p_s^{2m}[k]$ and calculated as follow:

$$X_{RMS}^{m} = \sqrt{\frac{1}{N}\sum_{k=1}^{N/2^s}\{p_s^m[k]\}^2} \tag{10}$$

When the wavelet tree analysis is done using the db20 family, which was chosen based on the Shannon entropy result, the effective value of the wavelet coefficients of each node is

determined using equation 10. Analysis up to level 6 is necessary to meet the frequency range criteria (above 2kHz). However, in the sixth level, the switching frequency corresponds to a signal with a frequency range of 27.344 - 31.250kHz and the greatest amplitude given in Fig. 14. The switching frequency is more readily noticed at the 11th level for the comparative assessment of wavelet packet analysis with STFT since there are nodes with a band gap of 122.0703 Hz. As a result, the switching frequency falls within the range of 29.785 - 29.907.

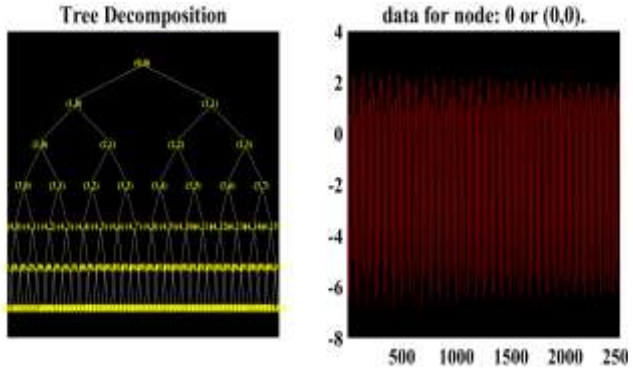

(a)

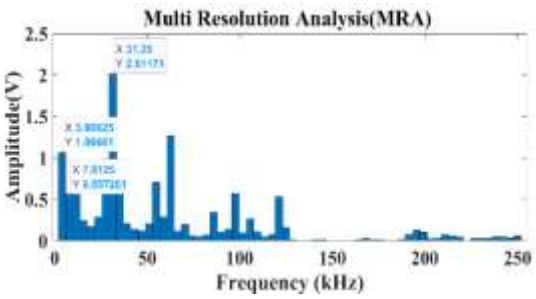

(b)

Figure 14. Energy change of the harmonic in the relevant frequency range according to the resolution level

In summary, discrete wavelet transform gives harmonics a wider band. MRA was used to harmonic analysis detailed to evaluate whether harmonic leakage exists. Wavelet analysis has performed an alternative for STFT. However, because wavelets cover a wide frequency range, they are inadequate for emissions investigation.

7. EMI FILTER for BUCK CONVERTER

It is necessary to utilize filters to reduce high-frequency noise because filters are frequently situated and created to satisfy standard criteria. Filtering makes a product less susceptible to any existing high-frequency noise in the environment while also preventing the product from causing high-frequency interference. Early design consideration of EMI could assist designers in efficiently meeting EMC regulations prior to implementation. To reduce design process and costs, EMI forecast should be properly taken care of by precise design. In this section in PSIM software environment suppression of noise was simulated and given in Fig. 17. PI controller of output voltage and LISN are seen in Fig. 15 and Fig. 16. Also, output voltage of converter is given in Fig. 18.

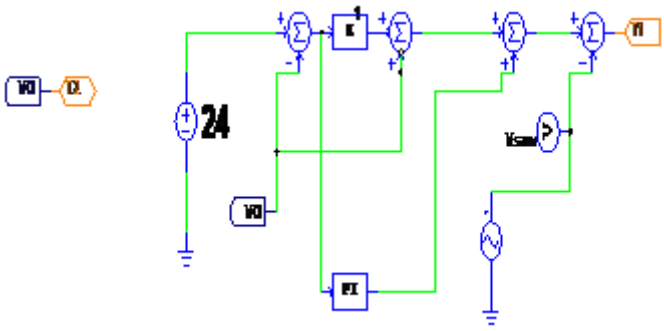

Figure 15. PI controller of buck converter

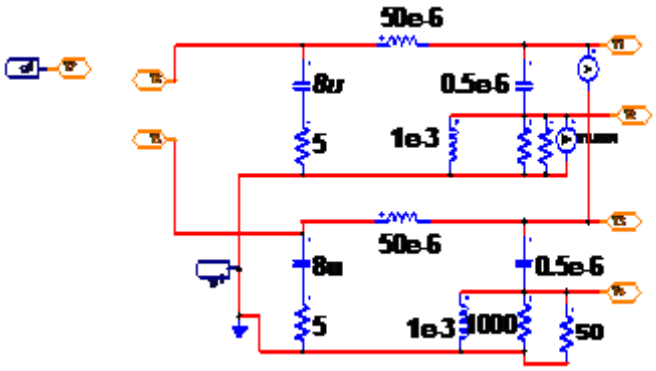

Figure 16. LISN device of buck converter

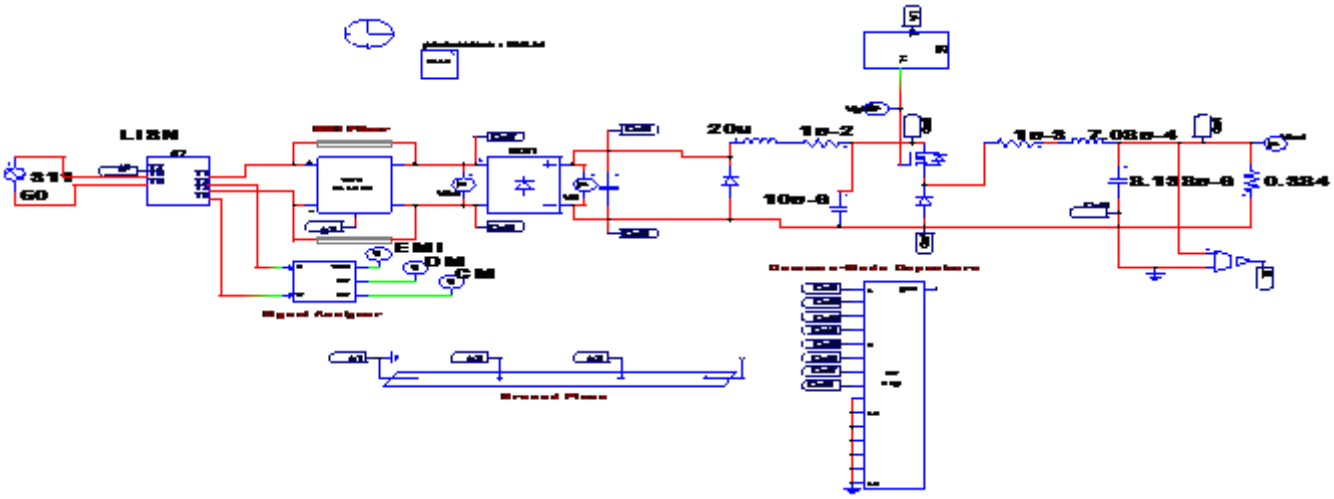

Figure 17. EMI Filter Design of Buck Converter (CISPR 22 Class-B)

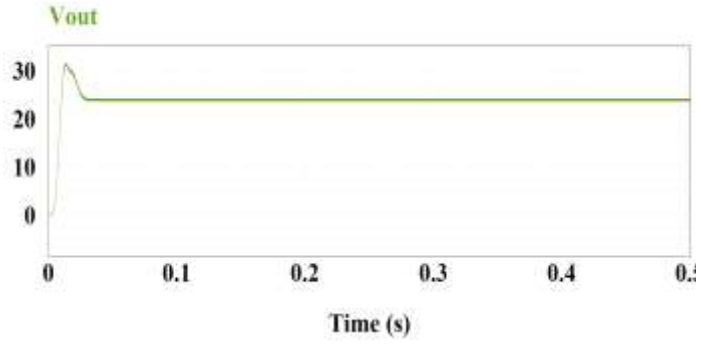

Figure 18. Output voltage of Converter

EMI, DM, and CM signals are obtained through 'signal analyzer' in the simulation and shown in Fig. 19.

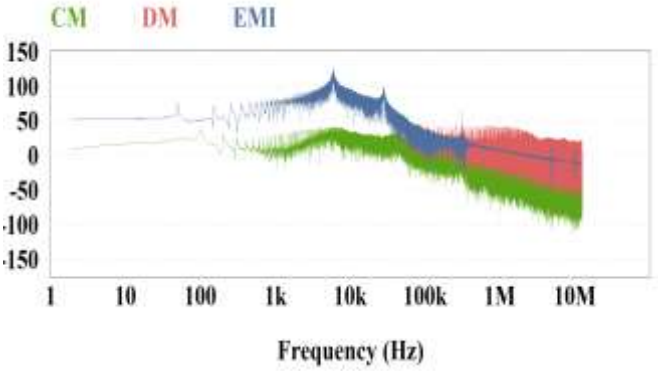

Figure 19. EMI, DM, and CM signals

For suppression of noise EMI filter parameters given in Table IV. When these filter parameters used for EMI filter, suppression of noise is supported with Fig. 20.

TABLE IV
EMI FILTER PARAMETERS

	Parameter	Value
EMI Filter	Filter enable	0
	Filter type	0
	Num. stage	1
	Cx	6.13nF
	R_Cx	0
	L_Cx	1.2µH
	Cy	2.04 nF
	R_Cy	0
	L_Cy	15.78 µH
	k_leakage_cm	0.05
	R_cm	0.1mΩ
	C_cm	0
	R_dm	0.1mΩ
	Cd	0
	R_Cd	0
Common Mode EMI	freq_cm_EMI	59.9kHz
	Amp_cm_EMI	55
	Amp_cm_EMI_Std	36.8
Differential Mode EMI	freq_dm_EMI	59.5kHz
	Amp_dm_EMI	128.6
	Amp_dm_EMI_Std	36.8
Common Mode Capacitance	Ccm1,Ccm2	500pF
	Ccm3,Ccm4, Ccm7,Ccm8	50pF
	Ccm5,Ccm6	100pF

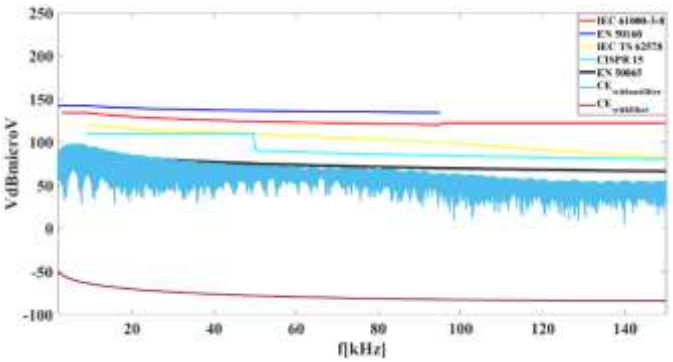

Figure 20. Suppression of noise

8. CONCLUSION

The goal of this project was to emphasize the importance of CEs, which will become more widespread as the use of electric vehicles and led driver grows in general. In this study power quality analysis of conducted emissions was performed for buck converter in MATLAB and PSIM software environments. The solution approach to reduce the power quality problem based on this converter is explained. Reducing CE with EMI filter design is difficult for power electronics applications, particularly inverters. Because a filter's design is unique to the circuit, it is necessary to construct a noise model of the circuit. In this research also, spectrum of the signals was calculated using the STFT technique in MATLAB™ tools for the evaluation of disturbances. The intended result could not be attained using db20, the most appropriate wavelet family for the signal among the standard wavelet families. The EMI requirements for converters because of international standards are discussed. It has been demonstrated that conducted emissions are higher in the case of nonfilter buck converter situation. As a result, the CE attenuation was preserved this buck converter system in PSIM. Another results are summarized as below:

• Power quality evaluation of DC-DC converter performed in Matlab simulation environment in terms of emissions.

• LFSD increased in loaded condition compared to unloaded condition. Considering the last half-time of the sampling time, which is out of the transient state, generally the CE to the grid side increases depending on the load increase.

• APD and ripple index decreased as the input voltage increased.

• CE and DFSB increase as the input voltage increases.

• While the DFSB index decreases in the last window intervals of the sampled time compared to the first time intervals, the fluctuation remains constant.

• When the spectrogram of the signal (analysis that gives the energy of the frequency dependent on time) of the 6 kHz frequency other than the switching frequency in the analysis with STFT is examined, it has been observed that this frequency does not occur during the entire sampling frequency, but during the temporary period. However, in wavelet transform, both low and high frequency analysis can be performed at the same time. At the same time, the change in frequency over time can be observed. For this purpose, when the discrete wavelet transform analysis was performed first, it

was seen that the energy of the relevant frequency range and the amplitude responses of the frequencies in the STFT were compatible. In order to make a more detailed and comparison, spleen packet analysis was performed by choosing the most suitable family from the traditional wavelet family. At the same time, the amplitude of the harmonics corresponding to the frequency range at the nodes was calculated to evaluate for the standard limits. However, since the response of the harmonics is incompatible with the STFT, it was thought that the analysis with the 'Vaidyanathan filter' used in the amplitude response of the harmonics in the wavelet packet analysis would be more appropriate.

ACKNOWLEDGEMENT

This work was supported in part by Ondokuz Mayis University under Projects PYO.MUH.1904.21.011 and PYO.MUH.1906.21.002

REFERENCES

[1] D D. Ritzmann, et al.,"Comparison of measurement methods for 2–150-kHz conducted emissions in power networks", IEEE Transactions on Instrumentation and Measurement,vol 70, pp. 1-10, 2020.

[2] A. D. Khilnani, et al. "Power quality analysis (0-2kHz) in DC/DC converters under steady state and transient conditions", presented at the International Symposium on Electromagnetic Compatibility-EMC EUROPE, Amsterdam, Netherlands, Aug. 2-5,27-30 2018.

[3] K. Niewiadomski, et al., "Time-domain assessment of data transmission errors in systems with multiple DC/DC converters", presented at the 2020 International Symposium on Electromagnetic Compatibility-EMC EUROPE, Rome, Italy, Sep. 23-25, 2020.

[4] A. Onur et al., "Determination of the optimum Hybrid renewable power system: a case study of Istanbul Gedik University Gedik Vocational School", Balkan Journal of Electrical and Computer Engineering, vol. 7, no.4, pp. 456-463, 2019.

[5] E. Aykut, et al. "Techno-economic and environmental analysis of grid connected hybrid wind/photovoltaic/biomass system for Marmara University Goztepe campus", International Journal of Green Energy, vol. 17, no.15, pp. 1036-1043, 2020.

[6] L. Ensini, et al. 2018. "Conducted emissions on DC power grids", presented at the 2018 International Symposium on Electromagnetic Compatibility (EMC EUROPE), Amsterdam, Netherlands, Aug, 27-30, 2018.

[7] D. Kumar, et al., "DC microgrid technology: system architectures, AC grid interfaces, grounding schemes, power quality, communication networks, applications, and standardizations aspects", IEEE Access, vol. 5, pp. 12230-12256, 2017.

[8] F. Leferink, "Conducted interference, challenges and interference cases", IEEE Electromagnetic Compatibility Magazine, vol. 4, no. 1, pp. 78-85, 2015.

[9] A. Mariscotti, "Discussion of power quality metrics suitable for DC power distribution and smart grids", presented at the Proc. 24th IMEKO TC4 Int. Symp, Sep. 17-20, Xi'an, China, 2019.

[10] M., Miloudi, et al.,"Common and differential modes of conducted electromagnetic interference in switching power converters", Rev. Roum. des Sci. Tech. Ser. Electrotech. Energ., vol. 62, no. 3, pp. 246–251, 2017.

[11] S. Weßling and S. Dickmann, "Prediction of conducted emissions produced by a DC-DC-converter using component parasitics and partial inductances", presented at the 2013 International Symposium on Electromagnetic Compatibility, Brugge, Belgium, Sep. 2-6,2017.

[12] E.A. Larsson, et al., "Measurements of high-frequency (2–150 kHz) distortion in low-voltage networks", IEEE Transactions on Power Delivery, vol. 25, no. 3, pp. 1749-1757, 2010

[13] F. Krug and P. Russer, "Quasi-peak detector model for a time-domain measurement system." IEEE Transactions on Electromagnetic Compatibility, vol. 47,no.2, pp. 320-326, 2005.

[14] G. Spadacini, et al., "Conducted emissions in the powertrain of electric vehicles", presented at the 2017 IEEE International Symposium on Electromagnetic Compatibility & Signal/Power Integrity (EMCSI), Washington, DC, USA, Aug 7-11, 2017.

[15] G. Spadacini, et al., "SPICE simulation in time-domain of the CISPR 25 test setup for conducted emissions in electric vehicles", presented at the 2015 Asia-Pacific Symposium on Electromagnetic Compatibility (APEMC), Taipei, Taiwan, May 26-29, 2015.

[16] A. Larrson, and M. Bollen “A proposal for emission and immunity of equipment including power-line communication.” [Online]. Available: https://www.arbenelux.com/wp-content/uploads/2017/11/Tekbox-TBOH01-LISN.pdf. [Accessed: 7-Dec-2022].

[17] N. Mutoh, et al., "Control methods for EMI noises appearing in electric vehicle drive systems", presented at the Twentieth Annual IEEE Applied Power Electronics Conference and Exposition, Austin, TX, USA, Mar, 6-10, 2015.

[18] H. Shall and M. Kadi, "Study of the radiated emissions of an electric vehicle battery charger during the charge cycle", presented at the 2015 IEEE 12th International Multi-Conference on Systems, Signals & Devices (SSD15), Mahdia, Tunisia,Mar 16-19,2015.

[19] P.K.P. Ferraz, et al., "A high frequency model for predicting the behavior of lithium-ion batteries connected to fast switching power electronics", Journal of Energy Storage, vol. 18, pp. 40-49,2018.

[20] T. Karaca, et al., "EMI-receiver simulation model with quasi-peak detector", 2015 IEEE International Symposium on Electromagnetic Compatibility, Dresden, Germany, Aug 16-22, 2015.

[21] T. Sonmezocak et al., "High performance adaptive high performance adaptive active harmonic filter design for nonlinear led loads", Light & Engineering, vol. 30, no.1, 2022.

[22] S. Dursun, et al., "Comparative analysis of lighting elements’ effects on electric system", European Journal of Technique (EJT), vol. 11, no. 2, pp. 153-164, 2021.

[23] V. Fahri, "RMS and power measurement using the dual-tree complex wavelet transform", Scientific Research and Essays, vol. 5, no. 18 pp. 2645-2655, 2010.

BIOGRAPHIES

Secil GENC was born in Elazıg in 1992. She received her B.Sc degree from Firat University in 2014 and M.Sc. degree from Ondokuz Mayis University in 2018. She is currently pursuing Ph.D. degree in Electrical and Electronics Engineering Department at Ondokuz Mayis University, Samsun, Turkiye. She is also a research assistant at Ondokuz Mayis University. Her research interests include power electronics, electromagnetic interference, renewables and machine learning.

Okan OZGONENEL was born in Samsun in 1967. He worked for Goztepe SSK Hospital as an engineer from 1989 to 1991. Then he received a special grant and promoted as Lecturer in Amasya Technical and Vocational Higher School by means of World Bank Second Industrial Training Project. He has worked there for 10 years and then joined Ondokuz Mayis University, Electrical & Electronic Engineering Department in 2002. He was promoted as full Professor in 2014 and since then he has been working for Ondokuz Mayis University where he is full time Professor. He joined The University of Nottingham many times for his post-doctoral studies.
His main research includes power system modeling, protection, and renewables.

Orkut Onat YILDIZ received his bachelor's degree in Materials Science and Ceramics Engineering from Dumlupnar University in 2011, and he is currently pursuing my master's degree in the Textile Engineering Department at Istanbul Technical University. He worked as a production manager at Işıldar Aydınlatma between 2013 and 2017, and as of 2019, He worked as a lighting group R&D and quality manager at Borsan Kablo ve Lighting. His specialties include 3D modeling and automation systems.

İbrahim Hakkı KILIÇ graduated from Karadeniz Technical University's Electrical Department in 2002 and He graduated from Anadolu University's Faculty of Economics in 2019. He worked as a laboratory supervisor at Borsan Kablo from 2006 to 2010, as a Quality Manager from 2010 to 2018, and as an R&D manager since 2019.
.